



Design of a horizontal axis wind turbine for experimental investigation in a large water towing tank

Master Thesis

Sascha Krumbein 406916

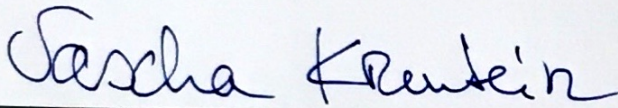
Scientifically graded by
Prof. Dr.-Ing. C. O. Paschereit
Supervised by
M.Sc. Marvin Jentzsch

April 27th, 2023
Berlin

Eigenständigkeitserklärung

Hiermit erkläre ich, dass ich die vorliegende Arbeit selbstständig und eigenhändig sowie ohne unerlaubte fremde Hilfe und ausschließlich unter Verwendung der aufgeführten Quellen und Hilfsmittel angefertigt habe.

Berlin, 27. April 2023



Sascha Krumbein

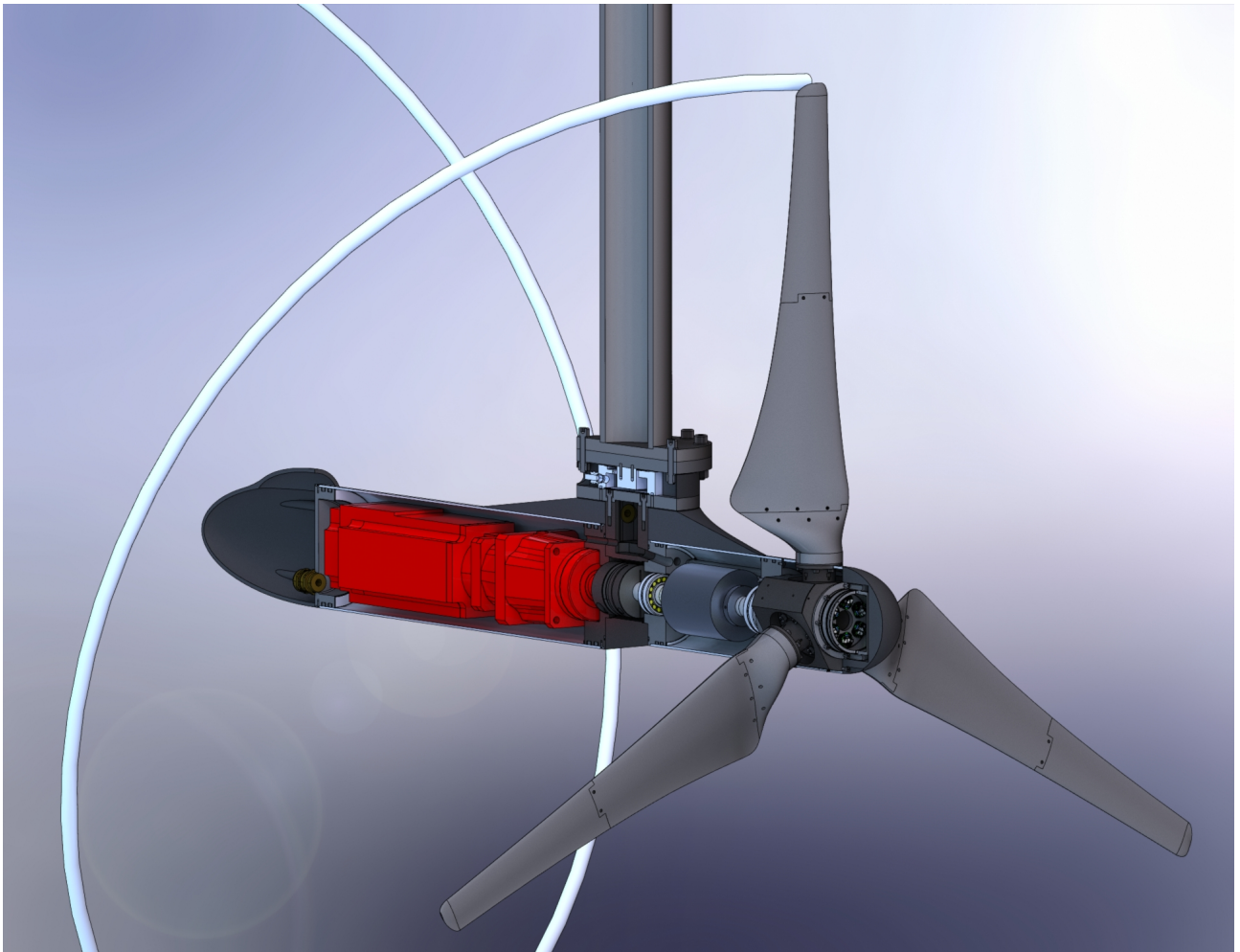
Abstract

This thesis presents the engineering workflow for designing a 1.3 m-diameter horizontal axis wind turbine model for measuring tip vortex instabilities in a large water towing tank (Underwater Berlin Research Turbine - UBeRT). A range of low-REYNOLDS number airfoils is investigated using XFOIL, regarding their aerodynamic properties and the risk of surface cavitation onset. From the remaining candidates, blades according to SCHMITZ are designed, for investigating the structural resistance of the airfoils. The generated aerodynamic loads are derived, utilizing QBLADE. Ultimately, a finalized set of blades is designed and analyzed, constituted by the SG6040 low-REYNOLDS number airfoil. The study includes the characterization of the rotor and considers the angle of attack, the bound circulation, the risk of surface cavitation, and an assessment of the induced tip vortices throughout the operational regime. A suitable drive train is tailored to the aerodynamic requirements of the rotor. A load-resisting tower and tow carriage connection is conceptualized. All critical test rig components are evaluated for their structural safety, using product design guidelines. Sensors for thrust, torque, angular velocity, and undisturbed inflow velocity are included in the design. Additionally, the turbine equips fully deployed WHEATSTONE bridges for measuring individual flapwise and edgewise blade root bending moments. A variety of sensors for assuring the operational safety are integral components of the UBeRT test rig. The permanent exposure to water requires all components to have a high resistance against corrosion. Furthermore, a sophisticated and comprehensive waterproofing concept is developed. In the future, the UBeRT test rig will enable unique underwater particle image velocimetry measurements of inherent instabilities of the tip vortex helix. Means of passively inducing accelerated wake decay at chordwise REYNOLDS numbers, approaching 8×10^5 will be developed. Such wind turbine wakes cause substantial losses of up to 20 % of annual energy production of modern-day wind parks. The projected combination of the engineered strategies with highly resolved computational fluid dynamic methods has the considerable potential to contribute significantly to fighting man-made climate change.

Kurzfassung

Die vorliegende Arbeit stellt den Entwicklungsprozess eines Modells einer horizontalachsigen Windenergieanlage mit einem Rotordurchmesser von 1.3 m, für Messungen in einem großen Wasserschleppkanal vor (Underwater Berlin Research Turbine - UBeRT). Verschiedene für niedrige REYNOLDSzahlen geeignete Profile werden hinsichtlich ihrer aerodynamischen Eigenschaften und ihrer Tendenz zur Kavitation in XFOIL untersucht. Auf Basis der verbleibenden Kandidaten werden SCHMITZ-Blätter entworfen, um die Profile bezüglich ihres strukturellen Widerstands zu untersuchen. Die dafür nötigen aerodynamischen Kräfte werden mithilfe von QBLADE erzeugt. Letztlich wird das SG6040 Profil für den UBeRT-Prüfstand ausgewählt und tiefgehend analysiert. Die Untersuchung umfasst die resultierenden Charakteristiken des Rotors, das Verhalten des Anströmwinkels und der gebundenen Zirkulation, die Einschätzung der Kavitationsgefahr und eine Vorabschätzung der entstehenden Spitzenwirbel. Verschiedene Betriebspunkte werden verglichen. Ein zu den Anforderungen des Rotors passender Triebstrang wird projektiert. Eine Turmstruktur und ein Anschluss an den Schleppwagen wird konzeptionalisiert. Alle kritischen Prüfstandkomponenten werden hinsichtlich ihrer Sicherheitsfaktoren unter Benutzung von gängigen Auslegungsrichtlinien bewertet. Im Design sind Sensoren für Schub, Drehmoment, Winkelgeschwindigkeit und ungestörte Anströmgeschwindigkeit enthalten. Zusätzlich ist der Prüfstand mit Blattwurzelbiegemomentsensoren an allen Blätter ausgestattet. WHEATSTONEsche Vollbrücken, basierend auf Dehnmessstreifen, messen dafür an jedem Blatt die auftretenden Biegemomente in Tangential- und Normalenrichtung. Eine Reihe von Sensoren zur Gewährleistung der Betriebssicherheit des Prüfstands ist integraler Bestandteil des Designs. In der Zukunft wird der UBeRT-Prüfstand einzigartige *particle image velocimetry* Messungen von inhärenten Instabilitätsphänomenen der Wirbelschlepp von Windenergieanlagen ermöglichen. Passive

Methoden zum beschleunigten Auffüllen der Nachlaufdelle bei REYNOLDSzahlen bis zu 8×10^5 werden untersucht und entwickelt werden. Solche Nachlaufdellen sind für beachtliche Verluste von bis zu 20% an jährlicher Energieerzeugung in modernen Windparks verantwortlich. Die Kombination der so gesammelten, experimentellen Daten mit hochaufgelösten numerischen Methoden hat großes Potenzial, einen beachtlichen Beitrag zur Bewältigung des menschengemachten Klimawandels zu leisten.



Contents

List of Figures	ii
List of Tables	iv
1 Introduction	1
1.1 Research Motivation	1
1.2 Fluid Mechanics of Wind Turbine	2
1.3 Wind Turbine Wake Topology	19
1.4 State of the Research on Wake Vortex Instabilities	22
1.5 Thesis Motivation and Research Question	25
1.6 Test Rig Requirements	28
2 Methodology	31
2.1 Brief Introduction to Methods of Product Design	31
2.2 Design Workflow and System Identification	32
3 Realization	34
3.1 Parameter Space Assessment	34
3.2 Airfoil Selection	35
3.3 Rotor Blade Design	40
3.4 Drive Train and Tower Design	48
3.5 Sensors and Waterproofing	55
4 Conclusion	58
5 Outlook	60
Bibliography	62
Nomenclature and Abbreviations	73
A Data Sheets	79

List of Figures

1.1	Wind turbine wakes in large-scale wind park	3
1.2	Averaged undisturbed atmospheric boundary layer and main wind turbine components	4
1.3	Kinematic inflow conditions and aerodynamic forces on a two-dimensional profile	5
1.4	Aerodynamic profiles suitable for small wind turbine applications and corresponding polars	8
1.5	Example pressure coefficient distribution of airfoil SG6041 for two different angles of attack extracted from XFOIL	9
1.6	Representation of the flow around an airfoil by placing vortex filaments on its surface	10
1.7	Example pitch and chord distribution for blade based on the SG6041 airfoil and resulting angle of attack	11
1.8	Tip vortex helix generated by a rotating blade immersed in fluid flow	13
1.9	Sketched evolution of streamtube diameter, flow velocity, and pressure for BETZ's streamtube model upstream and downstream of actuator disc	16
1.10	Comparison of pitch and chord distribution derived from BETZ and SCHMITZ design for blade based on the SG6041 airfoil	19
1.11	Example characteristics of horizontal axis turbines	20
1.12	Time-averaged turbine wake topology and taxonomy	22
1.13	Part 1: Examples of visualized instantaneous near-wake structures	23
1.14	Part 2: Examples of visualized instantaneous near-wake structures	26
2.1	Product design workflow for the Underwater Berlin Research Turbine	32
2.2	Large towing tank and carriage at the Technische Universität Berlin	33
3.1	Initial estimate of the upper limits of the averaged absolute inflow velocity, the mean chordwise REYNOLDS number, and the cavitation number at the blade tip throughout the operational regime	35
3.2	Assessment of the depth effect of transversal surface waves for the prescribed tow carriage velocities	36
3.3	Airfoil geometries and aerodynamic coefficients included in the airfoil selection process	37
3.4	Assessment of the operable regime without cavitation onset for two different design angles of attack	38
3.5	Blade design workflow for the Underwater Berlin Research Turbine	39
3.6	Finalized airfoil polars of the SG6040 and the SG6041 for the comparative blade design	40
3.7	Comparative spanwise blade chord and pitch distributions based on the SCHMITZ design for the SG6040 and the SG6041 airfoil	41
3.8	Normal and tangential load distributions for rotors constituted by the SG6040 and the SG6041 airfoils	42
3.9	Implemented point force distributions on the SG6040 blade	43
3.10	Structural simulation results for the SG6040 and SG6041 blades	44
3.11	Final blade contour and blade sections from pressure side view of the Underwater Berlin Research Turbine	45
3.12	Final pitch and chord distributions of the Underwater Berlin Research Turbine	45
3.13	Aerodynamic performance characteristics of the Underwater Berlin Research Turbine assessed, using QBLADE's blade element momentum module	46
3.14	Circulation and angle of attack distributions for different inflow conditions of the Underwater Berlin Research Turbine assessed, using QBLADES blade element momentum module	47

3.15	Resulting parameter space of the Underwater Berlin Research Turbine test rig including a risk assessment for the onset of cavitation	48
3.16	Assessed circulation and diameter of the tip vortices generated by the Underwater Berlin Research Turbine	49
3.17	Final blade design and exploded view of pitch positioning mechanism	49
3.18	Travel profiles and corresponding loads at design conditions of the Underwater Berlin Research Turbine	51
3.19	Model used for proofing the structural safety of the drive train	52
3.20	Section view of the turbine	53
3.21	Model used for proofing the structural safety of the tower	54
3.22	The Underwater Berlin Research Turbine test rig	55

List of Tables

1.1	Dimensions and characteristics of the towing tank facility at Technische Universität Berlin	29
1.2	Required overall dimensions of the horizontal axis wind turbine model, parameter space, and definition of ambient conditions	29
3.1	Design conditions, operational regime, and finalized overall dimensions of the Underwater Berlin Research Turbine	50
3.2	Implemented components in the Underwater Berlin Research Turbine	50
3.3	Sensors included in the Underwater Berlin Research Turbine	57

1 Introduction

The following paragraphs motivate research on wind energy technologies generally (Section 1.1). Fundamental characteristics of **Wind Turbine (WT)** technologies (Section 1.2) and the fundamentals of the WT wake topology are introduced (Section 1.3). A brief overview of the current state of the research on wake inherent instabilities, including typical methods is given (Section 1.4). This culminates into the motivation of the present thesis in Section 1.5, including the research question at hand. Lastly, the test rig requirements for solving the stated research questions are defined (Section 1.6).

1.1 Research Motivation

Motivation for research on wind turbine wakes with specific focus on wake effects

The "Special Report" of the **I**ntergovernmental **P**anel on **C**limate **C**hange (IPCC) from 2022 clearly states that determined measures are indispensable in order to limit global warming to 1.5 °C. Mitigating the challenging aspects of such profound global changes, especially for low income and poverty beaten countries must be of top priority. Otherwise, the necessary actions become socially unbearable and contradict equally important steps for sustainable development, poverty eradication, and reduction of global disparities [1]. One crucial perspective is the reformation of the electricity sector towards a more sustainable future. [2-4]

All around the world, programs and strategies have been put into action in order to tackle climate change, including extensive investments in clean energy generation. Especially **P**hoto **V**oltaic (PV) and **W**ind **E**nergy (WE) attracted a large share of finance for new projects between 2010 and 2019 with \$1.4 trillion and \$1.1 trillion respectively. Other sources of clean energy¹ received a total of \$216.4 billion in the same time. [5]

Although major investments are already attributed to sources of renewable energy, the annual growth still needs to be significantly higher in order to satisfy the climate targets defined in the "Paris Agreement" [6]. For PV and WE, rates about three to four times higher than the average annual growth in 2016-2018 are necessary (500 to 520 TWh yr⁻¹ for wind and 360 to 380 TWh yr⁻¹ for solar). [7, 8]

Technically, reaching these necessary levels of market penetration and deployment is not a problem. Conservatively estimated, the global resources of land-based WE alone are already sufficient to cover five times the total global use of energy in all forms [9-11]. In order to harvest those resources whilst also meeting the **S**ustainable **D**evelopment **G**oals (SDG) and the "Paris Agreement", WE technologies must satisfy a range of requirements. They have to be cheap, safe for wildlife and humans, recyclable, emit as little noise as possible, and consume a minimized amount of space. Hence, WTs are typically arranged in **W**ind **P**arks (WPs) decreasing the **L**evelized **C**ost **O**f **E**nergy (LCOE) mainly due to cost reductions in **B**alance **O**f **S**ystem (BOS) and **O**peration **A**nd **M**aintenance (OAM).

LCOE balances costs and energy production of a power plant and is primarily used to measure its life cycle unit costs. It is the indicator of choice in order to compare the value of different sources of energy. Low LCOE benefits the electricity consumer, so minimizing LCOE is a key aspect of research on WT technologies. [12, 13]

If unlimited space is available, several studies show that LCOE decrease as wind power plant and turbine capacities are enlarged. Wiser et al. [14] carried out an extensive survey among over 160 of the world's foremost WE experts. The authors identified turbine rating as the main LCOE driver. Upscaling plant sizes ranked fourth. All in all, the survey revealed an anticipated median (50th percentile) LCOE reduction for onshore, offshore, and floating offshore wind of 35 to 41 % by 2050 relative to the

¹biomass, waste-to-energy, small hydro, biofuels, geothermal, marine

2014 baseline. Shields et al. [12] combined techno-economic cost models with calculations of **Annual Energy Production (AEP)**. They found that LCOE can be reduced significantly by using 20 MW WTs in a 2500 MW offshore power plant. The cost benefits culminate to a 23 % decrease relative to the global average turbine and plant size installed in 2019 (6 MW turbines in a 500 MW offshore plant). Generally, the interpretation of these studies appears to be intuitive: Increased WT nameplate capacities reduce the necessary number of WTs in a given plant. Fewer turbines lead to reduced numbers of substructures or foundations, downsized electrical infrastructure, and shorter installation times. Also, larger turbines increase the wind park's **Net Capacity Factor (NCF)** by driving AEP, hence diminishing LCOE. [15, 16]. Maximizing the plant capacity, on the other hand, implies the distribution of costs related to vessel mobilization, grid connection, and OAM over a larger number of assets [12, 17]. However, if the usage of space is considered, the growth of wind park capacity at a given site results in reduced distances between turbines. WTs generate far-reaching velocity deficits accompanied by increased turbulence (see Section 1.3), called *wake* (see Figure 1.1 for visual impression of wind turbine wakes in large-scale wind parks and (partial) shadowing effects). These wakes result in significant wind speed reductions within farms to less than 20 % compared to freestream conditions. Even 20 diameters downstream of the last turbine row, wake effects such as reduced mean wind speeds (90 % of freestream value) and increased values of turbulence can be measured [18]. Mikkelsen et al. [19] found that downstream turbines produce 40 to 60 % of the foremost turbine in an array imposed by lowered mean wind speeds, leading to significant losses of AEP of the entire wind park (10 to 20 % reduction of the theoretical possible AEP) [18, 20–22]. Downstream and cross-wind spacing guidelines of more than seven and four rotor diameters respectively were met [9, 23, 24]. In addition to energy losses, wakes significantly increase fatigue loads on downstream WTs, hence diminishing turbine lifetimes and driving OAM costs [24–26]. Especially in partial wake shadows, increased fatigue loading of up to 300 % can be measured [27].

The wake interactions in wind parks impose significant constraints on array layouts, affecting turbine lifetime and park AEP directly and LCOE of wind resources subsequently. A deeper understanding of wind turbine wake dynamics is essential if WE is supposed to continue its key role in tackling climate change in compliance with the "Paris Agreement". It also may lead the way to more sophisticated wake models and elaborate control strategies for accelerated wake recovery.

1.2 Fluid Mechanics of Wind Turbine

Introduction to fundamental aspects of fluid mechanics of horizontal axis wind turbines including definition of describing quantities and relevant parameters

The following paragraph summarizes the fundamentals of WT technologies important to the presented thesis. All key aspects are taken from [16, 24, 28–34].

The renewable energy content of the wind originates from the sun. Global winds are caused by uneven heating of the earth by solar radiation that induces pressure differences across the earth's surface. The circulation of the atmosphere is additionally influenced by the rotation of the earth and seasonal variations in the distribution of solar energy. The wind blows predominately in the horizontal plane, since vertical pressure gradients are usually canceled out by the downward pointing gravitational force. The atmospheric winds are greatly influenced by friction on the surface of the earth resulting in the creation of a turbulent boundary layer (see Figure 1.2 left side). [16]

A turbulent velocity field $\vec{U}(\vec{x}, t)$ (e.g., $[U \ V \ W]_i(\vec{x}, t)\mathbf{e}_i$) at three-dimensional (3D) position \vec{x} (e.g., $[x \ y \ z]_i \mathbf{e}_i$) at time t may be decomposed following the REYNOLDS decomposition (Equation (1.1)).

$$\vec{U}(\vec{x}, t) = \overline{\vec{U}}(\vec{x}, t) + \vec{u}(\vec{x}, t) \quad (1.1)$$



Figure 1.1: Visible wind turbine wakes in large-scale wind park (Horns Rev 2) from Dong Energy/Bel Air Aviation Denmark Helicopter Services (2017).

$\overline{(\cdot)}$ depicts a suitable average such as the time average over a time interval T of a statistically stationary flow $\vec{U}(t)$ (Equation (1.2a)) or the ensemble average for repeatable and reproducible flows (Equation (1.2b)).

$$\overline{\vec{U}}(t)_T := \frac{1}{T} \int_t^{t+T} \vec{U}(\tau) d\tau \quad (1.2a)$$

$$\overline{\vec{U}}(t)_N := \frac{1}{N} \sum_{n=1}^N \vec{U}^{(n)}(t) \quad (1.2b)$$

$U^{(n)}(t)$ is the n th repetition of the measurement. The remainder $\vec{u}(\vec{x}, t)$ (e.g., $[u \ v \ w]_i(\vec{x}, t)\mathbf{e}_i$) in Equation (1.1) is referred to as the turbulent flow field. The REYNOLDS stress tensor is constituted by $-\overline{\rho \vec{u} \otimes \vec{u}}$, describing momentum transfer imposed by the turbulent fluctuations. Its trace is the mean kinetic energy content per unit mass of the turbulent fluctuations, i.e., **Turbulent Kinetic Energy** (TKE) (Equation (1.3)). ρ is the fluid's mass density.

$$k = k(\vec{x}, t) := \frac{1}{2} \overline{\vec{u} \cdot \vec{u}} \quad (1.3)$$

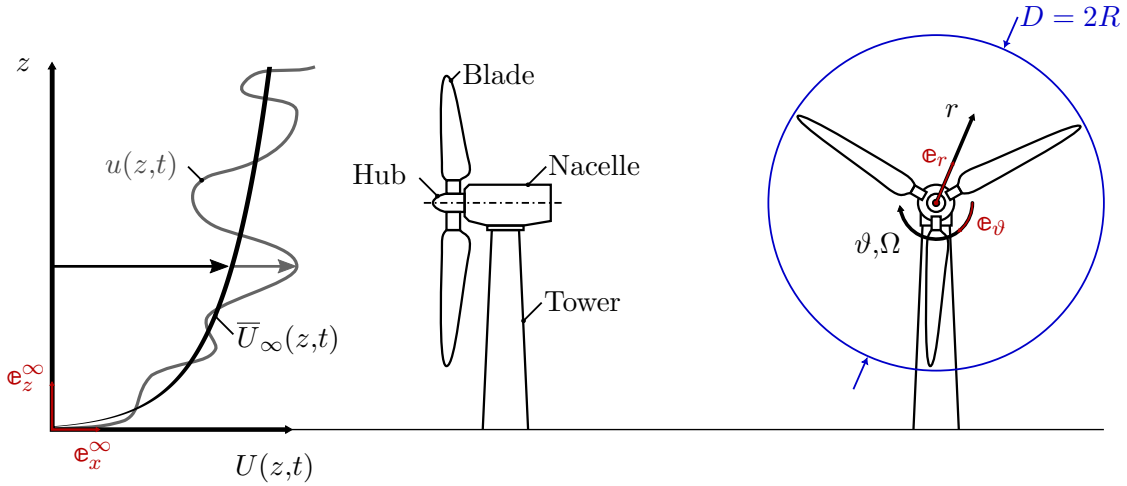


Figure 1.2: Averaged undisturbed atmospheric boundary layer $\bar{U}_\infty(z,t)$ with turbulent fluctuations $u(z,t)$ from [26] and [28]; Wind turbine components and definition of rotor radius R , diameter D , angular velocity Ω , and blade phase angle ϑ (\mathbf{e} depicts unit vectors).

Additionally, the turbulence intensity is introduced as a representation of the global degree of turbulence (Equation (1.4a)).

$$\text{TI}(\vec{x},t) := \frac{\text{rms } \vec{u}(\vec{x},t)}{|\vec{U}(\vec{x},t)|} \stackrel{\text{ONB}}{=} \frac{\sqrt{u(\vec{x},t)^2}}{\sqrt{U^2 + V^2 + W^2}} \quad (1.4a)$$

$$\text{rms } \vec{u}(\vec{x},t) = \sqrt{\frac{2}{3}k(\vec{x},t)} \stackrel{\text{ONB}}{=} \sqrt{\frac{1}{3}(u^2 + v^2 + w^2)} \quad (1.4b)$$

The rms operator is the **R**oot **M**ean **S**quare (RMS) defined in Equation (1.4b). [28, 30, 31, 33] Both quantities are used to measure the degree of turbulence in an entire flow field or at a specific point \vec{x} and time t . Typical values of turbulence intensity in onshore and offshore locations suitable for WT deployment range from 10 to 12% and 6 to 8% respectively. [20, 25, 35–37]

Airfoil Theory

On the left side of Figure 1.3 and the right side of Figure 1.2 the general specifics of a rotor with radius R rotating at angular frequency Ω are depicted. In Figure 1.3, $\bar{U}_{1,\infty}$ refers to the averaged \mathbf{e}_x component of the undisturbed inflow velocity (i.e., *freestream* velocity). \bar{U}_2 is the averaged inflow velocity in \mathbf{e}_x effected by the rotor at the location of the rotor plane (i.e., *plane* velocity). For WTs, $\bar{U}_{1,\infty} > \bar{U}_2$ holds true.

On the right side of Figure 1.3, the idealized² kinematic dependencies and forces acting on a 2D profile (i.e., airfoil) are depicted. Airfoils are bodies of much smaller thickness d than chord c . The chord is the line connecting the utmost point of the profile contour towards the inflow (i.e., **L**eading **E**dge (LE)) and the point furthest away from the LE (i.e., **T**railing **E**dge (TE)). The thickness d is defined as the largest diameter of the enveloped circles with center point at the mean line. The camber f of the profile is defined as the distance between the profile's mean line and the chord. Typically, the locations η_d and η_f of the maximum thickness d_{\max} and maximum camber f_{\max} measured by η from

²The flow is assumed to be solely two-dimensional (2D).

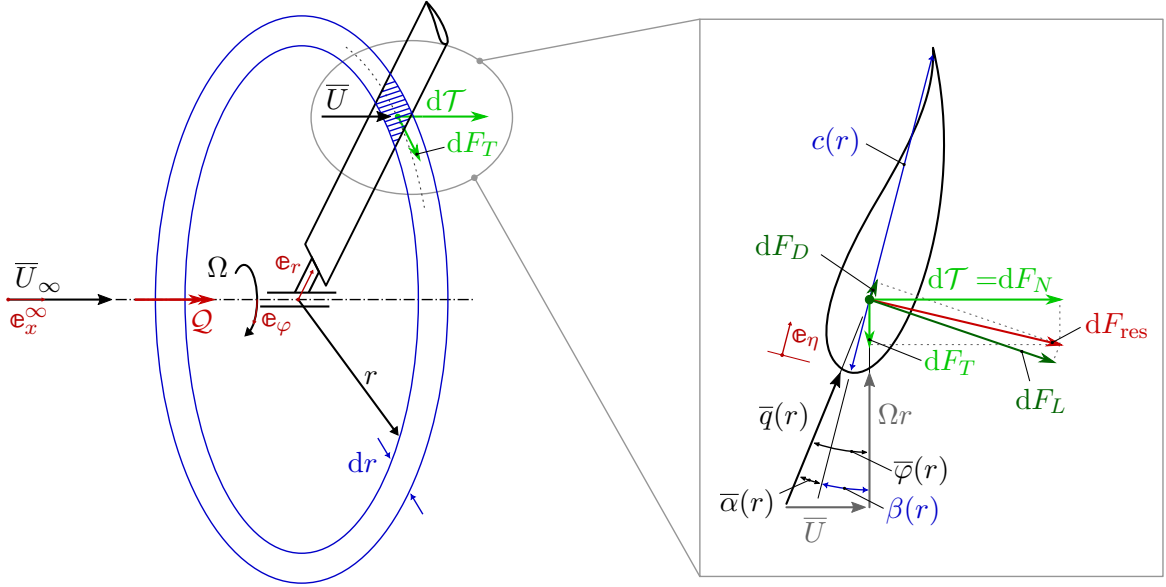


Figure 1.3: Kinematic inflow conditions and aerodynamic forces on a two-dimensional profile reproduced from [29]. With the undisturbed inflow velocity $\bar{U}_{1,\infty}$, the inflow velocity at the rotor plane \bar{U}_2 , the velocity Ωr due to the rotation of the blade with angular velocity Ω at radius location r and the resulting absolute mean velocity $\bar{q}(r)$. Blade chord $c(r)$, blade pitch angle $\beta(r)$, and angle of attack $\alpha(r)$. Infinitesimal lift dF_L and drag force dF_D . Resulting total force dF_{res} . Decomposed normal dF_n , i.e., thrust $d\mathcal{T}$, and tangential force dF_t . Rotor torque \mathcal{Q} .

the LE in the direction of the chord are given for comparison reasons.

$$\bar{\varphi}(r) = \bar{\alpha}(r) + \beta(r) = \arctan\left(\frac{\bar{U}_2}{\Omega r}\right) = \arctan\left(\frac{1}{\lambda_l}\right) \quad (1.5a)$$

$$\bar{q}(r) = \sqrt{(\Omega r)^2 + \bar{U}_2^2} = \bar{U}_2 \sqrt{\lambda_l(r)^2 + 1} \quad (1.5b)$$

$$\bar{q}(R) = \bar{U}_2 \sqrt{\lambda_l(R)^2 + 1} < \bar{U}_{1,\infty} \sqrt{\lambda^2 + 1} =: \bar{q}^* \quad \forall \bar{U}_{1,\infty} > \bar{U}_2 \quad (1.5c)$$

The relative angle α between the resulting direction φ of the absolute velocity q , and the chord is called **Angle of Attack (AoA)**. β is the blade pitch angle, which is a design-specific quantity. Equation (1.5a) summarizes their relation. The mean of the resulting absolute velocity q follows from Equation (1.5b). [29]

Both quantities may be expressed in terms of the **Local Speed Ratio (LSR)** λ_l . It quantifies the ratio between the rotational velocity component Ωr and the averaged plane velocity \bar{U}_2 (Equation (1.6a)). For radially constant \bar{U}_2 , λ_l increases linearly in r resulting in $\bar{\varphi} \rightarrow 0$ for $r \rightarrow \infty$ (Equation (1.5a)). Correspondingly, the **Tip Speed Ratio (TSR)** correlates the rotational velocity ΩR of the rotor blade tip and the undisturbed inflow velocity $\bar{U}_{1,\infty}$ (Equation (1.6b)). [16, 24, 31]

$$\lambda_l(r) := \frac{\Omega r}{\bar{U}_2} \quad (1.6a)$$

$$\lambda := \frac{\Omega R}{\bar{U}_{1,\infty}} \quad (1.6b)$$

$$\lambda < \lambda_l(R) \quad \forall \bar{U}_{1,\infty} > \bar{U}_2 \quad (1.6c)$$

Figure 1.4 shows examples of airfoils suitable for small-scale WT applications taken from Lyon et al. [38] (i.e., low-REYNOLDS number airfoils). The profile geometries (Figures 1.4a until 1.4c) and their corresponding lift C_L and drag C_D coefficients as function of α and the REYNOLDS number Re are presented (C_L Figures 1.4d until 1.4f, C_D Figures 1.4g until 1.4i). The aerodynamic lift coefficient

C_L is defined as the lift force dF_L generated by an airfoil of width dr divided by the resulting force of the dynamic pressure $\rho/2\bar{q}^2 cdr$ (Equation (1.7a)). The drag coefficient C_D is defined accordingly using the drag force dF_D (Equation (1.7b)). Per definition, the lift force is perpendicular to the inflow direction. The drag is collinear to the inflow. The presented characteristic curves of C_L and C_D against α and Re are called *polars* and summarize the key aspects of flow physic around an aerodynamic 2D profile. The ratio of lift and drag coefficient is called *glide ratio* (Equation (1.7c)). The maximum glide ratio ε_{\max} can be used to compare different airfoils and is interpreted as airfoil efficiency. [39]

$$C_L := \frac{2dF_L}{\rho\bar{q}(r)^2 c(r)dr} \quad (1.7a)$$

$$C_D := \frac{2dF_D}{\rho\bar{q}(r)^2 c(r)dr} \quad (1.7b)$$

$$\varepsilon := \frac{C_L}{C_D} = \frac{dF_L}{dF_D} \quad (1.7c)$$

The REYNOLDS number Re follows from dimensional considerations and is typically interpreted as the ratio of a characteristic inertial ($\rho\bar{q}^2$) to a characteristic viscous ($\nu\rho\bar{q}/c$) force. From its definition it can be seen that for *inviscid* flow states ($\nu \rightarrow 0$, ν is kinematic viscosity), $Re \rightarrow \infty$ follows. Modeling flow phenomena as inviscid enables significant simplifications of the describing equations³. Fortunately, most problems in aerodynamic and hydrodynamic applications can accurately be assumed inviscid [28, 30, 32, 39]. Equation (1.8a) determines the chordwise REYNOLDS number based on the average resulting inflow velocity. [31]

$$Re(r) := \frac{\bar{q}(r)c(r)}{\nu} = \frac{\sqrt{(\Omega r)^2 + \bar{U}_2^2} c(r)}{\nu} = \frac{\bar{U}_2 \sqrt{\lambda_l(r)^2 + 1} c(r)}{\nu} \quad (1.5b) \quad (1.8a)$$

$$Re(R) = \frac{\bar{U}_2 \sqrt{\lambda_l(R)^2 + 1} c(R)}{\nu} < \frac{\bar{U}_{1,\infty} \sqrt{\lambda^2 + 1} c(R)}{\nu} =: Re^* \quad (1.5c) \quad (1.8b)$$

The drag and lift coefficients (Equation (1.7)) of an airfoil are solely dependent on the REYNOLDS number. Generally, the drag coefficient increases as Re decreases. Below approximately $Re = 2 \times 10^5$, the boundary layer on the airfoil surface remains laminar, resulting in a sharp increase in C_D (Figures 1.4g and 1.4i, especially visible in Figure 1.4h). As can be seen from Figures 1.4d until 1.4f, the slope of the lift coefficient is unaffected by a changed REYNOLDS number. However, typically, an increase in Re delays stall, hence the maximum lift coefficient of the respective airfoil increases and is shifted to higher AoAs. [24, 30, 31, 34]

The lift and drag characteristics also depend on the airfoil geometry. An increase in profile curvature leads to increased lift to drag ratios for positive AoAs and allows for the generation of lift at $\alpha = 0$. Accordingly, all depicted airfoils in Figures 1.4a until 1.4c generate lift when aligned with the inflow direction. The operational point of zero lift generation is shifted to negative α . For symmetric profiles, it can be shown that the resulting aerodynamic force derived from integrating the pressure field around the airfoils contour goes through the quarter chord point $\eta_{25} = 0.25c$. Contrarily, for cambered airfoils, the neutral point moves towards the TE. Low-REYNOLDS number airfoils are often cusped on the lower airfoil side (i.e., pressure side) near the TE to increase surface curvature and cause rear loading (Figures 1.5). Consequently, the separation of the flow on the upper airfoil side (i.e., suction side) at high AoAs is delayed, hence increasing the maximum lift coefficient [24, 32, 40, 41]. The maximum thickness d_{\max} typically drives mainly drag forces and leads to reduced lift to drag ratios. At lower REYNOLDS numbers, thicker airfoils also increase the risk of laminar separation bubbles near the LE (visibly in Figure 1.4e and 1.4h for $Re = 10^5$ between $\alpha = 0$ to 5°). The location of the laminar separation bubble is affected by the location of maximum thickness η_d . Additionally, with larger η_d the maximum lift tends to decrease whilst the maximum lift to drag ratio increases [41–45].

³The NAVIER-STOKES Equations reduce to the EULER Equations.

Aerodynamic loading of WT blades occurs predominantly in the *flapwise* direction (i.e., normal to the rotor plane) of the airfoil (Figure 1.3). Therefore, thicker airfoils benefit the reduction of flapwise deflection. Nevertheless, airfoils with larger relative thickness usually also increase the blade mass, hence increasing the *edgewise* loading (i.e., within the rotor plane).

Most of the airfoil characteristics are derived from the pressure field $P(\vec{x},t)$ at point \vec{x} and time t around the airfoil. Just like the velocity field $\vec{U}(\vec{x},t)$ (Equation (1.1)), the turbulent pressure field $P(\vec{x},t)$ can be decomposed utilizing the REYNOLDS decomposition (Equation (1.9)). [28, 30]

$$P(\vec{x},t) = \bar{P}(\vec{x},t) + p(\vec{x},t) \quad (1.9)$$

The corresponding dimensionless pressure coefficient C_p correlates the locale pressure $P(\vec{x},t)$ and the undisturbed static pressure \bar{P}_∞ , with the dynamic freestream pressure $\rho/2\bar{U}_\infty^2$ (Equation (1.10a)). The coefficient is typically evaluated on the surface of a body, e.g., an airfoil, at different AoAs. It allows straightforward comparisons of different airfoils for different flow states (Figures 1.5). For *incompressible*⁴ applications, Equation (1.10a) can be reduced to a form solely depending on the absolute $|\cdot|$ of the local velocity $\vec{U}(\vec{x},t)$, and the freestream velocity \bar{U}_∞ . It can be seen that C_p is limited to $C_{p,\max} = 1$ for $|\vec{U}(\vec{x},t)| = 0$ (i.e., stagnation point). This holds true not only for the body surface, but for the entire flow field. Negative values occur in regions where either $|\vec{U}(\vec{x},t)| > \bar{U}_\infty$ or $P(\vec{x},t) < \bar{P}_\infty$. The lift of a body is directly related to the surface pressure distribution through Equation (1.10b), which must be evaluated around the body's surface $\partial\mathcal{A}$. The maximum of the negative pressure coefficient $-C_{p,\max} := \max(-C_p)$ at a certain AoA is of particular interest since it is a measure of minimum relative pressure generated by the airfoil geometry. [32]

$$C_p := \frac{2(P(\vec{x},t) - \bar{P}_\infty)}{\rho\bar{U}_\infty^2} \quad \Rightarrow \quad C_p = 1 - \left(\frac{|\vec{U}(\vec{x},t)|}{\bar{U}_\infty} \right)^2 \quad \text{for} \quad \frac{D\rho}{Dt} = 0 \quad (1.10a)$$

$$C_L = \int_{\partial\mathcal{A}} C_p d\vec{\eta} \quad (1.10b)$$

Figure 1.5 depicts two examples of the pressure coefficient distributions $C_p(\eta)$ at $\alpha = 1^\circ$ and $\alpha = 8^\circ$ of the low-REYNOLDS number airfoil SG6041 at $\text{Re} = 2 \times 10^5$. For clarity reasons, the negative pressure coefficient $-C_p$ is displayed. Both plots show fully attached flow conditions. The pressure distributions were generated using the software XFOIL with calculated transition from an e^9 -amplification model [38, 46]. From the comparison of Figures 1.5a and 1.5b, the dependency of the pressure distribution around an airfoil on the AoA can be seen. Moreover, a stagnation point ($-C_p = -1$) is typically located near or at the LE ($\eta = 0$). For moderate AoA, the pressure remains mostly constant over the pressure and suction side, with an abrupt start of pressure recovery near the TE on the suction side (Figure 1.5a). At larger AoAs, the pressure peak ΔC_p at the airfoil nose grows to $\Delta C_p \approx 4$ (Figure 1.5b) compared to $\Delta C_p \approx 1$ at $\alpha = 1^\circ$. Airfoils with large LE radii are often characterized by a flattened suction peak near the nose, resulting in a reduced sensitivity of the airfoils characteristics towards AoA deviations. Additionally, reducing the pressure peak results in improved separation behavior at high AoA. [32]

An alternative way of interpreting the generation of airfoil lift caused by the pressure distribution is immanent in KUTTA-JOUKOWSKI's theorem (Equation (1.11a)). It states that the lift per unit width f_L exerted on a body is proportional to the strength of a vortex substituting that body. The circulation of this *bound* vortex follows from Equation (1.11b) where the integration is to be carried out along a curve \mathcal{C} consisting always of the same fluid particles (i.e., *material* curve) surrounding that body. The theory of flows around lift force generating surfaces is therefore strongly connected to

⁴ $D\rho/Dt := \partial\rho/\partial t + \vec{U} \cdot \nabla\rho = 0$ [30, 32]

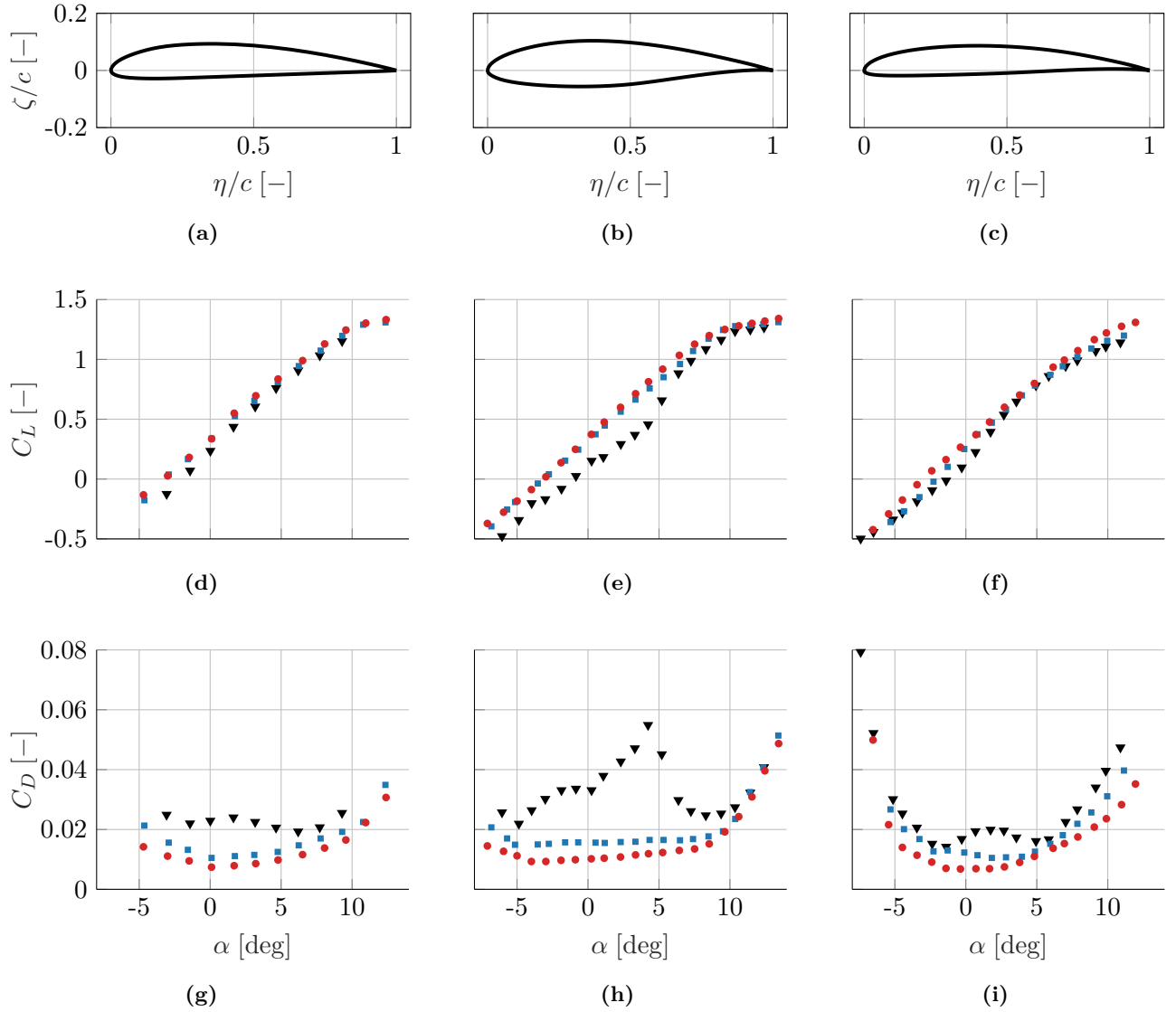


Figure 1.4: Aerodynamic profiles suitable for small wind turbine applications from Lyon et al. [38] from measurements without applied tripping: **a)** Clark-Y with maximum thickness $d_{\max} = 11.71\%$ at $\eta_d = 28\%$ and maximum camber $f_{\max} = 3.49\%$ at $\eta_f = 41.5\%$; **b)** SG6040 with $d_{\max} = 16\%$ at $\eta_d = 35.2\%$ and $f_{\max} = 2.53\%$ at $\eta_f = 58.79\%$; **c)** SG6041 with $d_{\max} = 10\%$ at $\eta_d = 35.68\%$ and $f_{\max} = 1.88\%$ at $\eta_f = 41.38\%$. Corresponding C_L and C_D characteristics at REYNOLDS numbers (\blacktriangledown) $Re = 10^5$, (\blacksquare) $Re = 2 \times 10^5$, (\bullet) $Re = 4 \times 10^5$ from Lyon et al. [38]. **d)** and **g)** Clark-Y; **e)** and **h)** SG6040; **f)** and **i)** SG6041.

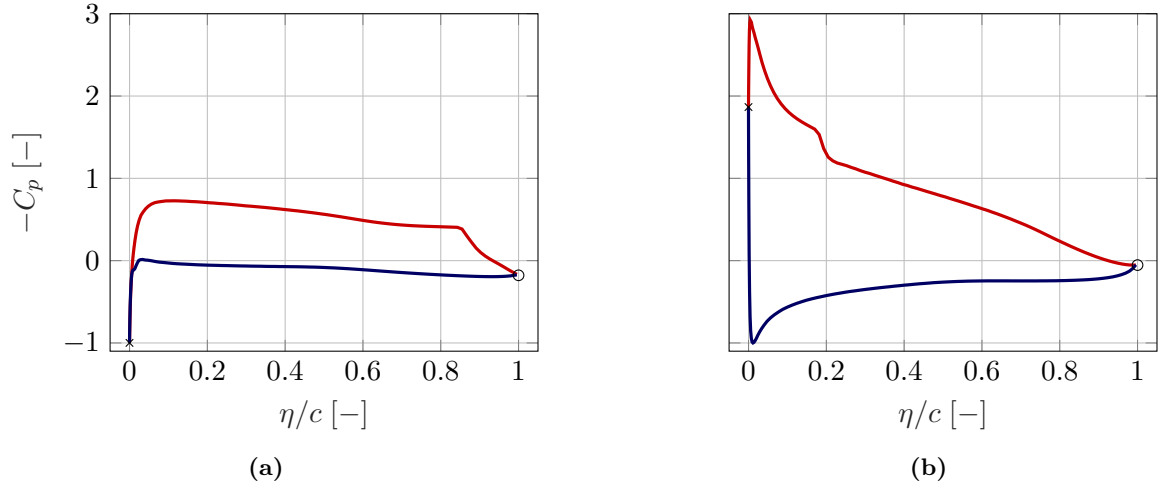


Figure 1.5: Pressure coefficient distribution of airfoil SG6041 (depicted in Figure 1.4b) for two different angles of attack extracted from XFoil (simulated with e^9 transition model) at $Re = 2 \times 10^5$ [46]. (\times) Leading edge, (\circ) trailing edge, — suction side, — pressure side. a) $\alpha = 1^\circ$; b) $\alpha = 8^\circ$.

the theory of vortex dynamics. Γ is the vortex strength or circulation. [30, 32, 47]

$$f_L = \rho \bar{U}_\infty \Gamma \quad \text{where} \quad f_L \perp \bar{U}_\infty \quad (1.11a)$$

$$\Gamma := - \oint_c \vec{U}(\vec{x}, t) \cdot d\vec{x} = \int_{\partial A} \gamma(s) ds \quad (1.11b)$$

For an airfoil of arbitrary shape and thickness immersed in inviscid and incompressible flow, the resulting flow field can be generated by vortex filaments of strength $\gamma(s)$ placed on the airfoils surface (Figure 1.6). The bound vortex strength then follows from integrating the vortex filaments along the surface contour ∂A (Equation (1.11b)) [32, 34]. However, the Equations (1.11) are not enough to properly determine the flow state. To close the system of equations, KUTTA's condition is needed. It states that for finite TE angles, a stagnation point exists at the TE. For cusped TEs, the upper and lower surface velocities are finite and equal in magnitude and direction. [32, 47]

Among others, THOMSON's vortex theorem describes the dynamics of vortices and vortex systems. It states that the circulation calculated along a closed material curve remains constant at all times if the fluid is inviscid and barotropic⁵ and the mass body force has a potential (Equation (1.12)) [30].

$$\frac{D\Gamma}{Dt} = \frac{\partial \Gamma}{\partial t} + \vec{U}(\vec{x}, t) \cdot \nabla \Gamma = 0 \quad (1.12)$$

Consequently, an airfoil releases a vortex into the flow, which is convected downstream of equal magnitude yet of opposite sign as the bound vortex. This vortex is called *startup* vortex because it is first created during the startup process of the airfoil⁶. However, whenever the lift generated by the profile changes, e.g., by change of AoA, the bound circulation changes due to Equation (1.11a) and a vortex forming a discontinuity surface is released from the TE. A curve piercing this surface violates THOMSON's vortex theorem, yielding nonzero circulation. Yet, the integral along a material curve enclosing the airfoil and the startup vortex yields again no circulation in accordance to Equation (1.12). Figure 1.6 visualizes the process. [30, 32, 33, 47]

⁵Density ρ depends solely on pressure $\rho = \rho(p)$

⁶Since THOMSON's vortex theorem does not allow the spontaneous creation of circulation, the generation of the pair of bound and startup vortex must be of viscous nature.

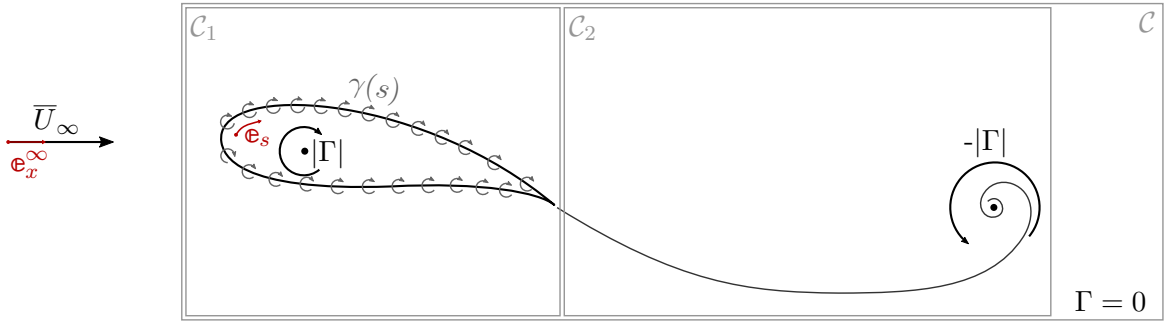


Figure 1.6: Representation of the flow around an airfoil by placing vortex filaments on its surface summing-up to the bound vortex. Viscous formation of a discontinuity plane at the trailing edge and roll-up of the starting vortex. Sketched examples of material curves (\mathcal{C}_1 , \mathcal{C}_2) and respective circulation. For curve \mathcal{C} , enclosing startup and bound vortex THOMSON’S vortex theorem (Equation (1.12)) holds true, hence $\Gamma = 0$. Reproduced from [32] and [30].

From THOMSON’S vortex theorem, fundamental aspects of vortex dynamics including the HELMHOLTZ vortex theorems can be derived:

- 1) Vortex lines are tangential to the vorticity field $\nabla \times \vec{U}(\vec{x}, t)$ ⁷ and are material curves. (Second HELMHOLTZ’S vortex theorem)
- 2) Vortex tubes are vortex lines that pass through a closed curve. Vortex tubes cannot end within the fluid but must either reach out to infinity, end at a boundary, or close itself forming a vortex ring.
- 3) The circulation of a vortex tube is invariant along the tube and constant in time. (First and third HELMHOLTZ’S vortex theorem)

In part, these theorems motivate the interest in research on vortex phenomena because they constitute the substantial stability of vortices in inviscid and barotropic flows. WT rotors operating in such flows release large coherent vortex systems into their shadow regions, affecting WTs positioned downstream significantly (as addressed in Section 1.1).

Blade Theory

The 3D extension of the 2D airfoil is called a rotor blade. A WT blade typically spans solely radially from the axis of rotation (Figure 1.3 left side). The point furthest away is called blade tip, the connection to the hub is called root. The blade surface geometry is mainly defined by the constituting airfoils. Modern electricity-generating **H**orizontal **A**xis **W**ind **T**urbines (HAWTs) equip $N_b \in \{2, 3\}$ blades. [26]

High absolute velocities drive aerodynamic forces, the overall torque (Equation (1.17b)), and power (Equation (1.17c)) of the rotor. Equation (1.5b) shows that the absolute velocity grows with r or $r/R \rightarrow 1$, leading to an increasing importance of deploying high-performance airfoils towards the blade tip. Aerodynamically efficient airfoils with maximized lift to drag ratio are characterized by small values of maximum thickness d_{\max} and moderate maximum camber f_{\max} . The blade root is usually made from circular profiles for structural reasons. To guarantee a smooth surface transition for $r/R \rightarrow 0$ either thick airfoils are implemented or geometric interpolation methods towards the circular root are used. [16, 31]

⁷If $\nabla \times \vec{U}(\vec{x}, t) = 0$, the flow is called *irrotational*

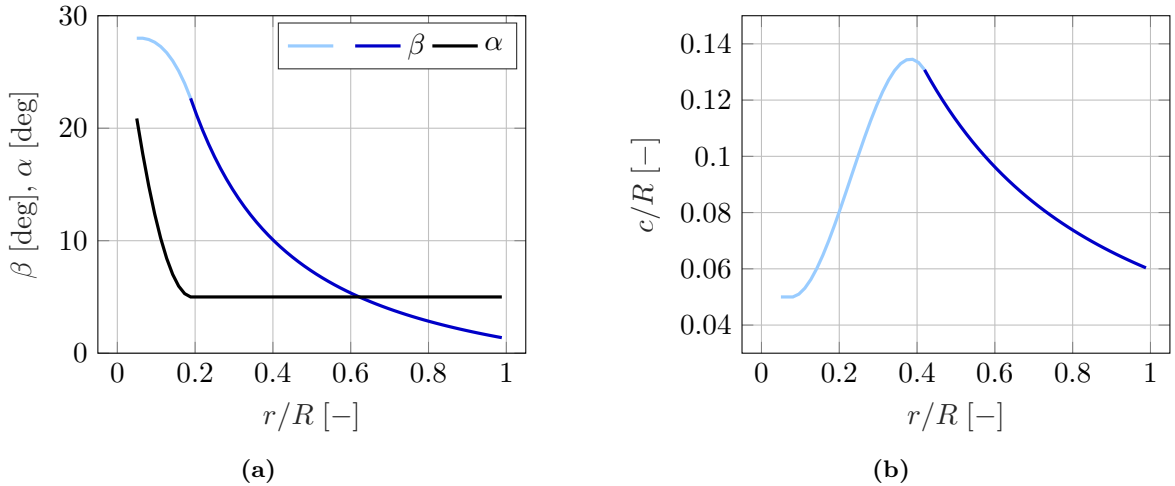


Figure 1.7: Example pitch and chord distribution for blade based on the SG6041 airfoil (depicted in Figure 1.4c) and resulting angle of attack α from Equation (1.31a). — Calculated from SCHMITZ design approach (Equations 1.31) with $\lambda_{\text{des}} = 6$, $\text{Re}_{\text{des}} = 4 \times 10^5$, $\alpha_{\text{des}} = 5^\circ$, and $C_L(\alpha_{\text{des}}, \text{Re}_{\text{des}}) = 0.85$. — Adjusted geometry in order to assure smooth transition towards the circular blade root with $R_{\text{root}}/R = 0.1$ and $R_{\text{hub}}/R = 0.05$. a) Pitch β and angle of attack α ; b) Blade chord c/R .

The **Blade Element Momentum Theory** (BEM) assumes that a blade can be partitioned into a sufficient number of blade elements (as depicted in Figure 1.3). These elements do not interact radially, and the forces on the element solely determine the change of axial momentum of the fluid passing through the swept annulus. Additionally, the local absolute velocity $q(r)$ has no radial component. The aerodynamic lift and drag forces are then the same as those acting on an identical airfoil of the same breadth in 2D flow [24]. Therefore, the starting point of the blade surface design process is the iterative selection of a set of airfoils adequate for a certain WT blade. The constituting airfoils are enlarged to the locale blade chord $c(r)$ and twisted by the pitch angle $\beta(r)$. Several methods exist for finding suitable or "optimized" chord and twist distributions for different operational conditions. A design AoA α_{des} based on the corresponding set of polars is selected (e.g., Figures 1.4). To achieve constant flow conditions around the blade independent of the radius coordinate r , a constant AoA over the entire blade span is usually aimed for. From Equation (1.5a), Equation (1.13) can be derived. It correlates the needed pitch angle $\beta(r)$, which has to be accounted for in the design, with the inflow conditions. Especially the calculation of the averaged plane velocity \bar{U}_2 requires more detailed modeling of the emerging flow. As does for deriving adequate formulas for the chord distribution $c(r)$. [24, 31]

$$\beta(r) = \bar{\varphi}(r) - \alpha_{\text{des}} = \arctan\left(\frac{\bar{U}_2}{\Omega r}\right) - \alpha_{\text{des}} \stackrel{(1.6a)}{=} \arctan\left(\frac{1}{\lambda_l}\right) - \alpha_{\text{des}} < \arctan\left(\frac{1}{\lambda}\right) - \alpha_{\text{des}} \quad (1.13)$$

Figure 1.7 shows representative pitch and chord distributions for small-scale WTs. They stem from the design approach developed by Glauert [48] and reformulated for WT blades by Schmitz [31, 49, 50]. As can be seen, for $r/R \rightarrow 1$, the blade segments are increasingly twisted towards the rotor plane. Independent of the chosen design approach, this is driven by $\beta \rightarrow -\alpha_{\text{des}}$ for $\lambda_l \rightarrow \infty$ (Equation (1.13)), for $r \rightarrow \infty$ (Equation (1.6a)). Where the mentioned blade design approach is followed, the AoA is constant. For $r/R \rightarrow 0$, a smooth transition from the outer airfoil geometry towards a circular blade root is implemented, visible in both figures. The blade becomes more slender towards the blade tip, with a maximum at approximately 30% of the rotor radius (Figure 1.7b). [16, 24, 29, 31]

Unlike airfoils which are 2D geometries spanning $\pm\infty$, blades are of finite length (i.e., radius R). The static pressure difference between the pressure and suction side of the blade induces a flow velocity around the blade tips. There, the lift approaches zero due to the pressure equalization, as does the

circulation (Equation (1.11a)). Accordingly, lift and circulation are not constant along the span, but become functions of the radius r ($F_L = F_L(r)$ and $\Gamma = \Gamma(r)$). HELMHOLTZ's first vortex theorem (Item 3) implies that a varying circulation cannot be represented by a single bound vortex but requires a vortex distribution $\gamma(s)$ (As depicted in Figure 1.6). For every change in circulation, the shedding of a corresponding vortex is initiated (Equation (1.14a)), resulting in the continuous formation of a vortex sheet [47]. Towards the blade tip and root, the vortex sheet rolls up to form the *tip* and *root* vortices (i.e., *trailing* vortices). Driven by the fact that vortices cannot end inside the fluid, they create a closed vortex ring together with the startup vortex. The lift force dF_L of a blade segment of breadth $dr = R_2 - R_1$, where $R_2 > R_1$, follows then from Equation (1.14b). [30, 32, 33, 47]

$$d\Gamma = \frac{\partial\Gamma}{\partial r} dr \quad (1.14a)$$

$$dF_L = \rho \int_{R_1}^{R_2} \bar{q}(r) \Gamma(r) dr \quad (1.14b)$$

The N_b blades of WTs rotate at angular velocity Ω . Figure 1.8a shows the upper half of a simplified vortex system generated by such blades when immersed in a stationary flow of velocity $[\bar{U}_{1,\infty} \ 0 \ 0]_i \mathbf{e}_i$. The reduction of axial velocity causes the helix radius R_{hel} to grow with x depending on the flow state $R_{\text{hel}} = R_{\text{hel}}(x, \lambda)$. The tip vortex distance δ_{hel} can be estimated by Equation (1.15a), when assuming that the tip vortices are convected with the plane velocity \bar{U}_2 . T_{rot} is the rotational period of the rotor. However, due to the interaction of the vortices⁸ the evolution of the tip vortex distance and the helix radius becomes highly nonlinear and unstable as can be seen in Figure 1.8b. [24, 51]

$$\delta_{\text{hel}}(\lambda) \approx \bar{U}_2 T_{\text{rot}} = \frac{2\pi R}{T_{\text{rot}} \lambda_l(R)} T_{\text{rot}} = \frac{2\pi R}{\lambda_l(R)} < \frac{2\pi R}{\lambda} \quad (1.15a) \quad (1.6a)$$

$$\tan \tau(\lambda) = \frac{h(\lambda)}{R_{\text{hel}}(x, \lambda)} \quad (1.15b)$$

Equations (1.16) relate the aerodynamic forces on the blade element to the *tangential* and *normal* force with respect to the rotor plane. The linear transformation is a rotation by the inflow angle $\bar{\varphi}$ (Figure 1.3).

$$dF_T = dF_L \sin \bar{\varphi}(r) - dF_D \cos \bar{\varphi}(r) \quad (1.16a)$$

$$dF_N = dF_L \cos \bar{\varphi}(r) + dF_D \sin \bar{\varphi}(r) \quad (1.16b)$$

The integration of the ϵ element-wise forces (Equations (1.16)) along the rotor span yields the turbine characteristics summarized in Equations (1.17). The integral force \mathcal{T} normal to the rotor is called thrust. For WTs, it causes the reduction of the averaged plane velocity \bar{U}_2 compared with the undisturbed inflow velocity $\bar{U}_{1,\infty}$. The thrust must be counteracted by the WT tower and therefore defines its main load cases. The torque \mathcal{Q} results from the integral over all in-plane components of the aerodynamic forces dF_T , imposed by every blade segment dr at radius location r . A typical HAWT consists of three (sometimes two) blades mounted to a hub, a main shaft, a gearbox, a generator, and auxiliary equipment, including the control system, and possibly a transformer (Figure 1.2). The torque causes the rotor of the generator to rotate and thereby generates the electricity. The aerodynamic power

⁸e.g., expressed by the BIOT-SAVART law

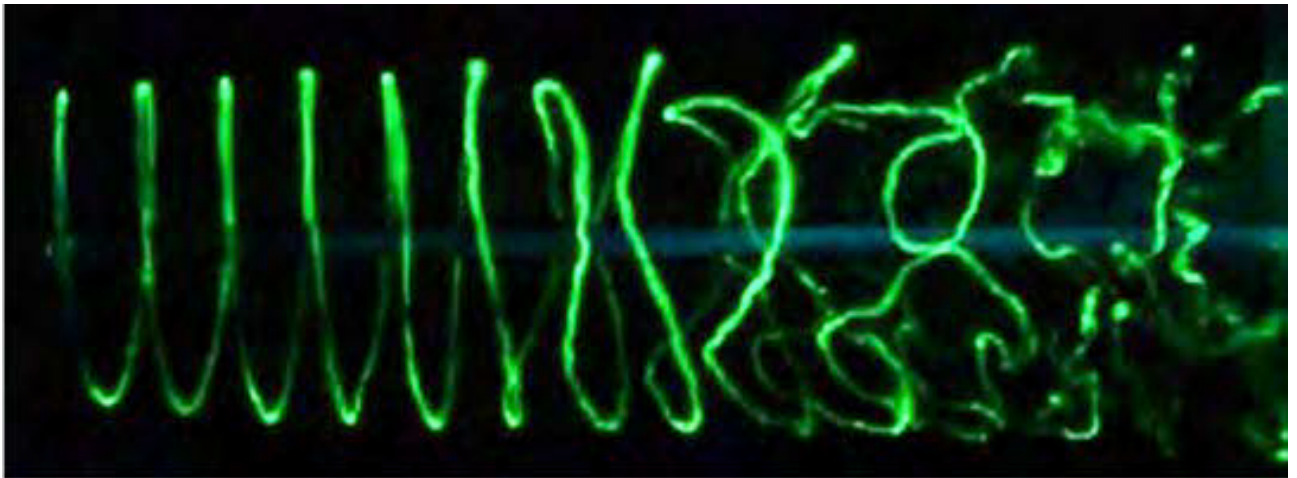
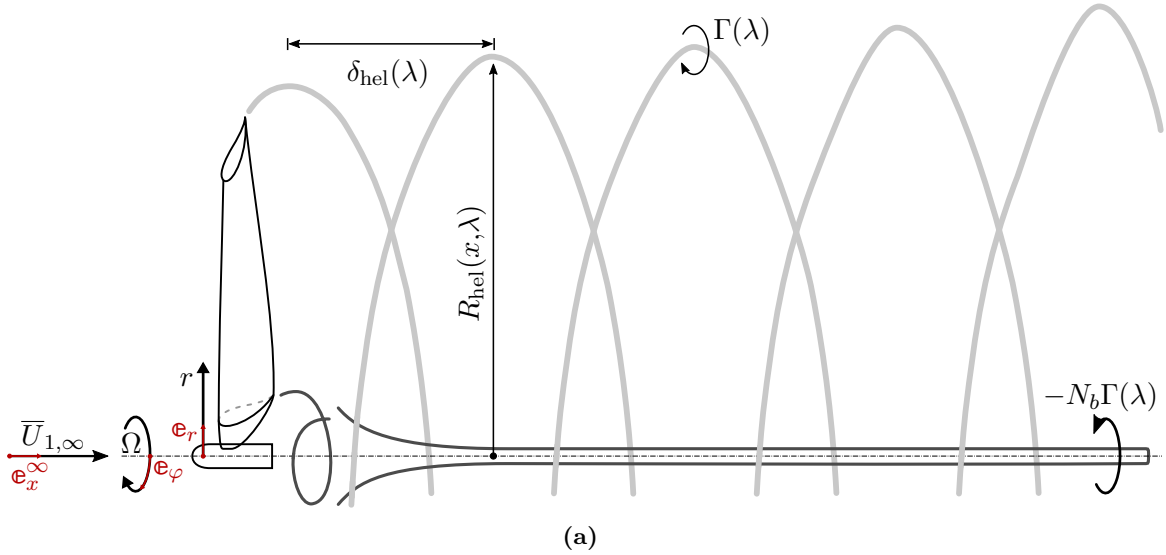


Figure 1.8: Tip vortex helix generated by a rotating blade immersed in fluid flow. **a)** Upper half of the simplified tip and root vortex system. Tip vortex distance δ_{hel} can be estimated from Equation (1.15a). N_b blade root vortices form the concentrated root vortex with strength equal to $-N_b\Gamma(\lambda)$ in accordance with HELMHOLTZ's first vortex theorem (Item 3). Inspired by [16, 51]. **b)** Picture taken from Leweke et al. [51] showing the unstable and nonlinear evolution of the tip vortex helix including their decay within 2 to $4D$ in accordance with [52]. Vortex is generated by single-bladed rotor ($N_b = 1$) attached to a main shaft. Flow visualization using dye.

output \mathcal{P} of the rotor follows from Equation (1.17c). [26]

$$\mathcal{T} := N_b \int_0^R d\mathcal{T} \approx N_b \sum_i^\epsilon \Delta\mathcal{T}_i \quad (1.17a)$$

$$\mathcal{Q} := N_b \int_0^R r dF_T \approx N_b \sum_i^\epsilon \Delta F_{T,i} r_i \quad (1.17b)$$

$$\mathcal{P} := \mathcal{Q}\Omega \quad (1.17c)$$

To enable comparisons between different turbine sizes at different locations, dimensionless representations of the WT characteristics are introduced (Equations 1.18). A reference force is defined, derived from the force of the dynamic pressure $\rho/2\bar{U}_\infty^2$ of the undisturbed inflow velocity imposed on a circular cross-section based on the rotor diameter $\pi/4D^2$. [31].

$$C_{\mathcal{T}} := \frac{8\mathcal{T}}{\rho\bar{U}_\infty^2\pi D^2} \quad (1.18a)$$

$$C_{\mathcal{Q}} := \frac{16\mathcal{Q}}{\rho\bar{U}_\infty^2\pi D^3} \quad (1.18b)$$

$$C_{\mathcal{P}} := \lambda C_{\mathcal{Q}} \quad (1.18c)$$

The aerodynamic characterization of WTs is typically done using a set of characteristic curves. They include the power, thrust, and torque (Equations (1.17)), and their coefficients (Equations (1.18)) as functions of the rotational speed, the undisturbed inflow velocity, and the TSR (Figures 1.11).

Limits to Flow Power Extraction

Betz [53] developed a theory for assessing the theoretical limit for the extraction of wind power for an idealized rotor operating in a simplified model environment. The model assumes (indices defined in Figure 1.9):

- Incompressible and *stationary*⁹ (i.e., *homogeneous*¹⁰) fluid flow
- Control volume is stream tube with inlet and outlet (indices 1 and 4)
- Static pressure far up- and downstream equal to undisturbed pressure ($\bar{P}_1 = \bar{P}_3 = \bar{P}_4 = \bar{P}_\infty$)
- Stream tube surface is material surface: mass flow only through inlet and outlet
- No frictional drag
- Infinite number of blades: rotor modeled as uniform actuator disc inducing discontinuity in pressure field (index 2)
- Uniform thrust over disc

From the conservation of linear momentum, the rotor thrust \mathcal{T} is found (Equation (1.19)). The cross-section of the stream tube is calculated from $A = \pi/4D^2$ with D as cross-sectional diameter (Figure 1.9). For steady conditions, the mass flow rate $\dot{m} := (\rho A \bar{U})_{1,\infty} = (\rho A \bar{U})_3$ is defined. $(\dot{\cdot}) := \partial/\partial t(\cdot)$ refers to a partial derivative with respect to time t .

$$\mathcal{T} = \bar{U}_{1,\infty}(\rho A \bar{U})_{1,\infty} - \bar{U}_3(\rho A \bar{U})_3 = \dot{m}(\bar{U}_{1,\infty} - \bar{U}_3) \quad (1.19)$$

⁹ $\partial/\partial t = 0$

¹⁰ $\nabla \rho = 0$

BERNOULLI's equation¹¹ is used to obtain the pressure configurations directly before (Equation (1.20a)) and after (Equation (1.20b)) the pressure discontinuity (Figure 1.9). Assuming that $\bar{P}_1 = \bar{P}_3 = \bar{P}_\infty$ and $\bar{U}_{2-} \rightarrow \bar{U}_{2+}$ yields Equation (1.20c), hence delivering an expression for the pressure difference.

$$\bar{P}_{2-} = \bar{P}_{1,\infty} - \frac{\rho}{2}\bar{U}_{2-}^2 + \frac{\rho}{2}\bar{U}_1^2 \quad (1.20a)$$

$$-\bar{P}_{2+} = -\bar{P}_3 + \frac{\rho}{2}\bar{U}_{2+}^2 - \frac{\rho}{2}\bar{U}_3^2 \quad (1.20b)$$

$$\Delta\bar{P}|_2 := \bar{P}_{2-} - \bar{P}_{2+} = \frac{\rho}{2}(\bar{U}_{1,\infty}^2 - \bar{U}_3^2) \quad (1.20c)$$

The pressure difference across the rotor disc (Equation (1.20c)) results in a net force normal to the rotor plane equal to the thrust (Equation (1.21)).

$$\mathcal{T} = A_2\Delta\bar{P}_2 = \frac{\rho}{2}A_2(\bar{U}_{1,\infty}^2 - \bar{U}_3^2). \quad (1.21)$$

Combining Equations (1.19) and (1.21) yields Equation (1.22) for the mean plane velocity \bar{U}_2 , which is known as FROUDE-RANKINE's theorem.

$$\bar{U}_2 = \frac{\bar{U}_{1,\infty} + \bar{U}_3}{2} \quad (1.22)$$

The axial induction factor a quantifies the axial velocity reduction as a result of the thrust (Equation (1.23a)). It allows for rewriting the stream tube velocities \bar{U}_2 and \bar{U}_3 (Equations (1.23b)).

$$a := \frac{\bar{U}_{1,\infty} - \bar{U}_2}{\bar{U}_{1,\infty}}, \quad 0 < a < 1 \quad \forall \bar{U}_{1,\infty} > \bar{U}_2 \quad (1.23a)$$

$$\bar{U}_2 = \bar{U}_{1,\infty}(1 - a) \quad \text{and} \quad \bar{U}_3 = \bar{U}_{1,\infty}(1 - 2a) \quad (1.23b)$$

Consequently, the power output \mathcal{P} of the rotor disc (Equation (1.24)) follows from multiplying the thrust \mathcal{T} from Equation (1.21) with the averaged plane velocity \bar{U}_2 using Equation (1.23b). For generalization purposes, $A_2 = A_{\text{turb}} = A$ and $\bar{U}_{1,\infty} = \bar{U}_\infty$ are set.

$$\mathcal{P} = \mathcal{T}\bar{U}_2 \stackrel{(1.26)}{=} \frac{\rho}{2}A_2(\bar{U}_{1,\infty}^2 - \bar{U}_3^2) \stackrel{(1.23b)}{=} \frac{\rho}{2}A_2\bar{U}_{1,\infty}^3 4a(1 - a)^2 = \frac{\rho}{2}A\bar{U}_\infty^3 4a(1 - a)^2 \quad (1.24)$$

The turbine power output is therefore cubic dependent on the undisturbed inflow velocity \bar{U}_∞ , and the axial induction a , quadratic dependent on the rotor diameter D , and proportional to the fluid density ρ . Dividing Equation (1.24) by the mean power of the flow through a cross-section equal to the swept area of the rotor (Equation (1.25a)) yields the aerodynamic efficiency $C_{\mathcal{P}}$ of the rotor (Equation (1.25b), alternative to Equation (1.18c)). Analyzing Equation (1.24) for a maximum reveals BETZ's limit for HAWTs.

$$\mathcal{P}_{\text{flow}} = \frac{\rho}{2}A\bar{U}_\infty^3 \quad (1.25a)$$

$$C_{\mathcal{P}} := \frac{\mathcal{P}}{\mathcal{P}_{\text{flow}}} = 4a(1 - a)^2 \quad C_{\mathcal{P},\text{B}} = \frac{16}{27} \approx 0.5926 \quad \text{at} \quad a = \frac{1}{3} \quad (1.25b)$$

¹¹For stationary conditions and z anti-parallel to the gravity vector \vec{g} : $\bar{P} + \rho/2|\vec{U}(\vec{x},t)|^2 + \rho gz = C$. C is the integration constant from integrating EULER's equations along a streamline. Generally, C differs between streamlines. For irrotational and inviscid flow, the velocity field has a potential (i.e., *potential* flow: $\vec{U}(\vec{x},t) = \nabla\Phi$). Then C is the same in the entire flow field.

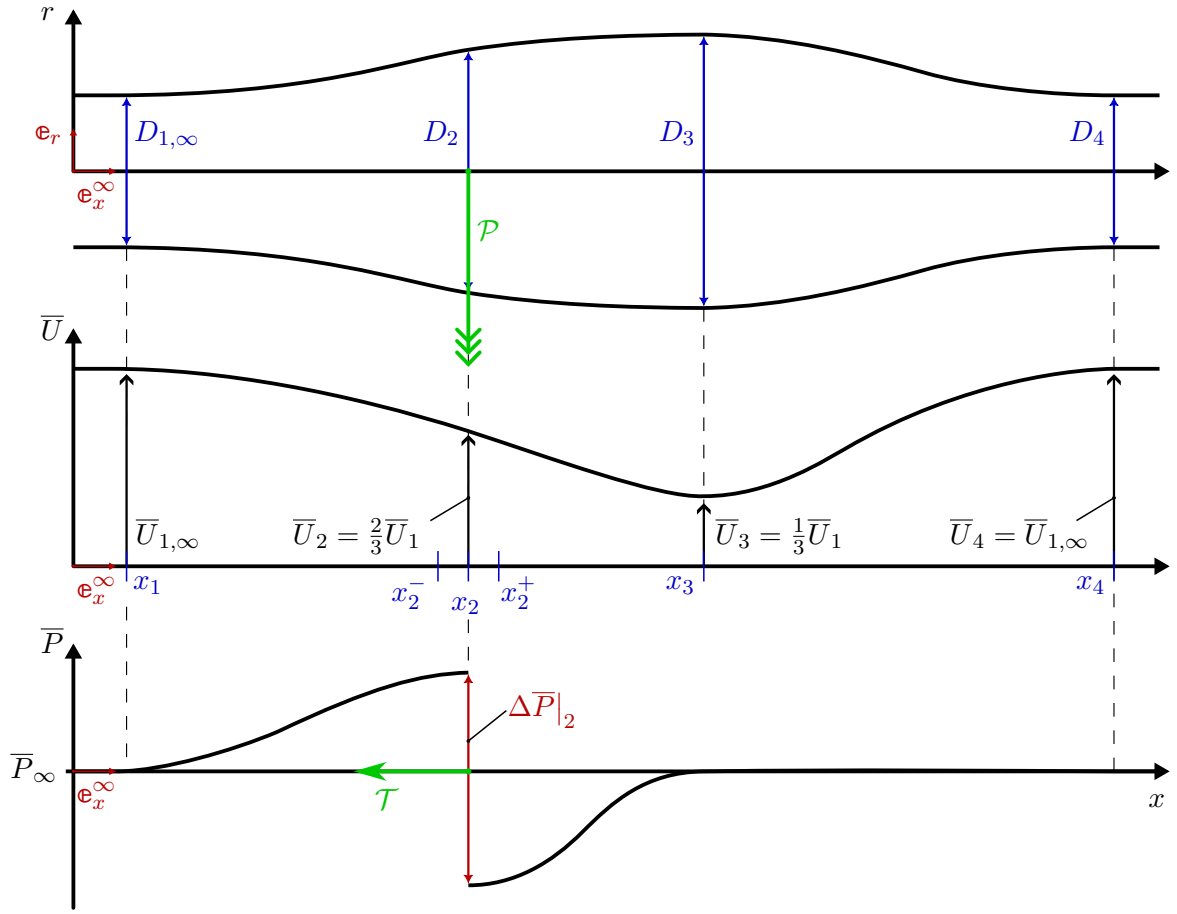


Figure 1.9: Sketched evolution of streamtube diameter, flow velocity, and pressure for BETZ's streamtube model upstream and downstream of actuator disc reproduced from [29]. Aerodynamic power \mathcal{P} is extract at location x_2 . Aerodynamic thrust \mathcal{T} is imposed at location x_2 .

Derived from Equation (1.21), the thrust can also be expressed as a function of the axial induction factor (Equation (1.26)).

$$\mathcal{T} = \frac{\rho}{2} A_2 \bar{U}_{1,\infty}^2 (4a(1-a)) = \frac{\rho}{2} A \bar{U}_\infty^2 (4a(1-a)). \quad (1.26)$$

Considering Equation (1.18a), the thrust coefficient reduces to Equation (1.27).

$$C_{\mathcal{T}} := 4a(1-a) \quad C_{\mathcal{T},B} = \frac{8}{9} \approx 0.8889 \quad \text{at} \quad a = \frac{1}{3} \quad (1.27)$$

Based on the stated model assumptions, a natural maximum turbine efficiency is found. It states that an idealized HAWT can extract up to approximately 60% of the power contained in a fluid flow when the plane velocity is reduced to $\bar{U}_2 = 2/3 \bar{U}_{1,\infty}$. Accordingly, the inflow velocity at index position 3 of the idealized rotor becomes $\bar{U}_3 = 1/3 \bar{U}_{1,\infty}$. As elaborated in Section 1.1, this velocity deficit reaches up to 20 diameters downstream (index position 4) of the turbine before being fully recovered by the surrounding undisturbed flow, causing shadowed turbines to contribute significantly less AEP to the turbine park. Figure 1.9 shows the worked out flow conditions imposed by BETZ's rotor, including the enlargement of the stream tube diameter, the inflow velocity reduction, and the pressure discontinuity. [16, 24, 29, 31]

From BETZ's model, a straightforward approach to finding an "optimal" chord distribution follows. A rotor annulus at radial location r of breadth dr can extract a maximum power $d\mathcal{P}_{\text{flow}}$, described by Equation (1.28a). The blade element at location r generates power through the generation of

tangential force dF_T . The force is related to the aerodynamic lift and drag force by Equation (1.16a), yielding Equation (1.28b). When assuming that the blade-element-constituting airfoil is operated at its "optimal" point, $F_L \gg F_D$ follows. Then, the tangential force depends solely on the lift force (Equation (1.28c)). [31]

$$d\mathcal{P}_{\text{flow}} = C_{\mathcal{P},B} \frac{\rho}{2} \bar{U}_{1,\infty}^3 (2\pi r dr) \quad (1.28a)$$

$$d\mathcal{P}_{\text{turb}} = N_b \Omega r dF_T = N_b \Omega r dF_L \left(\sin \bar{\varphi}(r) - \frac{dF_D}{dF_L} \cos \bar{\varphi}(r) \right) \quad (1.28b)$$

$$d\mathcal{P}_{\text{turb}} \approx N_b \Omega r dF_L \sin \bar{\varphi}(r) = N_b \Omega r C_L \frac{\rho}{2} q(r)^2 c(r) dr \sin \bar{\varphi}(r) \quad (1.28c)$$

BETZ's design prescribes $a_B = 1/3$, i.e., $\bar{U}_2 = 2/3\bar{U}_{1,\infty}$. Therefore, equating Equations (1.28a) and (1.28c) results in a formula for an "optimized" blade chord (Equation (1.29)). The pitch follows simply from Equation (1.13) where an "optimal" induction is assumed (Equation (1.29a)). The subscript *des* is allocated to quantities that have to be selected either apriori or iteratively. [31, 54]

$$\beta_B(r) = \bar{\varphi}(r) - \alpha_{\text{des}} = \arctan \left(\frac{2}{3} \frac{R}{r \lambda_{\text{des}}} \right) - \alpha_{\text{des}} \quad \left| \text{(1.13), (1.25b)} \right. \quad (1.29a)$$

$$c_B(r) = \frac{3}{2} C_{\mathcal{P},B} \frac{2\pi R}{N_{b,\text{des}} C_L(\alpha_{\text{des}}, \text{Re}_{\text{des}})} \frac{1}{\lambda_{\text{des}}^2 \sqrt{\lambda_{\text{des}} \left(\frac{r}{R} \right)^2 + \frac{4}{9}}} \quad (1.29b)$$

BETZ's blade design "optimizes" the blade chord and pitch at design conditions $(\lambda_{\text{des}}, \alpha_{\text{des}})$. Off-design operation of the blade consequently leads to a reduced aerodynamic performance of the turbine rotor. One corrective measure is to implement an actuator for changing the blade pitch depending on the operating point. This can assure a constant resulting AoA for varying conditions, i.e., slowly¹² changing inflow angles $\varphi(r) = \varphi(r,t)$ (Equation (1.13)). As can be seen, increasing the blade count or the design TSR leads to more slender blades. Selecting a small design AoA typically leads to comparatively small design lift coefficients, which also increases the "optimal" blade chord. As does the selection of less-efficient airfoils which have small lift coefficients even for high AoA. With $r/R \rightarrow 1$, the "optimal" chord requires slender blades towards the tip and deep blades near the root (i.e., a hyperbolic distribution). A small overall blade chord generally reduces the needed material and consequently the blade mass. However, a larger chord increases the blade thickness accordingly, resulting in a higher resistance to aerodynamic loading and reduced deflection (especially in the flapwise direction). Additionally, the chordwise REYNOLDS number grows, which is usually beneficial, especially for small-scale WTs. [29, 31, 54]

BETZ's optimal design neglects several effects, such as

- 4) the aerodynamic profile drag (Equation (1.28c)),
- 5) the azimuthal variation of the axial induction factor a due to the finite number of blades,
- 6) the generation of tip and root vortices causing the circulation to drop to zero (Figures 1.8),
- 7) and the overall rotation of the wake caused by the rotor torque \mathcal{Q} (Equation (1.28b)).

Considering these effects causes the maximum power coefficient to become a function of the TSR $C_{\mathcal{P},\text{max}} = C_{\mathcal{P},\text{max}}(\lambda)$. Hence, they are interpreted as losses to the possible power extraction. For

¹²Typically the blade pitch actuators are slow compared to the time scales of turbulent flow gusts and direction changes but can react to mean flow variations. [55]

Items 4 and 6, semi-empirical expressions can be found (Equations (1.30)). [16, 24, 31]

$$\xi_1 = \frac{3}{2} \frac{r}{R} \frac{\lambda_{\text{des}}}{\varepsilon_{\text{des}}} \quad (1.30a)$$

$$\xi_2 \approx \frac{0.92}{N_{b,\text{des}} \sqrt{\lambda_{\text{des}}^2 + \frac{4}{9}}} \quad (1.30b)$$

From Equation (1.30a) it can be seen that the losses attributed to the profile drag increase linearly towards the blade tip and are inversely dependent on the glide ratio ε_{des} . This gives yet another reason for selecting high-efficiency airfoils with maximized lift to drag ratios to be implemented at the blade tips. The losses attributed to the tip vortices (Equation (1.30b)) decrease with an increasing number of blades N_b and design TSR [31]. Glauert's [48] theory on wake losses for airplane propellers was later reformulated by Schmitz [49] for WTs. The inclusion of the wake rotation, resulted in the blade design formulas displayed in Equations (1.31). In SCHMITZ's model, the maximum power coefficient $C_{\mathcal{P},S}$ is a function of the TSR, where $C_{\mathcal{P},S} \rightarrow C_{\mathcal{P},B}$ for $\lambda \rightarrow \infty$. Especially for small TSR, Schmitz shows that the limit for maximum power extraction is smaller than the value derived by Betz (e.g., $C_{\mathcal{P},S}(2) = 0.5 \approx 0.84C_{\mathcal{P},B}$). This is caused by the fact that for small TSR, the turbine power \mathcal{P} is generated by comparatively low angular velocities Ω and high tangential forces dF_T (Equation (1.28b)). Hence, a high torque \mathcal{Q} is imposed on the fluid, which causes stronger wake rotation. [31]

$$\beta_S(r) = \frac{2}{3} \arctan\left(\frac{R}{r\lambda_{\text{des}}}\right) - \alpha_{\text{des}} \quad (1.31a)$$

$$c_S(r) = \frac{16\pi r}{N_{b,\text{des}} C_L(\alpha_{\text{des}}, \text{Re}_{\text{des}})} \sin^2\left(\frac{1}{3} \arctan\left(\frac{R}{r\lambda_{\text{des}}}\right)\right) \quad (1.31b)$$

In Figures 1.10 a comparison of the resulting blade geometries are shown, derived from the BETZ (Equations (1.29)) and the SCHMITZ (Equations (1.31)) design. The blade is constituted by the airfoil SG6041 displayed in Figure 1.4c. As can be seen, the design approaches differ mostly near the blade root ($r/R \rightarrow 0$). The BETZ design prescribes a chord $c(r/R)$ approaching infinity, whereas from the SCHMITZ's approach a finite blade chord follows (Figure 1.10b). The differences between the "optimal" pitch angles are also limited to the vicinity of the blade root (Figure 1.10a).

It should be noted that the designs are only "optimal" within their model assumptions. Since both models significantly simplify the effect of the wake of the rotor and neglect the effect of finite blade numbers, the derived pitch and chord distributions can generally only be considered a starting point in the blade design process.

It is worth mentioning that an elaborate theory exists for estimating the effect of a finite number of blades. The theory was first derived by Prandtl and extended by Betz and Glauert. It includes the definition of a tangential induction factor a^* in analogy to the axial induction factor a . Both factors vary spatially (i.e., radially and azimuthally) which is more accurate, as measurements across the rotor plane show. The model results in PRANDTL's *tip loss factor* (Equation (1.32)) where $\mu := r/R$. [24]

$$\xi_P(\mu, \lambda) = \frac{2}{\pi} \arccos\left(e^{-\frac{N_b}{2} \frac{1-\mu}{\mu} \sqrt{1 + \frac{(\lambda\mu)^2}{(1-a)^2}}}\right) \quad (1.32)$$

The (aerodynamic) performance of WTs is usually characterized by a set of curves displaying the power \mathcal{P} , torque \mathcal{Q} , and thrust \mathcal{T} as functions of the rotational speed n at different fluid velocities \bar{U}_∞ (Figures 1.11d until 1.11f). Alternatively, the characteristics can also be summarized using the dimensionless coefficients for power $C_{\mathcal{P}}$, torque $C_{\mathcal{Q}}$, and thrust $C_{\mathcal{T}}$ (Equations (1.18)) as functions of the TSR λ (Figures 1.11d until 1.11f). The power and torque curves are related by Equation (1.17c), the corresponding coefficients by Equation (1.18c). Hence, the torque curves reach their maximum at smaller rotational speed compared with the power curves. The maximum torque generated at the

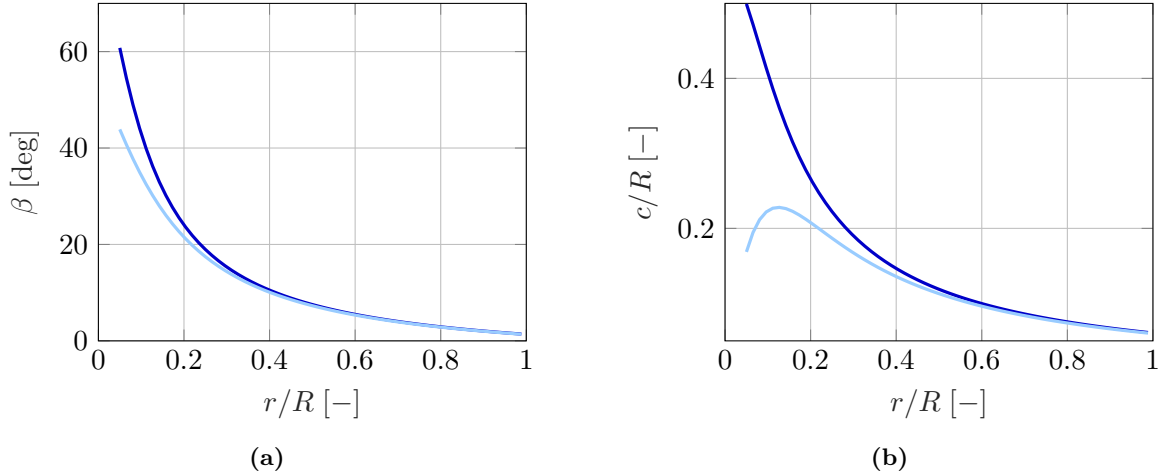


Figure 1.10: Comparison of pitch and chord distribution derived from BETZ (—, Equations (1.29)) and SCHMITZ (—, Equations (1.31)) design for blade based on the SG6041 airfoil (depicted in Figure 1.4c). Parameters set to $\lambda_{\text{des}} = 6$, $\text{Re}_{\text{des}} = 4 \times 10^5$, $\alpha_{\text{des}} = 5^\circ$, and $C_L(\alpha_{\text{des}}, \text{Re}_{\text{des}}) = 0.85$. a) Pitch β ; b) Blade chord c/R .

highest inflow velocity is used for dimensioning the main rotating components such as the shaft, the bearings, the gear, and the coupling if incorporated in the rotor design (Figure 1.11b). The maximum power is generated at higher rotational speeds compared to the respective torque maximum (Figure 1.11a). It drives the selection of the generator and additional downstream components attributed to the power circuit. For conditions below the maximum power generation, the power extraction follows the cubic power law of the power contained in the fluid flow (Equation (1.25a)). With fixed pitch operation, the AoA is larger than the chosen design AoA ($\bar{\alpha}(r) > \alpha_{\text{des}}$, Equation (1.13)) resulting in large aerodynamic forces, and imposing the risk of suction side separation. For rotational speeds exceeding the maximum, the power extraction becomes "suboptimal" due to a reduced AoA. As can be seen from Figure 1.11c, the thrust increases monotonously with n and \bar{U}_∞ . Its maximum does not correlate with the maximums of torque and power. To reduce the tower and bearing loads, the turbine should be operated at lower rotational speeds. [29]

In Figures 1.11d until 1.11f, the dimensionless coefficients are plotted for two undisturbed inflow velocities (i.e., $\bar{U}_\infty \in \{3, 6\}$) because the curves do not change over a large range of TSR. Only at low TSRs, the lower inflow velocity corresponds to smaller coefficients. This is caused by a reduced overall REYNOLDS number along the blade span (Equation (1.8b)). Therefore, the dimensionless flow state (e.g., quantified by the pressure coefficient C_p , Equation (1.10a)) around the blade sections is altered, resulting in changed aerodynamic forces. As expected, the power coefficient C_P is always smaller than BETZ's limit (Figure 1.11d) and reaches a maximum of $C_{P, \text{max}} \approx 41\%$. Modern large-scale WTs reach power coefficients of up to 50%. [31]

1.3 Wind Turbine Wake Topology

Definition of wake regions and fundamentals of flow phenomena in the wake of a horizontal axis wind turbine

The time-averaged wake of a turbine is characterized by a reduced mean flow velocity \bar{U} and an increased level of turbulence compared with the level of turbulence in the undisturbed flow. The low-velocity region extends 8 to 12D downstream of the turbine. An increased turbulence intensity

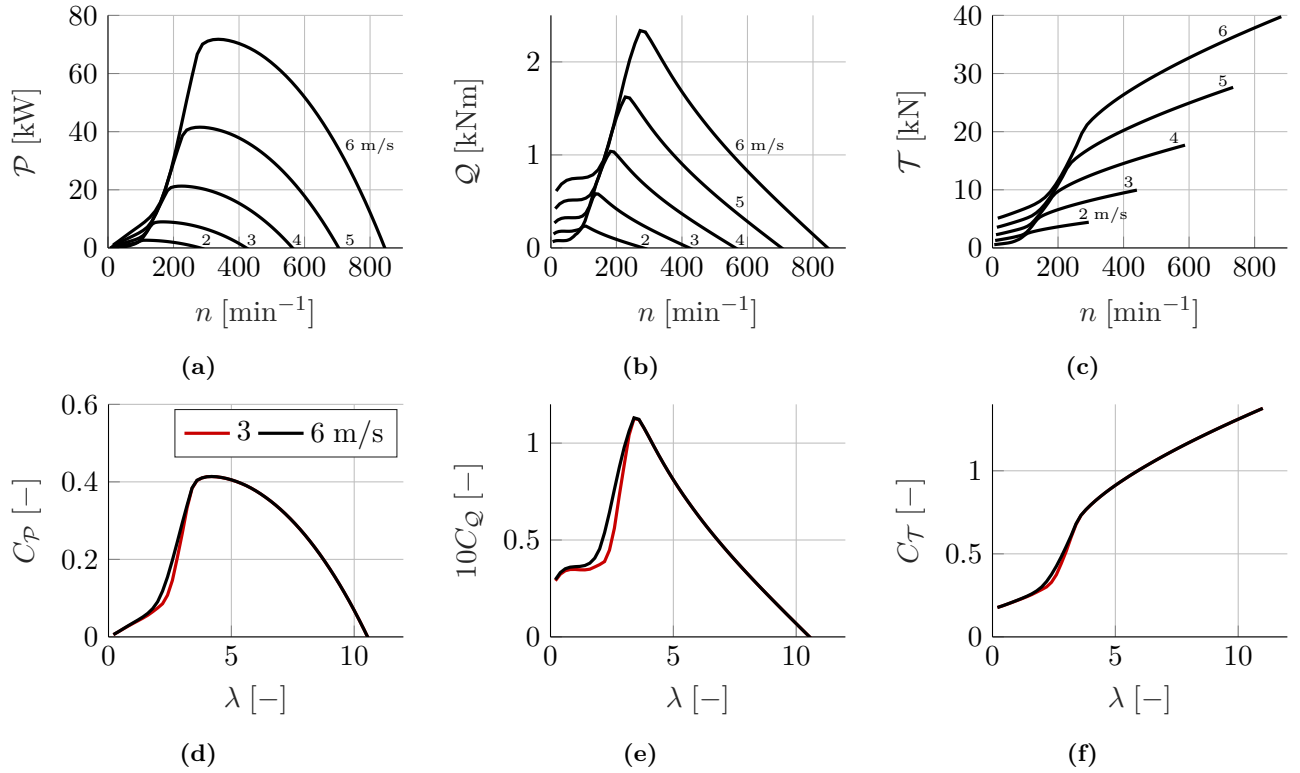


Figure 1.11: Example characteristics of horizontal axis turbines generated using QBLADE [56] for rotor blades based on the SG6041 airfoil. Rotor diameter $D = 1.43$ m, hub diameter $D_{\text{hub}} = 0.13$ m. Chord $c(r)$ and pitch $\beta(r)$ following SCHMITZ's design (Equations (1.31)). Design parameters: $\lambda_{\text{des}} = 5$, $\alpha_{\text{des}} = 5^\circ$, $\text{Re}_{\text{des}} = 4 \times 10^5$, $C_L(\alpha_{\text{des}}, \text{Re}_{\text{des}}) = 0.85$. Blade discretized into 30 blade elements. Fluid set to water at 20°C and 1.258 bar: density $\rho = 998.22 \text{ kg m}^{-3}$, kinematic viscosity $\nu = 10^{-6} \text{ m}^2 \text{ s}^{-1}$. PRANDTL's tip loss incorporated in simulation (Equation (1.32)). Simulated for various undisturbed inflow velocities $\bar{U}_\infty \in \{2, 3, 4, 5, 6\} \text{ m s}^{-1}$. Physical turbine quantities as function of rotational speed n : a) power \mathcal{P} , b) torque \mathcal{Q} , c) thrust \mathcal{T} . Dimensionless coefficients for: d) power $C_{\mathcal{P}}$, e) torque $C_{\mathcal{Q}}$, and f) thrust $C_{\mathcal{T}}$.

is measurable up to $15D$ downstream [18]. The wake is separated into the *near-*, *transitional*¹³-, and *far* wake (Figure 1.12) [36, 57]. The time-averaged near-wake is dominated by the equalization of axial and radial pressure gradients caused by the extraction of energy from the undisturbed mean flow ($\bar{U}_{1,\infty}$). Here, the vortex sheets emanated from the TEs form the N_b concentrated tip and root vortices. Quickly thereafter, the blade root vortices merge and create the turbine's root vortex (Figure 1.8a) [58]. This vortex induces a counter rotating motion on the overall wake relative to the rotor rotation [59]. The tip vortices create strong shear layers in their vicinity, leading to 130 to 150% increased turbulence levels compared with the ambient intensity [29]. Initially, the strong coherent tip vortices shield the low-velocity region directly behind the turbine, preventing the filling of the velocity deficit (i.e., *wake recovery*) [60]. However, the tip vortices decay typically between 2 to 4D downstream of the rotor due to the unstable growth of vortex distortions [51, 52, 61, 62] (Figure 1.8b). Accordingly, Sørensen et al. [63] define the length of the near-wake based on the onset of unstable growth of the tip vortex cores. They found that the length is inversely proportional to the thrust, the TSR, and the logarithm of the ambient turbulence intensity. Alternatively, the end of the near-wake is defined as the downstream position where the free shear layers generated by the tip vortices meet (Figure 1.12). The entire (near-) wake topology is considerably influenced by the operating point of the turbine. That is, the near-wake length, the growth of the shear layers, the overall expansion of the wake (i.e., *entrainment*), and the level of generated rotor turbulence. Additionally, the influence of the tower and the nacelle shadows contribute a large share to the TKE production [64]. In analogy to the aerodynamic blade drag, the velocity deficit in the downstream region of the turbine can be interpreted as the drag of the wake $F_{D,\text{wake}}$ (Equation (1.33)). R_{wake} is the radial position where the averaged axial velocity is equal to the undisturbed inflow velocity. The drag is converted along the wake. Hence, any time-averaged perpendicular velocity profile $\bar{U}(x,r)$ at a chosen downstream position x can be used, assuming an axisymmetric wake (Figure 1.12). [58]

$$F_{D,\text{wake}} = \frac{1}{\bar{U}_{1,\infty}^2} \int_{-R_{\text{wake}}}^{R_{\text{wake}}} \bar{U}(x,r)(\bar{U}_{1,\infty} - \bar{U}(x,r))r dr \quad (1.33)$$

The region where the characteristic time-averaged velocity profiles from the near-wake transform into the (roughly GAUSSIAN) profiles of the far-wake defines the transitional-wake (Figure 1.12) [29, 58, 65]. The velocity fluctuations generated by the rotor decay towards the end of the transitional-wake. In the far-wake, the centerline deficit reduces monotonically, with a rate strongly dependent on the turbulence intensity. The axial component of the turbulent velocity field vanishes towards the ambient level, with an exponent of approximately $-2/3$. Ultimately, the wake recovers through turbulent momentum transport driven by the ambient turbulence contained in the undisturbed flow [35, 60, 65, 66]. The atmospheric boundary layer (Figure 1.2) and the presence of the tower shadow cause the overall wake of WTs to be deformed along \mathbf{e}_z [64]. Accordingly, the turbulent mixing in the far-wake is stronger above the centerline, and the maximum of TKE (Equation (1.3)) is found above the turbine's hub height [67]. Figure 1.1 shows the wake of the large-scale Horns Rev 2 wind park off the coast of Denmark. Oversaturated air and the turbulent pressure field imposed by the WT rotors cause the generation of water bubbles. Assuming that the generated clouds indicate the extension of the wake sufficiently good, the (partial) shadowing of downstream turbines and the radial expansion of the time-averaged wake becomes visible. The length scales of the turbulence released into the flow are of the order of the rotor diameter.

Figure 1.12 shows a simplified model of the time-averaged turbine wake. Contrarily, the instantaneous near-wake is dominated by coherent vortex structures whose position, strength, and state are inherently unsteady. Moreover, the low-velocity region directly behind the nacelle (i.e., nacelle wake) causes the root vortex to oscillate. Periodic oscillations in fluid mechanics are often described using the dimensionless STROUHAL number (Equation (1.34)). It is derived from a problem specific length (e.g.,

¹³Also: *intermediate-wake*

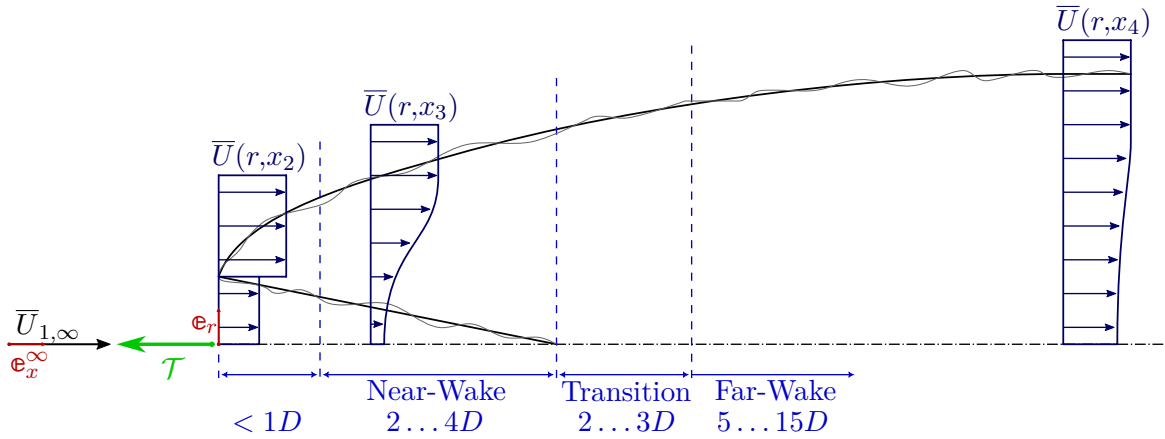


Figure 1.12: Time-averaged turbine wake topology and taxonomy reproduced from [36, 58]. Characteristic time-averaged velocity profiles displayed at different downstream positions of an actuator disc imposing a thrust \mathcal{T} onto an undisturbed fluid flow ($\bar{U}_{1,\infty}$). Indices allocated corresponding to Figure 1.9. Outer shear layer boundary indicated by black line. Transitional wake starts where inner shear layer reaches rotor axis. Transition is characterized by the development of the far-wake velocity profile.

turbine diameter D), a dominating frequency (e.g., shedding frequency f), and a flow characteristic velocity (e.g., undisturbed inflow velocity $\bar{U}_{1,\infty}$). Porté-Agel et al. [68] reports that the STROUHAL number attributed to WT root vortex oscillations reach from 0.12 to 0.85. This large range emphasizes the need for further research on the dominating phenomena.

$$\text{St} := \frac{fD}{\bar{U}_{1,\infty}} \quad (1.34)$$

The instantaneous far-wake of full-scale WTs shows random unsteady oscillations relative to the time-averaged wake centerline (i.e., *wake meandering*). The meandering is caused by large ($> 2D$) coherent flow structures in the incoming atmospheric boundary layer and is usually unaffected by the operating point of the turbine [68–70]. Figures 1.13 summarize examples of instantaneous near-wake structures taken from literature. Figure 1.13a depicts the immediate near-wake of a full-scale turbine, visualized using snowflake voids. The photo clearly shows the wake expansion directly after the passing of the rotor plane. The trailing sheet vortices are heretofore not completely rolled up to the concentrated tip and root vortices. All in all, the picture suggests the highly chaotic fluid flow in the direct vicinity of a WT in real-world conditions. Figures 1.13b and 1.13c focus on the generation of the tip vortex helix and its downstream development. Without the influence of a tower and exposed to constant inflow conditions, Figure 1.13c visualizes the strong coherence and great stability of the tip vortices. Figure 1.13b shows how unstable growth of tip vortex distortions are excited by the interactions with the turbine tower. Both examples from literature display experiments in controlled conditions, that is, a water flume and a wind tunnel. [67, 71, 72]

1.4 State of the Research on Wake Vortex Instabilities

State of the research on wake vortex instabilities with specific focus on exploitation possibilities for accelerated wake recovery

THOMSON’s vortex theorem states that vortices, once created, cannot vanish in barotropic, and inviscid fluid flow (Section 1.2, Equation (1.12)). However, vortex systems in nature decay over time. One driver is the distribution of vortex energy through viscous evolution and diffusion. More importantly, helical vortex systems consisting of a number of intertwined vortex filaments are governed by inherent

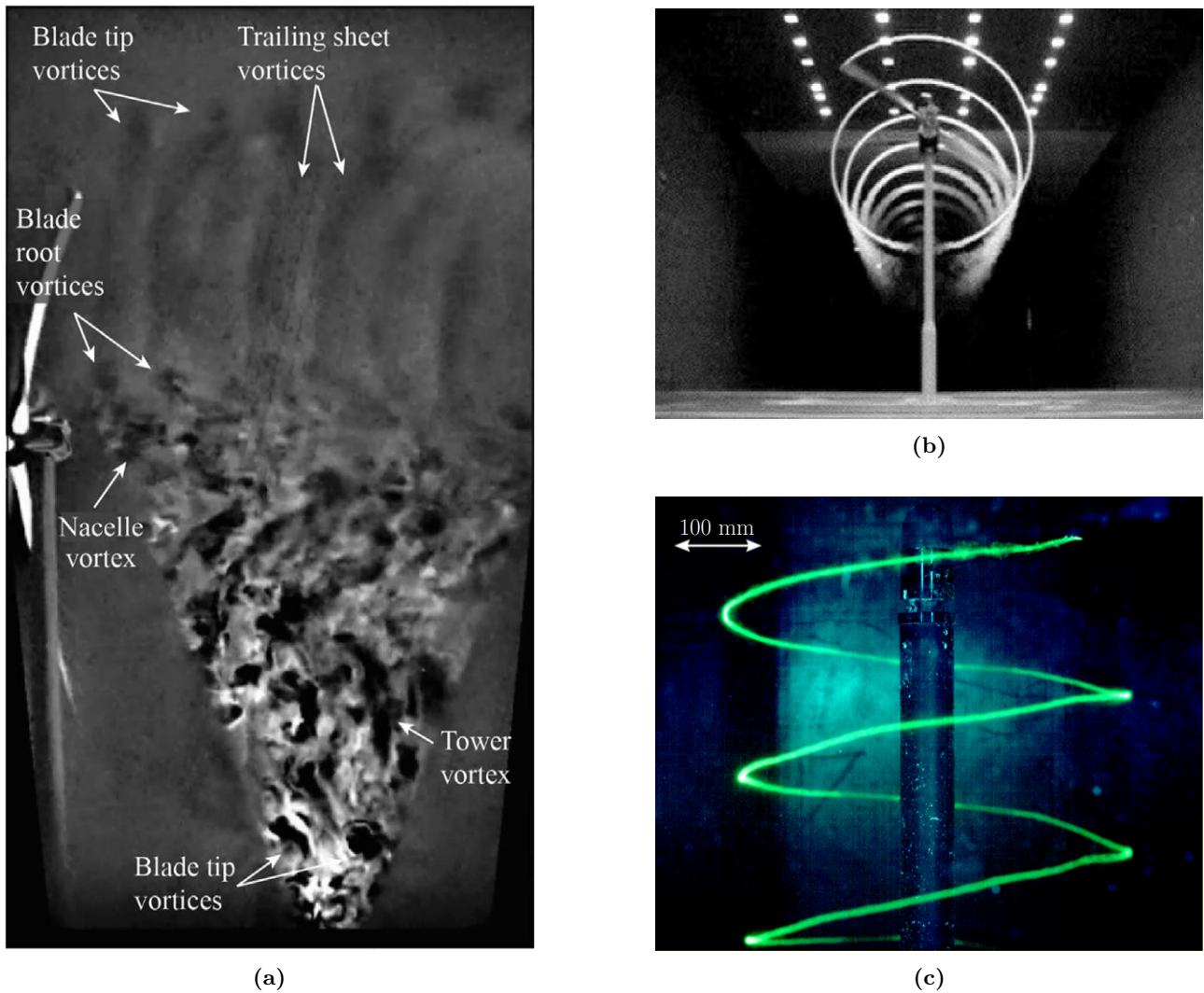


Figure 1.13: Examples of visualized instantaneous near-wake structures. **a)** Coherent patterns visualized using snow flake voids in the near-wake of a full-scale turbine including tip vortices, root vortex, nacelle vortex and the tower shadow. Taken from [67]. **b)** Tip vortex helix of a two-bladed wind turbine visualized using smoke, emanated from the blade tip. Vortex perturbations and breakdown visible induced by the turbine tower. Experiments on full-scale NREL turbine carried out in the NASA-Ames wind tunnel. Taken from [71]. **c)** Dye visualizations of a helical tip vortex. Water flume experiments on model-scale helicopter rotor in slow ascent. Taken from [72].

instability mechanisms, causing the system to deform, reconnect, and decay over time and space. Widnall [73] investigated a rotating helical vortex filament with finite core size subjected to sinusoidal perturbations. The system is unstable to small displacements, especially as the helix pitch (Equation (1.15b)) decreases. Then, the neighboring filaments interact strongly. She was able to identify three main instability modes: the *short wave*, *low wavenumber*, and the *mutual inductance* instability for small helical pitch. Gupta et al. [74] identified the mutual inductance instability of adjacent vortices as being correlated with the highest level of instability. Their model contained N_b interdigitated helical vortices. They showed that the maximum divergence rates increase for smaller helix pitch and larger number of vortices. These results were mostly reproduced by Bhagwat et al. [75]. They carried out an eigenvalue analysis of the occurring velocity field for propellers in hover and axial flight. Additionally, they showed that in numerical representations of the problem, the mutual inductance mode can be artificially excited by numerical errors. In early-stage research based on analytical considerations and stability analysis, helical vortex systems were found to be unconditionally unstable, which contradicts flow visualizations and real-world experience (e.g., visible in Figure 1.13b) [73–78]. Okulov et al. [79] extended the helical vortex system consisting of N_b tip vortices by a prescribed vorticity field and a root vortex ($N_b + 1$ representation). Their analytical approach was the first one to identify stable state regions where the tip vortex system is stabilized by the underlying vorticity field. The predictions were proven to be in good agreement with far-wake measurements. Meanwhile, Leweke et al. [80] ran water-tunnel experiments on counter-rotating straight vortex pairs. Their focus was to investigate unstable reactions of the system to 3D short wave perturbations. 2D flows with elliptical streamlines are inherently unstable with respect to 3D distortions (*elliptical* instability). Leweke et al. [80] proved that the observed unstable growth of perturbations is caused by underlying elliptical instabilities. More general, they found that the theory of elliptical instabilities is fundamental to the understanding of unstable phenomena occurring in vortical flows. Their research on straight vortices was extended by the study of a pair of co-rotating vortices [81] in axial flow [82], broadened by investigations of unstable vortex merging [83], later generalized by Meunier et al. [84, 85] (Figure 1.14a), and concluded for now in [86]. After investigating the stability of straight vortices, Leweke et al. [51] turned to helically intertwined vortices as they emerge in the near-wake of WTs. They conducted experiments in a water tunnel of a single bladed rotor and compared the results to theoretical predictions. They excited long wave and pairing instabilities by modulating the rotational speed of the rotor. Rather than reproducing the theoretical results of spatially constant but temporal growth of the instabilities, they observed spatial amplification of the unstable perturbations. The short wave instability is identified as an elliptical instability with sinusoidal modes and a *curvature* instability with helical modes. Both are of the order of the vortex core diameter. The superpositioning of the long and the short wave instabilities causes a rapid and violent wake breakdown of the system of concentrated tip vortices (Figure 1.14c). The study was later confirmed and extended by Particle Image Velocimetry (PIV) measurements by Quaranta et al. [87, 88]. Blanco-Rodríguez et al. [89–91] elaborated the theory of elliptical and curvature instabilities. Ivanell et al. [37] ran extensive investigations using Computational Fluid Mechanics (CFD) methods to investigate the stability behavior of the helical tip vortex system behind WTs. By superimposing sinusoidal perturbations of varying period and wavelength in the direct vicinity of the blade tips, they found critical frequencies which led to non-linear growth and unstable vortex breakdown. Lignarolo et al. [59] extended the knowledge on instability phenomena in WT wakes by conducting wind tunnel experiments on a model HAWT. The emerging flow patterns were subject to all three instability modes predicted by Widnall et al. [73]. The mutual inductance mode is referred to as *pairing* instability when it appears in helical vortex systems, consisting of more than one vortex filament. The pairing of neighboring vortices can result in *leapfrogging* of adjacent vortices, depending on their strength and distance. Okulov et al. [62] investigated the wake of a model HAWT in a water tunnel using Laser Doppler Velocimetry (LDV). Their analysis of the tip vortex helix revealed leapfrogging events (Figure 1.14b). Lately, the focus shifted slightly from the fundamental understanding of unstable phenomena in helical vortex system towards accelerating the tip vortex decay, i.e., controlling the dynamics of the tip

vortices beneficially. Schröder et al. [72, 92, 93] implemented a perpendicular fin on the pressure side of a rotating blade near the blade tip. The setup was immersed in a water tunnel and simulated a helicopter in slow vertical flight or hover. The thereby generated secondary vortex merges with the main one and causes its core to grow unstably, depending on the strength ratio and relative vortex distance. These approaches are inspired by comparable research on modified helicopter wing tip geometries, summarized by Brocklehurst et al. [94]. Abraham et al. [95] investigated the influence of asymmetric rotors, i.e., blade geometry differences, on the formation and stability of the occurring tip vortex helix. The investigations were also carried out in a water tunnel. An alternative approach to accelerating the wake recovery is by exciting the far-wake inherent meandering. Frederik et al. [96] investigates the resulting increase in wind park output and compares various methods and actuators. Imposing a counter-clockwise rotating motion on the wake of upstream turbines yields global helical wake fluctuations with an amplitude of 4° . Frederik et al. show a significant 7.5% of wind park AEP compared to a control baseline where all turbines are set to their respective maximum efficiency. The extensive decade-long research on the stability of helical vortex systems resulted in the accumulation of far-reaching and fundamental understanding of the underlying physic and phenomena. Nowadays, ways of using this knowledge to induce accelerated wake recovery attract a lot of attention. The research community identified the cascade from short wave instability to pairing instability to rapid wake breakdown as promising for inducing an accelerated wake recovery. As discussed in Section 1.1, the reduction of wake interactions in wind parks between adjacent wind turbines leads to a significant increase in global park AEP and reduced fatigue loads on downstream WTs. Flow control methods group into *active*, *passive*, and *reactive* flow control. Generally, active flow control allows for quick broadband reactions to changes in the operational or inflow conditions of the turbine. Passive strategies¹⁴ offer low OAM costs, and high robustness [97, 98]. Once proven effective, passive approaches are the most promising candidates to be implemented widely in large-scale wind parks.

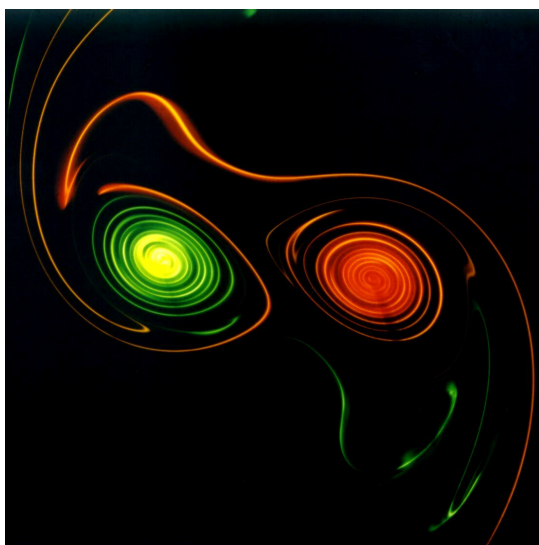
1.5 Thesis Motivation and Research Question

Motivation for designing a three-bladed horizontal axis wind turbine model for wake measurements in a water towing tank

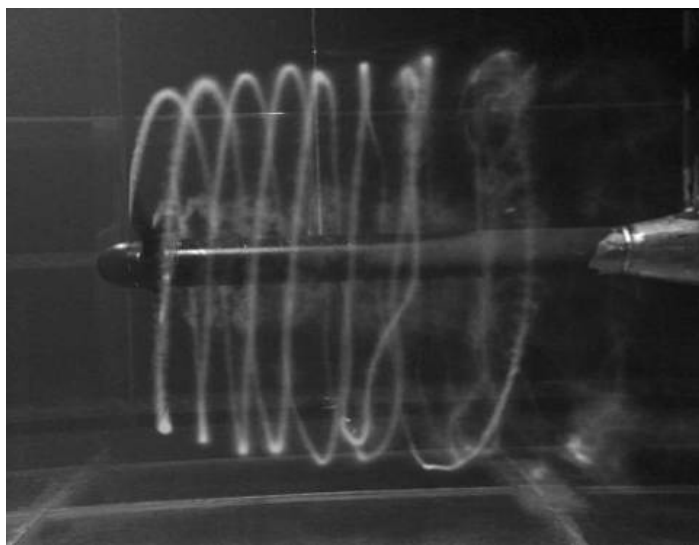
This thesis summarizes the design of a HAWT model suitable for near- and far-wake measurements using PIV in a large water towing tank. The long-term research aims for the development of passive flow control approaches for accelerating the wake decay of the turbine. For that, exciting short wave instabilities of the emerging tip vortex helix is considered the most promising strategy following the findings of Leweke et al. [51].

The reason for conducting the experiments in a large water towing tank rather than using a wind tunnel can be derived from the requirement of physical similarity. For scaling the results of experiments at model-scale to the full-scale representation correctly, all relevant dimensionless coefficients must be kept constant [99]. Fulfilling the REYNOLDS similarity (Equation (1.35a)) requires the model inflow velocity \bar{U}_M to be scaled by the factor $1/(\mathcal{D}\mathcal{V})$ [100]. For experiments where the model is smaller than in reality, $\mathcal{D} < 1$ follows. Hence, $\mathcal{V} > 1$, as it is the case for water with $\nu_M(20^\circ\text{C}) = 10^{-6} \text{ m}^2 \text{ s}^{-1}$ compared to air with $\nu_R(20^\circ\text{C}, 1.258 \text{ bar}) = 12.2 \times 10^{-6} \text{ m}^2 \text{ s}^{-1}$, eases the model speed requirement. Aerodynamic experiments conducted in water are therefore advantaged by reduced model velocities compared to similar experiments performed in air [101]. Wind tunnel experiments on model HAWT usually suffer from a high blockage which correlates the tunnel cross-section with the cross-section swept by the turbine rotor. This averts the free expansion of the wake, which results in significant alterations of its evolution and the overall performance of the rotor. Measurements which can be considered medium-scale were conducted either in the NASA Ames facility (Figure 1.13b) or as part

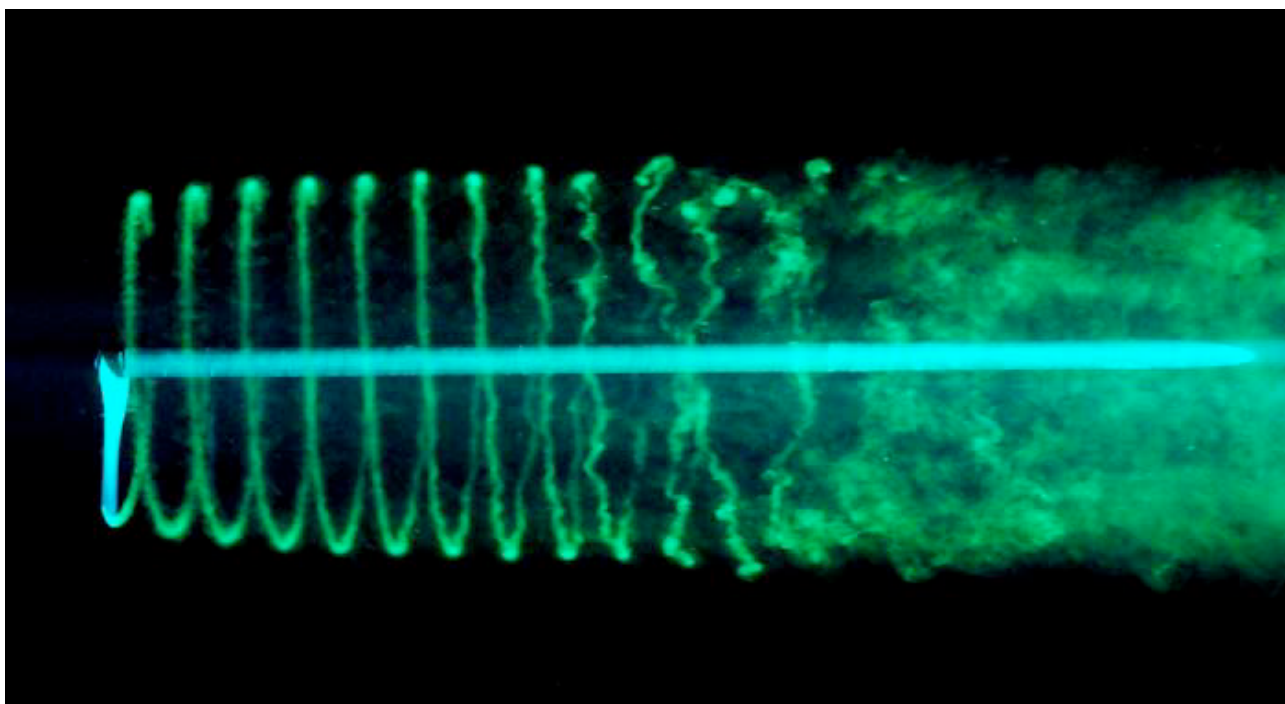
¹⁴e.g., *vortex generators*, *GURNEY flaps*, *winglets*, and generally geometric extensions and/or adjustments



(a)



(b)



(c)

Figure 1.14: a) Visualization of two co-rotating straight vortices with finite vortex core. Mutual inductance creates strain field resulting in elliptical deformation of the circular streamlines. Velocity field is unstable. Picture taken before non-linear vortex merging occurs. Taken from [84]. b) Three-bladed turbine submerged in water channel. Formation of three interdigitated tip vortices and vortex pairing visualized using dye. Breakdown of the tip vortex helix takes place approximately $1D$ downstream of rotor plane. Wake expansion and rapid root vortex decay visible. Taken from [62]. c) One-bladed rotor immersed in water flow including visualization of the tip vortex helix using dye. Short wave (i.e., elliptical or curvature) instabilities induced vortex pairing. Combination leads to rapid and violent wake breakdown. Taken from [51].

of the MEXICO project, where an open wind tunnel was used. Both projects required significant and incomparable cost [71, 102–106]. Large towing tanks are typically as sparsely distributed and rarely accessible. However, if available, the blockage becomes less of a problem since they enable the use of smaller models (Equation (1.35b)). [107]

$$\frac{\text{Re}_M}{\text{Re}_R} \stackrel{!}{=} 1 \Leftrightarrow \frac{\bar{U}_M}{\bar{U}_R} \frac{D_M}{D_R} \frac{\nu_R}{\nu_M} = \mathcal{U} \mathcal{D} \mathcal{V} = 1 \quad (1.35a)$$

$$\Rightarrow \bar{U}_M = \frac{1}{\mathcal{D}\mathcal{V}} \bar{U}_R \quad (1.35b)$$

$$\text{when } \mathcal{V} := \frac{\nu_R}{\nu_M} = 12.2, \quad \mathcal{D} := \frac{D_M}{D_R} < 1, \quad \mathcal{O}(\mathcal{D}) = 10^{-2}, \quad \mathcal{U} := \frac{\bar{U}_M}{\bar{U}_R} \quad (1.35c)$$

As by the STROUHAL similarity (Equation (1.36a)), characteristic real world time scales of period T_R are scaled by the factor $\mathcal{D}^2\mathcal{V}$. Thus, periodic aerodynamic phenomena in water at model-scale appear at a larger period, as observed in wind tunnels [101]. This is beneficial when measuring temporal instabilities using PIV, since the required temporal resolution of the cameras and other equipment is reduced. However, towing tanks of finite length combined with ensemble averaged measurements require more runs as time scales increase for the measured quantities to reach sufficient convergence.

$$\frac{\text{St}_M}{\text{St}_R} \stackrel{!}{=} 1 \Leftrightarrow \frac{D_M}{D_R} \frac{\bar{U}_R}{\bar{U}_M} \frac{T_R}{T_M} = \frac{\mathcal{D}}{\mathcal{U}} \frac{T_R}{T_M} = 1 \quad (1.36a)$$

$$\Rightarrow \mathcal{D}^2\mathcal{V} \frac{\text{Re}_R}{\text{Re}_M} \frac{T_R}{T_M} = \mathcal{D}^2\mathcal{V} \frac{T_R}{T_M} = 1 \quad \left| \begin{array}{l} (1.8a), (1.35a) \\ (1.36b) \end{array} \right. \quad (1.36b)$$

$$\Rightarrow T_M = \mathcal{D}^2\mathcal{V} T_R \quad \left| \begin{array}{l} (1.35c) \\ (1.36c) \end{array} \right. \quad (1.36c)$$

These similarities constitute the most important scalability conditions for incompressible aerodynamic experiments at model-scale. For investigations concerning WTs, the TSR represents another relevant dimensionless ratio. As can be seen from Figures 1.11d until 1.11f, the coefficient characteristics converge once REYNOLDS independence is reached. Therefore, if the REYNOLDS similarity is satisfied, geometric similar HAWTs can be compared by their respective dimensionless curves. However, model experiments rarely reach the sufficient sizes and velocities in order to comply with the requirements of the laws of similitude, due to channel size and budget limitations. It is then either argued to be sufficient to prove the independence of the acquired quantities from the relevant dimensionless numbers, or the **Experimental Fluid Mechanics** (EFD) campaign is combined with CFD strategies where real-world scaling is possible. [31, 99, 100]

Submerging a model HAWT in a water towing tank requires the inclusion of additional aspects into the design process compared to similar experiments conducted in a wind tunnel. The density of water at 20 °C and 1.258 bar is about 665 times higher than the density of air. Hence, the loading (e.g., thrust \mathcal{T} , Equation (1.18a)) and the power contained in the fluid flow (Equation (1.25a)) are significantly amplified. A towing tank (Figure 2.2) is a water channel with a free surface. The boundaries inhibit the free expansion of the wake if the model is not sufficiently submerged. Towing a model through the tank generates transversal waves, which can develop notable depth effects depending on the tow velocity. Additionally, weakly damped tank specific sloshing waves necessitate waiting times which add considerably to the duration of measurement campaigns. Conducting PIV measurements requires high quality optical accessibility. Therefore, the cameras must be submerged to the depth of the model. PIV campaigns in wind tunnels typically take a long time and require extensive calibration procedures for assuring high data quality. Running PIV experiments underwater is even more complicated and risky. Attaching the test bed to the carriage imposes the risk of artificial and intrusive vibrations excited by the carriage drives [101, 107–110]. Studying fluid mechanical effects attributed to compressibility are

not possible, due to the incompressibility of water. However, they cannot become intrusive either as the inflow velocity increases. Instead, for WT experiments, cavitation must unconditionally be prevented since air is already gaseous [111, 112]. If not, drawing conclusions from water tunnel experiments for fluid mechanical phenomena of HAWTs would be impossible [113].

Despite the numerous obvious advantages of conducting aerodynamic experiments in a large water tow tank, many challenges and risks arise. Hence, the main research question of the presented thesis reads as follows:

Research Question

How to develop a suitable design of a model HAWT for conducting PIV measurements of its wake in a large water towing tank?

The literature review revealed an extensive database of experimental horizontal axis turbine research gathered in the field of **Marine Current Turbines (MCTs)**. MCTs generate electric power from the energy stored in marine currents. They resemble HAWTs, although being fully submerged in the ocean. Most of the related research focused on the measurement of thrust and power curves for different designs of MCTs [113–122]. Additionally, similarly to WTs, MCTs are subject to large unsteady inflow variations due to waves and currents. Especially if both do not align. The research of the correlated unsteady loads and their prediction by numerical methods attracted a lot of research interest [123–128]. Lately, also MCT wakes were investigated experimentally, mostly using LDV [129–133]. Cavitation damages the blades significantly and causes considerable performance losses. Therefore, several campaigns were carried out in order to either "optimize" tidal turbine airfoils and blades with respect to cavitation onset or to improve the accuracy of its numerical predictions [134–137]. The experimental investigations were either conducted in cavitation tanks, flumes, or towing tanks using models with diameters ranging $D = 0.27$ to 1.2 m. Due to the similarities in the research on MCTs and HAWTs, a lot can be learned from the experimental investigations on MCTs regarding the research question of this thesis.

Among the mentioned literature, Payne et al. [138] contained eminent insights and highly relevant specifics on how to design and manufacture a suitable turbine. A lot of the design described in this thesis started with their publication.

1.6 Test Rig Requirements

Research facility and summary of design requirements

The PIV measurements of the wake will be conducted in the towing tank depicted in Figure 2.2. The basin has a length of $L_{\text{bs}} = 250$ m and a width of $W_{\text{bs}} = 8.1$ m. The first 60 m of the basin are $H_{\text{bs}} = 3.4$ m, the rest are $H_{\text{bs}} = 5.2$ m deep. The facility includes a preparation section which is $L_{\text{tr}} = 17$ m long, $W_{\text{tr}} = 2.1$ m wide, and $H_{\text{tr}} = 2.4$ m deep. The carriage weighs $m_{\text{to}} = 25$ t. It moves on two rails which are parallel to the mean water surface. Attached to the main carriage is a measurement platform that enables vertical and lateral traversability. Loads of up to 20 kN in vertical and 10 kN in longitudinal direction can be applied. Eight 55.5 kW direct current motors drive the carriage and allow for computer controlled velocity profiles of arbitrary shape. The programmable velocity in forward motion ranges $\bar{U}_{\text{to},+} = 0.125$ to 12.5 m s^{-1} , and in backward motion $\bar{U}_{\text{to},-} = -10$ to -0.125 m s^{-1} . Accelerations of $\ddot{U}_{\text{to}} = -3$ to 1 m s^{-2} are possible. Table 1.1 summarizes the characteristics of the towing tank facility at Technische Universität Berlin.

A three bladed ($N_b = 3$) HAWT has to be designed with a rotor diameter of $D = 2R = 1.3$ m. Compared to the basin cross-sections, the outer turbine dimensions cause a blockage of 3.15 % and 4.82 %, respectively.

Table 1.1: Dimensions and characteristics of the towing tank facility at Technische Universität Berlin from [107].

Quantity	Symbol	Range/Value	
<i>Basin</i>			
Length	L_{bs}	250 m	
Width	W_{bs}	8.1 m	
Depth	$H_{bs,1}$	3.4 m	$x_{bs} = 0$ to 60 m
	$H_{bs,2}$	5.2 m	$x_{bs} = 60$ to 250 m
<i>Trim Tank</i>			
Length	L_{tr}	17 m	
Width	W_{tr}	2.1 m	
Depth	H_{tr}	2.4 m	
<i>Carriage</i>			
Weight	m_{to}	25 t	
Possible velocities	\bar{U}_{to}	-10 to 12.5 m s ⁻¹	
Possible accelerations	$\dot{\bar{U}}_{to}$	-3 to 1 m s ⁻²	

Table 1.2: Required overall dimensions of the horizontal axis wind turbine model, parameter space, and definition of ambient conditions. Quantities with superscript "pr" are preliminarily set.

Quantity	Symbol	Range/Value
<i>Turbine</i>		
Rotor diameter	D	1.3 m
Submergence depth	H	2.5 m
Nacelle diameter	D_{nac}^{pr}	$\leq 0.1D = 0.13$ m
Nacelle length	L_{nac}^{pr}	$\mathcal{O}(D)$
Number of blades	N_b	3
<i>Operational Range</i>		
Inflow velocity range	$\bar{U}_{1,\infty}^{pr}$	0.5 to 3 m s ⁻¹
TSR range	λ^{pr}	4 to 10
Angular velocity range	Ω^{pr}	3.08 to 46.15 s ⁻¹
RPM range	n^{pr}	29.4 to 440.7 min ⁻¹
<i>Ambient Conditions</i>		
Gravity	g	9.81 m s ⁻¹
Tank temperature	θ	20 °C
Fluid density	ρ	998.22 kg m ⁻³
Kinematic viscosity	ν	10 ⁻⁶ m ² s ⁻¹
Atmospheric pressure	\bar{P}_{at}	1.013 25 bar
Ambient pressure	$\bar{P}_{\infty} = \bar{P}_{at} + \rho g H$	1.258 bar
Water vapor pressure	\bar{P}_v	2338 Pa

respectively. The depth of submergence is set to $H = 2.5$ m for minimizing free surface and tank wall effects. The nacelle diameter should be minimized ($D_{\text{nac}} \leq 0.1D = 0.13$ m), thus maximizing the distance between the generated tip vortices and the root vortex. The nacelle length is considered secondary since it does not influence the tip vortex helix generation and evolution significantly ($L_{\text{nac}} = \mathcal{O}(D)$). Jentzsch et al. [107] shows that test rig specific eigendynamics excited by, e.g., vortex shedding, or the carriage motors, appear in the acquired signals. Hence, the eigenfrequencies of the beam connecting the carriage with the turbine, i.e., the *tower*, must be raised as high as possible. Accordingly, the turbine's mass should be minimal. To reduce the tower drag and avoid tower vortex shedding, fairing must be attachable. The rotor dimensions cause large loads, whilst design and alignment imperfections cannot be avoided. For that, a small tip-to-tower distance of the blades is structurally beneficial. However, investigating pure tip vortex helix inherent instability phenomena requires minimized interference with the environment, such as the tower shadow. The a priori tip-to-tower distance is set to $\delta_{\text{ttt}} = 0.25D = 0.325$ m, although adjustments and studies of its influence on the vortex dynamics should be possible. For the same reason, the cross-section of the tower shall be minimized in the region where the tip vortices will pass. The turbine should be operable in downwind and upwind configuration. As many components as possible will be manufactured by the workshop of the institute. Thus, during the design, the in-house capacities must be considered, regarding overall dimensions, tolerances and manufacturing. The blades shall be machined using the institute's five-axis Computerized Numerical Control (CNC) mill. Studies on different tip geometries will be conducted. Hence, convenient exchanges and adjustments to the blade tips must be possible.

TSR set points over the entire typical range for HAWTs ($\lambda = 4$ to 10) must be possible. Tow carriage velocities are set to comparatively small values ($\bar{U}_{\text{to}} = 0.5$ to 3 m s^{-1}) resulting in bearable loads. The undisturbed inflow velocity \bar{U}_{∞} for the turbine is deemed equal to the tow velocity ($\bar{U}_{\infty} := \bar{U}_{\text{to}}$). The combination of inflow velocity, TSR and rotor radius yields a rotational speed range of $n = 22$ to 293.8 min^{-1} or a rotational frequency range of $f = 0.367$ to 4.897 Hz . The turbine dimensions and the parameter space are summarized in Table 1.2. Additional design requirements and global guidelines are summarized in the following list:

- | | |
|---|--|
| <p>8) Airfoil selection</p> <ul style="list-style-type: none"> • Selection of low-REYNOLDS number airfoil • Prevent surface cavitation • Avoid Laminar separation • Sufficient thickness for minimal deflection | <p>10) General test rig design aspects</p> <ul style="list-style-type: none"> • Structural safety of all critical components • Water proofing concept with redundancies • Modularity • Operational safety • Accessible for existing PIV system • Non-corrosive |
| <p>9) Blade design</p> <ul style="list-style-type: none"> • Maximized REYNOLDS number • Constant circulation over blade span • Creation of concentrated tip vortices of sufficient size • Attached flow conditions over entire span • Blades manually pitchable • Modular blades with exchangeable tips | <p>11) Turbine characterization</p> <ul style="list-style-type: none"> • Angular velocity Ω, inflow velocity \bar{U} • Thrust \mathcal{T}, torque \mathcal{Q}, power \mathcal{P} • Blade phase angle ϑ • Edge- and flapwise Blade Root Bending Moment (BRBM) $M_{b,f}$ and $M_{b,e}$ |

The testbed is called **Underwater Berlin Research Turbine** (UBeRT) in analogy to the preceding HAWT model of the institute, called **Berlin Research Turbine** (BeRT) [139–143]. The first-stage research including the investigations of short wave instabilities emerging in the tip vortex helix will be conducted between the years 2023 and 2025 at the Technische Universität Berlin.

2 Methodology

The following chapter gives a brief introduction to the methods of product design (Section 2.1), followed by an overview of the design workflow (Section 2.2).

2.1 Brief Introduction to Methods of Product Design

Introduction into relevant methods of product design following VDI 2221

The **V**erband **D**eutscher **I**ngenieur**e** (VDI) describes general methods of the product design in their guideline VDI-2221 [144, 145]. Generally, the design process is considered a feedback loop. Actions and their consequences are constantly compared to the overall aims of the product design. The process is concluded, once the design result is deemed consistent with the defined targets, whilst considering budget and time limitations. Decision-making competencies and strategies are essential for a successful design process. A typical design strategy in accordance with VDI-2221 contains the following steps:

- a) **Situation analysis**
Collection and identification of tasks and problems
 - b) **Objective formulation**
Definition of milestones and objectives
 - c) **Solution synthesis**
Development of a solution including alternatives
 - d) **Solution analysis**
Gathering multi-perspective information on solutions
 - e) **Assessment**
Assessing and grading of solutions
 - f) **Decision**
-
- Diagram illustrating the design process steps and feedback loops:
- Step c) **Solution synthesis** and Step d) **Solution analysis** are connected by an **Iterate** loop.
 - Step e) **Assessment** and Step c) **Solution synthesis** are connected by a **Compare** loop.
 - Steps a) through f) are collectively labeled as **Document and Evaluate**.

In academia, once the research questions are stated, the design process usually starts with an extensive *literature research* to identify (best-) practice examples and lessons-learned. Possible collaborations and competing institutions might be detected. The problem is augmented by the current state of the research and details on typical methods. Additionally, the *independent variables* of the engineering task are identified, resulting in the assessment of the parameter space. These quantities dictate the global framework of the issue at hand (Item a)). Numerous tools exist to support the decision-making. Among others, the following ones are used in the presented thesis. *Flow charts* can help to identify dependencies requiring chronology, and parallelization possibilities of sub-tasks in the design process. *GANTT charts* combine the sequential and parallel arrangement of tasks with a time schedule [144]. The *morphological box* is a matrix, which enables the systematic combination and comparison of competing solutions regarding their efficacy and quality. Design tasks are arranged in rows, corresponding solutions and strategies constitute the columns. Possible paths for solving the superior problem are measured using a defined metric and compared accordingly. Morphological boxes

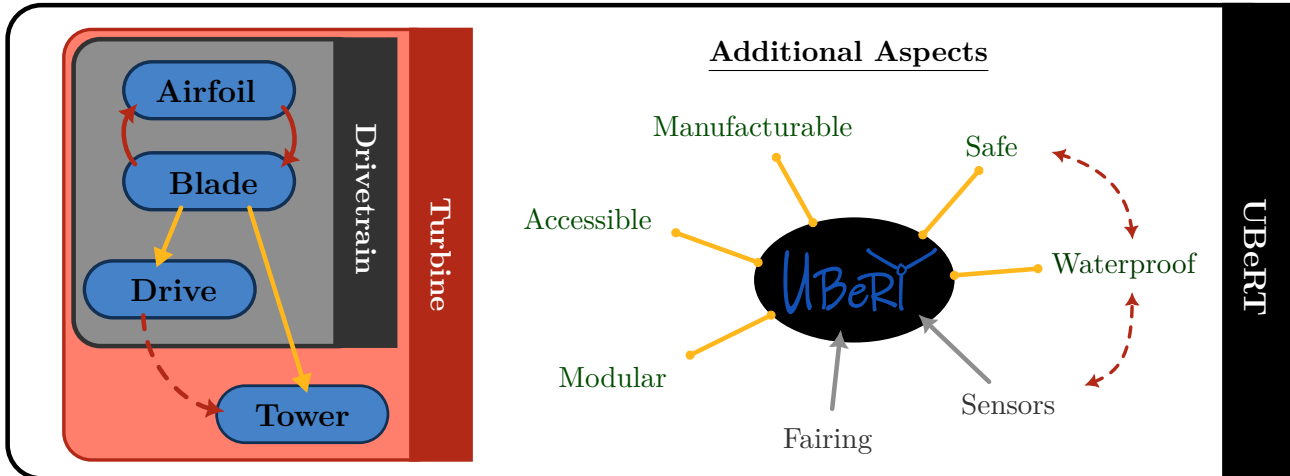


Figure 2.1: Product design workflow for the Underwater Berlin Research Turbine.

can be used for ranking solutions at all stages and levels of the design process, or for the entire solution strategy. [146]

The product design is governed by *creative, iterative, simultaneous, and concurrent* engineering. These tools are specifically important during the design steps *c)* and *d)*. *Early-Stage* assessment of the design process and reoccurring supervision (*Four-Eyes-Principle*) can help to identify possible dead ends and errors early in the development. Additionally, they are necessary for a profound solution assessment (Item *e)*) and the final decision-making (Item *f)*). The entire process should be fully documented to allow its qualitative and quantitative efficacy evaluation a posteriori [144]. Considerable insights can be gained from a logically documented and evaluated design process.

Critical (groups of) components of the product must be dimensioned according to their respective load cases. For complex and superimposed load cases, the **D**eutsches **I**nstitut für **N**ormung (DIN) and the VDI, and its supranational and international counterparts publish guidelines, which support the product design. The proceedings help with gaining confidence in the developed solutions, when best-practice examples and experiences are missing.

When numerical methods are used in fluid mechanics, *validation* and *mesh independence studies* must be conducted to gain confidence in the results. Tu et al. [147] state, that validation could be done against an experimental data set. The data should satisfy certain requirements, such as a high quality and accuracy. Additionally, the data should be specifically gathered for validation purposes of CFD approaches. Furthermore, the data must cover a similar region of interest, whose fluid mechanical phenomena can easily be isolated.

2.2 Design Workflow and System Identification

(Sub-) system identification and workflow for the Underwater Berlin Research Turbine design

Figure 2.1 depicts the workflow of the design process. Sub-systems, milestones, and dependencies can be identified. The main objective of the test rig is to create an accessible concentrated tip vortex helix. For that, the aerodynamic rotor design is crucial and used as a starting point. An iterative approach is needed for the selection of a suitable airfoil. By determining the design parameters AoA, TSR, and REYNOLDS number, the generated lift and drag forces are derived from the airfoil's polars (Figures 1.4). The extrusion of the airfoil to the rotor blade, allows the calculation of the spanwise load distributions, and subsequently the flap- and edgewise bending. If the deflections are

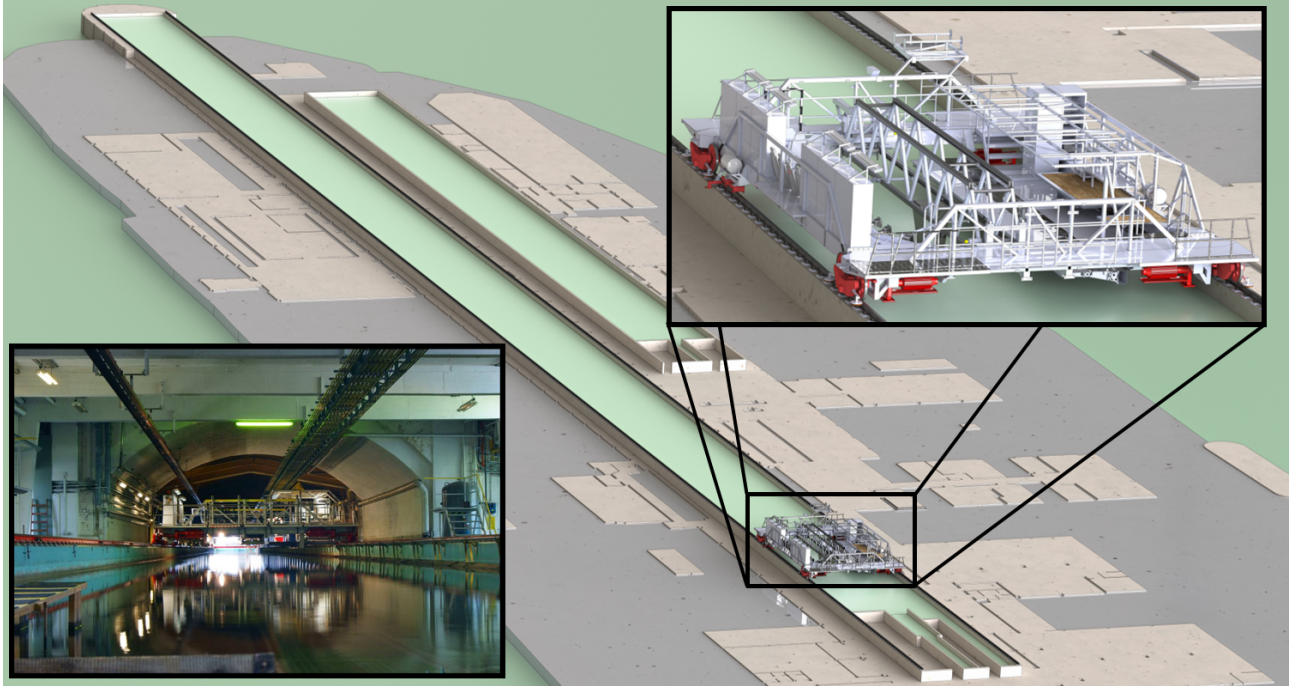


Figure 2.2: Large towing tank and carriage at the Technische Universität Berlin from [107].

considered too large or the structural safety limitations are violated, the constituting airfoil must be changed. Alternatively, an adjusted design AoA can be assigned. Once the airfoil selection is finalized and the preliminary blade geometry is determined, the design loads for the drive (rotational turbine speed, torque, and power), and for the tower (thrust and rotational turbine speed for avoiding excited eigenfrequencies) are determined. Drive projecting and tower design are only weakly related and can be engineered simultaneously. Structural parts must be evaluated regarding their manufacturability, modularity, and structural safety (e.g., blades, main shaft, hub). Other components are added to increase or ensure the general safety, the water proofing, and the accessibility of the overall design (e.g., traverse, sealing). Additionally, the placement of sensors and mounting possibilities for fairing must be accounted for throughout the engineering process.

According to the VDI-2221 [144], the development of UBeRT is considered a *complex problem* due to its multiperspectivity: the complexity of the engineering task cannot be fully assessed apriori (*lack of transparency*), several objectives have to be balanced (*multi-intentionality*), and complement or even contradict each other (*networking*), and the task grows over time, as experiences are gathered (*inner dynamics*). To assure the quality and the functionality and detect early-stage design errors, thorough documentation and frequent supervision is necessary. The remainder of the thesis is structured according to the visualized workflow in Figure 2.1.

3 Realization

The following paragraphs describe the necessary steps to design a model HAWT suitable for underwater PIV measurements of wake inherent instabilities in a large water towing tank. In Section 3.1, the parameter space is defined and assessed. Thereafter, the sequence of the UBeRT design process is presented. Appropriate airfoil candidates are identified and analyzed in Section 3.2. Competing rotor blades are derived from the candidates and compared regarding their fluid mechanic properties and resistance to aerodynamic loading in Section 3.3. The most suitable blade design is selected. An appropriate drive train and tower are tailored according to the requirements of the rotor in Section 3.4. Section 3.5 provides insights into the numerous implemented sealing strategies. Safety and operational signals are acquired. Necessary, redundant, and additional sensor systems are summarized.

3.1 Parameter Space Assessment

Estimation of the parameter space and derivation of design driving factors

Table 1.2 defines the operational regime requirement for the UBeRT test rig and the physical constants for all calculations. For an initial estimation of the *dependent variables* mean absolute inflow velocity $\bar{q}(r)$ and REYNOLDS number $\text{Re}(r)$ upper limits are calculated (Equations (1.5c) and (1.8b)) and displayed in Figures 3.1a and 3.1b. The cavitation number σ characterizes the risk of fluid vaporization, depending on the flow velocity $\bar{q}(r)$ and the static ambient pressure \bar{P}_∞ . At water depth $H = 2.5\text{ m}$, the static pressure is formed by the atmosphere and the water column above (Table 1.2). At points, where the ambient pressure falls below the vapor pressure of the fluid \bar{P}_v , cavitation must be expected. Low cavitation numbers correlate with a high risk of cavitation onset. [148, 149]

$$\sigma(r) := \frac{2(\bar{P}_\infty - \bar{P}_v)}{\rho \bar{q}(r)^2} \quad (3.1a)$$

$$\sigma(R) = \frac{2(\bar{P}_\infty - \bar{P}_v)}{\rho \bar{q}(R)^2} > \frac{2(\bar{P}_\infty - \bar{P}_v)}{\rho \bar{q}^*{}^2} =: \sigma^* \quad \left| \text{(1.5c)} \right. \quad (3.1b)$$

Figure 3.1a depicts the upper limit of the blade tip inflow velocity \bar{q}^* . The maximum velocity seen by the blade tips increases with TSR and $\bar{U}_{1,\infty}$. Values of up to 30 m s^{-1} are reached. The REYNOLDS number $\text{Re}(R)$ follows the same trend (Equation (1.8a)). Its upper bound Re^* approaches values of 1.2×10^6 for $\lambda = 10$ and $\bar{U}_{1,\infty} = 3\text{ m s}^{-1}$. Towards the lower end of the operational regime, Re^* drops to approximately 8×10^4 , resulting in an overall average of 4.5×10^5 . Accordingly, the conservative estimation σ^* of the cavitation number $\sigma(R)$ at the blade tip decreases towards the upper end of the parameter space (Figure 3.1c). Values as small as 0.27 are calculated, imposing the high risk of cavitation for the respective operation points.

From the prescribed tow carriage velocity range (Table 1.2) and the swept area of the rotor $A = 1.327\text{ m}^2$, a maximum fluid power of $\mathcal{P}_{\text{flow}} = 17.887\text{ kW}$ follows. Assuming a maximum $C_{\mathcal{P},\text{max}}(\lambda = 4.2) = 0.41$ based on the example characteristics in Figure 1.11d results in an upper bound of $\mathcal{P} = 7.334\text{ kW}$ for the aerodynamic power (Equation (1.25b)). The turbine thrust follows from Equation (1.18a). Its limit is evaluated to $\mathcal{T}_{\text{max}} = 7.811\text{ kN}$, for $C_{\mathcal{T},\text{max}}(\lambda = 10) = 1.31$ from Figure 1.11f. Accordingly, the estimated maximum torque reads $\mathcal{Q}_{\text{max}} = 437.93\text{ Nm}$ (Equation (1.18b)), where $C_{\mathcal{Q},\text{max}}(\lambda = 3,4) = 0.113$ (Figure 1.11e). These values illustrate the order of the upper bound of the static loading and indicate the necessary structural resistance of the components. Note, that the maxima of the turbine parameters appear at different operational points. Therefore, for each individual

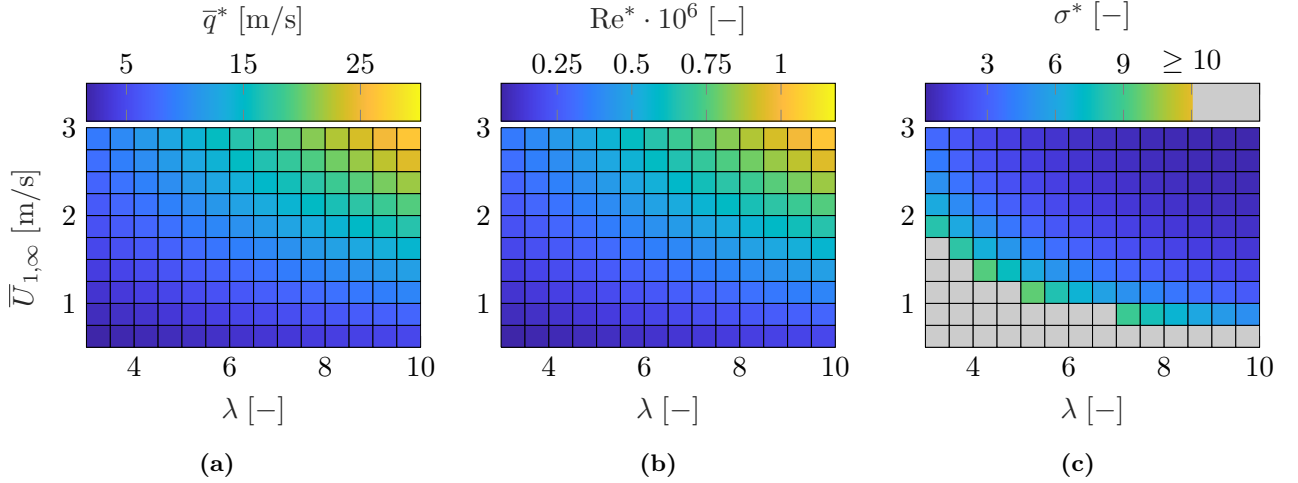


Figure 3.1: Initial estimation of the parameter space throughout the operational regime defined in Table 1.2: **a)** Upper limit \bar{q}^* for the averaged absolute inflow velocity at the blade tip $\bar{q}(R)$ calculated from Equation (1.5c). $\max \bar{q}^* = 30.15 \text{ m s}^{-1}$, $\text{mean } \bar{q}^* = 11.53 \text{ m s}^{-1}$. **b)** Calculated REYNOLDS number Re^* as an upper limit for the chordwise REYNOLDS number at the blade tip $Re(R)$ (Equation (1.8b)), with $c(R) = 0.0392 \text{ m}$ extracted from the chord distribution in Figure 1.7b. $\max Re^* = 1.18 \times 10^6$, $\text{mean } Re^* = 4.5 \times 10^5$. **c)** Conservative bound σ^* of the cavitation number σ calculated from Equation (3.1b). $\min \sigma^* = 0.272$, $\text{mean } \sigma^* = 6.797$.

part, a design driving load case must be derived, prior to the dimensioning and selection.

Following Jentzsch et al. [101], transversal waves of wavelengths δ_{trans} according to Equation (3.2a) are generated. For a sufficient decay of the orbital particle trajectories induced by the surface waves, $\delta_{\text{trans}} < H$ must be assured [107]. Another parameter for the evaluation of the depth effects of free surface waves is introduced by Aoki et al. [150] (Equation (3.2b)). The surface effects are considered sufficiently alleviated, as long as $C_H < 0.37$ holds true.

$$\delta_{\text{trans}} = \frac{2\pi\bar{U}_{\infty}^2}{g} \quad (3.2a)$$

$$C_H := \frac{\bar{U}_{\infty}}{\sqrt{gH}} \quad (3.2b)$$

Figures 3.2 display the dependency of the depth parameters (Equations (3.2)) on the tow carriage velocity \bar{U}_{∞} . The wavelength of the generated transversal waves is square dependent on the velocity. For carriage velocities exceeding 2 m s^{-1} , the threshold condition for the wavelength is violated. The same is true for the depth parameter. Hence, for tow velocities larger than 2 m s^{-1} , the effects of surface waves cannot be considered negligible.

3.2 Airfoil Selection

Airfoil selection and analysis regarding cavitation onset

From Lyon et al. [38], several low-REYNOLDS number airfoils are selected and analyzed regarding their risk of triggering cavitation and stall (Item 8). Three airfoil candidates are listed in Figures 3.3a until 3.3c. The Clark-Y airfoil constitutes the BeRT blades and is therefore used as a baseline case. According to Lyon et al. [38], the SG60XX series (SG6040-SG6043) is designed specifically for small HAWT. The SG6041, SG6042, and SG6043 are airfoils of high aerodynamic efficiency and designed for deployment towards the blade tip. All three airfoils have a fixed maximum thickness of $d_{\text{max}} = 10\%$.

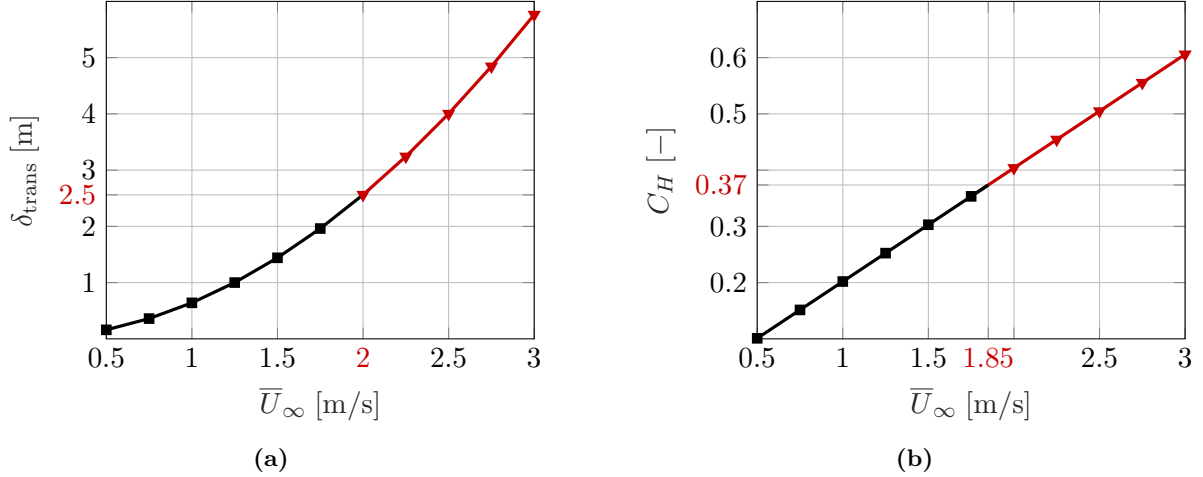


Figure 3.2: Assessment of the depth effect of transversal surface waves for the prescribed tow carriage velocities. **a)** Expected wavelength δ_{trans} of transversal waves, calculated from Equation (3.2a). **—** Operational regime, where threshold condition $\delta_{\text{trans}} < H$ is met, **—** where violated. **b)** Depth parameter C_H derived from Equation (3.2b). **—** Operational regime, where threshold condition $C_H < 0.37$ is met, **—** where violated.

The SG6040 airfoil is "optimized" for inner sections, i.e., $r/R = 0$ to 0.3 because of its larger maximum thickness $d_{\text{max}} = 16\%$, whilst still generating sufficient lift. The location of maximum thickness $\eta_d = 35\%$ is affixed comparatively high, to increase the structural integrity of the airfoil family. The thorough analysis of the Clark-Y, the SG6040 and the SG6041 is presented here. The SG6041 is included because it combines the small thickness of the Clark-Y with an increased η_d . However, due to the high expected loads, also the thicker SG6040 airfoil is added to the list. In Figure 3.3, the airfoils and a thickened configuration (Figures 3.3a until 3.3c), and their respective lift C_L (Figures 3.3d until 3.3f), drag C_D (Figures 3.3g until 3.3i), and maximum negative pressure coefficients $-C_{p,\text{max}}$ (Figures 3.3j until 3.3l) as functions of the AoA are depicted.

Airfoils have sharp TEs to comply with KUTTA's condition (Section 1.2). However, for manufacturing reasons and to assure the structural resistance of the rear part of the profile, the geometries are thickened. The thickening function of Equation (3.3) is used. ζ_T denotes the ζ coordinate of the *thick* airfoil, based on the ζ coordinate of the original (i.e., *sharp*) profile and a target TE thickness of $\Delta = 0.01c$. The thickening of the blade starts at the LE, where $\eta = 0$. Points attributed to the suction side are transformed by (+), pressure side points by (-). [128]

$$\zeta_T = \zeta \pm \frac{\Delta \eta}{2c} \quad (3.3)$$

From Lyon et al. [38], experimental data for the depicted airfoils is available for a range of REYNOLDS numbers (\blacktriangledown in Figures 3.3). The visualized results of the experiments were conducted in a wind-tunnel at REYNOLDS number $\text{Re} = 3 \times 10^5$, with zig-zag-type tripping applied at $\eta = 0.02c$ on the suction and $\eta = 0.05c$ on the pressure side. However, for the design process other REYNOLDS numbers (e.g., $\text{Re} = 4 \times 10^5$) are necessary. Therefore, XFOIL's capabilities to reproduce the 2D measurements are investigated. XFOIL is a tool for deriving the aerodynamic characteristics of 2D geometries numerically. Its approach is based on the potential theory. Additionally, semi-empirical methods are included for estimating the airfoil drag. XFOIL is thoroughly validated and obtains accurate results especially for incompressible flows [46]. The data set, generated for validating XFOIL in the presented thesis, is marked with (\blacksquare) in Figure 3.3. For that, forced transition at $\eta = 0.02c$ on the suction and $\eta = 0.05c$ on the pressure side is turned on. As can be seen from Figures 3.3d and 3.3e, the lift curves of the sharp Clark-Y and SG6040 profile are accurately reproduced by the simulation over a large range of AoAs. Only near stall, deviations are present. However, the ultimately chosen airfoil will be operated with sufficient margins towards stall. The lift curve of the SG6041 airfoil

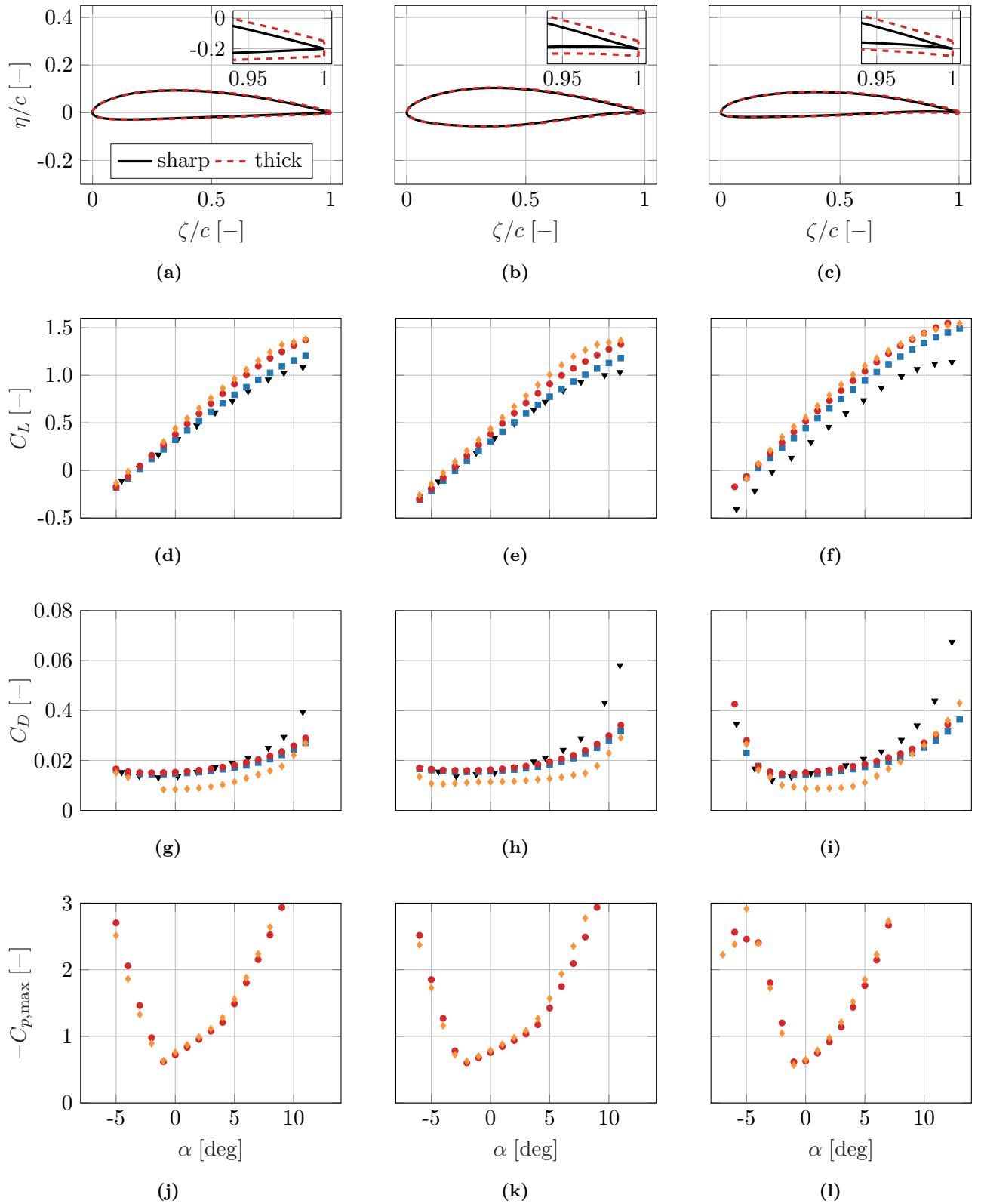


Figure 3.3: Sharp airfoil geometries (a) until (c) same as in Figures 1.4a until 1.4c. Thickened profiles depicted, derived from Equation (3.3). Corresponding lift C_L (d until f), drag C_D (g until i), and $-C_{p,\max}$ (j until l) as functions of angle of attack α at REYNOLDS number $Re = 3 \times 10^5$. (\blacktriangledown) Experimental 2D data for so-named sharp profiles from Lyon et al. [38]. Zig-zag-type tripping applied at $\eta = 0.02c$ on suction and $\eta = 0.05c$ on pressure side. XFOIL simulation with forced transition at $\eta = 0.02c$ on suction and $\eta = 0.05c$ on pressure side for (■) sharp and (●) thick airfoil. (◆) XFOIL simulation of thickened profile with transition simulated by an e^9 model.

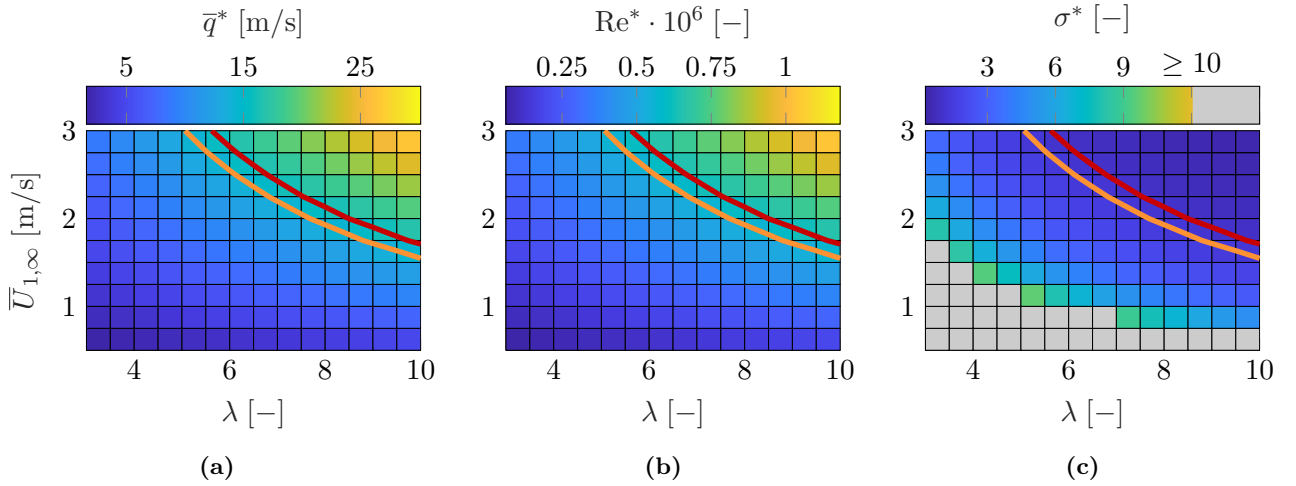


Figure 3.4: Assessment of the operable regime without cavitation onset based on the SG6040 airfoil for $\alpha_{\text{des}} = 1^\circ$ and $\alpha_{\text{des}} = 3^\circ$ as design angles of attack. Values derived at $\text{Re} = 3 \times 10^5$ from Figure 3.3k. **a)** Absolute inflow velocity. **b)** REYNOLDS number. **c)** Cavitation number. Upper right section of operational regime imposes the risk of surface cavitation.

is overestimated by XFOIL over the entire AoA range (Figure 3.3f). The constant offset measures approximately $\Delta C_L \approx 0.2 \approx 0.44 C_{L,\text{exp}}$. All three drag characteristics (Figures 3.3g until 3.3i) are well reproduced by XFOIL for low AoAs. Starting at $\alpha = 5^\circ$, the simulation underestimates the drag coefficient for all three sharp airfoils. Especially large deviations can be seen in Figure 3.3i. Again, the design AoA of the final airfoil will be sufficiently small for maximizing the margin towards stall and for reducing the overall blade loads. Hence, the simulation data is deemed accurate for the AoA region of interest. Assuming XFOIL also generates valid results for the thick airfoils, the presented data can be used to evaluate the influence of the thickening. Figures 3.3a until 3.3c include the thickened geometries of the Clark-Y, the SG6040, and the SG601, focusing on the resulting TE. For all three airfoils, the thickening results in a slightly increased slope of the lift coefficient (\bullet) in Figures 3.3d until 3.3i). The influence on the drag coefficient is rather small. A slight increase over the entire AoA range can be seen, compared to the simulated results for the sharp airfoils. Additionally, the influence of the tripping on the airfoil characteristics is investigated. For that, the forced transition in XFOIL is set to the TE. XFOIL then treats the transition with an e^9 -amplification formulation [46]. Assuming accurate results, free transition affects the lift coefficients marginally (\diamond) in Figures 3.3d until 3.3i). Only for the SG6040 airfoil, a slight increase in C_L can be seen at $\alpha = 5$ to 10° , compared to the simulation of the thick airfoil with forced transition. Contrarily, the effects on the drag coefficient are significant. For the Clark-Y and the SG6040 airfoil, free transition results in reduced C_D values almost for the entire AoA range. For the SG6041, the drag reduction is immanent between $\alpha = -2$ to 8° . This can be attributed to the reduced surface friction of laminar boundary layers. If the simulated chordwise point of transition lays closer to the TE than for the tripped simulations, the frictional drag forces will be smaller. The application of tripping assures a stable and defined flow state around the airfoil. It might also prevent the formation of laminar separation bubbles, as can be seen in the polars in Figure 1.4h of the SG6040 for a REYNOLDS number of $\text{Re} = 10^5$. As of now, all three airfoils appear to be suitable for the application in the UBeRT test rig. Their linear response over a large range of AoA is beneficial for the numerical estimation and representation of the aerodynamic rotor properties. Following Eppler et al. [148, 149], the cavitation number (Equation (3.1)) can be correlated with the pressure coefficient (Equation (1.10a)). For points \vec{x} in the mean pressure field $\bar{P}(\vec{x})$, where $\bar{P}(\vec{x}) = \bar{P}_v$, the negative pressure coefficient \bar{C}_p is equal to the cavitation number σ (Equation (3.4)). Note, that for 2D considerations, \bar{q} is set equal to \bar{U}_∞ . Therefore, the highest risk of surface cavitation of an airfoil can be assessed by comparing the maximum negative pressure coefficient $-C_{p,\text{max}}$ to the

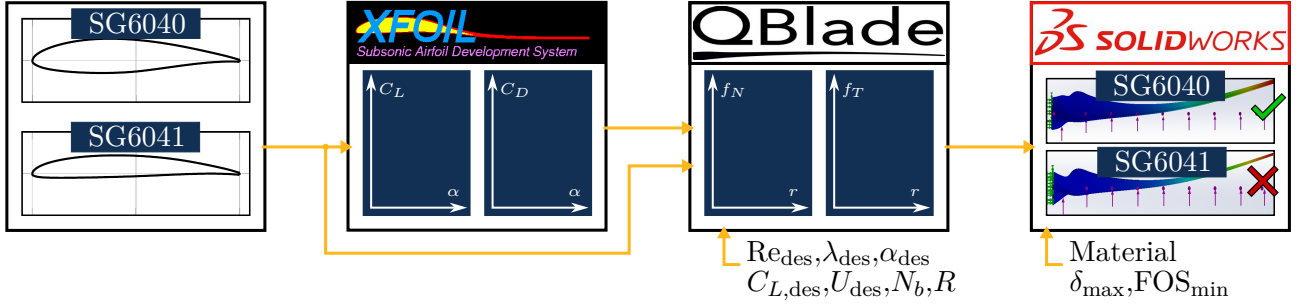


Figure 3.5: Blade design workflow for the Underwater Berlin Research Turbine using XFOIL [46], QBLADE [56], and SOLIDWORKS SIMULATION.

cavitation number, conservatively estimated by Equation (3.1b).

$$\begin{aligned} \bar{C}_p(\bar{P}_\infty - \bar{P}_v) &= \sigma(\bar{P}(\vec{x}) - \bar{P}_\infty) && \left| \begin{array}{l} (3.1a), (1.10a) \end{array} \right. \\ -\bar{C}_p &= \sigma && \left| \begin{array}{l} \bar{P}(\vec{x}) = \bar{P}_v \end{array} \right. \end{aligned} \quad (3.4)$$

Figures 3.3j until 3.3l show the dependency of $-C_{p,max}$ on the AoA α for all three profiles. From Figure 3.1c, the minimum cavitation number is $\sigma_{min}^* = 0.272$. Comparing this to the $-C_{p,max}$ curves of the airfoils reveals, that all three profiles impose the risk of surface cavitation. Even if a comparatively small design AoA is prescribed, the airfoils will most definitely cavitate towards the upper-right end of the parameter regime. Figures 3.4 show the upper bounds for the absolute inflow velocity, the REYNOLDS number, and the cavitation number in analogy to Figures 3.1. Representatively, the maximum negative pressure contour for the SG6040 profile is superimposed. Values are taken from Figure 3.3k for two different AoAs $\alpha \in \{1,3\}^\circ$. As can be seen, a fair section of the a priori parameter space (Table 1.2) becomes inoperable according to the assessment of cavitation onset. The risk is decreased for lower design AoA assuming, that the rotor blades will be operated at their design conditions.

From the three displayed airfoils, the SG6040 and the SG6041 profiles will be investigated regarding their suitability for the UBeRT design. Both airfoils offer high-quality characteristics. Additionally, the larger values of $\eta_d = 36\%$ compared to the 28% of the Clark-Y are deemed beneficial regarding their structural resistance and manufacturability (Item 8 and Section 1.6). The analysis of the resulting risk of surface cavitation shows, that the operational regime has to be reduced to a maximum tow velocity of $\bar{U}_{1,\infty} = 1.5 \text{ m s}^{-1}$. For a design AoA of $\alpha_{des} = 1^\circ$, Figures 3.4a until 3.4c suggest that no surface cavitation must be expected throughout the resulting parameter regime (Item 8). Additionally, reducing the maximum tow velocity agrees well with the estimated depth effects (Figure 3.2). The upper bound REYNOLDS numbers Re^* (Figure 3.4b) is considered sufficiently high for creating representative flow states. Thus, answering the stated research questions will be possible at the reduced REYNOLDS number (Item 9). To assure sufficient safety factors, the design inflow velocity is set to $U_{des} = 2 \text{ m s}^{-1}$. The design driving load cases (e.g., thrust, blade loads, Table 3.1) are derived from this operational point (Item 10). For $\alpha_{des} = 1^\circ$, The SG6040 and SG6041 airfoils generate representative flow states, whilst offering large margins towards stall. Additionally, the comparatively small design AoAs result in reduced design lift coefficients, causing increased blade chords (Equations (1.31) and (1.29)). This benefits the maximization of the spanwise REYNOLDS number (Item 8, 9) and the initial core size of the generated tip vortex (Equation 3.7a, Figure 3.16)

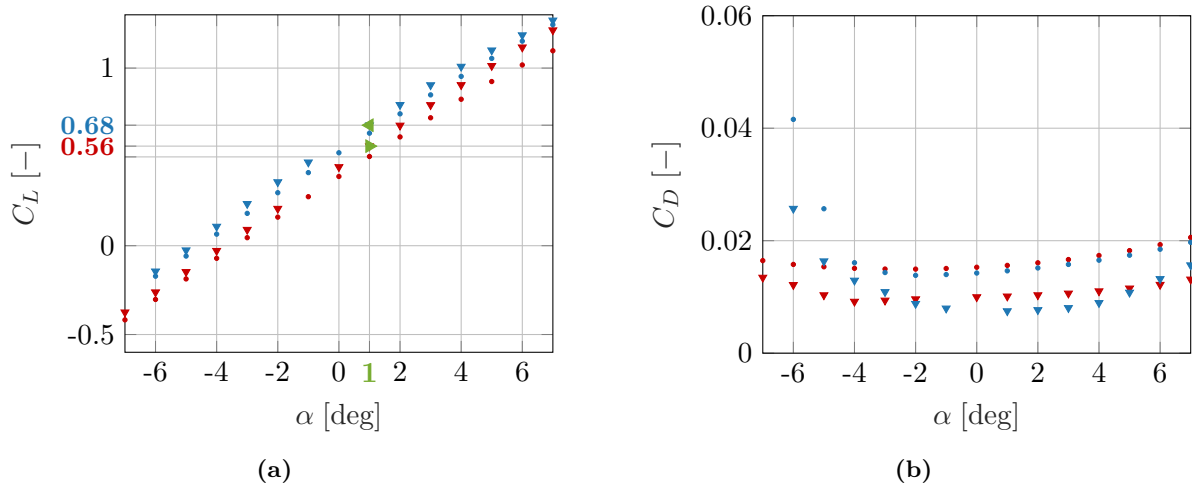


Figure 3.6: Simulated polars of the ($\blacktriangledown, \bullet$) SG6040 and ($\blacktriangledown, \bullet$) SG6041 airfoils at $Re = 4 \times 10^5$. (\bullet) Forced transition set at $\eta = 0.02c$ on suction and $\eta = 0.05c$ on pressure side. (\blacktriangledown) Free transition. **a)** Lift C_L and **b)** drag C_D coefficient. Design angle of attack set to $\alpha_{des} = 1^\circ$ (Section 3.2). Design lift coefficients $C_{L,des}$ of the (\blacktriangleright) SG6040 ($C_{L,des} = 0.56$) and the (\blacktriangleleft) SG6041 airfoil ($C_{L,des} = 0.68$).

3.3 Rotor Blade Design

Design and assessment of two rotor blades based on the SG6040 and SG6041 airfoil, regarding their aerodynamic and structural applicability

The two selected airfoils are analyzed regarding their suitability for the UBeRT test rig. Polars for a range of REYNOLDS numbers are created using XFOIL without forced transition. Thereafter, two sets of blades are designed using SCHMITZ'S approach (Equations (1.31)) and implemented in QBLADE. The tangential and normal aerodynamic loads at design conditions are derived ($U_{des} = 2 \text{ m s}^{-1}$, $Re_{des} = 4 \times 10^5$, $\alpha_{des} = 1^\circ$, $\lambda_{des} = 7$). The loads are imported into the Finite Element Method (FEM) environment of SOLIDWORKS. A material is assigned. Mesh-independence-studies are carried out to gain confidence in the acquired results. Lastly, the resulting minimum Factor Of Safety (FOS) and the maximum deflections at the blade tip are compared against thresholds. From the two airfoil shown here, one is selected for constituting the final set of blades for the UBeRT test rig. The described workflow is visualized in Figure 3.5.

Figure 3.6 comprises the polars, used to locate the design lift coefficients $C_{L,des}$ for both airfoils at $Re_{des} = 4 \times 10^5$. This is smaller than $\overline{Re}^* = 4.5 \times 10^5$ (Figure 3.1b) because the constrained parameter regime causes a reduced averaged REYNOLDS number (Figure 3.4b). Simulation results with and without forced transition on the suction and pressure sides are shown. The lift coefficients are taken from the curves without forced transition because for the initial tests, the blades will be operated without tripping. Aerodynamically, the SG6041 outperforms the SG6040. However, the simulation tends to overestimate the lift coefficients of the SG6041 (Figure 3.3f). Additionally, a smaller $C_{L,des}$ leads to increased overall blade chords (Equations (1.31) and (1.29)), which benefits the resulting REYNOLDS number. The drag coefficient of the SG6040 is constant over a large AoA range, whereas the SG6041's has a smaller minimum drag coefficient.

Two blade designs of a three-bladed rotor ($N_b = 3$), constituted by the SG6040 and the SG6041, respectively, are engineered using SCHMITZ'S design approach (Equations (1.31)). The design TSR is set to $\lambda_{des} = 7$, since it is representative for modern HAWTs [31]. The resulting chord distributions are shown in Figure 3.7a. Qualitatively, both curves match. Yet, as expected, the blade made from the SG6041 encompasses a smaller overall blade chord $c_S(r)$. Both blades become more slender towards the tip, approaching chords of $c_S(R) = 43.4 \text{ mm}$ and 35.9 mm , respectively. The blade pitch $\beta_S(r)$ is

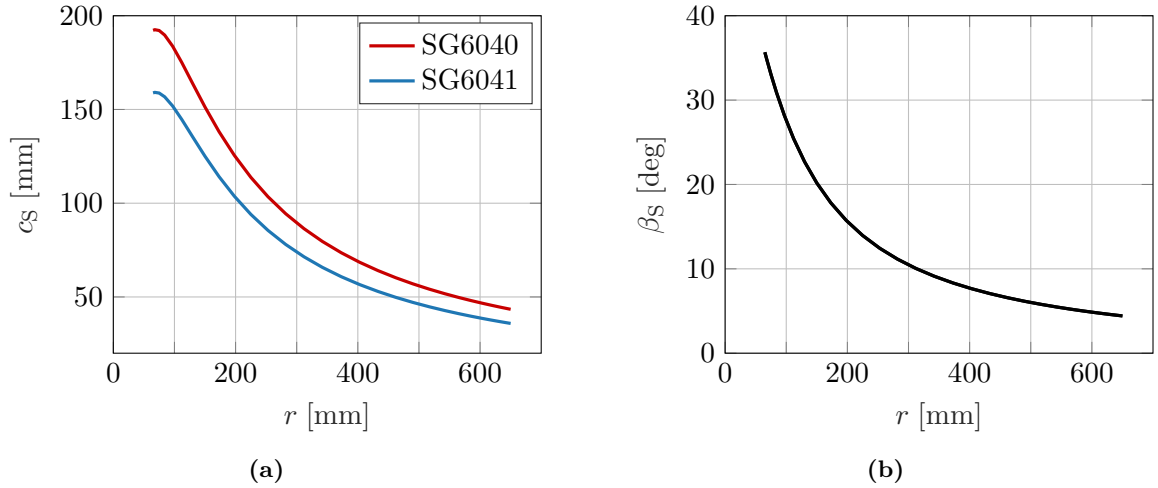


Figure 3.7: Comparative spanwise blade chord **a)** and pitch **b)** distributions based on the SCHMITZ design approach (Equations (1.31)) for the SG6040 and the SG6041 airfoil. Design parameters: Tip speed ratio $\lambda_{\text{des}} = 7$, Reynolds number $\text{Re}_{\text{des}} = 4 \times 10^5$, angle of attack $\alpha_{\text{des}} = 1^\circ$, lift coefficients from Figure 3.6a, number of blades $N_b = 3$, rotor radius $R = 0.65$ m, hub radius $R_{\text{hub}} = 0.1R = 65$ mm.

of pure kinematic nature (Equation (1.31a)), and therefore the same for both blades (Figure 3.7b). Near the blade root, the profiles are increasingly twisted towards the inflow direction, to account for smaller locale velocities caused by the blade's rotation Ωr (Figure 1.3). At the blade tip, it remains positive with values of $\beta_s(R) = 4.4^\circ$.

QBLADE's steady-state BEM module is used to calculate the normal f_N and tangential force f_T distributions. The results are summarized in Figure 3.8. Simulations are carried out at the design inflow velocity of $\bar{U}_{\text{des}} = 2 \text{ m s}^{-1}$ for a range of TSRs. Operational points just outside the initial parameter set (Table 1.2) and at expected maxima are extracted. The normal force can be seen to increase for both blades towards the blade tip. With increasing TSR, the maximum load per unit width increases. The tangential load profile can be considered constant over most of the blade's span. With larger TSR, the inboard blade sections see increased tangential loads. Generally, the tangential forces per unit width grow for reduced TSRs. The overall loading on the SG6040 (Figures 3.8a and 3.8b) is greater than on the SG6041 blade (Figures 3.8c and 3.8d) due to the larger blade chord (Figure 3.7a). The resulting maximum forces in either direction are used to derive the driving load cases. For both blades, the loading in the normal direction is one order greater than in the tangential direction. Integrating the load distributions over the entire span, e.g., using the *trapezoidal rule*, yields the resultants (Equation (3.5a)) [151]. The line load causing the highest resulting force is utilized as design case. In the upper part of Figure 3.8, for each direction (i.e., N: normal, T: tangential), the design load cases and the respective TSRs are highlighted using thicker lines. The corresponding perpendicular load distributions are marked using dashed lines.

$$F_{i,\text{res}} = \int_0^R f_i(r) dr \approx \Delta r \left(\frac{f_1(r_1)}{2} + f_2 + \dots + f_{\epsilon-1} + \frac{f_\epsilon(r_\epsilon)}{2} \right) = \sum_j^\epsilon dF_{i,j} \quad (3.5a)$$

$$r_{i,\text{res}} = \frac{\int_0^R f_i(r) r dr}{\int_0^R f_i(r) dr} = \frac{\int_0^R g_i(r) dr}{\int_0^R f_i(r) dr} \approx \frac{\Delta r}{F_{i,\text{res}}} \left(\frac{g_1(r_1)}{2} + g_2 + \dots + g_{\epsilon-1} + \frac{g_\epsilon(r_\epsilon)}{2} \right) \quad (3.5b)$$

$$dF_{i,j} = \frac{\Delta r_j}{2} (f_j(r_j) + f_{j+1}(r_{j+1})) \quad (3.5c)$$

$$r_{i,j} = \frac{\Delta r_j}{3} \frac{f_i(r_i) + 2f_{i+1}(r_{i+1})}{f_i(r_i) + f_{i+1}(r_{i+1})} \quad i \in \text{N,T} \quad (3.5d)$$

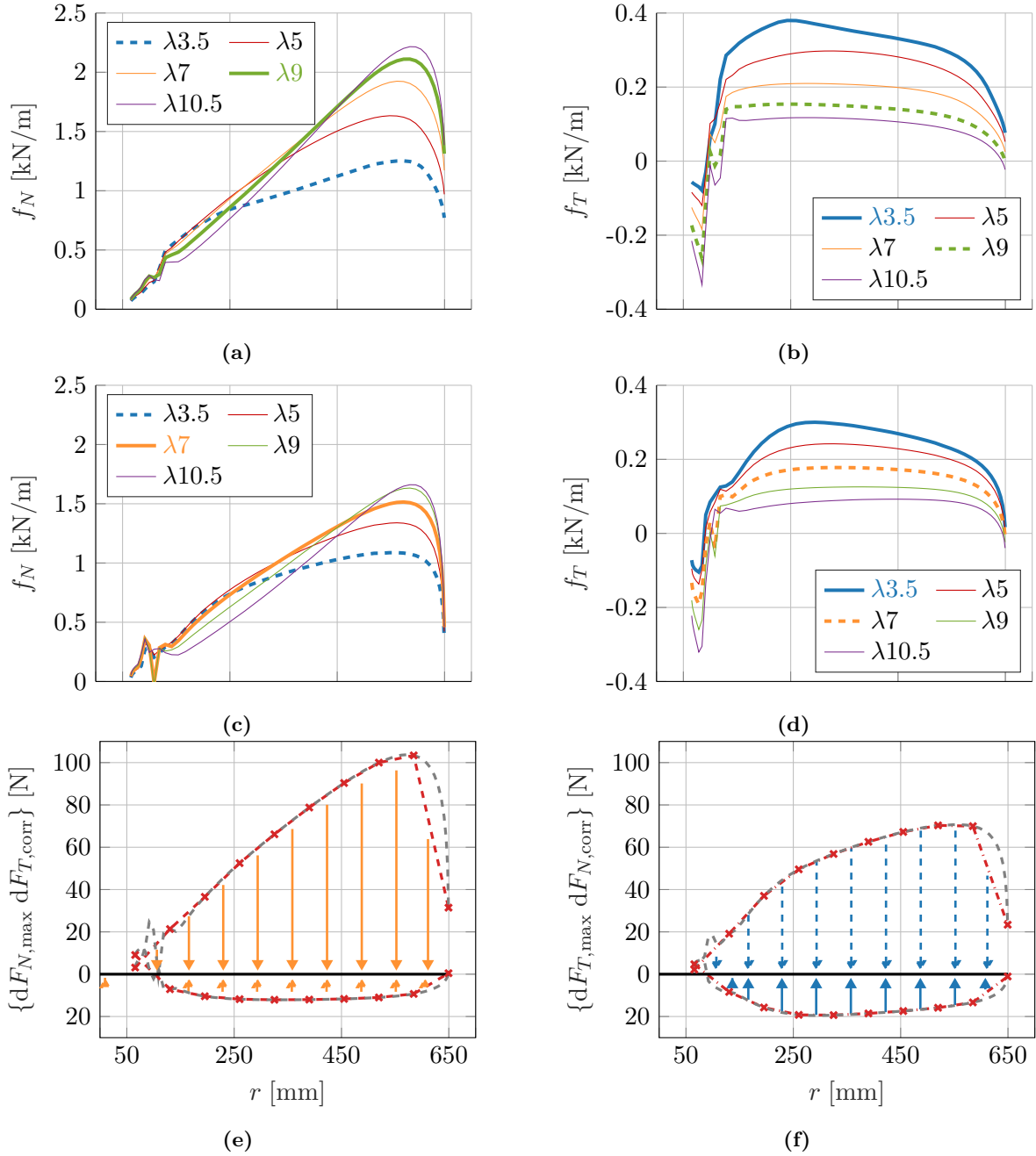


Figure 3.8: Load distributions for rotors constituted by the SG6040 and the SG6041 airfoils. Data extracted from QBLADE’s steady-state blade element momentum module at design inflow velocity $U_{\text{des}} = 2 \text{ m s}^{-1}$. Blade discretized into 30 elements. Ambient conditions set to values, summarized in Table 1.2. Decisive load cases are identified by comparing the load resultants derived from Equation (3.5a). **SG6040** airfoil: **a)** Normal force per unit width $f_N(r)$. — Maximum normal force $F_{N,\text{res,max}} = 714.36 \text{ N}$ at $\lambda = 9$. - - - Normal force $F_{N,\text{corr}} = 507.2 \text{ N}$ at maximum tangential force. **b)** Tangential force per unit width $f_T(r)$. — Maximum tangential force $F_{T,\text{res,max}} = 162.62 \text{ N}$ at $\lambda = 3.5$. - - - Tangential force $F_{T,\text{cor}} = 67.29 \text{ N}$ at maximum normal force. **SG6041** airfoil: **c)** Normal force per unit width $f_N(r)$. — Maximum normal force $F_{N,\text{res,max}} = 543.66 \text{ N}$ at $\lambda = 7$. - - - Normal force $F_{N,\text{corr}} = 446.72 \text{ N}$ at maximum tangential force. **d)** Tangential force per unit width $f_T(r)$. — Maximum tangential force $F_{T,\text{res,max}} = 125.93 \text{ N}$ at $\lambda = 3.5$. - - - Tangential force $F_{T,\text{cor}} = 56.55 \text{ N}$ at maximum normal force. Resulting point forces. — Quarter-chord line. Arrows above visualize the normal forces. Arrows below the tangential forces. Lengths scaled accordingly. - - - Identified decision driving load distributions from Figures 3.8c and 3.8d. - - - Reduced load distributions used for integration. Both only qualitatively depicted. (x) Evaluation locations. **e)** Maximum normal and corresponding tangential forces. **f)** Maximum tangential and corresponding normal forces.

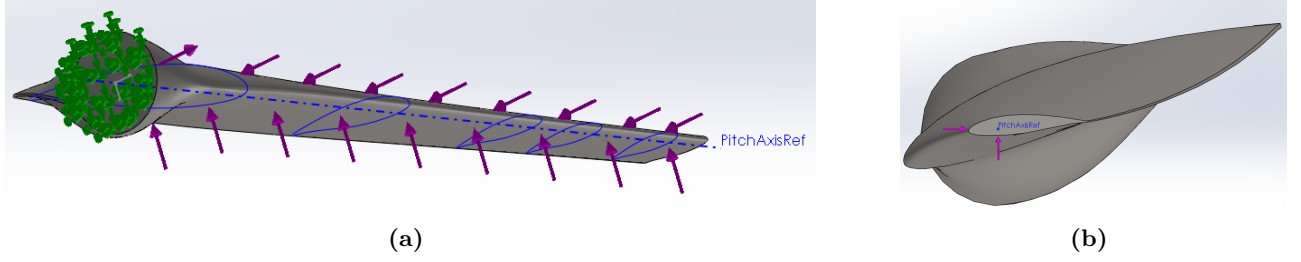


Figure 3.9: Blade, derived from the SG6040 airfoil. a) Point force distribution along the blade span in normal and tangential direction. *Fixed* constraint assigned at blade root. b) Visualization of the force directions. Forces applied on the blade surface, pointed at the quarter-chord line in normal and tangential blade direction.

For the inclusion of the identified load cases in SOLIDWORKS’s FEM environment SOLIDWORKS SIMULATION, point forces rather than load distributions are needed. For that, the loads per unit width are integrated to point forces using the trapezoidal rule at $(\epsilon + 1)$ locations, yielding ϵ segments (Equation (3.5c)). The point force locations along the radius are derived from Equation (3.5d).

The resulting set of point forces are visualized in Figures 3.8e and 3.8f for the SG6041 blade. The forces are represented by arrows, pointing to their respective spanwise locations. The loads are modeled as being applied at the blade’s pitch axis, which coincides with the quarter-chord line. Arrows above the pitch axis are normal forces, arrows below tangential forces.

From QBLADE, the blade designs are exported into SOLIDWORKS. A macro is used inside SOLIDWORKS’ Visual Basic for Applications (VBA) environment for the automatic import of the blade sections and the blade surface generation. From the surfaces, a volume body and subsequently, a solid body is constituted. Using the FEM tool SOLIDWORKS SIMULATION inside SOLIDWORKS, the identified decision driving load cases are implemented. Figure 3.9 depicts the blade representations in SOLIDWORKS. The point forces are visualized by arrows of equal length, independent of the magnitude of the applied force. The blade is constrained at the root by a *fixed* condition, resulting in the modeling of the blade as a cantilever beam. Figure 3.9a shows the single-sided constraint by green arrows. The pitch axis is equal to the quarter-chord line, with a short transition at the blade root towards a centered location. The thickened SG6040 profiles are highlighted at selected locations. Figure 3.9b visualizes the load directions, i.e., tangential and normal relative to the blade rotation. The point forces are applied at the blade surface, pointing towards the quarter-chord line. The blades will be manufactured from stainless-steel of 1.4301 quality. It is inherently non-corrosive (Item 10), offers high tensile strength, is widely available, thus comparatively cheap, machinable, and weldable. Non-corrosive aluminum alloys were considered but discarded. The high loads imposed by the water and possible dynamic loads due to added-mass effects necessitate large safety factors. For the numerical assessment of the rotor blades, three simulations with increasing number of elements N_{elem} per load case are conducted, to gain confidence in the derived results. The suitability of the constituting airfoils are evaluated by the resulting blade tip deflections δ_{tip} and the minimum FOS_{min}. The SG6041 is simulated using the *large deflection* option in SOLIDWORKS. The FOS is calculated using VON-MISES’ yield criterion. It superimposes the principal components $\Sigma_i(\vec{x})\mathbf{e}_i$ of the structural stress tensor $\mathbb{T}(\vec{x})$ to form a scalar approximation of the local stress state at point \vec{x} (Equation (3.6b)). Dividing the material dependent maximum permissible stress Σ^* by the VON-MISES stress, yields the FOS (Equation (3.6a)). [152]

$$\text{FOS} := \frac{\Sigma^*}{\Sigma_{\text{vM}}} \quad (3.6a)$$

$$\text{where } \Sigma_{\text{vM}}(\vec{x}) \stackrel{\text{ONB}}{=} \sqrt{\frac{1}{2}((\Sigma_1 - \Sigma_2)^2 + (\Sigma_2 - \Sigma_3)^2 + (\Sigma_1 - \Sigma_3)^2)} \quad (3.6b)$$

In SOLIDWORKS, the automatic calculation of the local FOS is possible, after solving the FEM. Figure 3.10a shows the blade tip deflections of both blades imposed by the normal and tangential load

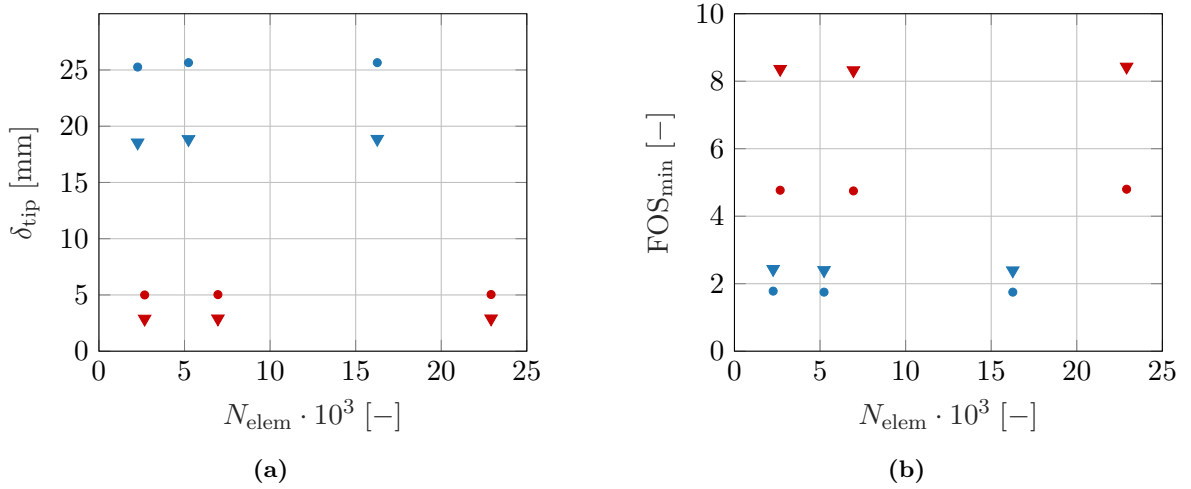


Figure 3.10: Structural simulation results for the (▼,●) SG6040 and (▼,●) SG6041 blade. (●) Normal force load case. (▼) Tangential force load case. Meshes: SG6040 - $N_{\text{elem}} \in \{2671, 6952, 22912\}$, SG6041 - $N_{\text{elem}} \in \{2262, 5233, 16262\}$. a) Blade tip deflections δ_{tip} and b) minimum factors of safety FOS_{min} for three different mesh sizes.

cases. The tip deflection of the SG6041 is more than five times greater than of the SG6040, despite generating smaller aerodynamic loads. It deflects up to $\delta_{\text{tip}} = 25$ mm, compared to the 5 mm of the SG6040. The larger blade thickness results in a larger structural resistance, although higher loads are generated. Accordingly, its minimum FOS is of greater magnitude, with $\text{FOS}_{\text{min}} = 4.8$. The SG6041 blade's minimum FOS yields 1.75 (Figure 3.10b). The results are considered mesh-size-independent. All aspects considered, the blade design is decided to be constituted by the SG6040 airfoil. Various reasons exist: the minimal blade tip deflection, when operated at design conditions, the high resulting FOS, the larger overall blade chord, and the maximum negative pressure coefficient being constant over a large range of AoA. Additionally, the manufacturing of thicker blades is easier due to an improved structural resistance to vibrations.

The remainder of the paragraph describes the finalized blade design and characterizes the aerodynamic properties of the UBeRT test rig. Figure 3.17a shows a render of the final blade design. It is made from three sections, which are positioned and force fitted by pins. The pinhole exits are solely on the pressure side of the blade because at this location their influence on the flow field is less invasive. The pins will be secured with glue, cut to length and sanded to be flush with the blade surface. Remaining gaps will be filled with filler. The structural transmission of the large flapwise loading is assured by a tongue and groove connection. The modular design allows the blades to be machined on the available in-house five-axis CNC mill. Additionally, it allows for convenient blade tip exchanges. Parameter studies on different tip geometries only necessitate the manufacturing of outboard blade sections (Item 9). Towards the root, the cross-section becomes thicker and eventually circular. An adapter piece connects the blade with the hub of the rotor. The blade root diameter is $D_{\text{root}} = 57$ mm. Between the hub connector and the blade root, a thin disc is placed. The three pieces are aligned using a common centering pin. Two more machined centering pinholes are part of the manual pitching mechanism. It enables reproducible changes of the blade pitch without the need for adapted connectors or blade roots. Only a set of pitch discs is necessary [138]. The blade contour is displayed in Figure 3.11. The starting locations of the circular and the SG6040 blade are shown. In between, interpolated profiles generated in QBLADE are introduced to assure a smooth transition (Profile 1: 66% circular, 33% SG6040; Profile 2: 33% circular, 66% SG6040). The total blade length results in $L_{\text{bl}} = 583$ mm. The pitch axis connects the quarter-chord points η_{25} of the blade sections. Only towards the blade root, the sections are centered on the pitch axis to allow convenient angular changes (Item 9).

The finalized blade chord and pitch distributions are shown in Figure 3.12. As can be seen, for the

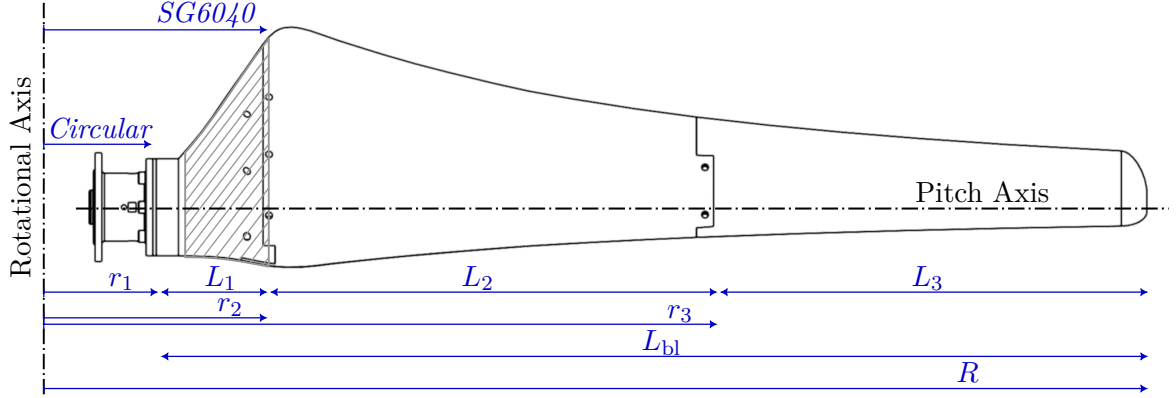


Figure 3.11: Final blade contour and blade sections from pressure side view of the Underwater Berlin Research Turbine. $L_1 = 63$ mm from $r_1 = 67$ mm. $L_2 = 265$ mm from $r_2 = 137$ mm. $L_3 = 255$ mm from $r_3 = 395$ mm. $L_{bl} = 583$ mm. — Blade section made from interpolated airfoils. Pitch axis is equal to quarter-chord line over majority of the blade. Transition towards center chord location is realized in interpolated section.

majority of the blade ($r \geq 0.2R$), SCHMITZ's blade design is followed. Only near the blade root, deviations are needed to assure a smooth transition towards the circular blade root. The blade has a maximum chord length of $c_{\max} = 150$ mm. Towards the tip it becomes more slender until a chord of $c(R) = 44.5$ mm is reached. The design conditions are the same as used for the blade comparison (Figure 3.7). The blade pitch decreases monotonically in an asymptotic manner after the transition piece. At the utmost location, $\beta(R) = 4.42^\circ$ are yielded.

Figures 3.13 depict the aerodynamic performance characteristics of the UBeRT rotor, derived from BEM simulations inside QBLADE. As can be seen (Figures 3.13a until 3.13c), the maximum loading always occurs at the highest tow carriage velocity of $\bar{U}_{1,\infty} = 2$ m s⁻¹. The rotor generates a maximum aerodynamic power of $\mathcal{P}_{\max} = 2.35$ kW at $n_p = 176$ min⁻¹. However, according to the cubic power law of the fluid's kinetic energy (Equation (1.25a)), the power generation is much smaller for smaller inflow velocities. The electrical specifications of the drive train must be tuned to fit this range. For increasing tow velocities, the maximum is shifted towards higher RPMs. The maximum torque is $\mathcal{Q}_{\max} = 186$ Nm at $n_Q = 102$ min⁻¹. The blade roots and the main shaft must be capable of transmitting this torque to the generator. The torque increases earlier than the corresponding power and decreases sharply after the peak. The turbine generates its largest thrust of $\mathcal{T}_{\max} = 2.22$ kN at $n_T = 264$ min⁻¹. The thrust constitutes the main load on the tower and the included bearings in the design. The force causes the tower to deflect, which can lead to turbine misalignment, and to large periodic loads. The operational design load conditions are highlighted and collected in Table 3.1. The non-dimensional coefficients are depicted in Figures 3.13d until 3.13f. They vary with changing inflow velocities. For $\bar{U}_{1,\infty} = 0.5$ m s⁻¹, REYNOLDS numbers down to $Re = 10^5$ result (Figures 3.15b). Due to the large thickness of the SG6040 airfoil, laminar separation bubbles probably occur, imposing a sharp increase in drag and reduced lift coefficients (Figures 1.4h and 1.4e). This could be the reason for the "suboptimal" performance of the rotor

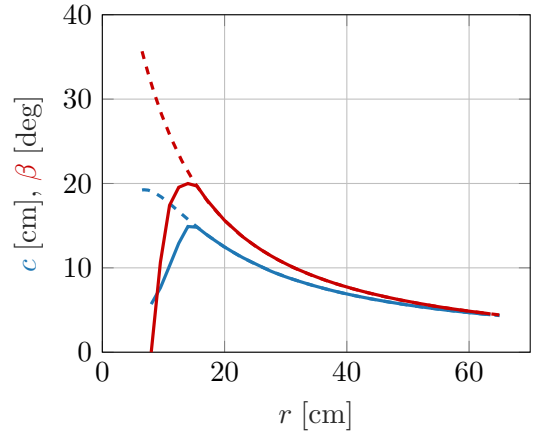


Figure 3.12: Final pitch β and chord c distributions over radius r . ■■■ SCHMITZ's blade design. Differences near blade root attributed to geometric transition. Design conditions according to Figure 3.7 for the SG6040 blade.

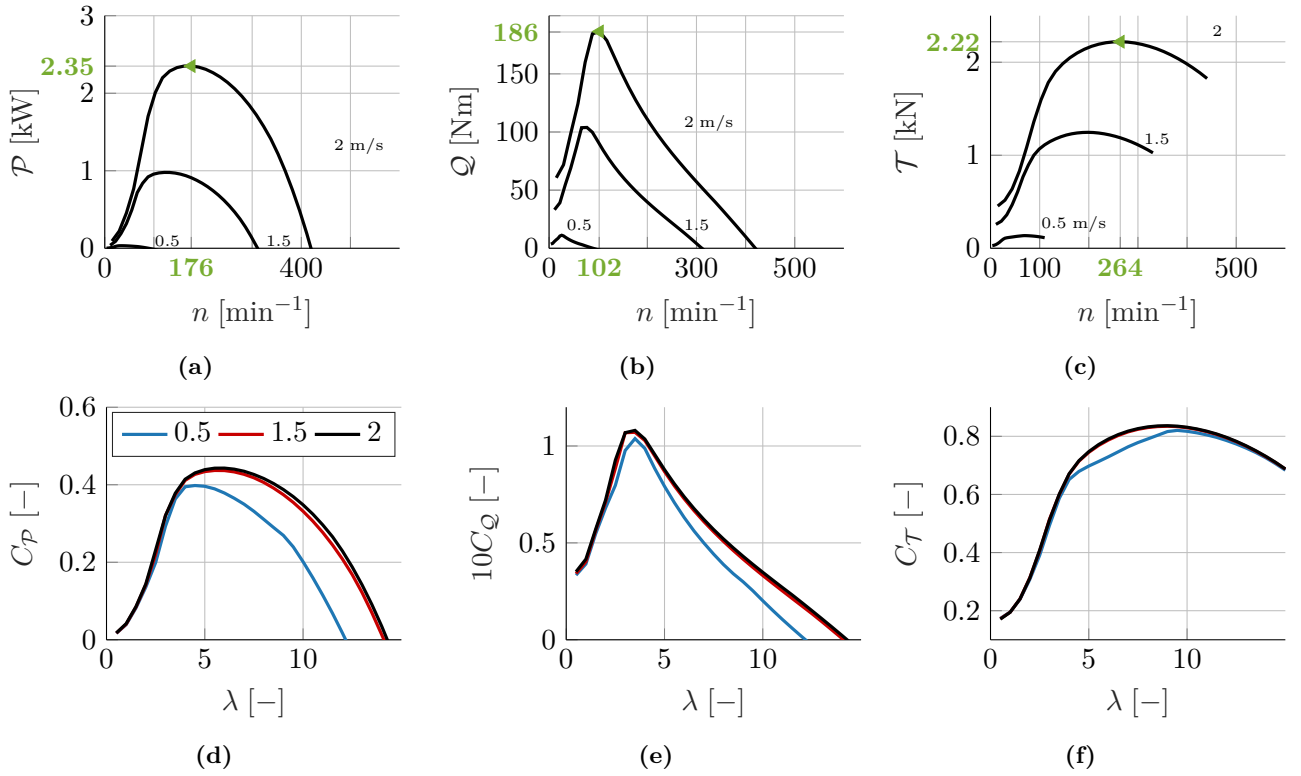


Figure 3.13: Aerodynamic performance characteristics of the Underwater Berlin Research Turbine assessed, using QBLADE’s blade element momentum module. **a)** Power \mathcal{P} , **b)** torque \mathcal{Q} , and **c)** thrust \mathcal{T} over rotational speed n . Maximum values highlighted. Coefficients for **d)** power C_P , **e)** torque C_Q , and **f)** thrust C_T over tip speed ratio λ . Tow carriage velocity $\bar{U}_{1,\infty}$ as a parameter.

for small inflow velocities. For larger velocities, the coefficients increasingly converge. The maximum power coefficient of the SG6040 rotor approaches $C_{P,\max} = 44.3\%$ at $\lambda_P = 6$. Compared to BETZ’s limit of $C_{P,B} = 59.26\%$, the UBRT rotor offers room for improvements. The thrust coefficient peaks at $C_{T,\max} = 0.8365$ at $\lambda_T = 9$ and decreases for larger TSRs. This behavior is surprising, since the thrust coefficient of modern HAWT usually increases monotonically. However, this might be due to problems in the numerical representation. The initial measurement campaigns during commissioning will help clarify this issue.

From QBLADE, the distributions of the bound circulation Γ and the resulting AoA for different inflow velocities and TSRs are analyzed and visualized in Figures 3.14. As discussed, for an increasing TSR, the resulting AoA decreases (Figure 3.14b), reaching from approximately 7° for $\lambda = 4$ to -2° for $\lambda = 10$. At $\lambda = 7$, the design target of $\alpha_{\text{des}} = 1^\circ$ is met. Consequently, the airfoil generates less lift. The circulation around the blade is related to its lift by KUTTA-JOUKOWSKI’S theorem (Equation (1.11a)). Accordingly, the overall bound circulation decreases for increasing TSRs values (Figure 3.14a). For all three TSRs, the bound circulation is rather constant, which will result in the generation of a pair of concentrated vortices at the tip and the root (Item 9). Increasing the inflow velocity from $\bar{U}_{1,\infty} = 0.5 \text{ m s}^{-1}$ to 1.5 m s^{-1} results in an enlarged bound circulation. The curves show larger radial gradients. Only for the design TSR, the circulation remains tolerably constant. Especially for $\lambda = 4$, considerable variations can be seen near the blade root. The AoA changes due to the enlarged inflow velocity are insignificant. Only at the design TSR, the radial distribution converges closer to its design condition α_{des} . The diverging behavior for decreasing radius coordinates is purely kinematic. The aerodynamic properties of the circular cross-sections near the blade root become less and less dependent on the local inflow angle. The large changes of the resulting AoA throughout the operation regime might cause blade surface cavitation due to larger maximum negative pressure coefficients $-C_{p,\max}$ (Item 8). As a countermeasure, the blades could be pitched according to Equa-

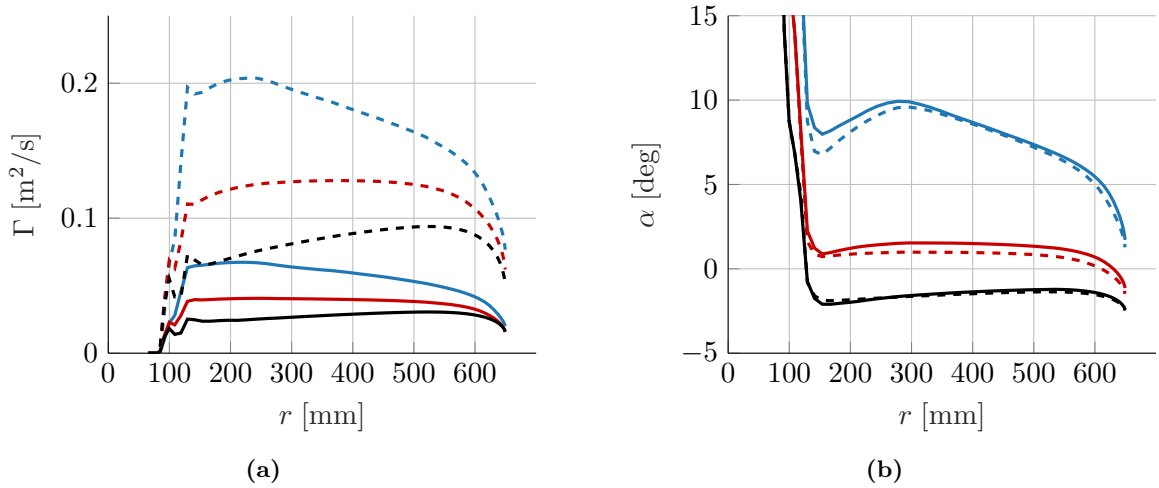


Figure 3.14: a) Bound circulation Γ and b) angle of attack over radius r . Different inflow velocity $\bar{U}_{1,\infty}$ and tip speed ratios are depicted: — $\bar{U}_{1,\infty} = 0.5 \text{ m s}^{-1}$, - - - $\bar{U}_{1,\infty} = 1.5 \text{ m s}^{-1}$, — $\lambda = 4$, — $\lambda = 7$, — $\lambda = 10$. Color-code for dashed curves accordingly.

tion (1.13). However, this changes the turbine's characteristics and might interfere with the aim of creating representative conditions of modern HAWTs. From the gained insights into the aerodynamic performance of the UBeRT, a final analysis of the operational domain is conducted (Figure 3.15). The absolute inflow velocity at the blade tip is derived from $\bar{q}(R) = \bar{U}_{1,\infty} \sqrt{\lambda^2 + 1/9}$. Independently of the point of operation, QBLADE yields an axial induction factor of $a = 1/3$ at the blade tip. Therefore, Equation (1.5b) is altered to obtain more accurate results. Within the parameter space, the inflow velocity exceeds 15 m s^{-1} , leading to REYNOLDS numbers of $\text{Re}_{\text{max}} = 8 \times 10^5$. For the lower-left corner of the parameter regime, small REYNOLDS numbers below 10^5 are reached. In this regime, the operating flow state of the turbine is substantially altered, causing significant performance deviations (Figure 3.13). To avoid laminar separation bubbles on the blade and preliminary stall, tripping should be considered. The comparison of the resulting cavitation number and the maximum negative pressure coefficient at design conditions suggests avoiding the upper-right part of the parameter regime. Beyond the threshold, the onset of surface cavitation is theoretically predicted. Aggravatingly, especially for low TSRs, the spanwise AoA is considerably larger than $\alpha_{\text{des}} = 1^\circ$ (Figure 3.14b). Thus, for the reduced parameter regime of tow velocities up to $\bar{U}_{\text{to}} = 1.5 \text{ m s}^{-1}$, cavitation cannot completely be ruled-out. Cormier et al. [153] derive two semi-empirical equations for assessing the near-wake development depending on the azimuthal position ϑ . Without extensive simulations or test campaigns, formulas like that offer the only opportunity to assess the evolution of the near-wake properties preliminarily. The initial vortex core diameter is calculated from the blade chord at 93% span, $c_{0.93R}$. Its evolution $D_c(\vartheta)$ is operational point dependent and grows with $\sqrt{\vartheta}$. Cormier et al. [153] proofs the qualitative accuracy against a CFD simulation, although it heavily under-estimates the core radii. The values remain accurate for approximately $x/R < 0.5R$. Considering Equation (1.15a), this is equal to a phase angle of $\vartheta < 360^\circ$. Both empirical parameters of $a = 5 \times 10^{-6}$ and $b = -1.932 \times 10^{-3} \text{ rad}^{-1}$ are calibrated against an extensive set of PIV measurements in the near-wake. The circulation $\Gamma_c(\vartheta)$ of the tip vortices depends on an initial circulation $\Gamma_{c,0}$, which is operational point and thrust coefficient C_T dependent. After their creation, the circulation is modeled as being exponentially damped.

$$D_c(\vartheta) = D_{c,0} \sqrt{1 + a \left(\frac{2R}{D_{c,0}} \right)^2 \frac{R}{\lambda \bar{U}_{1,\infty}} \vartheta} \quad \text{where} \quad D_{c,0} = 0.1 c_{0.93R}, a = 5 \times 10^{-6} \quad (3.7a)$$

$$\Gamma_c(\vartheta) = \Gamma_{c,0} e^{b\vartheta} \quad \text{where} \quad \Gamma_{c,0} = C_T \frac{\pi \bar{U}_{1,\infty} R}{N_b \lambda}, b = -1.932 \times 10^{-3} \text{ rad}^{-1} \quad (3.7b)$$

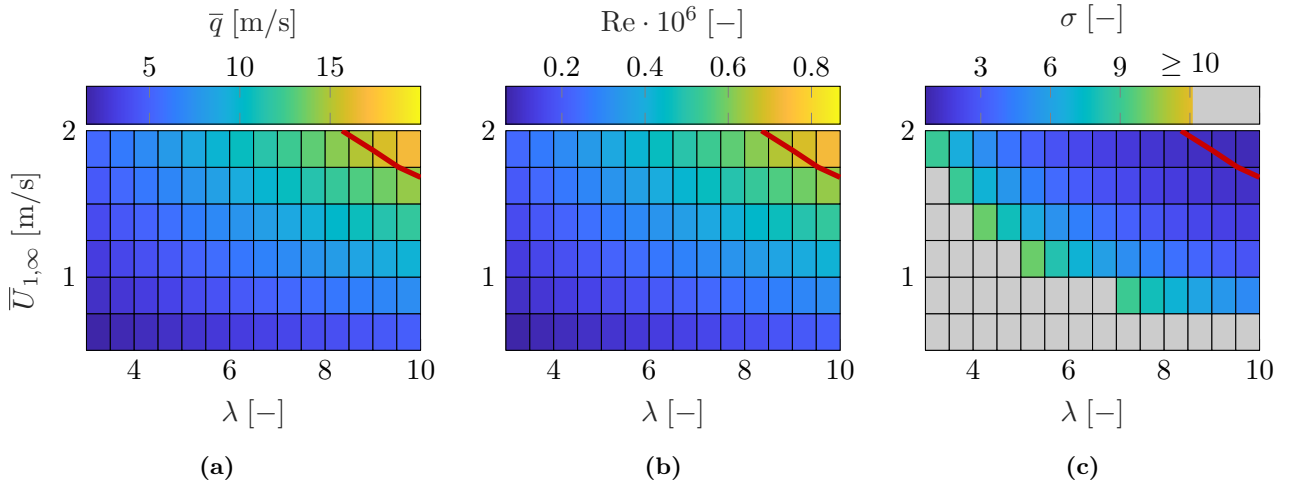


Figure 3.15: Resulting parameter space of the Underwater Berlin Research Turbine test rig including a risk assessment for the onset of cavitation. Design angle of attack set to $\alpha_{\text{des}} = 1^\circ$. Pressure field for cavitation risk assessment derived at $\text{Re} = 4 \times 10^5$. — $-C_{p,\max} = 0.8876$. **a)** Absolute inflow velocity $\bar{q}(R) = \bar{U}_{1,\infty} \sqrt{\lambda^2 + 1/9}$. The axial induction factor at the blade tip of $a(R) = 1/3$ is extracted from QBLADE. **b)** Operational point dependent REYNOLDS number $\text{Re}(R)$ and **c)** cavitation number $\sigma(R)$ at the blade tip.

The resulting estimations for the UBeRT test rig are depicted in Figure 3.16. In agreement with the bound circulation Γ (Figure 3.14a), the circulation of the tip vortices is projected to decrease for increasing TSRs. Changing the tow carriage velocity from $\bar{U}_{1,\infty} = 0.5 \text{ m s}^{-1}$ to 1.5 m s^{-1} results in a significantly increased initial tip vortex circulation. Compared to the bound circulation around the blades, the tip vortices are of the same order of strength. This agrees well with the described theory of 3D vortex systems. With growing phase angles ϑ , the circulation decays. The tip vortex diameters D_c are initially solely dependent on the blade chord near the tip, and therefore the same for all operational conditions (Figure 3.16b). The diameter grows monotonically over the depicted azimuthal range. Its magnitude decreases for larger TSRs and tow velocities \bar{U}_{to} . Values of 10 to 30 mm are observed in the investigated regime. This order assures the visibility of the tip vortices with the existing PIV system at the institute (Item 10). Additionally, the predicted underestimation of the tip vortex sizes detected by Cormier et al. [153] even amplifies the gained confidence.

The extensive analysis of the resulting aerodynamic performance characteristics of UBeRT's rotor design proves the suitability of the SG6040 airfoil for wake investigations. Furthermore, the described engineering approach and its findings are not limited to this airfoil. Since the blades can be manufactured in-house, new sets of blades can be machined, if necessary. The collected requirements concerning the airfoil selection and the blade design are comprehensively considered and balanced (Item 8 and 9).

3.4 Drive Train and Tower Design

Notes on the drive train and tower design including critical safety factors

The drive train is required to be able to accelerate the turbine to the operational point dependent rotational speed, even when the tow carriage is at rest ($\bar{U}_{1,\infty} = 0$). The necessary motor torque is estimated from the tangential aerodynamic forces $dF_{T,i}$ of ϵ blade elements at location r_i with width dr_i ($i \in \{1 \dots \epsilon\}$). At rest, $dF_{T,i}$ results purely from the blade drag, imposed at $\alpha(r_i) = -\beta(r_i)$ (Figure 1.3). Using the BEM, the drag coefficient $C_D(\alpha(r_i))$ is identified from the 2D SG6040 polars. Utilizing Equation (1.17b), Equation (3.8a) is derived. The required driving torque is quadratic depen-

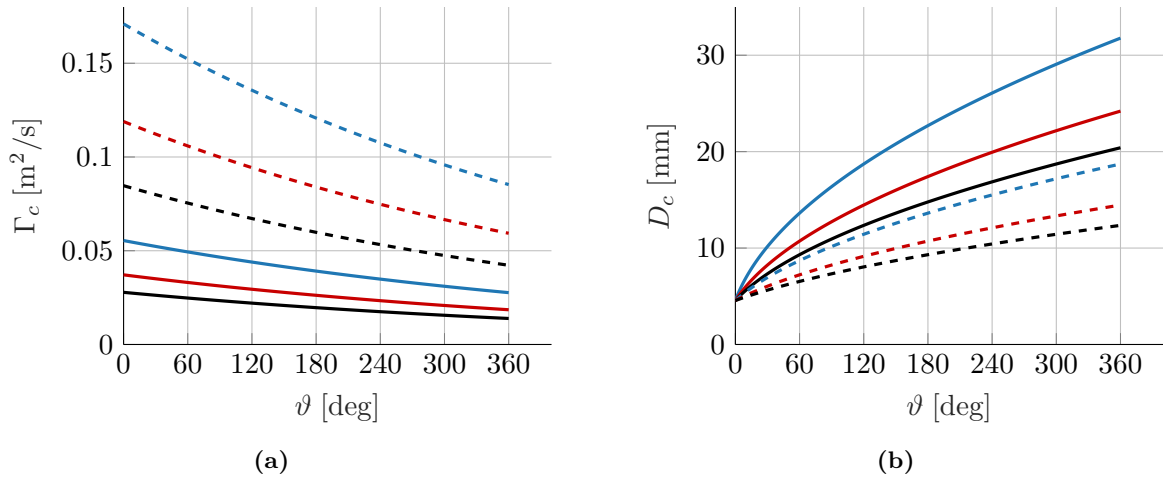


Figure 3.16: a) Circulation Γ and b) tip vortex diameter as functions of the azimuthal angle ϑ . Calculated, using Cormier et al.'s [153] semi-empirical approach (Equations (3.7)). Different inflow velocity $\bar{U}_{1,\infty}$ and tip speed ratios are depicted: — $\bar{U}_{1,\infty} = 0.5 \text{ m s}^{-1}$, - - - $\bar{U}_{1,\infty} = 1.5 \text{ m s}^{-1}$, — $\lambda = 4$, — $\lambda = 7$, — $\lambda = 10$. Color-code for dashed curves accordingly.

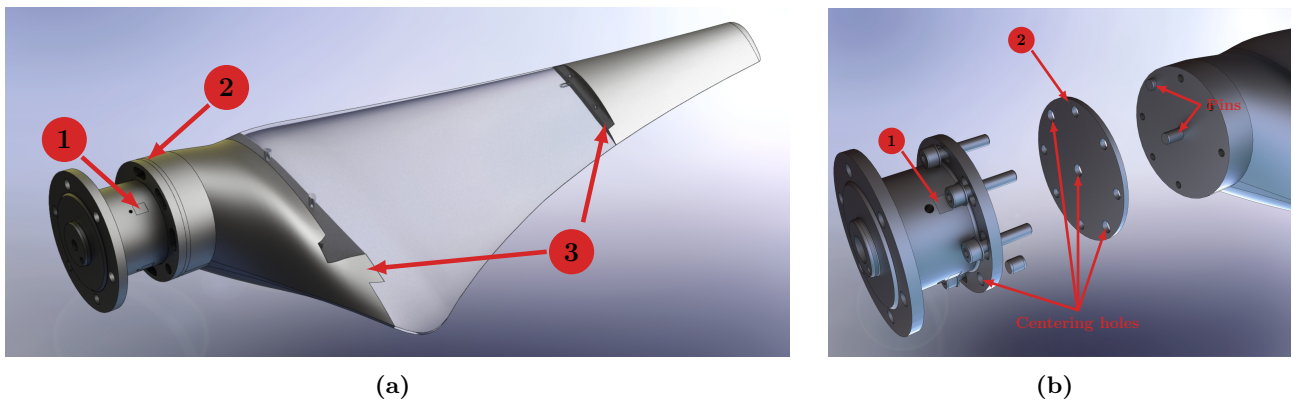


Figure 3.17: (1) Location of the suction side strain gauge for measuring the flapwise blade root bending moment. (2) Pitch positioning disk. a) Final blade design. Blade made from three sections. For clarity, the center section is set transparent. (3) Groove and tongue connection for transmitting the large flapwise loading securely. b) Explosion view of the pitch positioning mechanism. Three centering holes are located in the pitch disk. The center one and one on the perimeter aligns the disk and the hub connection piece. The other one and the center one aligns the blade and the disk. Slotted holes allow pitch adjustments of $\Delta\beta = \pm 7.5^\circ$. Sensors listed in Table 3.3. The concept is reproduced from Payne et al. [138].

Table 3.1: Design conditions, operational regime, and finalized overall dimensions of the Underwater Berlin Research Turbine.

Quantity	Symbol	Range/Value	
<i>Design Conditions</i>			
Design tow velocity	$\bar{U}_{\text{to,des}}$	2 m s^{-1}	
Design RPM	n_{des}	294 min^{-1}	at $\bar{U}_{\text{to,des}}$ and $\lambda_{\text{max}} = 10$
Design thrust	\mathcal{T}_{des}	2.22 kN	at $n_{\mathcal{T}} = 264 \text{ min}^{-1}$
Design torque	\mathcal{Q}_{des}	186 Nm	at $n_{\mathcal{Q}} = 102 \text{ min}^{-1}$
Design power (Generator)	\mathcal{P}_{des}	2.35 kW	at $n_{\mathcal{P}} = 176 \text{ min}^{-1}$
Maximum power (Motor)	$(\mathcal{M}\Omega)_{\text{des}}$	1.99 kW	at n_{des}
<i>Operational Range</i>			
Inflow velocity	$\bar{U}_{1,\infty}$	$0.5 \text{ to } 1.5 \text{ m s}^{-1}$	
TSR	λ	$4 \text{ to } 10$	
Angular velocity	Ω	$3.08 \text{ to } 23.08 \text{ s}^{-1}$	
RPM range	n	$29.4 \text{ to } 220.4 \text{ min}^{-1}$	
<i>Blade Design Parameters</i>			
Airfoil		Thickened SG6040, $\Delta = 0.01c$	
REYNOLDS number	Re_{des}	400 000	
TSR	λ_{des}	7	
AoA	α_{des}	1°	
<i>Turbine</i>			
Nacelle length	L_{nac}	$1.56 \text{ m} = 1.2D$	
Nacelle diameter	$D_{\text{nac},1}$	$0.13 \text{ m} = 0.1D$	$x_{\text{nac}} = 0.082 \text{ to } 0.458 \text{ m}$
	$D_{\text{nac},2}$	$0.155 \text{ m} \approx 0.12D$	$x_{\text{nac}} = 0.575 \text{ to } 1.2 \text{ m}$

Table 3.2: Implemented components in the Underwater Berlin Research Turbine.

Component	Description	Supplier	Specifications
<i>Structural</i>			
Fixed bearing	SKF 22206 E	SKF	Self-aligning roller bearing
Floating bearing	SKF 22205 E	SKF	Self-aligning roller bearing
Coupling	KB 4K/200- 60 - 32 -24	KBK Antriebstechnik	Rated torque: 200 Nm
<i>Drive</i>			
Motor	CMPZ71M	SEW Eurodrive	Rated power: 7.5 kW
Planetary gear	PSF522	SEW Eurodrive	Gear ratio: 12/1
Encoder	AK1H	SEW Eurodrive	12 bit rotations, 15 bit rev^{-1}
Holding Break	BY	SEW Eurodrive	Moment: 10 Nm
Frequency Inverter	MDX61B0110-5A3-4-00	SEW Eurodrive	Rated electrical power 11 kW Protocol MODBUS TCP
<i>Tower</i>			
Fixed bearing	23024 CC/W33	SKF	Self-aligning roller bearing
Floating bearing	23024 CC/W33	SKF	Self-aligning roller bearing

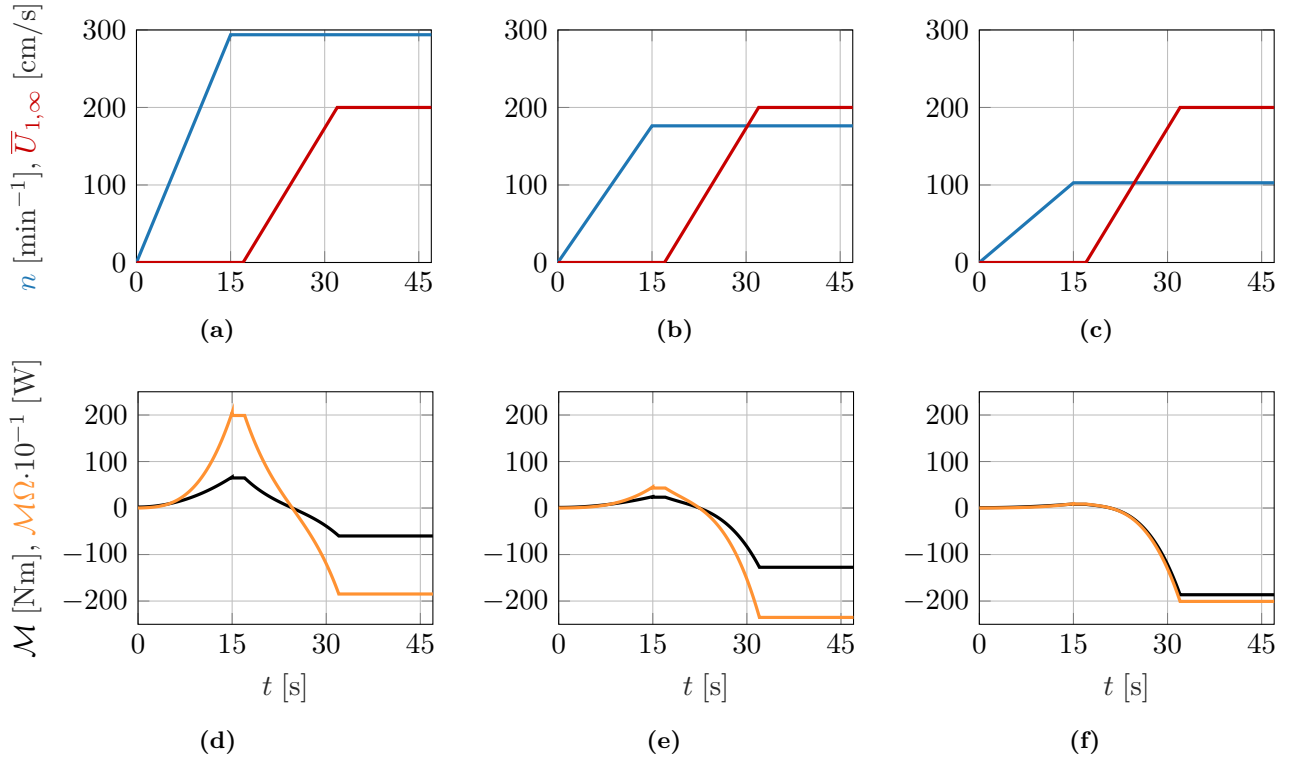


Figure 3.18: Travel profiles and corresponding loads at design conditions of the Underwater Berlin Research Turbine. Tow carriage always accelerated from standstill to $\bar{U}_{to} = 2 \text{ m s}^{-1}$. ($t = 0$ to 15 s): *Drive* state, calculated from Equation (3.8). ($(\mathcal{M}\Omega) < 0$): *Generator* state, derived from turbine characteristics Figure 3.13. Interpolated in between. a) Acceleration to design RPM $n_{des} = 294 \text{ min}^{-1}$. d) Corresponding loads with maximum drive power $(\mathcal{M}\Omega)_{max} = 1.99 \text{ kW}$. b) Acceleration to $n_P = 176 \text{ min}^{-1}$. e) Corresponding loads with maximum generator power $\mathcal{P} = 2.35 \text{ kW}$. c) Acceleration to $n_Q = 102 \text{ min}^{-1}$. f) Corresponding loads with maximum generator torque $\mathcal{Q} = 186 \text{ Nm}$.

dent on the angular velocity Ω . Additionally, during changing angular velocities (e.g., acceleration), the inertia of all rotating parts $J = 1.0324 \text{ kg m}^2$ contributes to the drive demand. The total motor torque \mathcal{M} then follows from combining both (Equation (3.8c)).

$$\mathcal{Q}_D = \frac{N_b \varrho}{2} \Omega(t)^2 \sum_i^{\epsilon} C_D(r_i) c(r_i) r_i^3 dr_i \quad (3.8a)$$

$$\mathcal{Q}_J = J \dot{\Omega}(t) \quad (3.8b)$$

$$\mathcal{M} = \mathcal{Q}_D + \mathcal{Q}_J \quad (3.8c)$$

At standstill, the drive must be capable of accelerating the rotor to every rotational speed of the operational domain. The desired time to reach the set-point velocities is set to 15 s for minimizing the resulting accelerations. The maximum RPM $n_{max} = 293 \text{ min}^{-1}$ follows at $\bar{U}_{1,\infty} = 2 \text{ m s}^{-1}$ and $\lambda = 10$. Utilizing Equation (3.8c) yields a maximum motor power of $(\mathcal{M}\Omega)_{max} = 1.99 \text{ kW}$ (travel profile in Figure 3.18a, loads in Figure 3.18d). Figures 3.18b and 3.18c depict velocity profiles to extreme conditions of generated power $\mathcal{P}_{max} = 2.35 \text{ kW}$ (Figure 3.18e), and torque $\mathcal{Q}_{max} = 186 \text{ Nm}$ (Figure 3.18f). The maximum power required during acceleration $(\mathcal{M}\Omega)_{max}$ is smaller than the maximum generated rotor power. Therefore, to select an appropriate drive, the latter is considered. The figures visualize the sign change, once the towing carriage accelerates to its set-point velocity.

A drive train concept is realized and dimensioned in accordance with the travel profiles and the design thrust predicted by QBLADE's BEM module ($\mathcal{T}_{des} = 2.22 \text{ k}$). Figure 3.19 shows a sketch of the used drive train model for assessing the structural requirements of the shaft and the main bearing. In

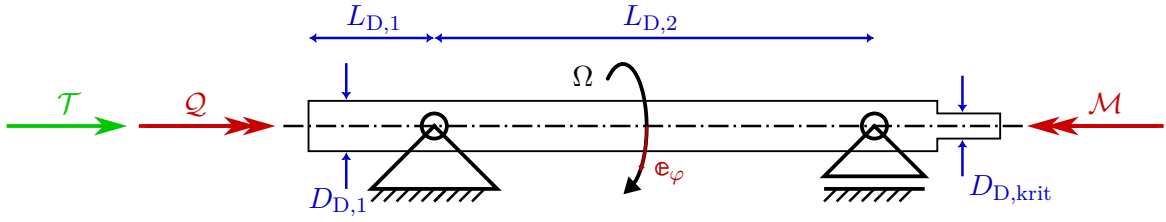


Figure 3.19: Drive train model. Design loads specified in Table 3.1. $D_{D,1} = 30$ mm, $D_{D,krit} = 24$ mm, $L_{D,1} = 220$ mm, $L_{D,2} = 110$ mm. Material: 1.2316.

compliance with the outer dimensional constraints of the nacelle ($D_{nac}^{Pr} \mathcal{O}(0.1D)$) the initial diameter of the main shaft is preliminary set to $D_{D,1} = 30$ mm. A pair of self-aligning roller bearings (Fixed bearing: *SKF 22206 E*, floating bearing: *SKF 22205 E*) is chosen at distance $L_{D,2} = 220$ mm for counteracting the gravitational bending moment imposed by the rotor (lever arm $L_{D,1} = 110$ mm). The fixed bearing is exposed to the turbine's thrust. Its dynamic structural FOS is calculated to $\psi = 8.68$, following the manufacturer's guidelines. The radial loading of the floating bearing is insignificant. The turbine shaft is planned to be made from 1.2316 because of the high tensile strength and resistance to corrosion of the material. The outer limitations necessitate a critical shaft diameter of $D_{D,krit} = 24$ mm. According to DIN 743 [154–158], the resulting FOS of the diameter is $\psi = 1.55$. The shaft is milled, tempered, and ultimately abraded to accommodate the bearings and the coupling in a defined and durable manner.

The *KB 4K/200 - 60 - 32 - 24* metal bellows coupling, made by *KBK Antriebstechnik*, is selected to transmit the torque imposed by the rotor and the drive. These couplings tolerate small alignment errors between the drive and the main shaft, whilst offering high rotational and axial stiffness. Due to the highly limited design of the turbine, such misalignment cannot be prevented. The coupling is rated for a maximum torque transmission of $Q_{max} = 200$ Nm, which yields a FOS of $\psi = 1.08$. Based on the defined travel profiles and resulting loads, suppliers are contacted to project a suitable drive train. Ultimately, the drive unit is purchased from *SEW Eurodrive*. The offer consists of a frequency inverter unit (*MDX61B0110-5A3-4-00*) and a 7.5 kW servo planetary gear motor (*PSF522 CMPZ71M*) with a gear ratio of 12/1. For phase angle dependent PIV triggering, an absolute multi-turn encoder is included (*AK1H*). The encoder resolves 12 bit motor shaft rotations with 15 bit, resulting in a blade angle resolution of $9.2 \times 10^{-4} \text{ }^\circ \text{ inc}^{-1}$. Additionally, the turbine is equipped with a holding brake, capable of applying 10 Nm on the motor shaft.

Figure 3.20 shows a section cut of the final turbine design. The blades are connected to the hub in the described way. The main shaft is supported by two self-aligning roller bearings, and connected to the metal bellows coupling and subsequently to the main drive. The required outer nacelle diameter of $0.1D$ is maintained for the first part of the turbine. Downstream of the coupling, the nacelle diameter is enlarged to $155 \text{ mm} \approx 0.12D$ to accommodate the drive. The overall nacelle length is $L_{nac} = 1.56 \text{ m} = 1.2D$. The included components are summarized in Table 3.2.

In analogy to the turbine bearing concept, two self-aligning roller bearings are selected to support the center beam, i.e., the tower, at two points of distance $L_{T,1} = 1.559$ m. The upper bearing is a fixed, the lower bearing a floating one. Both bearings are of the *23024 CC/W33* kind, made by *SKF*. Placing an axial roller bearing at the upper tower location was considered. However, the high radial loading due to the design thrust violates the bearing limitations. The turbine is submerged to a depth of $H = 2.5$ m. Including the distance of the bottom of the carriage platform to the free water surface, the distance of the turbine to the floating bearing follows to $L_{T,2} = 3.402$ m. The model depicted in Figure 3.21 is utilized to derive the maximum radial loads on the bearings imposed by the thrust. The maximum loads at the upper and lower bearing locations reaches $\max(F_{T,1}) = -5257$ N and $\max(F_{T,2}) = 7666$ N. Together, the dynamic FOS reaches $\psi = 23.2$ for the fixed bearing and $\psi = 9.8$ for the floating one. Additionally, the maximum deflection of the turbine considering the thrust is analytically investigated. EULER-BERNOULLI's beam theory is used to derive the deflection

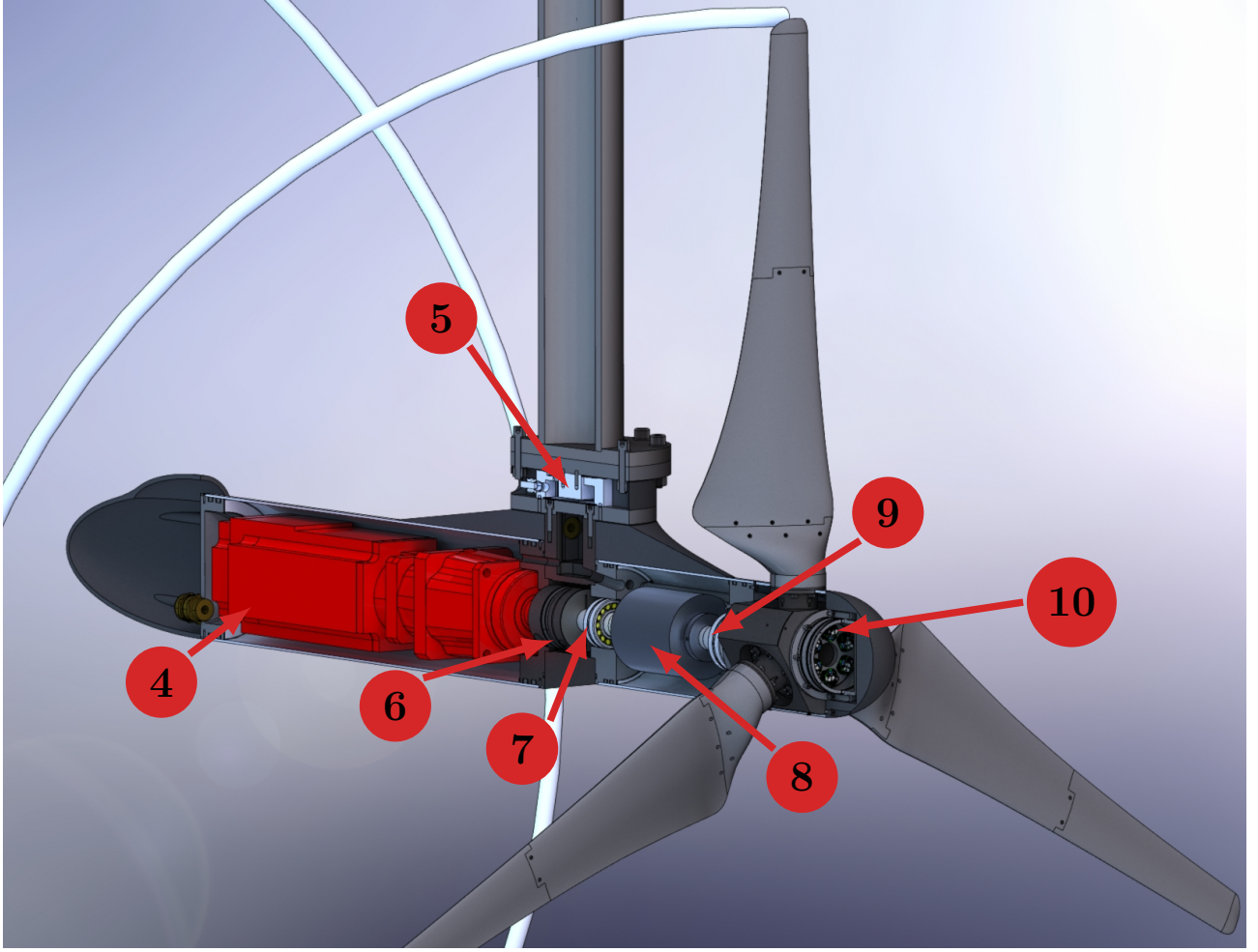


Figure 3.20: Section view of the turbine including identifiers for main drive train components. (4) Drive unit, including holding break, encoder, servo motor with planetary gear. (5) Three-component thrust gauge. (6) Metal bellows coupling. (7) Self-aligning roller bearing (floating). (8) Slip ring. (9) Self-aligning roller bearing (fixed). (10) Root bending strain gauge amplifiers. Drive train components listed in Table 3.2, Sensors listed in Table 3.3.

curve, which is subsequently evaluated at the bottom flange. The tower is designed to be made from a 1.4301 stainless-steel tube with a circular cross-section of $D_{T,1} = 0.2$ m and $D_{T,2} = 0.18$ m. YOUNG's modulus is extracted from the 1.4301 data sheet ($E_T = 2 \times 10^{11}$ N m⁻²). The structural properties of the tower are calculated utilizing the Equations (3.9).

$$A_T = \frac{\pi}{4}(D_{T,1}^2 - D_{T,2}^2) \quad (3.9a)$$

$$I_{T,yy} = \frac{\pi}{4} \left(\left(\frac{D_{T,1}}{2} \right)^2 - \left(\frac{D_{T,2}}{2} \right)^2 \right) \quad (3.9b)$$

$$B_{T,yy} = E_T I_{T,yy} \quad (3.9c)$$

For solving the spatial differential equations of the beam theory, the inner forces and moments along the tower axis are required. Figure 3.21 depicts the used tower model. For the selected bearings, the boundary and transition conditions stated in Equation (3.10) follow. The deflection at both bearing locations is set to zero for ideally stiff bearings, and the rotation at the floating bearing must be

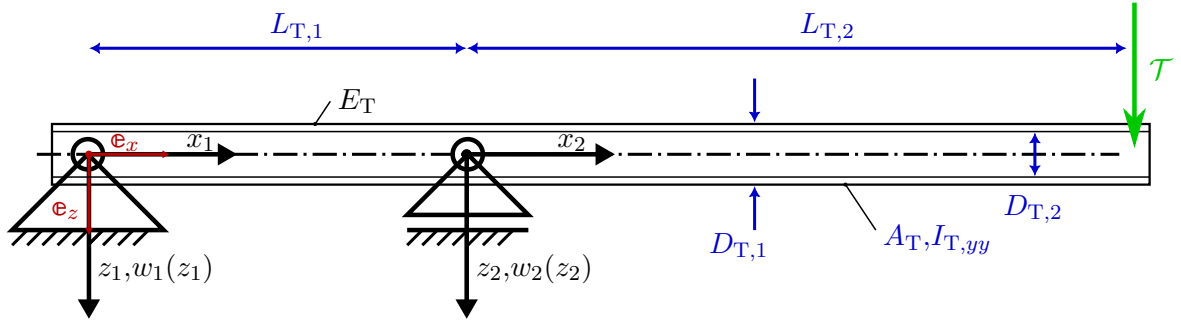


Figure 3.21: Tower model. Design loads specified in Table 3.1. $D_{T,1} = 200$ mm, $D_{T,2} = 180$ mm, $L_{T,1} = 1.559$ m, $L_{T,2} = 3.402$ m. $E_T = 2 \times 10^{11}$ N m⁻², $A_T = 0.006$ m², $I_T = 2.701 \times 10^{-5}$ m⁴. Material: 1.4301.

continuous.

$$w_1(0) = 0 \qquad w_1(L_{T,1}) = 0 \qquad (3.10a)$$

$$w_2(0) = 0 \qquad \rho_1(L_{T,1}) = \rho_2(0) \qquad (3.10b)$$

EULER-BERNOULLI's spatial differential equation relates the inner loads, i.e., the bending moment, with the curvature of the deflection $w(x)$. $\iota(\cdot) := \partial/\partial\vec{x}(\cdot)$ depicts the spatial derivative. Integrating the equation twice yields an undefined deflection curve for every point of the domain. Including the boundary, and transition conditions (Equation (3.10)) defines the expression.

$$EI_{yy}w''(x) = -M_y(x), \quad w'(x) =: \rho(x) \qquad (3.11)$$

For the model, depicted in Figure 3.21, the deflection curve $w(x)$ is described by the Equations (3.12). Its maxima can be found by identifying the roots of the tower rotation $\rho(x)$. Additionally, the analytical expressions allow analyzing the sensitivity of the bending to changing parameters, e.g., the influence of the bearing distance $L_{T,1}$ can be investigated.

$$w_1(x_1) = -\frac{\mathcal{T}L_{T,1}^2L_{T,2}}{6B_{T,yy}} \left(1 - \left(\frac{x_1}{L_{T,1}} \right)^2 \right) \frac{x_1}{L_{T,1}} \qquad (3.12a)$$

$$\rho_1(x_1) = \frac{\mathcal{T}L_{T,2}}{6B_{T,yy}} \left(3 \frac{x_1^2}{L_{T,1}} - L_{T,1} \right) \qquad (3.12b)$$

$$w_2(x_2) = \frac{\mathcal{T}L_{T,2}^3}{6B_{T,yy}} \left(- \left(\frac{x_2}{L_{T,2}} \right)^2 + 3 \left(\frac{x_2}{L_{T,2}} \right) + 2 \frac{L_{T,1}}{L_{T,2}} \right) \frac{x_2}{L_{T,2}} \qquad (3.12c)$$

$$\rho_2(x_2) = -\frac{\mathcal{T}L_{T,2}^2}{2B_{T,yy}} \left(\left(\frac{x_2}{L_{T,2}} \right)^2 - 2 \frac{x_2}{L_{T,2}} - \frac{2}{3} \frac{L_{T,1}}{L_{T,2}} \right) \qquad (3.12d)$$

For the turbine location ($x_2 = L_{T,2}$), a maximum deflection of $w_2(L_{T,2}) = 7.8$ mm and a rotation of $\rho = 0.18^\circ$ follow. Both cause the rotor plane to be deflected relatively to the inflow direction. However, the magnitude of the rotation at the design point is considered insignificant for answering the stated research question. The tower is placed on rails to achieve traversability along x (Figure 1.2). The travel length is limited to approximately 6.5 m, which allows the investigation of the wake, up to $5D$ downstream of the rotor plane, using the current PIV setup. For increasing the tower's aerodynamic transparency, the tower cross-section becomes more slender for the last 800 mm. The outer diameter reduces to $D_{T,3} = 0.112$ m. The inner tube diameter is $D_{T,4} = 0.09$ m. The radial distance from the blade tip to the larger tower section is 325 mm $\approx 0.5R$. Thus, the influence on the wake expansion is minimized. The tower is mostly made of welded stainless-steel tubes, which are segmented for increased

manageability during installation. Hence, tower segments can easily be exchanged, if adjusted diameters or lengths are required. Fairing of various kinds can be screwed to the tower at different positions. Utilizing an adapter plate between the turbine and the tower enables investigating the influence of rotor-to-tower distance on the dynamics and development of the tip vortex helix. The same strategy can be used to investigate downwind configurations. The tower mass is minimized, whilst approaching maximized stiffness for well tuned eigendynamics. A tilt mechanism is implemented, e.g., for changing the blade pitch without the need for driving the tow carriage to its resting position inside the trim basin. Additionally, the tilting mechanism is used as a safety feature, as it allows a quick evacuation of the turbine in case water ingress into the nacelle is detected. The tower can be rotated (i.e., *yawed*) along its axis due to the support by bearings. A clamp fixes its position, once the turbine is aligned with the inflow direction. Figure 3.22 shows a render of the entire test rig. The location of the free water surface is depicted as a semi-transparent plane. The locations of the fixed and the floating bearings are highlighted. The upper bearing structure is supported by the rails, which run on top of the existing tow carriage platform. The lower bearing is installed in a light-weight structure made from tie rods. The welded frame surrounding it is supported by low friction plain bearings. Just above the water surface, the tilting hinge is visible. For the submerged tower segment of large diameter, classic fairing concepts such as symmetric profiling made from bent metal sheets or helical strakes are planned but not included in the image. For the tower part, which imposes the risk of interacting with UBeRT's wake, fairing will be implemented as well. However, investigations are necessary on how possible interactions can be minimized or potentially avoided. The tower's main function is to reduce the turbine deflection as much as possible, throughout the parameter region. Additionally, its mass is "optimized" for delaying the appearance of its lowest eigenfrequencies. Finally, the handling and installation of the tower is considered in the design process, and should be as easy as possible (Items 10). The presented section summarized the workflow for finding a well-balanced answer to the stated requirements.

3.5 Sensors and Waterproofing

Description of implemented sensors and waterproofing strategies

Various sensors, necessary for characterizing the turbine and its respective operational point, are included in the UBeRT design (Item 11). The undisturbed inflow velocity $\bar{U}_{1,\infty}$ is assumed to be equal

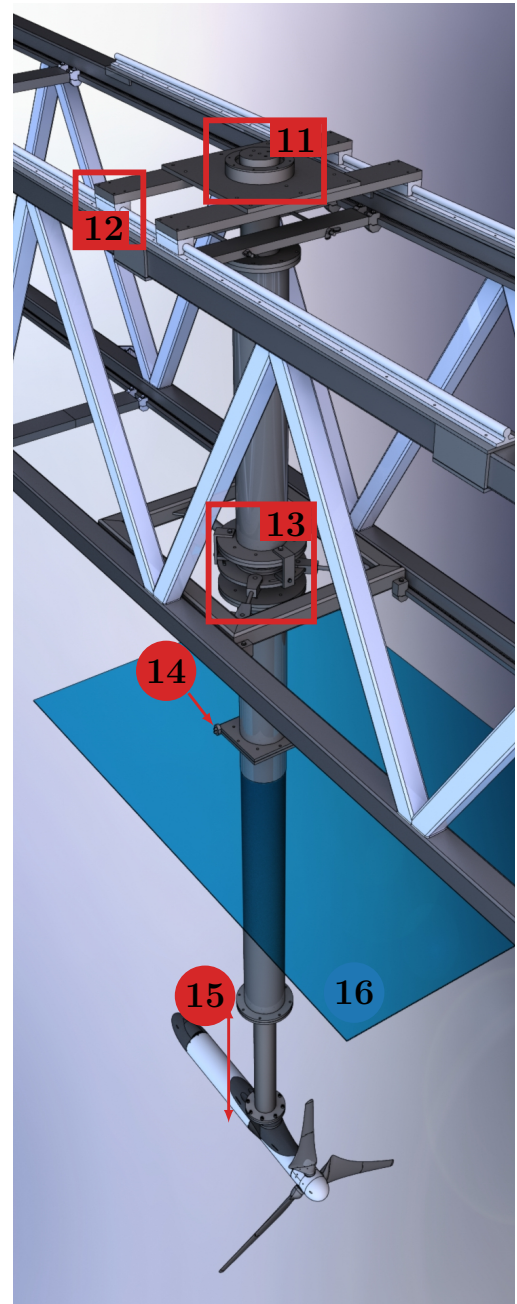


Figure 3.22: The Underwater Berlin Research Turbine test rig. (11) Fixed bearing. (12) Rail carriage and rails for axial traversability. (13) Floating bearing. (14) Tilting hinge for quick blade pitch changes and evacuation in case of water ingress. (15) Tower segment of 800 mm length with reduced outer diameter. (16) Location of the free water surface.

to the tow carriage velocity \bar{U}_{to} . It is obtained from the carriage control system and fed into the data acquisition system of the UBeRT test rig. The angular velocity Ω is gathered from the encoder signal, that is part of the drive train (*AK1H*, *SEW Eurodrive*). The corresponding velocity is generated and provided by the downstream control system (*DEH11B* of the *MDX61B0110-5A3-4-00*, *SEW Eurodrive*). The encoder signal also resolves the blade phase angle. Together with an **Once Per Revolution** (OPR) sensor, consisting of reflective tape on the low-speed shaft and an optical sensor, sawtooth signals are generated for PIV triggering. The stationary turbine torque \mathcal{Q} is measured, using the electrical generator torque, that is also provided by the inverter. The encoder and the generator are located inside the nacelle and can be seen in Figure 3.20 at Mark (4). The turbine thrust \mathcal{T} is measured using the three-component strain gauge *K3D120* from *ME-Meßsysteme* rated for ± 5 kN. The gauge is placed between the tower and the turbine, as can be seen in Figure 3.20 at Mark (5). Additional sensors are implemented in the design for extending the capabilities of the test rig. Fully deployed WHEATSTONE bridges are part of every blade root for measuring individual flap- and edgewise BRBMs. The sensors encompass strain gauges of type *N2A-06-S5092R-350*, purchased from *ME-Meßsysteme* with a resistance of 350 Ohm. The strain gauges are glued to the blade root adapters, visible in Figure 3.17b at Mark (1). The wiring is fed through the blade root and the hub, into the spinner (Figure 3.20, Mark (10)). The signals are amplified and conditioned by six *ICA6H* miniature strain gauge amplifiers supplied by *ZSE Electronics*. The amplified signals are then transformed from the rotating into the stationary system utilizing a 24-channel slip ring of type *7KC000008* made by *Schleifring*.

For assuring a safe operation for the involved personnel and the equipment, several sensors are deployed. Water ingress is the largest safety issue for the electrical equipment. However, it is unlikely, that water enters through an open breach of the hull. Instead, it will likely creep in as leakage around the o-ring. Thus, exposed pairs of contacts are located at adequate points of water ingress. Once, the contacts are shorted by agglomerated water, the ingress is detected and indicated by *M158* modules made by *Kemo*. The nacelle is equipped with a *BME 280* humidity and temperature sensor made by *Bosch Sensortec*. Its signals are used as indicators for possibly damaging ambient conditions for all electrical components. The aforementioned OPR sensor is also used to detect slip between the drive shaft and the turbine shaft. Deviations between both signals indicate coupling errors, e.g., caused by a motor or a rotor torque beyond the ratings. The BRBM sensor signals are used as additional indicators. The nacelle acceleration is measured with a three-axis accelerometer and compared against thresholds. Especially during start-ups and break maneuvers, the signal is used to tune the ramps for assuring safe operation. After commissioning of the test rig, the eigendynamics of the tower-turbine-system will be known. The accelerometer then allows the online monitoring of the vibrational behavior of the turbine during operation. Vortex shedding frequencies and interfering and possibly dangerous turbine-tower-interactions are detected.

Several redundant components for waterproofing are included in the test rig design. The overall strategy is extracted from Payne et al. [138]. The inside of the nacelle is completely shielded against the surrounding water (Figure 3.20). The hull consists mainly of two E235+C seamless precision tubes of different diameters, which are spray-painted against corrosion [159–161]. The downstream one with diameter $D_{\text{nac},2} = 155$ mm encapsulates the drive. It is radially screwed to a cap, through which the motor, encoder, and break cables are fed. Stainless-steel cable glands, rated IP68K and up to 30 bar are used. Two o-rings (*NBR70*, 135.9×6.99) are placed on the perimeter of the end cap. On the tower side of the rear housing, the drive mount is located. Two radial o-rings shield the inside (*NBR70*, 135.9×6.99). An axial o-ring (*NBR70*, 120.25×3.53) is located between the drive mount and the centerpiece of the turbine. The centerpiece connects the rear and the front part of the turbine with the tower flange. It houses the coupling (Mark (6), Figure 3.20) and accommodates two cable glands as outlets for the data cables from the slip ring (Mark (8), Figure 3.20). The upper side of the center piece is sealed with a gasket. The upstream side connects to the floating bearing block (Mark (7), Figure 3.20). An axial o-ring is placed in between (*NBR70*, 107.54×3.53). The front piece of the nacelle hull with an outer diameter of $D_{\text{nac},1} = 130$ mm is sealed in analogy to the rear end (four radial

Table 3.3: Sensors included in the Underwater Berlin Research Turbine.

Quantity	Sensor	Supplier	Specifications
<i>Characterization</i>			
Inflow velocity		<i>Tow carriage velocity from control</i>	
Angular velocity	AK1H	SEW Eurodrive	Absolute encoder
Torque		<i>Electrical torque from UBeRT control</i>	
Thrust	K3D120	ME-Meßsysteme	Three axis gauge, ± 5 kN
Revolution count		<i>To be decided</i>	
<i>Extra</i>			
Slip ring	7KC000008	Schleifring	24-channel slip ring
Blade moments	N2A-06-S5092R-350	ME-Meßsysteme	Gauge, 350 Ohm
	ICA6H	ZSE Electronics	Gain, ± 10 V, 3-wire
Nacelle acceleration		<i>To be decided</i>	
<i>Safety</i>			
Water ingress	M158	Kemo	Several exposed contacts
Humidity	BME 280	Bosch Sensortec	
Temperature			
Over speed		<i>To be decided</i>	
Nacelle acceleration		<i>To be decided</i>	
Blade moments		<i>See above</i>	

o-rings, *NBR70*, 113.67×5.33). Upstream of the fixed bearing (Mark (9), Figure 3.20), two lip seals are positioned back-to-back (*AS NBR*, $50 \times 62 \times 7$). They secure water ingress along the rotating surface of the shaft. Here, the shaft is hollow, allowing the strain gauge data cables to be fed to the slip ring. The concept is reproduced from Payne et al. [138]. The downstream side of the hub is screwed to a flange, whereby the waterproofing is assured, utilizing an axial o-ring (*NBR70*, 53.57×3.53). The strain gauge amplifiers are placed inside a waterproof housing (Mark (10), Figure 3.20). Two radial o-rings (*NBR70*, 72.76×1.78) and an axial o-ring (*NBR70*, 50.4×3.53) are used to assure its safety. All o-rings are selected, using the DIN ISO 3601 series [162–165]. Where the wiring of the strain gauges enters the blade root adapter (Mark (1), Figure 3.17b), a waterproof shrinking tube is used. All cables are routed through the tower. Cable glands are used to breach the skin of the tower. The entire nacelle is pressurized to counteract the static pressure of the water column. If necessary, an excess pressure will be applied. The motor cable is fed through a separate tube inside the tower to further shield its electromagnetic influence on the sensitive data cables.

The implemented sensors allow the characterization of the turbine at every operational point of the parameter regime. The sensors are selected in accordance with the design loads and their specifications. The data quality is "optimized" by spatially separating the drive cables and the sensitive data cables. Redundant waterproofing strategies are included in the turbine design. They are based on the best-practice experience published by Payne et al. [138].

4 Conclusion

Summary of the followed design approach with reference to the specification list

The presented thesis summarizes the engineering workflow for designing a HAWT model for underwater PIV measurements in a large water towing tank. A range of airfoils is compared and evaluated regarding their applicability for the underwater rotor. Various aspects ranging REYNOLDS effects, cavitation, and structural integrity are considered. From the selected airfoils, rotor blades using SCHMITZ's design approach are derived. Ultimately, the SG6040 airfoil is selected for the UBeRT rotor, based on its structural resistance to high loads. The decision-making culminates from an extensive FEM analysis, considering normal and tangential force distributions, derived from QBLADE's BEM module. The blade is concluded by designing a root transition. The finalized rotor is then thoroughly investigated with QBLADE. Specifically, the bound circulation is analyzed at different operational points. The aim was to achieve a constant circulation along the span for inducing the creation of concentrated tip vortices. The analysis shows the successful accomplishment of the goal. The generated tip vortices and their near-wake development are pre-assessed regarding their dimensions and circulation utilizing a semi-empirical model from the literature. The tip vortex core size is deemed sufficient to be visible with the existing underwater PIV system. A pitching strategy is implemented, which allows reproducible manual pitch adjustments. The segmented design of the blades enables the exchange of the tips. Thus, studies on auspicious passive flow control devices for exciting tip vortex instabilities and subsequently accelerating the wake decay are pioneered.

A suitable drive system is fitted to the aerodynamic specifications of the rotor. Travel profiles including the tow carriage ramp-up are defined. All critical drive train parts are dimensioned regarding their structural integrity, utilizing common design guidelines. A high-quality absolute encoder is integrated in the drive train, which allows blade phase angle dependent triggering of the PIV system. The entire drive train is kept as compact as possible. Hence, interference and possibly dangerous eigendynamics of the drive system are avoided. A bearing concept is chosen, that counteracts possible rotor induced vibrations, whilst compensating for potential alignment errors. The drive train is operable in both rotational directions. Thus, upwind and downwind campaigns are possible.

The tower and the tow carriage connection are designed for minimum mass and maximum stiffness. The tower's influence on the tip vortex generation is regarded. However, measurement campaigns must be conducted, to optimize a fairing concept and quantify the tower's effect. A reduced cross-section is selected on the turbine's level to reduce the aerodynamic influence of the tower. The tower is modular for enabling its efficient "optimization" and increase manageability. The test rig moves on rails for convenient changes in the downstream location of the field of view. A tower hinge allows for onboard changes of the blade pitch, without the need to drive the towing carriage to its resting position inside the trim tank. Additionally, the hinge constitutes the safety procedure, when water ingress in the nacelle is detected. All test rig components are evaluated regarding their resistance to corrosion. Mostly high-quality alloys like 1.4301 stainless steel are chosen.

All necessary sensors for characterizing the turbine's operational point are included in the design. The undisturbed inflow velocity is assumed to be equal to the tow carriage velocity. From the electrical control of the UBeRT turbine, the torque and the angular velocity are derived. The rotational encoder is selected to enable high-resolution blade phase angle correlations for PIV triggering and phase-averaging. Additionally, every turbine blade is equipped with flapwise and edgewise BRBM sensors. They allow the online monitoring of the blade loads, which is used for assuring a safe operation. The BRBM signals are transformed from the rotating into the stationary system utilizing a slip ring. Finally, all cables are fed through the nacelle and into the tower. The interfering influence of the motor cable is accounted for by feeding it through a separate tube. Additional safety sensors for

detecting water ingress, increasing nacelle humidity and temperature, and over-speed of the turbine shaft are integrated. The nacelle is completely redundantly waterproofed utilizing o-rings, lip seals, and gaskets.

All aspects of the specification lists are considered and solved, so that a comprehensive answer to the stated research question is found. Deviations or limitations are justified. Due to the dimension of the test rig, its exposure to water, and the resulting loading, opportunities for improvements remain. Only an extensive commissioning will reveal, which components and aspects are sufficiently covered, and which must be "optimized" or adjusted. Concluding, the UBeRT test rig offers the unique opportunity to investigate tip vortex instabilities and their efficacy for passively inducing accelerated wake decay, at a never-reached REYNOLDS number in experiments. The combination of the experimental results with CFD strategies allows the investigation of scale effects and has the considerable potential, to contribute to fighting climate change.

5 Outlook

Future work and possible following steps

After manufacturing, the test rig will be used for measuring occurring instability phenomena emerging in helical vortex systems. An extensive system characterization is necessary. The following aspects must be included:

- Commissioning and Characterization
 - The sensing systems, including all implemented wiring, must be calibrated. For the calibration of the BRBM sensors, threaded holes at the blade segments are included in the design, to attach calibration weights. Possible interference between the motor and the data signals should be investigated, signal-to-noise ratios quantified.
 - The rotor must be mass-balanced for minimizing the otherwise resulting unsteady loading.
 - A data acquisition and test rig control software must be coded. Safety procedures and protocols must be accounted for.
 - Thrust, torque, and power curves of the UBeRT turbine must be measured and could be compared to the QBLADE simulation. The correlation of the edgewise bending moment and the aerodynamic rotor torque could be analyzed.
- Modal Analysis
 - The dynamics of the test rig should be analyzed numerically. QBLADE's turbine module can be used to investigate different operational points of the entire turbine. Even added-mass and hydrodynamic damping can be considered. Potentially, the included lifting line method is suitable to assess the magnitude of the low-pressure region inside the tip vortices in the near-wake.
 - The results should be compared with an experimental modal and operational vibration analysis. The influences of a flooded tower and the effect of hydrodynamic damping could be more thoroughly investigated. Dry-testing inside the emptied trim tank could be compared with experiments in water.
- Test Rig Configurations
 - Fairing concepts must be implemented and thoroughly tested, regarding their influence on the tip vortex helix.
 - The differences between upwind and downwind configurations, and adjusted tip-to-tower distances, should be investigated.
 - The potential of utilizing passive and active flow control devices, attached to the tower, for exciting tip vortex instabilities and subsequently accelerating wake decay could be assessed.
- PIV Measurements
 - Extensive PIV measurements at several wake cross-sections will be conducted.
 - The data will be post-processed, using for instance (spectral) proper orthogonal decomposition and FOURIER mode analysis.

Considering the long list of open questions, this thesis only contains the starting point of the whole measurement series. Along the way, components or even entire concepts of the here presented UBeRT design will be adjusted, "optimized", or conceptualized anew. However, the first steps of conducting research at the Technische Universität Berlin on strategies to alleviate wake effects in modern wind parks have been taken.

Bibliography

1. United Nations: Department of Economic and Social Affairs. *The sustainable development goals report 2022* ISBN: 978-92-1-101448-8. <https://unstats.un.org/sdgs/report/2022/The-Sustainable-Development-Goals-Report-2022.pdf> (2023) (UNITED NATIONS, New York, 2022) (cit. on p. 1).
2. Allen, M., Dube, O., Solecki, W., Aragón-Durand, F., Cramer, W., Humphreys, S., Kainuma, M., Kala, J., Mahowald, N., Mulugetta, Y., Perez, R., Wairiu, M. & Zickfeld, K. In *Global Warming of 1.5°C* (ed IPCC) 49–92 (Cambridge University Press, 2022). ISBN: 9781009157940. doi:10.1017/9781009157940.003 (cit. on p. 1).
3. *World Energy Outlook 2020* (ed IEA) <https://www.iea.org/reports/world-energy-outlook-2020> (2022) (Paris, 2020) (cit. on p. 1).
4. Barthelmie, R. J. & Pryor, S. C. Potential contribution of wind energy to climate change mitigation. *Nature Climate Change* **4**, 684–688. ISSN: 1758-678X. doi:10.1038/NCLIMATE2269 (2014) (cit. on p. 1).
5. McCrone, A.: *Global Trends in Renewable Energy Investment 2020* (ed United Nations) Frankfurt am Main, 2020. https://www.fs-unep-centre.org/wp-content/uploads/2020/06/GTR_2020.pdf (2023) (cit. on p. 1).
6. United Nations: Framework Convention on Climate Change: *The Paris Agreement* 2016. https://unfccc.int/sites/default/files/resource/parisagreement_publication.pdf (2023) (cit. on p. 1).
7. Cherp, A., Vinichenko, V., Tosun, J., Gordon, J. A. & Jewell, J. National growth dynamics of wind and solar power compared to the growth required for global climate targets. *Nature Energy* **6**, 742–754. doi:10.1038/s41560-021-00863-0 (2021) (cit. on p. 1).
8. Luderer, G., Krey, V., Calvin, K., Merrick, J., Mima, S., Pietzcker, R., van Vliet, J. & Wada, K. The role of renewable energy in climate stabilization: results from the EMF27 scenarios. *Climatic Change* **123**, 427–441. ISSN: 0165-0009. doi:10.1007/s10584-013-0924-z (2014) (cit. on p. 1).
9. Lu, X., McElroy, M. B. & Kiviluoma, J. Global potential for wind-generated electricity. *Proceedings of the National Academy of Sciences of the United States of America* **106**, 10933–10938. doi:10.1073/pnas.0904101106 (2009) (cit. on pp. 1, 2).
10. Marvel, K., Kravitz, B. & Caldeira, K. Geophysical limits to global wind power. *Nature Climate Change* **3**, 118–121. ISSN: 1758-678X. doi:10.1038/nclimate1683 (2013) (cit. on p. 1).
11. Jacobson, M. Z. & Archer, C. L. Saturation wind power potential and its implications for wind energy. *Proceedings of the National Academy of Sciences of the United States of America* **109**, 15679–15684. doi:10.1073/pnas.1208993109 (2012) (cit. on p. 1).
12. Shields, M., Beiter, P., Nunemaker, J., Cooperman, A. & Duffy, P. Impacts of turbine and plant upsizing on the levelized cost of energy for offshore wind. *Applied Energy* **298**, 117189. ISSN: 03062619. doi:10.1016/j.apenergy.2021.117189 (2021) (cit. on pp. 1, 2).
13. Walter, S., Packey, D. & Holt, T. A manual for the economic evaluation of energy efficiency and renewable energy technologies. doi:10.2172/35391. <https://www.osti.gov/biblio/35391> (2023) (1995) (cit. on p. 1).

14. Wisser, R., Jenni, K., Seel, J., Baker, E., Hand, M., Lantz, E. & Smith, A. Expert elicitation survey on future wind energy costs. *Nature Energy* **1**. doi:[10.1038/nenergy.2016.135](https://doi.org/10.1038/nenergy.2016.135) (2016) (cit. on p. 1).
15. Stehly, T., Beiter, P. & Duffy, P.: *2019 Cost of Wind Energy Review* Golden, Colorado, 2020. <https://www.nrel.gov/docs/fy21osti/78471.pdf> (2022) (cit. on p. 2).
16. Manwell, J. F. *Wind energy explained: Theory, design and application* 2nd ed. ISBN: 9780470686287. doi:[10.1002/9781119994367](https://doi.org/10.1002/9781119994367). <https://onlinelibrary.wiley.com/doi/book/10.1002/9781119994367> (Wiley, Chichester, U.K, 2009) (cit. on pp. 2, 5, 10, 11, 13, 16, 18).
17. Feltes, J., Hendriks, R., Stapleton, S., Voelzke, R., Lam, B. & Pfuntner, N. Twixt Land and Sea: Cost-Effective Grid Integration of Offshore Wind Plants. *IEEE Power and Energy Magazine* **10**, 53–61. ISSN: 1540-7977. doi:[10.1109/MPE.2011.2178289](https://doi.org/10.1109/MPE.2011.2178289) (2012) (cit. on p. 2).
18. Barthelmie, R., Politis, E., Prospathopoulos, J., Rados, K., Schlez, W., Phillips, J., Neubert, A., Frandsen, S., Rathmann, O., Hansen, K., Cabezón, D., van der Pijl, S. & Schepers, J. Flow and wakes in large wind farms in complex terrain and offshore (2008) (cit. on pp. 2, 21).
19. Mikkelsen, R., Sørensen, J. N., Øye, S. & Troldborg, N. Analysis of Power Enhancement for a Row of Wind Turbines Using the Actuator Line Technique. *Journal of Physics: Conference Series* **75**, 012044. ISSN: 1742-6588. doi:[10.1088/1742-6596/75/1/012044](https://doi.org/10.1088/1742-6596/75/1/012044) (2007) (cit. on p. 2).
20. Barthelmie, R. J., Frandsen, S. T., Nielsen, M. N., Pryor, S. C., Rethore, P.-E. & Jørgensen, H. E. Modelling and measurements of power losses and turbulence intensity in wind turbine wakes at Middelgrunden offshore wind farm. *Wind Energy* **10**, 517–528. ISSN: 10954244. doi:[10.1002/we.238](https://doi.org/10.1002/we.238) (2007) (cit. on pp. 2, 4).
21. Méchali, M., Barthelmie, R., Frandsen, S., Jensen, L. & Réthoré, P.-E. Wake effects at Horns Rev and their influence on energy production. *European Wind Energy Conference*. (2023) (2006) (cit. on p. 2).
22. Herbert-Acero, J., Probst, O., Réthoré, P.-E., Larsen, G. & Castillo-Villar, K. A Review of Methodological Approaches for the Design and Optimization of Wind Farms. *Energies* **7**, 6930–7016. doi:[10.3390/en7116930](https://doi.org/10.3390/en7116930) (2014) (cit. on p. 2).
23. Masters, G. M. *Renewable and efficient electric power systems* 2nd ed. ISBN: 9781118633519 (John Wiley & Sons Inc, Hoboken, NJ, 2013) (cit. on p. 2).
24. Burton, T., Jenkins, N., Sharpe, D. & Bossanyi, E. *Wind Energy Handbook* ISBN: 9780470699751. doi:[10.1002/9781119992714](https://doi.org/10.1002/9781119992714) (Wiley, 2011) (cit. on pp. 2, 5, 6, 11, 12, 16, 18).
25. Chacón, L., Crespo, A., Enevoldsen, P., Gómez-Elvira, R., Hernández, J., Højstrup, J., Manuel, F., Thomsen, K. & Sørensen, P.: *Measurements on and Modelling of Offshore Wind Farms* (ed Frandsen, S.) Roskilde, 1996. <https://www.osti.gov/etdeweb/servlets/purl/434951> (2022) (cit. on pp. 2, 4).
26. Frandsen, S.: Turbulence and turbulence-generated structural loading in wind turbine clusters. *Dissertation* (DTU, Roskilde, 2007). <https://www.osti.gov/etdeweb/servlets/purl/20685756> (2023) (cit. on pp. 2, 4, 10, 14).
27. Dahlberg, J., Poppen, M. & Thor, S. E. Load/fatigue effects on a wind turbine generator in a wind farm. *Journal of Wind Engineering and Industrial Aerodynamics* **39**, 199–209. ISSN: 01676105. doi:[10.1016/0167-6105\(92\)90546-M](https://doi.org/10.1016/0167-6105(92)90546-M) (1992) (cit. on p. 2).
28. Pope, S. B. *Turbulent flows* 10. print. ISBN: 9780521598866 (Cambridge Univ. Press, Cambridge, 2013) (cit. on pp. 2, 4, 6, 7).

29. Hau, E. & von Renouard, H. *Wind Turbines* ISBN: 978-3-540-24240-6. doi:[10.1007/3-540-29284-5](https://doi.org/10.1007/3-540-29284-5) (Springer Berlin Heidelberg, Berlin, Heidelberg, 2006) (cit. on pp. [2](#), [5](#), [11](#), [16](#), [17](#), [19](#), [21](#)).
30. Spurk, J. H. & Aksel, N. *Fluid Mechanics* ISBN: 978-3-540-73536-6. doi:[10.1007/978-3-540-73536-6](https://doi.org/10.1007/978-3-540-73536-6) (Springer Berlin Heidelberg, Berlin, Heidelberg, 2008) (cit. on pp. [2](#), [4](#), [6](#), [7](#), [9](#), [10](#), [12](#)).
31. Gasch, R. & Twele, J. *Wind Power Plants* ISBN: 978-3-642-22937-4. doi:[10.1007/978-3-642-22937-4](https://doi.org/10.1007/978-3-642-22937-4) (Springer Berlin Heidelberg, Berlin, Heidelberg, 2012) (cit. on pp. [2](#), [4–6](#), [10](#), [11](#), [14](#), [16–19](#), [27](#), [40](#)).
32. Anderson, J. D. *Fundamentals of aerodynamics* Sixth edition. ISBN: 978-1-259-12991-9 (McGraw-Hill Education, New York, NY, 2017) (cit. on pp. [2](#), [6](#), [7](#), [9](#), [10](#), [12](#)).
33. Batchelor, G. K. *An introduction to fluid dynamics* 1. Cambridge mathematical ed., 14. print. ISBN: 9780521663960 (Cambridge Univ. Press, Cambridge, 2010) (cit. on pp. [2](#), [4](#), [9](#), [12](#)).
34. Bertin, J. J. & Cummings, R. M. *Aerodynamics for Engineers* ISBN: 9781009105842. doi:[10.1017/9781009105842](https://doi.org/10.1017/9781009105842) (Cambridge University Press, 2021) (cit. on pp. [2](#), [6](#), [9](#)).
35. Lignarolo, L. E., Ragni, D., Simao Ferreira, C. & van Bussel, G. G. Experimental quantification of the entrainment of kinetic energy and production of turbulence in the wake of a wind turbine with Particle Image Velocimetry. *32nd ASME Wind Energy Symposium* (American Institute of Aeronautics and Astronautics, Reston, Virginia, 2014). ISBN: 978-1-62410-313-1. doi:[10.2514/6.2014-0706](https://doi.org/10.2514/6.2014-0706) (cit. on pp. [4](#), [21](#)).
36. Vermeer, L. J., Sørensen, J. N. & Crespo, A. Wind turbine wake aerodynamics. *Progress in Aerospace Sciences* **39**, 467–510. ISSN: 03760421. doi:[10.1016/S0376-0421\(03\)00078-2](https://doi.org/10.1016/S0376-0421(03)00078-2) (2003) (cit. on pp. [4](#), [21](#), [22](#)).
37. Ivanell, S., Mikkelsen, R., Sørensen, J. N. & Henningson, D. Stability analysis of the tip vortices of a wind turbine. *Wind Energy* **13**, 705–715. ISSN: 1095-4244. doi:[10.1002/we.391](https://doi.org/10.1002/we.391) (2010) (cit. on pp. [4](#), [24](#)).
38. Lyon, C., Broeren, A., Giguère, P., Goopalarthnam, A. & Selig, M. S. *Summary of low speed airfoil data* ISBN: 978-0964674714 (SoarTech Publications, Virginia Beach, Va., 1995) (cit. on pp. [5](#), [7](#), [8](#), [35–37](#)).
39. Schlichting, H. & Truckenbrodt, E. *Aerodynamik des Flugzeuges: Erster Band: Grundlagen aus der Strömungstechnik Aerodynamik des Tragflügels (Teil I)* 3. Auflage. ISBN: 978-3-642-63148-1. doi:[10.1007/978-3-642-56911-1](https://doi.org/10.1007/978-3-642-56911-1) (Springer Berlin Heidelberg, Berlin, Heidelberg and s.l., 2001) (cit. on p. [6](#)).
40. Jones, R. T. *Wing Theory Course Book*. ISBN: 9780691633381. <https://permalink.obvsg.at/> (Princeton University Press, Princeton, NJ, 2014) (cit. on p. [6](#)).
41. Roy, S., Das, B. & Biswas, A. In *Recent Advances in Mechanical Engineering* (eds Pandey, K. M., Misra, R. D., Patowari, P. K. & Dixit, U. S.) 729–737 (Springer Singapore, Singapore, 2021). ISBN: 978-981-15-7710-9. doi:[10.1007/978-981-15-7711-6](https://doi.org/10.1007/978-981-15-7711-6) (cit. on p. [6](#)).
42. Ma, D., Zhao, Y., Qiao, Y. & Li, G. Effects of relative thickness on aerodynamic characteristics of airfoil at a low Reynolds number. *Chinese Journal of Aeronautics* **28**, 1003–1015. ISSN: 10009361. doi:[10.1016/j.cja.2015.05.012](https://doi.org/10.1016/j.cja.2015.05.012) (2015) (cit. on p. [6](#)).
43. Motta, V., Guardone, A. & Quaranta, G. Influence of airfoil thickness on unsteady aerodynamic loads on pitching airfoils. *Journal of Fluid Mechanics* **774**, 460–487. ISSN: 0022-1120. doi:[10.1017/jfm.2015.280](https://doi.org/10.1017/jfm.2015.280) (2015) (cit. on p. [6](#)).

44. Li, Z., Zhang, P., Pan, T., Li, Q. & Zhang, J. Study on effects of thickness on airfoil-stall at low Reynolds numbers by cusp-catastrophic model based on GA(W)-1 airfoil. *Chinese Journal of Aeronautics* **33**, 1444–1453. ISSN: 10009361. doi:[10.1016/j.cja.2019.12.024](https://doi.org/10.1016/j.cja.2019.12.024) (2020) (cit. on p. 6).
45. Abbott, I. H. & von Doenhoff, A. E. *Theory of wing sections: Including a summary of airfoil data* ISBN: 9781621986218 (Dover Publications, New York, 1959) (cit. on p. 6).
46. Drela, M. In *Low Reynolds Number Aerodynamics* (eds Brebbia, C. A., Orszag, S. A., Seinfeld, J. H., Spanos, P., Cakmak, A. S., Silvester, P., Desai, C. S., Pinder, G., McCrory, R., Yip, S., Leckie, F. A., Ponter, A. R. S., Holz, K.-P., Bathe, K.-J., Connor, J., Wunderlich, W., Argyris, J. & Mueller, T. J.) 1–12 (Springer Berlin Heidelberg, Berlin, Heidelberg, 1989). ISBN: 978-3-540-51884-6. doi:[10.1007/978-3-642-84010-4](https://doi.org/10.1007/978-3-642-84010-4) (cit. on pp. 7, 9, 36, 38, 39).
47. Wu, J.-Z., Ma, H.-Y. & Zhou, M.-D. *Vortical flows* ISBN: 978-3-662-47061-9 (Springer, Heidelberg et al., 2015) (cit. on pp. 9, 12).
48. Glauert, H. In *Aerodynamic Theory* (ed Durand, W. F.) 169–360 (Springer Berlin Heidelberg, Berlin, Heidelberg, 1935). ISBN: 978-3-642-89630-9. doi:[10.1007/978-3-642-91487-4](https://doi.org/10.1007/978-3-642-91487-4) (cit. on pp. 11, 18).
49. Schmitz, G. Theorie und Entwurf von Windrädern optimaler Leistung. *Wissenschaftliche Zeitschrift der Universität Rostock* **5** (1955) (cit. on pp. 11, 18).
50. Naumann, D. T. N.: *Beitrag zur Berechnung von Windenergirotoren unter Beachtung der Gleitzahl* 2016. doi:[10.14279/depositonce-5077](https://doi.org/10.14279/depositonce-5077) (cit. on p. 11).
51. Leweke, T., Quaranta, H. U., Bolnot, H., Blanco-Rodríguez, F. J. & Le Dizès, S. Long- and short-wave instabilities in helical vortices. *Journal of Physics: Conference Series* **524**, 012154. ISSN: 1742-6588. doi:[10.1088/1742-6596/524/1/012154](https://doi.org/10.1088/1742-6596/524/1/012154) (2014) (cit. on pp. 12, 13, 21, 24–26).
52. Connell, J. R. & George, R. L.: *Wake of the MOD-0A1 wind turbine at two rotor diameters downwind on December 3, 1981* 1982. doi:[10.2172/6665635](https://doi.org/10.2172/6665635) (cit. on pp. 13, 21).
53. Betz, A. *Wind-Energie und ihre Ausnutzung durch Windmühlen* (Vandenhoeck and Ruprecht, Göttingen, 1926) (cit. on p. 14).
54. Heier, S. *Windkraftanlagen: Systemauslegung, Netzintegration und Regelung ; mit 15 Tabellen* 5., überarb. und aktualisierte Aufl. ISBN: 9783835101425 (Vieweg + Teubner, Wiesbaden, 2009) (cit. on p. 17).
55. Bartholomay, S., Wester, T. T. B., Perez-Becker, S., Konze, S., Menzel, C., Hölling, M., Spickenheuer, A., Peinke, J., Nayeri, C. N., Paschereit, C. O. & Oberleithner, K. Pressure-based lift estimation and its application to feedforward load control employing trailing-edge flaps. *Wind Energy Science* **6**, 221–245. doi:[10.5194/wes-6-221-2021](https://doi.org/10.5194/wes-6-221-2021) (2021) (cit. on p. 17).
56. Marten, D., Saverin, J. & Behrens de Luna, R.: *QBlade: Next Generation Wind Turbine Design and Simulation* (ed Technische Universität Berlin) Berlin, 2022. <https://qblade.org/> (2022) (cit. on pp. 20, 39).
57. Sørensen, J. N. Instability of helical tip vortices in rotor wakes. *Journal of Fluid Mechanics* **682**, 1–4. ISSN: 0022-1120. doi:[10.1017/jfm.2011.277](https://doi.org/10.1017/jfm.2011.277) (2011) (cit. on p. 21).
58. Lissaman, P. B. S. Energy Effectiveness of Arbitrary Arrays of Wind Turbines. *Journal of Energy* **3**, 323–328. ISSN: 0146-0412. doi:[10.2514/3.62441](https://doi.org/10.2514/3.62441) (1979) (cit. on pp. 21, 22).
59. Lignarolo, L. E. M., Ragni, D., Scarano, F., Simão Ferreira, C. J. & van Bussel, G. J. W. Tip-vortex instability and turbulent mixing in wind-turbine wakes. *Journal of Fluid Mechanics* **781**, 467–493. ISSN: 0022-1120. doi:[10.1017/jfm.2015.470](https://doi.org/10.1017/jfm.2015.470) (2015) (cit. on pp. 21, 24).

60. Crespo, A. & Hernatndez, J. Turbulence characteristics in wind-turbine wakes. *Journal of Wind Engineering and Industrial Aerodynamics* **61**, 71–85. ISSN: 01676105. doi:[10.1016/0167-6105\(95\)00033-X](https://doi.org/10.1016/0167-6105(95)00033-X) (1996) (cit. on p. 21).
61. Lignarolo, L., Ragni, D., Krishnaswami, C., Chen, Q., Simão Ferreira, C. J. & van Bussel, G. Experimental analysis of the wake of a horizontal-axis wind-turbine model. *Renewable Energy* **70**, 31–46. ISSN: 09601481. doi:[10.1016/J.RENENE.2014.01.020](https://doi.org/10.1016/J.RENENE.2014.01.020) (2014) (cit. on p. 21).
62. Okulov, V. L., Naumov, I. V., Mikkelsen, R. F. & Sørensen, J. N. Wake effect on a uniform flow behind wind-turbine model. *Journal of Physics: Conference Series* **625**, 012011. ISSN: 1742-6588. doi:[10.1088/1742-6596/625/1/012011](https://doi.org/10.1088/1742-6596/625/1/012011) (2015) (cit. on pp. 21, 24, 26).
63. Sørensen, J. N., Mikkelsen, R., Sarmast, S., Ivanell, S. & Henningson, D. Determination of Wind Turbine Near-Wake Length Based on Stability Analysis. *Journal of Physics: Conference Series* **524**, 012155. ISSN: 1742-6588. doi:[10.1088/1742-6596/524/1/012155](https://doi.org/10.1088/1742-6596/524/1/012155) (2014) (cit. on p. 21).
64. Zhu, X., Sun, C., Ouyang, H. & Du, Z. Numerical investigation of the effect of towers and nacelles on the near wake of a horizontal-axis wind turbine model. *Energy* **238**, 121782. ISSN: 03605442. doi:[10.1016/j.energy.2021.121782](https://doi.org/10.1016/j.energy.2021.121782) (2022) (cit. on p. 21).
65. Ainslie, J. F. Calculating the flowfield in the wake of wind turbines. *Journal of Wind Engineering and Industrial Aerodynamics* **27**, 213–224. ISSN: 01676105. doi:[10.1016/0167-6105\(88\)90037-2](https://doi.org/10.1016/0167-6105(88)90037-2) (1988) (cit. on p. 21).
66. Santoni, C., Carrasquillo, K., Arenas-Navarro, I. & Leonardi, S. Effect of tower and nacelle on the flow past a wind turbine. *Wind Energy* **20**, 1927–1939. ISSN: 1095-4244. doi:[10.1002/we.2130](https://doi.org/10.1002/we.2130) (2017) (cit. on p. 21).
67. Abraham, A., Dasari, T. & Hong, J. Effect of turbine nacelle and tower on the near wake of a utility-scale wind turbine. *Journal of Wind Engineering and Industrial Aerodynamics* **193**, 103981. ISSN: 01676105. doi:[10.1016/j.jweia.2019.103981](https://doi.org/10.1016/j.jweia.2019.103981) (2019) (cit. on pp. 21–23).
68. Porté-Agel, F., Bastankhah, M. & Shamsoddin, S. Wind-Turbine and Wind-Farm Flows: A Review. *Boundary-layer meteorology* **174**, 1–59. ISSN: 0006-8314. doi:[10.1007/s10546-019-00473-0](https://doi.org/10.1007/s10546-019-00473-0) (2020) (cit. on p. 22).
69. Okulov, V. L., Naumov, I. V., Mikkelsen, R. F., Kabardin, I. K. & Sørensen, J. N. A regular Strouhal number for large-scale instability in the far wake of a rotor. *Journal of Fluid Mechanics* **747**, 369–380. ISSN: 0022-1120. doi:[10.1017/jfm.2014.174](https://doi.org/10.1017/jfm.2014.174) (2014) (cit. on p. 22).
70. Medici, D.: Experimental Studies of Wind Turbine Wakes: Power Optimisation and Meandering. *Dissertation* (Kungliga Tekniska högskolan, Stockholm, 2005). <https://www.diva-portal.org/s mash/get/diva2:14563/FULLTEXT01.pdf>Power (2023) (cit. on p. 22).
71. Hand, M. M., Simms, D. A., Fingersh, L. J., Jager, D. W., Cotrell, J. R., Schreck, S. & Larwood, S. M.: *Unsteady Aerodynamics Experiment Phase VI: Wind Tunnel Test Configurations and Available Data Campaigns* 2001. doi:[10.2172/15000240](https://doi.org/10.2172/15000240) (cit. on pp. 22, 23, 27).
72. Schröder, D., Leweke, T., Hörnschemeyer, R. & Stumpf, E. Experiments on helical vortex pairs in the wake of a rotor. *AIAA Scitech 2021 Forum* (American Institute of Aeronautics and Astronautics, Reston, Virginia, 2021). ISBN: 978-1-62410-609-5. doi:[10.2514/6.2021-1088](https://doi.org/10.2514/6.2021-1088) (cit. on pp. 22, 23, 25).
73. Widnall, S. E. The stability of a helical vortex filament. *Journal of Fluid Mechanics* **54**, 641–663. ISSN: 0022-1120. doi:[10.1017/S0022112072000928](https://doi.org/10.1017/S0022112072000928) (1972) (cit. on p. 24).

74. Gupta, B. P. & Loewy, R. G. Theoretical Analysis of the Aerodynamic Stability of Multiple, Interdigitated Helical Vortices. *AIAA Journal* **12**, 1381–1387. ISSN: 0001-1452. doi:[10.2514/3.49493](https://doi.org/10.2514/3.49493) (1974) (cit. on p. 24).
75. Bhagwat, M. J. & Leishman, J. G. Stability Analysis of Helicopter Rotor Wakes in Axial Flight. *Journal of the American Helicopter Society* **45**, 165. ISSN: 00028711. doi:[10.4050/JAHS.45.165](https://doi.org/10.4050/JAHS.45.165) (2000) (cit. on p. 24).
76. Joukowski, N. E. Vortex Theory of Screw Propeller (1912) (cit. on p. 24).
77. Boersma, J. & Wood, D. H. On the self-induced motion of a helical vortex. *Journal of Fluid Mechanics* **384**, 263–279. ISSN: 0022-1120. doi:[10.1017/S002211209900422X](https://doi.org/10.1017/S002211209900422X) (1999) (cit. on p. 24).
78. Okulov, V. L. On the stability of multiple helical vortices. *Journal of Fluid Mechanics* **521**, 319–342. ISSN: 0022-1120. doi:[10.1017/S0022112004001934](https://doi.org/10.1017/S0022112004001934) (2004) (cit. on p. 24).
79. Okulov, V. L. & Sørensen, J. N. Stability of helical tip vortices in a rotor far wake. *Journal of Fluid Mechanics* **576**, 1–25. ISSN: 0022-1120. doi:[10.1017/S0022112006004228](https://doi.org/10.1017/S0022112006004228) (2007) (cit. on p. 24).
80. Leweke, T. & Williamson, C. H. K. Cooperative elliptic instability of a vortex pair. *Journal of Fluid Mechanics* **360**, 85–119. ISSN: 0022-1120. doi:[10.1017/S0022112097008331](https://doi.org/10.1017/S0022112097008331) (1998) (cit. on p. 24).
81. Meunier, P. & Leweke, T. In *Vortex Structure and Dynamics* (eds Beig, R., Ehlers, J., Frisch, U., Hepp, K., Hillebrandt, W., Imboden, D., Jaffe, R. L., Kippenhahn, R., Lipowsky, R., Löhneysen, H. v., Ojima, I., Weidenmüller, H. A., Wess, J., Zittartz, J., Maurel, A. & Petitjeans, P.) 241–251 (Springer Berlin Heidelberg, Berlin, Heidelberg, 2000). ISBN: 978-3-540-67920-2. doi:[10.1007/3-540-44535-8\u007B\u005C\u005Ctextunderscore\u007D15](https://doi.org/10.1007/3-540-44535-8\u007B\u005C\u005Ctextunderscore\u007D15) (cit. on p. 24).
82. Roy, C., Schaeffer, N., Le Dizès, S. & Thompson, M. Stability of a pair of co-rotating vortices with axial flow. *Physics of Fluids* **20**, 094101. ISSN: 1070-6631. doi:[10.1063/1.2967935](https://doi.org/10.1063/1.2967935) (2008) (cit. on p. 24).
83. Meunier, P. & Leweke, T. Three-dimensional instability during vortex merging. *Physics of Fluids* **13**, 2747–2750. ISSN: 1070-6631. doi:[10.1063/1.1399033](https://doi.org/10.1063/1.1399033) (2001) (cit. on p. 24).
84. Meunier, P., Le Dizès, S. & Leweke, T. Physics of vortex merging. *Comptes Rendus Physique* **6**, 431–450. ISSN: 16310705. doi:[10.1016/j.crhy.2005.06.003](https://doi.org/10.1016/j.crhy.2005.06.003) (2005) (cit. on pp. 24, 26).
85. Meunier, P. & Leweke, T. Elliptic instability of a co-rotating vortex pair. *Journal of Fluid Mechanics* **533**. ISSN: 0022-1120. doi:[10.1017/S0022112005004325](https://doi.org/10.1017/S0022112005004325) (2005) (cit. on p. 24).
86. Leweke, T., Le Dizès, S. & Williamson, C. H. Dynamics and Instabilities of Vortex Pairs. *Annual Review of Fluid Mechanics* **48**, 507–541. ISSN: 0066-4189. doi:[10.1146/annurev-fluid-122414-034558](https://doi.org/10.1146/annurev-fluid-122414-034558) (2016) (cit. on p. 24).
87. Quaranta, H. U., Bolnot, H. & Leweke, T. Long-wave instability of a helical vortex. *Journal of Fluid Mechanics* **780**, 687–716. ISSN: 0022-1120. doi:[10.1017/jfm.2015.479](https://doi.org/10.1017/jfm.2015.479) (2015) (cit. on p. 24).
88. Quaranta, H. U., Brynjell-Rahkola, M., Leweke, T. & Henningson, D. S. Local and global pairing instabilities of two interlaced helical vortices. *Journal of Fluid Mechanics* **863**, 927–955. ISSN: 0022-1120. doi:[10.1017/jfm.2018.904](https://doi.org/10.1017/jfm.2018.904) (2019) (cit. on p. 24).
89. Blanco-Rodríguez, F. J., Le Dizès, S., Selçuk, C., Delbende, I. & Rossi, M. Internal structure of vortex rings and helical vortices. *Journal of Fluid Mechanics* **785**, 219–247. ISSN: 0022-1120. doi:[10.1017/jfm.2015.631](https://doi.org/10.1017/jfm.2015.631) (2015) (cit. on p. 24).

90. Blanco-Rodríguez, F. J. & Le Dizès, S. Elliptic instability of a curved Batchelor vortex. *Journal of Fluid Mechanics* **804**, 224–247. ISSN: 0022-1120. doi:[10.1017/jfm.2016.533](https://doi.org/10.1017/jfm.2016.533) (2016) (cit. on p. 24).
91. Blanco-Rodríguez, F. J. & Le Dizès, S. Curvature instability of a curved Batchelor vortex. *Journal of Fluid Mechanics* **814**, 397–415. ISSN: 0022-1120. doi:[10.1017/jfm.2017.34](https://doi.org/10.1017/jfm.2017.34) (2017) (cit. on p. 24).
92. Schröder, D., Leweke, T., Hörschemeyer, R. & Stumpf, E. Instability and merging of a helical vortex pair in the wake of a rotor. *Journal of Physics: Conference Series* **1934**, 012007. ISSN: 1742-6588. doi:[10.1088/1742-6596/1934/1/012007](https://doi.org/10.1088/1742-6596/1934/1/012007) (2021) (cit. on p. 25).
93. Schröder, D., Leweke, T., Hörschemeyer, R. & Stumpf, E. Generation of a wingtip vortex pair using a pressure-side fin. *Aerospace Science and Technology* **130**, 107860. ISSN: 12709638. doi:[10.1016/j.ast.2022.107860](https://doi.org/10.1016/j.ast.2022.107860) (2022) (cit. on p. 25).
94. Brocklehurst, A. & Barakos, G. N. A review of helicopter rotor blade tip shapes. *Progress in Aerospace Sciences* **56**, 35–74. ISSN: 03760421. doi:[10.1016/j.paerosci.2012.06.003](https://doi.org/10.1016/j.paerosci.2012.06.003) (2013) (cit. on p. 25).
95. Abraham, A. & Leweke, T. Experimental investigation of blade tip vortex behavior in the wake of asymmetric rotors. *Springer Nature*. doi:[10.21203/rs.3.rs-2446805/v1](https://doi.org/10.21203/rs.3.rs-2446805/v1). (2023) (2023) (cit. on p. 25).
96. Frederik, J. A., Doekemeijer, B. M., Mulders, S. P. & Wingerden, J.-.-W. The helix approach: Using dynamic individual pitch control to enhance wake mixing in wind farms. *Wind Energy* **23**, 1739–1751. ISSN: 1095-4244. doi:[10.1002/we.2513](https://doi.org/10.1002/we.2513) (2020) (cit. on p. 25).
97. Gad-el-Hak, M. *Flow control: Passive, active, and reactive flow management* ISBN: 9780521770064. <http://www.loc.gov/catdir/description/cam0210/99052941.html> (Cambridge University Press, Cambridge and New York, 2000) (cit. on p. 25).
98. Wang, J. & Feng, L. *Flow Control Techniques and Applications* ISBN: 9781316676448. doi:[10.1017/9781316676448](https://doi.org/10.1017/9781316676448) (Cambridge University Press, 2018) (cit. on p. 25).
99. Tropea, C., Yarin, A. L. & Foss, J. F. *Springer Handbook of Experimental Fluid Mechanics* ISBN: 978-3-540-25141-5. doi:[10.1007/978-3-540-30299-5](https://doi.org/10.1007/978-3-540-30299-5) (Springer Berlin Heidelberg, Berlin, Heidelberg, 2007) (cit. on pp. 25, 27).
100. Eckelmann, H. *Einführung in die Strömungsmeßtechnik* ISBN: 978-3-663-09882-9 (Teubner and Springer Fachmedien, Stuttgart and Wiesbaden, 1997) (cit. on pp. 25, 27).
101. Jentsch, M., Dahms, J. M., Wosidlo, R., Nayeri, C. N. & Paschereit, C. O. Free surface effects and the utility of a skim plate for experiments in a water towing tank at steady and unsteady model velocity. *Experiments in Fluids* **63**. ISSN: 1432-1114. doi:[10.1007/s00348-022-03502-w](https://doi.org/10.1007/s00348-022-03502-w) (2022) (cit. on pp. 25, 27, 35).
102. Hand, M. M., Simms, D. A., Fingersh, L. J., Jager, D. W. & Cotrell, J. R.: *Unsteady Aerodynamics Experiment Phase V: Test Configuration and Available Data Campaigns* 2001. doi:[10.2172/787980](https://doi.org/10.2172/787980) (cit. on p. 27).
103. Hand, M. M., Simms, D. A., Fingersh, L. J., Jager, D. W., Cotrell, J. R., Schreck, S. & Larwood, S. M.: *Unsteady Aerodynamics Experiment Phase VI: Wind Tunnel Test Configurations and Available Data Campaigns* 2001. doi:[10.2172/15000240](https://doi.org/10.2172/15000240) (cit. on p. 27).
104. Snel, H., Schepers, J. G. & Montgomerie, B. The MEXICO project (Model Experiments in Controlled Conditions): The database and first results of data processing and interpretation.

- Journal of Physics: Conference Series* **75**, 012014. ISSN: 1742-6588. doi:[10.1088/1742-6596/75/1/012014](https://doi.org/10.1088/1742-6596/75/1/012014) (2007) (cit. on p. 27).
105. Schepers, J., Boorsma, K., Cho, T., Gomez-Iradi, S., Schaffarczyk, P., Jeromin, A., Shen, W., Meister, K., Stoevesandt, B., Schreck, S., Micallef, D., Pereira, R., Sant, T., Madsen, H. & Sorensen, N.: *Final report of IEA Task 29, Mexnext (Phase 1): Analysis of Mexico wind tunnel measurements* Petten, 2012. (2022) (cit. on p. 27).
 106. Boorsma, K. & Schepers, J. G. Rotor experiments in controlled conditions continued: New Mexico. *Journal of Physics: Conference Series* **753**, 022004. ISSN: 1742-6588. doi:[10.1088/1742-6596/753/2/022004](https://doi.org/10.1088/1742-6596/753/2/022004) (2016) (cit. on p. 27).
 107. Jentzsch, M., Schmidt, H.-J., Woszidlo, R., Nayeri, C. N. & Paschereit, C. O. Challenges and procedures for experiments with steady and unsteady model velocities in a water towing tank. *Experiments in Fluids* **62**, 1–20. ISSN: 1432-1114. doi:[10.1007/s00348-021-03151-5](https://doi.org/10.1007/s00348-021-03151-5). <https://link.springer.com/article/10.1007/s00348-021-03151-5#citeas> (2021) (cit. on pp. 27, 29, 30, 33, 35).
 108. Greenblatt, D., Mueller-Vahl, H., Strangfeld, C., Ol, M. V. & Granlund, K. O. High Advance-Ratio Airfoil Streamwise Oscillations: Wind Tunnel vs. Water Tunnel. *54th AIAA Aerospace Sciences Meeting* (American Institute of Aeronautics and Astronautics, Reston, Virginia, 2016). ISBN: 978-1-62410-393-3. doi:[10.2514/6.2016-1356](https://doi.org/10.2514/6.2016-1356) (cit. on p. 27).
 109. Schmidt, H.-J., Woszidlo, R., Nayeri, C. N. & Paschereit, C. O. Separation control with fluidic oscillators in water. *Experiments in Fluids* **58**. ISSN: 1432-1114. doi:[10.1007/s00348-017-2392-0](https://doi.org/10.1007/s00348-017-2392-0) (2017) (cit. on p. 27).
 110. Nayeri, C. N., Glas, J. & Paschereit, C. O. In *The Aerodynamics of Heavy Vehicles III* (eds Dillmann, A. & Orellano, A.) 303–308 (Springer International Publishing, Cham, 2016). ISBN: 978-3-319-20121-4. doi:[10.1007/978-3-319-20122-1_19](https://doi.org/10.1007/978-3-319-20122-1_19) (cit. on p. 27).
 111. Felli, M., Camussi, R. & Di Felice, F. Mechanisms of evolution of the propeller wake in the transition and far fields. *Journal of Fluid Mechanics* **682**, 5–53. ISSN: 0022-1120. doi:[10.1017/jfm.2011.150](https://doi.org/10.1017/jfm.2011.150) (2011) (cit. on p. 28).
 112. Astolfi, J.-A., Dorange, P., Billard, J.-Y. & Tomas, I. C. An Experimental Investigation of Cavitation Inception and Development on a Two-Dimensional Eppler Hydrofoil. *Journal of Fluids Engineering* **122**, 164–173. ISSN: 0098-2202. doi:[10.1115/1.483239](https://doi.org/10.1115/1.483239) (2000) (cit. on p. 28).
 113. Bahaj, A. S., Batten, W. & McCann, G. Experimental verifications of numerical predictions for the hydrodynamic performance of horizontal axis marine current turbines. *Renewable Energy* **32**, 2479–2490. ISSN: 09601481. doi:[10.1016/j.renene.2007.10.001](https://doi.org/10.1016/j.renene.2007.10.001) (2007) (cit. on p. 28).
 114. Bahaj, A. S., Molland, A. F., Chaplin, J. R. & Batten, W. Power and thrust measurements of marine current turbines under various hydrodynamic flow conditions in a cavitation tunnel and a towing tank. *Renewable Energy* **32**, 407–426. ISSN: 09601481. doi:[10.1016/j.renene.2006.01.012](https://doi.org/10.1016/j.renene.2006.01.012) (2007) (cit. on p. 28).
 115. Lust, E. E., Luznik, L., Flack, K. A., Walker, J. M. & van Benthem, M. C. The influence of surface gravity waves on marine current turbine performance. *International Journal of Marine Energy* **3-4**, 27–40. ISSN: 22141669. doi:[10.1016/j.ijome.2013.11.003](https://doi.org/10.1016/j.ijome.2013.11.003) (2013) (cit. on p. 28).
 116. Mycek, P., Gaurier, B., Germain, G., Pinon, G. & Rivoalen, E. Experimental study of the turbulence intensity effects on marine current turbines behaviour. Part I: One single turbine. *Renewable Energy* **66**, 729–746. ISSN: 09601481. doi:[10.1016/j.renene.2013.12.036](https://doi.org/10.1016/j.renene.2013.12.036) (2014) (cit. on p. 28).

117. Mycek, P., Gaurier, B., Germain, G., Pinon, G. & Rivoalen, E. Experimental study of the turbulence intensity effects on marine current turbines behaviour. Part II: Two interacting turbines. *Renewable Energy* **68**, 876–892. ISSN: 09601481. doi:[10.1016/j.renene.2013.12.048](https://doi.org/10.1016/j.renene.2013.12.048) (2014) (cit. on p. 28).
118. Doman, D. A., Murray, R. E., Pegg, M. J., Gracie, K., Johnstone, C. M. & Nevalainen, T. Tow-tank testing of a 1/20th scale horizontal axis tidal turbine with uncertainty analysis. *International Journal of Marine Energy* **11**, 105–119. ISSN: 22141669. doi:[10.1016/j.ijome.2015.06.003](https://doi.org/10.1016/j.ijome.2015.06.003) (2015) (cit. on p. 28).
119. Kolekar, N. & Banerjee, A. Performance characterization and placement of a marine hydrokinetic turbine in a tidal channel under boundary proximity and blockage effects. *Applied Energy* **148**, 121–133. ISSN: 03062619. doi:[10.1016/j.apenergy.2015.03.052](https://doi.org/10.1016/j.apenergy.2015.03.052) (2015) (cit. on p. 28).
120. Gaurier, B., Germain, G., Facq, J. V., Johnstone, C. M., Grant, A. D., Day, A. H., Nixon, E., Di Felice, F. & Costanzo, M. Tidal energy “Round Robin” tests comparisons between towing tank and circulating tank results. *International Journal of Marine Energy* **12**, 87–109. ISSN: 22141669. doi:[10.1016/j.ijome.2015.05.005](https://doi.org/10.1016/j.ijome.2015.05.005) (2015) (cit. on p. 28).
121. Rahimian, M., Walker, J. & Penesis, I. Performance of a horizontal axis marine current turbine—A comprehensive evaluation using experimental, numerical, and theoretical approaches. *Energy* **148**, 965–976. ISSN: 03605442. doi:[10.1016/j.energy.2018.02.007](https://doi.org/10.1016/j.energy.2018.02.007) (2018) (cit. on p. 28).
122. Alamian, R., Shafaghat, R., Amiri, H. A. & Shadloo, M. S. Experimental assessment of a 100 W prototype horizontal axis tidal turbine by towing tank tests. *Renewable Energy* **155**, 172–180. ISSN: 09601481. doi:[10.1016/j.renene.2020.03.139](https://doi.org/10.1016/j.renene.2020.03.139) (2020) (cit. on p. 28).
123. Barltrop, N., Varyani, K. S., Grant, A., Clelland, D. & Pham, X. Wave-current interactions in marine current turbines. *Proceedings of the Institution of Mechanical Engineers, Part M: Journal of Engineering for the Maritime Environment* **220**, 195–203. ISSN: 1475-0902. doi:[10.1243/14750902JEME45](https://doi.org/10.1243/14750902JEME45) (2006) (cit. on p. 28).
124. Milne, I. A., Day, A. H., Sharma, R. N. & Flay, R. Blade loads on tidal turbines in planar oscillatory flow. *Ocean Engineering* **60**, 163–174. ISSN: 00298018. doi:[10.1016/j.oceaneng.2012.12.027](https://doi.org/10.1016/j.oceaneng.2012.12.027) (2013) (cit. on p. 28).
125. Galloway, P. W., Myers, L. E. & Bahaj, A. S. Quantifying wave and yaw effects on a scale tidal stream turbine. *Renewable Energy* **63**, 297–307. ISSN: 09601481. doi:[10.1016/j.renene.2013.09.030](https://doi.org/10.1016/j.renene.2013.09.030) (2014) (cit. on p. 28).
126. Payne, G. S., Stallard, T., Martinez, R. & Bruce, T. Variation of loads on a three-bladed horizontal axis tidal turbine with frequency and blade position. *Journal of Fluids and Structures* **83**, 156–170. ISSN: 08899746. doi:[10.1016/j.jfluidstructs.2018.08.010](https://doi.org/10.1016/j.jfluidstructs.2018.08.010) (2018) (cit. on p. 28).
127. Draycott, S., Steynor, J., Nambiar, A., Sellar, B. & Venugopal, V. Experimental assessment of tidal turbine loading from irregular waves over a tidal cycle. *Journal of Ocean Engineering and Marine Energy* **5**, 173–187. ISSN: 2198-6444. doi:[10.1007/s40722-019-00136-9](https://doi.org/10.1007/s40722-019-00136-9) (2019) (cit. on p. 28).
128. Tucker Harvey, S., Chen, X., Rowe, D., Bhavsar, K., Allsop, T., Gilbert, J., Stallard, T., Vogel, C. & Willden, R. Tidal Turbine Benchmarking Exercise: Geometry Specification and Environmental Characterisation. *Proceedings of the 11th European Wave and Tidal Energy Conference 2021*. (2023) (2021) (cit. on pp. 28, 36).
129. Germain, G., Bahaj, A. S., Huxley-reynard, C. & Roberts, P. Facilities for marine current energy converter characterization. *7th European Wave and Tidal energy Conference* **7**. <https://archimer.ifremer.fr/doc/00023/13436/10444.pdf> (2023) (2007) (cit. on p. 28).

130. Maganga, F., Germain, G., King, J., Pinon, G. & Rivoalen, E. Experimental characterisation of flow effects on marine current turbine behaviour and on its wake properties. *IET Renewable Power Generation* **4**, 498. ISSN: 17521416. doi:[10.1049/iet-rpg.2009.0205](https://doi.org/10.1049/iet-rpg.2009.0205) (2010) (cit. on p. 28).
131. Tedds, S. C., Owen, I. & Poole, R. J. Near-wake characteristics of a model horizontal axis tidal stream turbine. *Renewable Energy* **63**, 222–235. ISSN: 09601481. doi:[10.1016/j.renene.2013.09.011](https://doi.org/10.1016/j.renene.2013.09.011) (2014) (cit. on p. 28).
132. Stallard, T., Feng, T. & Stansby, P. K. Experimental study of the mean wake of a tidal stream rotor in a shallow turbulent flow. *Journal of Fluids and Structures* **54**, 235–246. ISSN: 08899746. doi:[10.1016/j.jfluidstructs.2014.10.017](https://doi.org/10.1016/j.jfluidstructs.2014.10.017) (2015) (cit. on p. 28).
133. Morandi, B., Di Felice, F., Costanzo, M., Romano, G. P., Dhomé, D. & Allo, J. C. Experimental investigation of the near wake of a horizontal axis tidal current turbine. *International Journal of Marine Energy* **14**, 229–247. ISSN: 22141669. doi:[10.1016/j.ijome.2016.02.004](https://doi.org/10.1016/j.ijome.2016.02.004) (2016) (cit. on p. 28).
134. Molland, A. F., Bahaj, A. S., Chaplin, J. R. & Batten, W. M. J. Measurements and predictions of forces, pressures and cavitation on 2-D sections suitable for marine current turbines. *Proceedings of the Institution of Mechanical Engineers, Part M: Journal of Engineering for the Maritime Environment* **218**, 127–138. ISSN: 1475-0902. doi:[10.1243/1475090041651412](https://doi.org/10.1243/1475090041651412) (2004) (cit. on p. 28).
135. Grasso, F. Design and Optimization of Tidal Turbine Airfoil. *Journal of Aircraft* **49**, 636–643. ISSN: 0021-8669. doi:[10.2514/1.C031617](https://doi.org/10.2514/1.C031617) (2012) (cit. on p. 28).
136. Murray, R.: *Predicting Cavitation on Marine and Hydrokinetic Turbine Blades with AeroDyn V15.04* 2017. doi:[10.2172/1393384](https://doi.org/10.2172/1393384) (cit. on p. 28).
137. Zaresharif, M., Ravelet, F., Kinahan, D. J. & Delaure, Y. M. C. Cavitation control using passive flow control techniques. *Physics of Fluids* **33**, 121301. ISSN: 1070-6631. doi:[10.1063/5.0071781](https://doi.org/10.1063/5.0071781) (2021) (cit. on p. 28).
138. Payne, G. S., Stallard, T. & Martinez, R. Design and manufacture of a bed supported tidal turbine model for blade and shaft load measurement in turbulent flow and waves. *Renewable Energy* **107**, 312–326. ISSN: 09601481. doi:[10.1016/j.renene.2017.01.068](https://doi.org/10.1016/j.renene.2017.01.068) (2017) (cit. on pp. 28, 44, 49, 56, 57).
139. Pechlivanoglou, G., Fischer, J., Eisele, O., Vey, S., Nayeri, C. N. & Paschereit, C. O. Development of a medium scale research HAWT for inflow and aerodynamic research in the TU Berlin wind tunnel. *German Wind Energy Conference DEWEK 2015* (2015) (cit. on p. 30).
140. Günes, O.: Auslegung eines Rotorblattes mit Adaptive Camber Profile für die Versuchswindkraftanlage BeRT: Design of a Rotorblade with Adaptive Camber Airfoil for the Berlin Research Turbine. *Masterarbeit* (Technische Universität Darmstadt, Darmstadt, 2017). (2023) (cit. on p. 30).
141. Jahnke, A.: Analyse des Schwingungsverhaltens einer Forschungswindenergieanlage und Neuauslegung der Lagerung sowie des Antriebsstranges. *Masterarbeit* (Technische Universität Berlin, Berlin, 2018). (2023) (cit. on p. 30).
142. Bartholomay, S., Krumbein, S., Deichmann, V., Gentsch, M., Perez–Becker, S., Soto–Valle, R., Holst, D., Nayeri, C. N., Paschereit, C. O. & Oberleithner, K. Repetitive model predictive control for load alleviation on a research wind turbine using trailing edge flaps. *Wind Energy* **25**, 1290–1308. ISSN: 10954244. doi:[10.1002/we.2730](https://doi.org/10.1002/we.2730) (2022) (cit. on p. 30).
143. Bartholomay, S., Krumbein, S., Perez–Becker, S., Soto–Valle, R., Nayeri, C. N., Paschereit, C. O. & Oberleithner, K. Experimental assessment of a blended fatigue–extreme controller employing

- trailing edge flaps. *Wind Energy* **26**, 201–227. ISSN: 10954244. doi:10.1002/we.2795 (2023) (cit. on p. 30).
144. Verein Deutscher Ingenieure: *VDI 2221-1: Entwicklung technischer Produkte und Systeme - Modell der Produktentwicklung: Design of technical products and systems - Model of product design* Düsseldorf, 2019. <https://www.vdi.de/richtlinien/details/vdi-2221-blatt-1-entwicklung-technischer-produkte-und-systeme-modell-der-produktentwicklung> (2023) (cit. on pp. 31–33).
 145. Verein Deutscher Ingenieure: *VDI 2221-2: Entwicklung technischer Produkte und Systeme - Gestaltung individueller Produktentwicklungsprozesse: Design of technical products and systems - Configuration of individual product design processes* Düsseldorf, 2019. <https://www.vdi.de/richtlinien/details/vdi-2221-blatt-2-entwicklung-technischer-produkte-und-systeme-gestaltung-individueller-produktentwicklungsprozesse> (2023) (cit. on p. 31).
 146. Verein Deutscher Ingenieure: *VDI 2222-1: Konstruktionsmethodik - Methodisches Entwickeln von Lösungsprinzipien* Düsseldorf, 1997. <https://www.vdi.de/richtlinien/details/vdi-2222-blatt-1-konstruktionsmethodik-methodisches-entwickeln-von-loesungsprinzipien> (2023) (cit. on p. 32).
 147. Tu, J., Liu, C. & Yeoh, G. H. *Computational fluid dynamics: A practical approach* Third edition. ISBN: 978-0-08-101127-0. <http://www.sciencedirect.com/science/book/9780081011270> (Butterworth-Heinemann, Amsterdam, 2018) (cit. on p. 32).
 148. Eppler, R. & Shen, Y. T. Wing Sections for Hydrofoils—Part 1: Symmetrical Profiles. *Journal of Ship Research* **23**, 209–217. ISSN: 0022-4502. doi:10.5957/jsr.1979.23.3.209 (1979) (cit. on pp. 34, 38).
 149. Shen, Y. T. & Eppler, R. Wing Sections for Hydrofoils—Part 2: Nonsymmetrical Profiles. *Journal of Ship Research* **25**, 191–200. ISSN: 0022-4502. doi:10.5957/jsr.1981.25.3.191 (1981) (cit. on pp. 34, 38).
 150. Aoki, K., Miyata, H., Kanai, M., Hanaoka, Y. & Zhu, M. A Water-Basin Test Technique for the Aerodynamic Design of Road Vehicles. *SAE Technical Paper Series* (SAE International 400 Commonwealth Drive, Warrendale, PA, United States, 1992). doi:10.4271/920348 (cit. on p. 35).
 151. Brontejn, I. N., Semendjaev, K. A., Musiol, G. & Mühlig, H. *Taschenbuch der Mathematik* 10. Auflage. ISBN: 9783808557907 (Verlag Europa-Lehrmittel, Haan, 2016) (cit. on p. 41).
 152. Wittel, H., Spura, C. & Jannasch, D. *Roloff/Matek Maschinenelemente* 25. Auflage. ISBN: 9783658341596 (Springer Vieweg, Wiesbaden, 2021) (cit. on p. 43).
 153. Cormier, M., Bühler, M., Mauz, M., Lutz, T., Bange, J. & Krämer, E. CFD Prediction of Tip Vortex Aging in the Wake of a Multi-MW Wind Turbine. *Journal of Physics: Conference Series* **1618**, 062029. ISSN: 1742-6588. doi:10.1088/1742-6596/1618/6/062029 (2020) (cit. on pp. 47–49).
 154. DIN Deutsches Institut für Normung e.V.: *DIN 743-1: Tragfähigkeitsberechnung von Wellen und Achsen: Teil 1: Grundlagen* Berlin, 2012. <https://www.beuth.de/en/standard/din-743-1/145165373> (2023) (cit. on p. 52).
 155. DIN Deutsches Institut für Normung e.V.: *DIN 743-2: Tragfähigkeitsberechnung von Wellen und Achsen: Teil 2: Formzahlen und Kerbwirkungszahlen* Berlin, 2012. <https://www.beuth.de/en/standard/din-743-2/145165516> (2023) (cit. on p. 52).
 156. DIN Deutsches Institut für Normung e.V.: *DIN 743-3: Tragfähigkeitsberechnung von Wellen und Achsen: Teil 3: Werkstoff-Festigkeitswerte* Berlin, 2012. <https://www.beuth.de/en/standard/din-743-3/145165619> (2023) (cit. on p. 52).

157. DIN Deutsches Institut für Normung e.V.: *DIN 743-4: Tragfähigkeitsberechnung von Wellen und Achsen: Teil 4: Zeitfestigkeit, Dauerfestigkeit - Schädigungsäquivalente Spannungsamplitude* Berlin, 2012. <https://www.beuth.de/en/standard/din-743-4/145165733> (2023) (cit. on p. 52).
158. DIN Deutsches Institut für Normung e.V.: *DIN 743 Bbl 2: Tragfähigkeitsberechnung von Wellen und Achsen: Beiblatt 2: Anwendungsbeispiele zu Teil 4* Berlin, 2012. <https://www.beuth.de/en/standard/din-743-beiblatt-2/145487828> (2023) (cit. on p. 52).
159. DIN Deutsches Institut für Normung e.V.: *DIN EN 10305-1: Präzisionsstahlrohre - Technische Lieferbedingungen - Teil 1: Nahtlose kaltgezogene Rohre* Berlin, 2016. <https://www.beuth.de/de/norm/din-en-10305-1/251709111> (2023) (cit. on p. 56).
160. DIN Deutsches Institut für Normung e.V.: *DIN EN 10305-2: Präzisionsstahlrohre - Technische Lieferbedingungen - Teil 2: Geschweißte kaltgezogene Rohre* Berlin, 2016. <https://www.beuth.de/de/norm/din-en-10305-2/251709396> (2023) (cit. on p. 56).
161. DIN Deutsches Institut für Normung e.V.: *DIN EN 10305-3: Präzisionsstahlrohre - Technische Lieferbedingungen - Teil 3: Geschweißte massgewalzte Rohre* Berlin, 2022. <https://www.beuth.de/de/norm/din-en-10305-3/251709158> (2023) (cit. on p. 56).
162. DIN Deutsches Institut für Normung e.V.: *DIN ISO 3601-1: Fluidtechnik - O-Ringe - Teil 1: Durchmesser, Schnur Stärken, Toleranzen und Bezeichnung* Berlin, 2013. <https://www.beuth.de/de/norm-entwurf/din-iso-3601-1/356057550> (2023) (cit. on p. 57).
163. DIN Deutsches Institut für Normung e.V.: *DIN ISO 3601-2: Fluidtechnik - O-Ringe - Teil 2: Einbauräume für allgemeine Anwendungen* Berlin, 2010. <https://www.beuth.de/de/norm/din-iso-3601-2/127926330> (2023) (cit. on p. 57).
164. DIN Deutsches Institut für Normung e.V.: *DIN ISO 3601-3: Fluidtechnik - O-Ringe - Teil 3: Form- und Oberflächenabweichungen* Berlin, 2010. <https://www.beuth.de/de/norm/din-iso-3601-3/127926376> (2023) (cit. on p. 57).
165. DIN Deutsches Institut für Normung e.V.: *DIN ISO 3601-4: Fluidtechnik - O-Ringe - Teil 4: Stützringe* Berlin, 2010. <https://www.beuth.de/de/norm/din-iso-3601-4/127926408> (2023) (cit. on p. 57).

Nomenclature and Abbreviations

Roman

a	Axial induction factor
a^*	Tangential induction factor
C	Integration constant
c	Airfoil chord
D	Diameter, without subscript: turbine diameter
d	Airfoil thickness
E	YOUNG's modulus
f	Airfoil camber, Frequency
F_D	Drag force
F_L	Lift force
f_L	Lift force per unit width
F_N	Normal force
f_N	Normal force per unit width
F_T	Tangential force
f_T	Tangential force per unit width
g	Gravity
H	Depth
I	Cross-sectional moment of inertia
J	Moment of inertia
L	Length
m	Mass
$M_{b,e}$	Edgewise blade root bending moment
$M_{b,f}$	Flapwise blade root bending moment
N_b	Number of blades
$P(\vec{x},t)$	Instantaneous pressure field
q	Resulting absolute velocity
R	Radius, without subscript: turbine radius
r	Control variable in direction of \mathbf{e}_r
t	Time variable
T	Period
$\vec{u}(\vec{x},t)$ (e.g., $[u \ v \ w]_i(\vec{x},t)\mathbf{e}_i$)	Instantaneous velocity field fluctuations
$\vec{U}(\vec{x},t)$ (e.g., $[U \ V \ W]_i(\vec{x},t)\mathbf{e}_i$)	Instantaneous velocity field
w	Deflection
W	Width
\vec{x} (e.g., $[x \ y \ z]_i \mathbf{e}_i$)	Vectorial position in space

Greek

α	Angle of attack
β	Blade pitch angle

Δ	Trailing edge thickness, Difference
δ	Distance, Wavelength, Deflection
ε	Glide ratio
ϵ	Number of elements used for discretization
η	Natural profile coordinate in chord direction
η_{25}	Quarter chord location
Γ	Circulation
μ	Non-dimensional radius coordinate r/R
ν	Kinematic viscosity
φ	Inflow Angle
Φ	Velocity potential, i.e., $\vec{U}(\vec{x},t) = \nabla\Phi$
ψ	Factor of safety
ϱ	Mass density
ρ	Rotational angle of deflection
Σ	Normal stress
τ	Helix pitch
θ	Temperature
ϑ	Blade phase angle
ξ	Losses attributed to the extraction of wind power
ξ_P	PRANDTL's tip loss factor
ζ	Natural profile coordinate perpendicular to chord direction
Ω	Angular velocity

Coefficients

C_D	Drag coefficient
C_H	Depth coefficient
C_L	Lift coefficient
C_P	Power coefficient
C_p	Pressure coefficient
C_Q	Torque coefficient
C_T	Thrust coefficient
FOS	Factor of safety
λ	Tip speed ratio
λ_l	Local speed ratio
Re	REYNOLDS number
St	STROUHAL number

Letter-like symbols

\mathcal{D}	Diameter ratio
\mathbf{e}	Unit vector
\dot{m}	Mass flow rate in steady state flow
∇	Nabla operator
\mathcal{O}	Order of ...

$\partial\mathcal{A}$	Boundary of surface \mathcal{A}
∂	Used to emphasize partial derivatives or the boundary of a surface or body
\mathcal{P}	Power, without subscript: aerodynamic turbine power
\mathcal{Q}	Rotor torque, without subscript: aerodynamic turbine torque
\mathcal{T}	Thrust, without subscript: aerodynamic turbine thrust
\mathbb{T}	Stress tensor
\mathcal{U}	Inflow velocity ratio
\mathcal{V}	Kinematic viscosity ratio

Subscript

at	Atmospheric
bs	Towing basin related
B	BETZ design approach
bl	Blade related
corr	Corresponding
c	Vortex core related
des	Design driving quantity typically chosen apriori
D	Drive train related
elem	Elements in simulations
exp	Experimental
flow	Flow (e.g., water or wind) related
hel	Rotor tip vortex helix related
hub	Rotor hub related
i	Running index/variable
j	Running index/variable
M	Model-world quantity, i.e., experiment-scale quantity
max	Maximum derived e.g., by means of maximum search
min	Minimum
nac	Nacelle related
R	Real-world quantity, i.e., full-scale quantity
res	Resulting quantity (e.g., resulting force)
root	Blade root related
rot	Rotation related quantity (rotational period, rotational frequency, ...)
S	SCHMITZ design approach
tip	Blade tip related
to	Tow carriage related
T	Tower related
trans	Transversal
tr	Trim tank related
ttt	Tip-to-tower
turb	Turbine related
v	Vapor
vM	VON-MISES stress

wake Wake related

Superscript

$ \cdot $	Absolute of vector quantity
$\overline{(\cdot)}$	Suitably averaged quantity
pr	Apriori defined quantity or range
$\prime(\cdot) := \partial/\partial\vec{x}(\cdot)$	Partial component-wise spatial derivative
*	Upper limit
$\dot{(\cdot)} := \partial/\partial t(\cdot)$	Partial time derivative

Acronyms

2D	two-dimensional
3D	three-dimensional
AEP	A nnual E nergy P roduction
AoA	A nge of A ttack
BEM	B lade E lement M omentum Theory
BeRT	B erlin R esearch T urbine
BOS	B alance O f S ystem
BRBM	B lade R oot B ending M oment
CFD	C omputational F luid M echanics
CNC	C omputerized N umerical C ontrol
DIN	D eutsches I nstitut für N ormung
EFD	E xperimental F luid M echanics
FEM	F inite E lement M ethod
FOS	F actor O f S afety
HAWT	H orizontal A xis W ind T urbine
IPCC	I ntergovernmental P anel on C limate C hange
LCOE	L evelized C ost O f E nergy
LDV	L aser D oppler V elocimetry
LE	L eading E dge
LSR	L ocal S peed R atio
MCT	M arine C urrent T urbine
NCF	N et C apacity F actor
OAM	O peration A nd M aintenance
OPR	O nce P er R evolution
PIV	P article I mage V elocimetry
PV	P hoto V oltaic
RMS	R oot M ean S quare
RPM	R evolutions P er M inute
SDG	S ustainable D evelopment G oals
TE	T railing E dge
TKE	T urbulent K inetic E nergy
TSR	T ip S peed R atio
UBeRT	U nderwater B erlin R esearch T urbine
VBA	V isual B asic for A pplications
VDI	V erband D eutscher I ngenieure
WE	W ind E nergy
WP	W ind P ark
WT	W ind T urbine

Appendix A

Data Sheets

A selection of data sheets of the test rig are attached here. The total costs of the test rig accumulate as of now to approximately 35000 €. Balanced are the drive train, the coupling, the slip ring, the BRBM sensors, the strain gauge amplifiers, material for the turbine, and an estimation of the costs for the tower.

K3D120 ±5kN/VA



Beschreibung

Der 3-Achs Kraftsensor K3D120 eignet sich für die Kraftmessung in drei zueinander senkrechten Achsen.

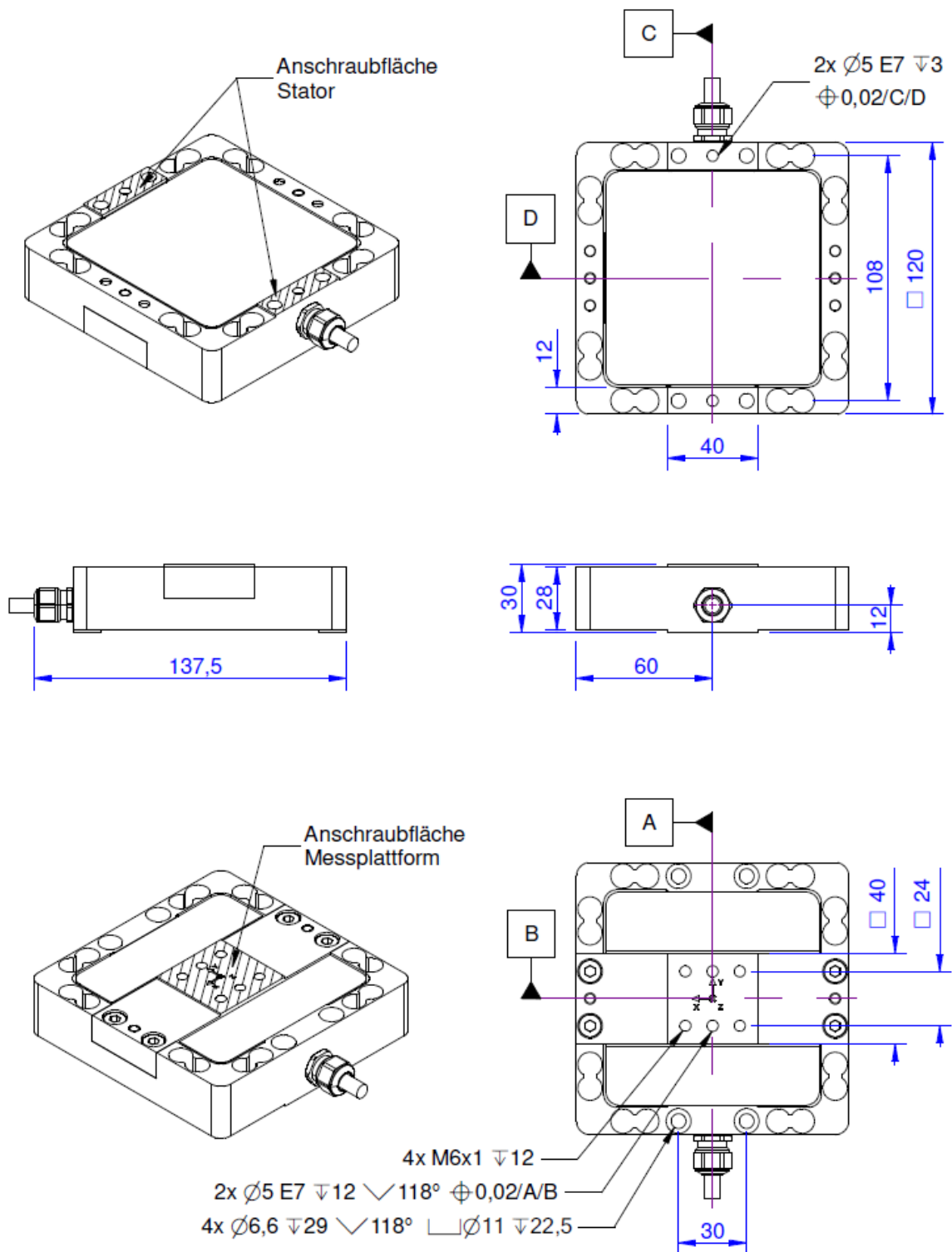
Er ist verfügbar für 50N bis 5kN in allen drei Achsen und kann optional in anderen Messbereichen gefertigt werden.

Bis zum Messbereich 1kN wird der Kraftsensor aus einer hochfesten Aluminium-Legierung gefertigt. Ab 1kN ist der Kraftsensor aus Edelstahl 1.4542 gefertigt (Option "VA").

Der 3-Achs Kraftsensor zeichnet sich durch eine besonders kompakte Bauform mit einer Grundfläche von 120mm x 120mm und einer geringen Gesamthöhe von nur 30mm aus.

Einsatzgebiete sind zum Beispiel die Kraftmessung bei Fertigungsprozessen, Kraftregelung bei Handhabungsmaschinen, Kraftmessung bei Montageprozessen, dreidimensionale Lastmessung, Messung von Reibkräften.

Abmessungen





Technische Daten

Kraftsensor

Typ	3-Achsen Kraftsensor
Kraftrichtung	Zug / Druck
Nennkraft F _x	5 kN
Nennkraft F _y	5 kN
Nennkraft F _z	5 kN
Krafteinleitung	Innengewinde
Abmessung 1	4xM6
Sensor Befestigung	Durchgangsbohrung
Abmessung 2	4xØ6,6
Gebrauchskraft	150 %FS
Nennmessweg	0.06 mm
Material	Edelstahl
Eigenfrequenz	6 kHz
Höhe	30 mm
Länge oder Durchmesser	120 mm
Grenzdrehmoment	300 Nm
Grenzbiegemoment	300 Nm

Genauigkeitsdaten

Genauigkeitsklasse	0,5%
relative Linearitätsabweichung	0.2 %FS
Temperatureinfluss auf das Nullsignal	0.02 %FS/K
Temperatureinfluss auf den Kennwert	0.01 %RD/K
relatives Kriechen	0.1 %FS

Anschlussdaten

Anschlusstyp	12-Leiter offen
Anschlussbezeichnung	Unitronic FD CP (TP) Plus 6 x 2 x 0,14
Kabellänge	3 m

Exzentrizität und Übersprechen

Zulässige Exzentrizität der Krafteinleitung	100 Nm
Einfluss exzentrischer Krafteinleitung auf FS	1 %FS / 100Nm
Übersprechen von x auf y bei Nennlast	1 %FS
Übersprechen von y auf x bei Nennlast	1 %FS
Übersprechen von z auf x/y bei Nennlast	1 %FS
Übersprechen von x/y auf z bei Nennlast	2

Umweltdaten

Nenntemperaturbereich	-10 ... 70 °C
Gebrauchstemperaturbereich	-10 ... 85 °C
Lagertemperaturbereich	-10 ... 85 °C
Schutzart	IP67

Elektrische Daten

Nennkennwert x-Achse	1 mV/V
Nennkennwert y-Achse	1 mV/V
Nennkennwert z-Achse	1 mV/V
Nullsignal	0.05 mV/V
Nennbereich der Speisespannung	2.5 ... 5 V
Gebrauchsbereich der Speisespannung	1 ... 10 V
Eingangswiderstand x-Achse	740 Ohm
Ausgangswiderstand x-Achse	700 Ohm
Eingangswiderstand y-Achse	740 Ohm
Ausgangswiderstand y-Achse	700 Ohm
Eingangswiderstand z-Achse	740 Ohm
Ausgangswiderstand z-Achse	700 Ohm
Isolationswiderstand	5 GOhm
Toleranz Eingangswiderstand	10 Ohm
Toleranz Ausgangswiderstand	5 Ohm

Abkürzungen: RD: Istwert („Reading“); FS: Endwert („Full Scale“);
1) 0,5mV/V bis 50N; 1mV/V ab 100N.
Der exakte Kennwert wird im Prüfprotokoll ausgewiesen.






Anschlussbelegung

Kanal	Abkürzung	Bezeichnung	Aderfarbe	PIN
X-Achse	+Us	Sensorspeisung	braun	2
	-Us	Sensorspeisung	weiß	1
	+Ud	Brückenausgang	grün	3
	-Ud	Brückenausgang	gelb	4
Y-Achse	+Us	Sensorspeisung	rosa	6
	-Us	Sensorspeisung	grau	5
	+Ud	Brückenausgang	blau	7
	-Ud	Brückenausgang	rot	8
Z-Achse	+Us	Sensorspeisung	violett	10
	-Us	Sensorspeisung	schwarz	9
	+Ud	Brückenausgang	grau / rosa	11
	-Ud	Brückenausgang	rot / blau	12

Druckbelastung: positives Ausgangssignal.

Schirm - transparent.

Zubehör

	Bezeichnung	Beschreibung
	GSV-1A4 SubD37/2	4-Kanal DMS Messverstärker für Sensoren mit Dehnungsmessstreifen. Adaptierung des Sensors über <u>Sub-D-37 Stecker</u> . Ausgang $\pm 10V$ und $4 \dots 20mA$ über 15polige SUB-D (female); Eingangsempfindlichkeit $2mV/V$;
	Configuration SubD37/m	Konfektionieren des Steckers an Sensorkabel; Steckverbinder Typ SubD, 37 polig, Stifte (male), mit Haube;
	GSV-4USB SubD37	4-Kanal DMS Messverstärker mit USB-Port mit konfigurierbarem Eingang für Dehnungsmessstreifen, Temperatursensoren, aktive Sensoren, Wegsensoren und andere Sensoren. Sensoranschluss über <u>1 Stück Sub D37</u> Steckverbinder
	High Accuracy Calibration/3D	Erhöhung der Genauigkeitsklasse bis zu $0,1\%$; inklusive 5-Punkt Werkskalibrierschein und Nachweis der Rückführbarkeit auf DAkkS Kraftmessnormaleinrichtung
	Werkskalibrierschein kN/20/5/K3D	Werkskalibrierschein für Kraft bis 20 kN nach DIN EN ISO/IEC 17025 für die Prüfmittelüberwachung nach DIN ISO 9001:2008 mit 5 Laststufen und 3 Messreihen.

Angebot

Angebots-Nr.: 419640036D
vom: 04.11.2022
Kunden-Nr.: 16096384
Tel.: 015144632164

Seite 1 / 12

SEW-EURODRIVE, Postfach 3023, 76642 Bruchsal
 Technische Universität Berlin
 Experimentelle Strömungsmechanik
 Herrn Sascha Krumbein
 Charlottenburg
 Müller-Breslau-Str. 8
 10623 Berlin

Ihr(e) Ansprechpartner
Frau Schacha
 DC Berlin (Service)
 Tel. 030 6331131 - 54
 tina.schacha@sew-eurodrive.de

Ihr Technisches Büro
DC Berlin
 Tel. 030 6331131 - 30 Fax 030 6331131 - 36
 dc-berlin@sew-eurodrive.de

Ihre Anfrage: per e-Mail v. 04.07.2022
 Turbinenprüfstand
Anfrage vom: 04.11.2022

Sehr geehrter Herr Krumbein,

vielen Dank für Ihr Interesse an unserem Produktportfolio. Gemäß Ihrer Anfrage erhalten Sie heute Ihr individuelles Angebot:

Die derzeitige unklare Versorgungslage macht verbindliche Liefertermin-Aussagen schwierig. Wir bemühen uns dennoch, Ihrem Lieferterminwunsch soweit als möglich nachzukommen. Allerdings bitten wir um Ihr Verständnis, dass jede Lieferterminangabe vorbehaltlich unserer eigenen richtigen und rechtzeitigen Selbstbelieferung erfolgt.

 Angebotsversion D (04.11.22, TS): gemäß Telefonat mit Hr. Krumbein vom 03.11.2022
 Entfernung Pos. 2, 4

 Angebotsversion C (20.10.22, TS): Auftragsrabatt und Fracht und Verpackung frei

 Angebotsversion B (17.10.22, TS): gemäß Email von Hr. Krumbein
 Anpassung Kabellängen, Preisanpassung, Pos. 9 entfällt (Alternative)

 Angebotsversion A (19.08.22, DM):
 Neuprojektierung aufgrund längerer Pausenzeiten, Servogetriebemotor optional mit PxG-
 Getriebe; gem. Telefonat H. Krumbein v. 18.08.22,

Pos	Menge	Bezeichnung Sachnummer Ihre Materialnummer:	Stückpreis netto EUR	Gesamtpreis netto EUR
01	1 ST	Servo-Planetengetriebemotor PSF522 CMPZ71M/BY/PK/AK1H/SB1	2.916,77	2.916,77
02	1 ST	Konfektioniertes Kabel Cable 13354280 / 10.0	169,00	169,00
03	1 ST	Konfektioniertes Kabel Cable 13324535 / 10.0	106,14	106,14
04	1 ST	Umrichter / Optionen / Zubehör MDX61B0110-5A3-4-00/L/DEH11B/DFE33B	3.586,43	3.586,43

Hauptverwaltung / Headquarters

SEW-EURODRIVE GmbH & Co KG
 Ernst-Blickle-Straße 42
 76646 Bruchsal · Germany

www.sew-eurodrive.de
 sew@sew-eurodrive.de

Bankverbindungen / Bank accounts

Deutsche Bank AG IBAN DE61660700040200425700 BIC DEUTDE33
 Commerzbank Bruchsal IBAN DE22663400180470888900 BIC COBADE33
 LBBW IBAN DE21600501010008628604 BIC SOLADE33
 Sparkasse Kraichgau IBAN DE85663500360000020313 BIC BRUSDE33

USt.-Ident.-Nr. / VAT Regist. No. DE 143080517

Kommanditgesellschaft, Sitz: Bruchsal, RG Mannheim HRA 230970
 Komplementärin: SEW-EURODRIVE Verwaltungs-GmbH
 Sitz: Bruchsal, RG Mannheim HRB 230207
 Geschäftsführender Gesellschafter: Jürgen Blickle
 Geschäftsführung: Jürgen Blickle (Vorsitzender), Udo Aull, Dr. Jörg Hermes,
 Dr. Hans Krattenmacher, Christian Mayer, Johann Soder, Dr. Jürgen Zanghellini

Telefon 07251 75-0
 Telefax 07251 75-1970

Angebot

Angebots-Nr.: **419640036D**

vom: 04.11.2022

2 / 12

Pos	Menge	Bezeichnung Sachnummer Ihre Materialnummer:	Stückpreis netto EUR	Gesamtpreis netto EUR
		inklusive: BW347-T, DBG60B-10, USM21A.		
05	1 ST	Netzfilter NF035-503 8271283	250,64	250,64
06	1 ST	Netzdrossel ND030-023 8271518	85,73	85,73
		Auftragsrabatt -3,00 % von 2.916,77		-87,50
		Auftragsrabatt -3,00 % von 169,00		-5,07
		Auftragsrabatt -3,00 % von 106,14		-3,18
		Auftragsrabatt -3,00 % von 3.586,43		-107,59
		Auftragsrabatt -3,00 % von 250,64		-7,52
		Auftragsrabatt -3,00 % von 85,73		-2,57
Gesamtwert o. MWST EUR				6.901,28

Dieses Angebot ist freibleibend und erfolgt im Falle eines Komponentenverkaufs zu unseren Verkaufs- und Lieferbedingungen Fassung von 2022 sowie im Falle der Beauftragung von Service-Leistungen zu unseren Service-Bedingungen, Fassung 2014, beide zu finden unter:

https://www.sew-eurodrive.de/meta-seiten/allgemeine_geschaeftsbedingungen_agb.html

Die nachfolgenden aufgeführten technischen Daten und Beschreibungen kennzeichnen allein die vertraglich vereinbarte Beschaffenheit der zu liefernden Produkte und Dienstleistungen.

Die offerierten Konditionen und Preise sind exklusiv für Sie bestimmt. Eine Weitergabe an Dritte ist nicht erlaubt.

Detaillierte Informationen zu den Positionen und zur Auftragsabwicklung entnehmen Sie bitte den folgenden Seiten.

Zahlungsbedingung: innerhalb von 14 Tagen 2 % Skonto
innerhalb von 30 Tagen ohne Abzug

Lieferbedingung: DAP Empfangsort "Incoterms 2020"

Versandstelle: SEW-EURODRIVE - Werk Graben, Ernst-Blickle-Straße 1, 76676 Graben-Neudorf



Weitere Services

[24/7: Beratung, Lieferung, Ersatzteile, Antriebstechnik und Reparatur](#)

[Plus 12 Monate Gewährleistung für 100% Sicherheit!](#)

Hauptverwaltung / Headquarters

SEW-EURODRIVE GmbH & Co KG
Ernst-Blickle-Straße 42
76646 Bruchsal · Germany

Postadresse / Postal address
SEW-EURODRIVE GmbH & Co KG
76642 Bruchsal · Germany

Telefon 07251 75-0
Telefax 07251 75-1970

www.sew-eurodrive.de
sew@sew-eurodrive.de

Bankverbindungen / Bank accounts

Deutsche Bank AG IBAN DE61660700040200425700 BIC DEUTDE33
Commerzbank Bruchsal IBAN DE22663400180470888900 BIC COBADE33
LBBW IBAN DE21600501010008628604 BIC SOLADE33
Sparkasse Kraichgau IBAN DE85663500360000020313 BIC BRUSDE33

USt.-Ident.-Nr. / VAT Regist. No. DE 143080517

Kommanditgesellschaft, Sitz: Bruchsal, RG Mannheim HRA 230970
Komplementärin: SEW-EURODRIVE Verwaltungs-GmbH
Sitz: Bruchsal, RG Mannheim HRB 230207
Geschäftsführender Gesellschafter: Jürgen Blickle
Geschäftsführung: Jürgen Blickle (Vorsitzender), Udo Aull, Dr. Jörg Hermes,
Dr. Hans Krattenmacher, Christian Mayer, Johann Soder, Dr. Jürgen Zanghellini

Angebot

Angebots-Nr.: **419640036D**

vom: 04.11.2022

Seite 3 / 12

Pos	Menge	Sachnummer	Stückpreis EUR	Gesamtpreis EUR
01	Ihre Projektreferenz:	UBeRT Projekt		
	1 ST		netto 2.916,77	2.916,77
	Servo-Planetengetriebemotor PSF522 CMPZ71M/BY/PK/AK1H/SB1			



Hinweis:

Farbe und technische Ausführung können von diesem Bild abweichen. Die technische Ausführung entnehmen Sie den nachfolgenden Daten.

Möchten Sie gleich bestellen?



Links zu den Dokumenten:



Benötigen Sie Unterstützung?



Drehzahl [r/min]	: 4500 / 375
Übersetzung gesamt [i]	: 12,00 / endlich
Zähnezah Zähler / Nenner	: 12/1
Sonderübersetzung	: Ja
Bauform IM	: M0, Universalbauform
Lage Klemmen. [°]/Kabeleingf.	: 270 / Lage ausrichtbar
Schmierstoff / -menge [l]	: CLP PG 220 Synth.Öl / PSS / 0,380
Öl-Herstellerbezeichnung	: SEW GearOil Poly 220 E1
Antriebsdrehzahl nepk [1/min]	: 7000
Abtriebsdrehzahl na_pk [1/min]	: 583,00
Abtriebsdrehmoment Mapk [Nm]	: 280

Hauptverwaltung / Headquarters

SEW-EURODRIVE GmbH & Co KG
Ernst-Blickle-Straße 42
76646 Bruchsal · Germany

Postadresse / Postal address
SEW-EURODRIVE GmbH & Co KG
76642 Bruchsal · Germany

Telefon 07251 75-0
Telefax 07251 75-1970

www.sew-eurodrive.de
sew@sew-eurodrive.de

Bankverbindungen / Bank accounts

Deutsche Bank AG IBAN DE61660700040200425700 BIC DEUTDE33
Commerzbank Bruchsal IBAN DE22663400180470888900 BIC COBADE33
LBBW IBAN DE21600501010008628604 BIC SOLADE33
Sparkasse Kraichgau IBAN DE85663500360000020313 BIC BRUSDE33

USt.-Ident.-Nr. / VAT Regist. No. DE 143080517

Kommanditgesellschaft, Sitz: Bruchsal, RG Mannheim HRA 230970
Komplementärin: SEW-EURODRIVE Verwaltungs-GmbH
Sitz: Bruchsal, RG Mannheim HRB 230207
Geschäftsführender Gesellschafter: Jürgen Blickle
Geschäftsführung: Jürgen Blickle (Vorsitzender), Udo Aull, Dr. Jörg Hermes,
Dr. Hans Krattenmacher, Christian Mayer, Johann Soder, Dr. Jürgen Zanghellini

Angebot

Angebots-Nr.: **419640036D**

vom: 04.11.2022

Seite 4 / 12

Pos	Menge	Sachnummer	Stückpreis EUR	Gesamtpreis EUR
		Korrosionsschutz	: Ja	
		Oberflächenschutz	: OS1, nach techn.Datenblatt 01802__94	
		Farbanstrich	: Deckanstrich RAL9005-Tiefschwarz	
		Getriebe	: PSF522	
		Abtriebswellenende	: 32x58mm lg.	
		Abtr.Wellen Ausführung	: ohne Passfedernut / ohne Passfeder	
		Ausführungsart	: Flanschausführung	
		Flansch	: Zentrierrand 90mm, Lochkreis Durchgangs- löcher 120mm	
		WDR-Abtrieb Werkstoff	: FKM	
		Verdrehspiel PHI [°]	: 8 Winkelminuten	
		Dokumentation Nr. A	: 20050933	
		Einzelteilliste	: 572620303	
		Motor	: CMPZ71M/BY/PK/AK1H/SB1	
		Motor-WDR-Abtrieb Werkstoff	: Premium Sine Seal - FKM	
		Bemessungsdrehzahl nN [1/min]	: 4500	
		Stillstands Drehmoment M0 [Nm]	: 9,40	
		Max. Grenzmoment Mpk [Nm]	: 30,80	
		Stillstandsstrom I0 [A]	: 10,90	
		Max. zulässiger Strom I _{max} [A]	: 57,00	
		Einschaltdauer S1-S10	: S1	
		Motor-Spannung [V]	: 400	
		Max. zulässige Frequenz [Hz]	: 375	
		Schaltbild-Nr.	: 080870805	
		Wärmeklasse/Schutzart[IP]	: F / 66	
		Zus. Allgemein	: SB1 Steckverbinder	
		Zus. Bremse / Handlüftung	: BY / ohne	
		Bremsspannung [V]/-moment [Nm]	: 400 AC / 10	
		Bremsen-Haltestrom AC [A]	: 0.087	
		Brems-Gleichrichter	: BMKB1.5	
		Temperaturrefassung	: PK = 1x PT1000 Temperatursensor	
		Zus. Geber	: AK1H Hiperface Geber Multi-Turn, Achtung: digitaler Wert der Absolutposition nur bis max. 6.000 rpm gültig. Sin/Cos Signale bis max. 12.000 rpm gültig.	
		Elektro. Typenschild Variante	: ET1000 ETS HIPERFACE®	
		Fertigungsvorschrift Nr.	: 081440706	
			Synchrone Servomotoren CM/CMP in IP56/66	
		Dokumentation Nr. A	: 21923574	
			: 26854694	
		Einzelteilliste	: 084812008 / 096970611	
		Typenschild	: Deutsch	
		Betriebsanl. A Sprache/Anz.	: Deutsch / 0	
		Einzelteilliste/Sprache/Anzahl	: Deutsch / 0	

Hauptverwaltung / Headquarters

SEW-EURODRIVE GmbH & Co KG Postadresse / Postal address
Ernst-Blickle-Straße 42 SEW-EURODRIVE GmbH & Co KG
76646 Bruchsal · Germany 76642 Bruchsal · Germany

Telefon 07251 75-0
Telefax 07251 75-1970

www.sew-eurodrive.de
sew@sew-eurodrive.de

Bankverbindungen / Bank accounts

Deutsche Bank AG IBAN DE61660700040200425700 BIC DEUTDE33
Commerzbank Bruchsal IBAN DE22663400180470888900 BIC COBADE33
LBBW IBAN DE21600501010008628604 BIC SOLADE33
Sparkasse Kraichgau IBAN DE85663500360000020313 BIC BRUSDE33

USt.-Ident.-Nr. / VAT Regist. No. DE 143080517

Kommanditgesellschaft, Sitz: Bruchsal, RG Mannheim HRA 230970
Komplementärin: SEW-EURODRIVE Verwaltungs-GmbH
Sitz: Bruchsal, RG Mannheim HRB 230207
Geschäftsführender Gesellschafter: Jürgen Blickle
Geschäftsführung: Jürgen Blickle (Vorsitzender), Udo Aull, Dr. Jörg Hermes,
Dr. Hans Krattenmacher, Christian Mayer, Johann Soder, Dr. Jürgen Zanghellini

Angebot

**Angebots-Nr.: 419640036D**

vom: 04.11.2022

Seite 5 / 12

Pos	Menge	Sachnummer	Stückpreis EUR	Gesamtpreis EUR
		Statistische Warennummer : 85015220		
		Nettogewicht [KG] : ca. 23/ST 23/Pos.		
		Lieferzeit: Lieferdatum wird bei Bestellung ermittelt		

Übertrag EUR**2.916,77****Hauptverwaltung / Headquarters**

SEW-EURODRIVE GmbH & Co KG Postadresse / Postal address
Ernst-Blickle-Straße 42 SEW-EURODRIVE GmbH & Co KG
76646 Bruchsal · Germany 76642 Bruchsal · Germany

Telefon 07251 75-0
Telefax 07251 75-1970

www.sew-eurodrive.de
sew@sew-eurodrive.de

Bankverbindungen / Bank accounts

Deutsche Bank AG IBAN DE61660700040200425700 BIC DEUTDE33
Commerzbank Bruchsal IBAN DE22663400180470888900 BIC COBADE33
LBBW IBAN DE21600501010008628604 BIC SOLADE33
Sparkasse Kraichgau IBAN DE85663500360000020313 BIC BRUSDE33

USt.-Ident.-Nr. / VAT Regist. No. DE 143080517

Kommanditgesellschaft, Sitz: Bruchsal, RG Mannheim HRA 230970
Komplementärin: SEW-EURODRIVE Verwaltungs-GmbH
Sitz: Bruchsal, RG Mannheim HRB 230207
Geschäftsführender Gesellschafter: Jürgen Blickle
Geschäftsführung: Jürgen Blickle (Vorsitzender), Udo Aull, Dr. Jörg Hermes,
Dr. Hans Krattenmacher, Christian Mayer, Johann Soder, Dr. Jürgen Zanghellini

Angebot

Angebots-Nr.: **419640036D**

vom: 04.11.2022

Seite 6 / 12

Pos	Menge	Sachnummer	Stückpreis EUR	Gesamtpreis EUR
02	Ihre Projektreferenz:	UBeRT Projekt		
	1 ST		netto 169,00	169,00
	Konfektioniertes Kabel Cable 13354280 / 10.0			

Hinweis:

Zur folgenden Position konnte kein Produktbild generiert werden.

Möchten Sie gleich bestellen?



Links zu den Dokumenten:



Benötigen Sie Unterstützung?



Benennung Kabel	:	Bremsmotorkabel mit 2 Stecker; SB12/Phoenix
Länge [m]	:	10,00
Produktfamilie	:	Bremsmotorenkabel; Bremse BY
Querschnitt	:	(4x2,5+(3x1))mm ²
Verlegung	:	feste Verlegung
Konfektionierung A-Seite	:	Steckverbinder SB12; Buchsenkontakte
Konfektionierung B-Seite	:	offen, (4x2,5+(3x1)), 3 pol. Stecker für Bremsenansteuerung, Kabelschuhe M6 im Zubehörbeutel
Umgebungstemperatur min [°C]	:	-20
Umgebungstemperatur max [°C]	:	+80
Mindestbiegeradius [mm]	:	68,00
Außendurchmesser Rohkabel [mm]	:	13,40
Mantelwerkstoff Rohkabel	:	PVC
Max. Spannung Leistgskabel [V]	:	500
Statistische Warennummer	:	85444290
Nettogewicht [KG]	:	ca. 3,2/ST 3,2/Pos.
Lieferzeit:	:	Lieferdatum wird bei Bestellung ermittelt

Übertrag EUR
3.085,77

Hauptverwaltung / Headquarters

SEW-EURODRIVE GmbH & Co KG Postadresse / Postal address
Ernst-Blickle-Straße 42 SEW-EURODRIVE GmbH & Co KG
76646 Bruchsal · Germany 76642 Bruchsal · Germany

Telefon 07251 75-0
Telefax 07251 75-1970

www.sew-eurodrive.de
sew@sew-eurodrive.de

Bankverbindungen / Bank accounts

Deutsche Bank AG IBAN DE61660700040200425700 BIC DEUTDE33
Commerzbank Bruchsal IBAN DE22663400180470888900 BIC COBADE33
LBBW IBAN DE21600501010008628604 BIC SOLADE33
Sparkasse Kraichgau IBAN DE85663500360000020313 BIC BRUSDE33

USt.-Ident.-Nr. / VAT Regist. No. DE 143080517

Kommanditgesellschaft, Sitz: Bruchsal, RG Mannheim HRA 230970
Komplementärin: SEW-EURODRIVE Verwaltungs-GmbH
Sitz: Bruchsal, RG Mannheim HRB 230207
Geschäftsführender Gesellschafter: Jürgen Blickle
Geschäftsführung: Jürgen Blickle (Vorsitzender), Udo Aull, Dr. Jörg Hermes,
Dr. Hans Krattenmacher, Christian Mayer, Johann Soder, Dr. Jürgen Zanghellini

Angebot

Angebots-Nr.: **419640036D**

vom: 04.11.2022

Seite 7 / 12

Pos	Menge	Sachnummer	Stückpreis EUR	Gesamtpreis EUR
03	Ihre Projektreferenz:	UBeRT Projekt		
	1 ST		netto 106,14	106,14
	Konfektioniertes Kabel			
	Cable 13324535 / 10.0			

Hinweis:

Zur folgenden Position konnte kein Produktbild generiert werden.

Möchten Sie gleich bestellen?



Links zu den Dokumenten:



Benötigen Sie Unterstützung?



Benennung Kabel	: Geb.Kab.m.2 St. MDX-B
Länge [m]	: 10,00
Produktfamilie	: Geberkabel
Querschnitt	: (4x2x0,25+2x0,5) mm ²
Verlegung	: feste Verlegung
Konfektionierung A-Seite	: Rundstecker 12-polig Buchsenkontakte - ASTA
Konfektionierung B-Seite	: SUB-D Stecker 15-polig; Stiftkontakt abgewinkelt
Umgebungstemperatur min [°C]	: -20
Umgebungstemperatur max [°C]	: +80
Mindestbiegeradius [mm]	: 53,00
Außendurchmesser Rohkabel [mm]	: 8,80
Mantelwerkstoff Rohkabel	: PVC
Betriebsspannung Rohkabel [V]	: 300

Statistische Warennummer : 85444290

Nettogewicht [KG] : ca. 1,2/ST 1,2/Pos.

Lieferzeit: Lieferdatum wird bei Bestellung ermittelt

Übertrag EUR

3.191,91

Hauptverwaltung / Headquarters

SEW-EURODRIVE GmbH & Co KG Postadresse / Postal address
Ernst-Blickle-Straße 42 SEW-EURODRIVE GmbH & Co KG
76646 Bruchsal · Germany 76642 Bruchsal · Germany

Telefon 07251 75-0
Telefax 07251 75-1970

www.sew-eurodrive.de
sew@sew-eurodrive.de

Bankverbindungen / Bank accounts

Deutsche Bank AG IBAN DE61660700040200425700 BIC DEUTDE33
Commerzbank Bruchsal IBAN DE22663400180470888900 BIC COBADE33
LBBW IBAN DE21600501010008628604 BIC SOLADE33
Sparkasse Kraichgau IBAN DE85663500360000020313 BIC BRUSDE33

USt.-Ident.-Nr. / VAT Regist. No. DE 143080517

Kommanditgesellschaft, Sitz: Bruchsal, RG Mannheim HRA 230970
Komplementärin: SEW-EURODRIVE Verwaltungs-GmbH
Sitz: Bruchsal, RG Mannheim HRB 230207
Geschäftsführender Gesellschafter: Jürgen Blickle
Geschäftsführung: Jürgen Blickle (Vorsitzender), Udo Aull, Dr. Jörg Hermes,
Dr. Hans Krattenmacher, Christian Mayer, Johann Soder, Dr. Jürgen Zanghellini

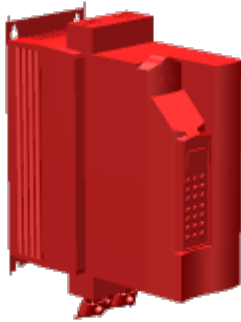
Angebot

Angebots-Nr.: **419640036D**

vom: 04.11.2022

Seite 8 / 12

Pos	Menge	Sachnummer	Stückpreis EUR	Gesamtpreis EUR
04	Ihre Projektreferenz:	UBeRT Projekt		
	1 ST		2.532,52	2.532,52
	Umrichter / Optionen / Zubehör			
	MDX61B0110-5A3-4-00/L/DEH11B/DFE33B			



Hinweis:

Farbe und technische Ausführung können von diesem Bild abweichen. Die technische Ausführung entnehmen Sie den nachfolgenden Daten.

Möchten Sie gleich bestellen?



Links zu den Dokumenten:



Benötigen Sie Unterstützung?



Sachnummer	: 18400191
Baugröße	: 2
Geräteausführung	: Standardausführung
Lackierte Ausführung	: x
Integrierter Netzfilter	: Kategorie C2
Netzennspannung [V]	: 3x380-500 +/- 10%
Netzennstrom [A]	: 21.60
Netzennfrequenz [Hz]	: 50-60 +/- 5%
Ausgangsnennleistung [kW]	: 11,00
Ausgangsnennleistung [HP]	: 15,00
Ausgangsscheinleistung [kVA]	: 16.8

Hauptverwaltung / Headquarters

SEW-EURODRIVE GmbH & Co KG
Ernst-Blickle-Straße 42
76646 Bruchsal · Germany

Postadresse / Postal address
SEW-EURODRIVE GmbH & Co KG
76642 Bruchsal · Germany

Telefon 07251 75-0
Telefax 07251 75-1970

www.sew-eurodrive.de
sew@sew-eurodrive.de

Bankverbindungen / Bank accounts

Deutsche Bank AG IBAN DE61660700040200425700 BIC DEUTDE33
Commerzbank Bruchsal IBAN DE22663400180470888900 BIC COBADE33
LBBW IBAN DE21600501010008628604 BIC SOLADE33
Sparkasse Kraichgau IBAN DE85663500360000020313 BIC BRUSDE33

USt.-Ident.-Nr. / VAT Regist. No. DE 143080517

Kommanditgesellschaft, Sitz: Bruchsal, RG Mannheim HRA 230970
Komplementärin: SEW-EURODRIVE Verwaltungs-GmbH
Sitz: Bruchsal, RG Mannheim HRB 230207
Geschäftsführender Gesellschafter: Jürgen Blickle
Geschäftsführung: Jürgen Blickle (Vorsitzender), Udo Aull, Dr. Jörg Hermes,
Dr. Hans Krattenmacher, Christian Mayer, Johann Soder, Dr. Jürgen Zanghellini

Angebot

Angebots-Nr.: **419640036D**

vom: 04.11.2022

Seite 9 / 12

Pos	Menge	Sachnummer	Stückpreis EUR	Gesamtpreis EUR
		Leistungsverluste (90;100) [%]	: 1.9	
		International efficiency class	: IE2	
		Ausgangsspannung [V]	: 3x0-U input	
		Ausgangsnennstrom [A]	: 24,00	
		Ausgangsfrequenz [Hz]	: 0-599	
		Motorbelastung linear [kW]	: 11	
		Motorbelastung quadratisch[kW]	: 15	
		Umgebungstemperatur min [°C]	: 0	
		Umgebungstemperatur max [°C]	: +50	
		Schutzart IP	: 20	
		Gebersteckplatz	: DEH11B	
			zulässige Geber:Hiperface, sin/cos, TTL	
		Feldbussteckplatz	: DFE33B, Sachnummer 18213464	
			Industrial Ethernet für	
			Protokoll Modbus/TCP & EtherNet/IP	
		Optionsstatus	: Optionen eingebaut	
		Bremswiderstand	: BW347-T, Sachnummer 18201350	
			Ausführung m.integr.Temperaturschalter	
			Leistung bei 100% ED [kW] 4,00	
			Leistung bei 12% ED [kW] 14,40	
			Widerstand [Ohm] 47 +/-10%	
			Schutzart IP20	
		Status Bremswiderstand	: beigelegt	
		Anzahl Bremswiderstand	: 1	
		Bediengerät	: DBG60B-10, Sachnummer 28229150	
			Sprachausführung	
			DE/EN/FR/ES/PT/IT/NL/DA	
			SV/FI/TR/RU/PL/CS/ZH	
			Schutzart IP40	
		Schnittstelle	: USM21A, Sachnummer 28231449	
			Schnittstellenwandler	
			USB2.0 auf CAN und RS485	
			einschließlich MOVITOOLS und MOVISUITE	
		Dokumentation Sprache / Anzahl	: Deutsch / 1	
		Dokumentation Nr. A	: 11532602	
			16725603	
			19387202	
			23534842	
			25823124	
		Statistische Warennummer	: 85044088	
		Nettogewicht [KG]	: ca. 18/ST 18/Pos.	
		Lieferzeit:	Lieferdatum wird bei Bestellung ermittelt	
		Bediengerät		92,53
				92,53

Hauptverwaltung / Headquarters

SEW-EURODRIVE GmbH & Co KG Postadresse / Postal address
Ernst-Blickle-Straße 42 SEW-EURODRIVE GmbH & Co KG
76646 Bruchsal · Germany 76642 Bruchsal · Germany

Telefon 07251 75-0
Telefax 07251 75-1970

www.sew-eurodrive.de
sew@sew-eurodrive.de

Bankverbindungen / Bank accounts

Deutsche Bank AG IBAN DE61660700040200425700 BIC DEUTDE33
Commerzbank Bruchsal IBAN DE22663400180470888900 BIC COBADE33
LBBW IBAN DE21600501010008628604 BIC SOLADE33
Sparkasse Kraichgau IBAN DE85663500360000020313 BIC BRUSDE33

USt.-Ident.-Nr. / VAT Regist. No. DE 143080517

Kommanditgesellschaft, Sitz: Bruchsal, RG Mannheim HRA 230970
Komplementärin: SEW-EURODRIVE Verwaltungs-GmbH
Sitz: Bruchsal, RG Mannheim HRB 230207
Geschäftsführender Gesellschafter: Jürgen Blickle
Geschäftsführung: Jürgen Blickle (Vorsitzender), Udo Aull, Dr. Jörg Hermes,
Dr. Hans Krattenmacher, Christian Mayer, Johann Soder, Dr. Jürgen Zanghellini

Angebot

Angebots-Nr.: **419640036D**

vom: 04.11.2022

Seite 10 / 12

Pos	Menge	Sachnummer	Stückpreis EUR	Gesamtpreis EUR
		Bremswiderstand	545,38	545,38
		Option Feldbus	225,49	225,49
		Option Gebersteckplatz	116,64	116,64
		Schnittstelle	73,87	73,87
	netto		3.586,43	3.586,43

05 Ihre Projektreferenz: UBeRT Projekt

1 ST 8271283

netto 250,64

250,64

Netzfilter NF035-503

Möchten Sie gleich bestellen?



Links zu den Dokumenten:



Typ/Größe : NF035-503
 Nennstrom : 35 A
 Spannung [V] : 3X500 +/- 10%
 Schutzart IP : 20
 Statistische Warennummer : 85045000

Nettogewicht [KG] : ca. 1,4/ST 1,4/Pos.

Lieferzeit: Lieferdatum wird bei Bestellung ermittelt

06 Ihre Projektreferenz: UBeRT Projekt

1 ST 8271518

netto 85,73

85,73

Netzdrossel ND030-023

Möchten Sie gleich bestellen?



Links zu den Dokumenten:



Hauptverwaltung / Headquarters

SEW-EURODRIVE GmbH & Co KG Postadresse / Postal address
 Ernst-Blickle-Straße 42 SEW-EURODRIVE GmbH & Co KG
 76646 Bruchsal · Germany 76642 Bruchsal · Germany

Telefon 07251 75-0
 Telefax 07251 75-1970

www.sew-eurodrive.de
 sew@sew-eurodrive.de

Bankverbindungen / Bank accounts

Deutsche Bank AG IBAN DE61660700040200425700 BIC DEUTDE33
 Commerzbank Bruchsal IBAN DE22663400180470888900 BIC COBADE33
 LBBW IBAN DE21600501010008628604 BIC SOLADE33
 Sparkasse Kraichgau IBAN DE85663500360000020313 BIC BRUSDE33

USt.-Ident.-Nr. / VAT Regist. No. DE 143080517

Kommanditgesellschaft, Sitz: Bruchsal, RG Mannheim HRA 230970
 Komplementärin: SEW-EURODRIVE Verwaltungs-GmbH
 Sitz: Bruchsal, RG Mannheim HRB 230207
 Geschäftsführender Gesellschafter: Jürgen Blickle
 Geschäftsführung: Jürgen Blickle (Vorsitzender), Udo Aull, Dr. Jörg Hermes,
 Dr. Hans Krattenmacher, Christian Mayer, Johann Soder, Dr. Jürgen Zanghellini

Angebot

Angebots-Nr.: **419640036D**

vom: 04.11.2022

Seite 11 / 12

Pos	Menge	Sachnummer	Stückpreis EUR	Gesamtpreis EUR
	Typ/Größe	: ND030-023		
	Induktivität	: 0,2000 mH		
	Nennstrom	: 40 A		
	Spannung [V]	: 3X380-500 +/-10%		
	Schutzart IP	: 00		
	Statistische Warennummer	: 85045000		
	Nettogewicht [KG]	: ca. 1,8/ST 1,8/Pos.		
	Lieferzeit:	Lieferdatum wird bei Bestellung ermittelt		

Netto-Gesamtwegicht ca. 49 KG

Auftragsrabatt -3,00 % von 2.916,77	-87,50
Auftragsrabatt -3,00 % von 169,00	-5,07
Auftragsrabatt -3,00 % von 106,14	-3,18
Auftragsrabatt -3,00 % von 3.586,43	-107,59
Auftragsrabatt -3,00 % von 250,64	-7,52
Auftragsrabatt -3,00 % von 85,73	-2,57

Gesamtwert o. MWST**EUR****6.901,28****Benötigen Sie weitere Informationen zu Ihrem Angebot?**

Die Vorgangsübersicht liefert Ihnen nach einmaliger Freischaltung einen kompakten Überblick über Ihre aktuellen Angebote:

[https://www.sew-eurodrive.de/os/c/main.do?](https://www.sew-eurodrive.de/os/c/main.do?viewset=OVERVIEW&type=quotation&language=DE_DE&utm_source=output)

[viewset=OVERVIEW&type=quotation&language=DE_DE&utm_source=output](https://www.sew-eurodrive.de/os/c/main.do?viewset=OVERVIEW&type=quotation&language=DE_DE&utm_source=output)

Dort erhalten Sie auch CAD-Daten, Dokumentationen oder technische Produktdaten zu den angebotenen Produkten.

Links zu den Maßblättern:

Position 01

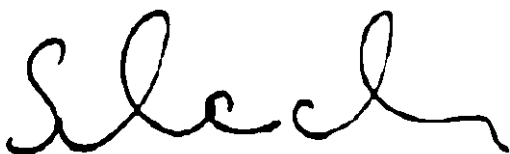
- <https://docu.sew-eurodrive.com/StorageService/api/Download/b792ad4f-876c-4228-94ad-8ac9dfff3c71>

- <https://docu.sew-eurodrive.com/StorageService/api/Download/882ad9e3-ac33-4955-b9a3-ac4d809b4161>

Wir freuen uns, wenn Ihnen unser Angebot zusagt und Sie uns Ihren persönlichen Auftrag erteilen. Sie haben noch Fragen oder benötigen Beratung? Natürlich stehen wir Ihnen sehr gerne jederzeit persönlich zur Verfügung!

Mit freundlichen Grüßen

SEW-EURODRIVE GmbH & Co KG



Die angegebene Lieferzeit ergibt sich nach Auftragseingang und technischer Klärung. Darüber hinaus kann die Lieferzeit auch abweichend vereinbart werden.

Hauptverwaltung / Headquarters

SEW-EURODRIVE GmbH & Co KG
Ernst-Blickle-Straße 42
76646 Bruchsal · Germany

Postadresse / Postal address
SEW-EURODRIVE GmbH & Co KG
76642 Bruchsal · Germany

Telefon 07251 75-0
Telefax 07251 75-1970

www.sew-eurodrive.de
sew@sew-eurodrive.de

Bankverbindungen / Bank accounts

Deutsche Bank AG IBAN DE61660700040200425700 BIC DEUTDE33
Commerzbank Bruchsal IBAN DE22663400180470888900 BIC COBADE33
LBBW IBAN DE21600501010008628604 BIC SOLADE33
Sparkasse Kraichgau IBAN DE85663500360000020313 BIC BRUSDE33

USt.-Ident.-Nr. / VAT Regist. No. DE 143080517

Kommanditgesellschaft, Sitz: Bruchsal, RG Mannheim HRA 230970
Komplementärin: SEW-EURODRIVE Verwaltungs-GmbH
Sitz: Bruchsal, RG Mannheim HRB 230207
Geschäftsführender Gesellschafter: Jürgen Blickle
Geschäftsführung: Jürgen Blickle (Vorsitzender), Udo Aull, Dr. Jörg Hermes,
Dr. Hans Krattenmacher, Christian Mayer, Johann Soder, Dr. Jürgen Zanghellini

Angebot

**Angebots-Nr.: 419640036D**

vom: 04.11.2022

Seite 12 / 12

Geben Sie bitte bei jeglicher Korrespondenz unsere Angebots-Nr. 419640036D mit an. Sie ermöglichen uns dadurch ein rationelles Arbeiten, was sich in einer verkürzten Bearbeitung Ihres Vorgangs auswirkt.

Die uns von Ihnen mitgeteilten Daten dienen als Grundlage unserer Berechnung. Richtigkeit und Vollständigkeit dieser Daten für den geplanten Einsatzzweck der Produkte werden vorausgesetzt.
Bitte überprüfen Sie die korrekte Übernahme Ihrer Daten sowie die von uns getroffenen Annahmen.

Wir verwenden auch Ihre E-Mail-Adresse für Marketing-Maßnahmen. Sie können hiergegen jederzeit widersprechen. Informationen zur Verarbeitung Ihrer Daten erhalten Sie unter <https://www.sew-eurodrive.de/datenschutzerklaerung/>

Hauptverwaltung / Headquarters

SEW-EURODRIVE GmbH & Co KG Postadresse / Postal address
Ernst-Blickle-Straße 42 SEW-EURODRIVE GmbH & Co KG
76646 Bruchsal · Germany 76642 Bruchsal · Germany

Telefon 07251 75-0
Telefax 07251 75-1970

www.sew-eurodrive.de
sew@sew-eurodrive.de

Bankverbindungen / Bank accounts

Deutsche Bank AG	IBAN DE61660700040200425700	BIC DEUTDE33
Commerzbank Bruchsal	IBAN DE22663400180470888900	BIC COBADE33
LBBW	IBAN DE21600501010008628604	BIC SOLADE33
Sparkasse Kraichgau	IBAN DE85663500360000020313	BIC BRUSDE33

USt.-Ident.-Nr. / VAT Regist. No. DE 143080517

Kommanditgesellschaft, Sitz: Bruchsal, RG Mannheim HRA 230970
Komplementärin: SEW-EURODRIVE Verwaltungs-GmbH
Sitz: Bruchsal, RG Mannheim HRB 230207
Geschäftsführender Gesellschafter: Jürgen Blickle
Geschäftsführung: Jürgen Blickle (Vorsitzender), Udo Aull, Dr. Jörg Hermes,
Dr. Hans Krattenmacher, Christian Mayer, Johann Soder, Dr. Jürgen Zanghellini



eCATALOGsolutions



BIM catalogs.net



PARTsolutions



Erstellen Sie Ihr Individuelles 3D PDF Datenblatt ▶

Mehr über Produktkataloge für den Bereich Maschinenbau ▶

Mehr über Produktkataloge für den Bereich Architektur/BIM ▶

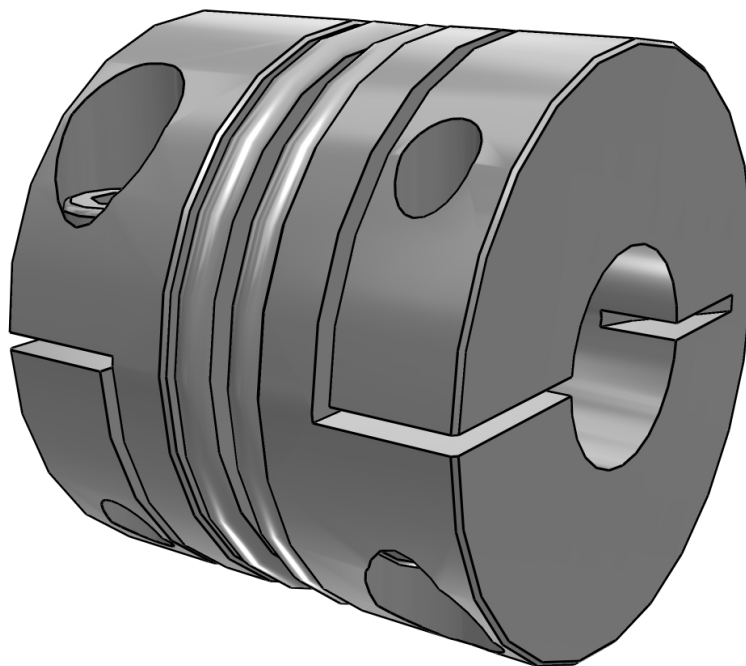
Kosten für Engineering und Einkauf reduzieren ▶

**KB4K-200-60-32-24**

Metallbalgkupplung mit Klemmnabe

3D Ansicht

Im Adobe Acrobat dem Dokumentinhalt vertrauen (siehe Hinweis oben) und auf das Fragezeichen klicken, um die interaktive 3D Ansicht zu aktivieren.


 **Zoom**

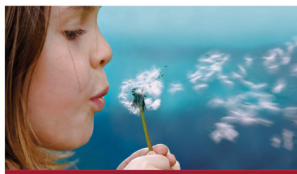
Vergößert oder verkleinert die Objekte bei vertikaler Bewegung. Sie können außerdem bei gedrückter SHIFT-Taste mit dem Hand-Werkzeug zoomen.

 **Schwenken**

Bewegt das Modell horizontal oder vertikal auf einer Ebene. Sie können außerdem bei gedrückter STRG-Taste mit dem Hand-Werkzeug schwenken.

 **Drehen**

Dreht 3D Objekte relativ zum sichtbaren Bereich. Wie sich Objekte bewegen ist abhängig von der Start-Ansicht, wo sie die Bewegung ansetzen und die Richtung in die Sie ziehen.



eCATALOGsolutions



BIM catalogs.net



PARTsolutions



Erstellen Sie Ihr Individuelles 3D PDF Datenblatt



Mehr über Produktkataloge für den Bereich Maschinenbau



Mehr über Produktkataloge für den Bereich Architektur/BIM



Kosten für Engineering und Einkauf reduzieren

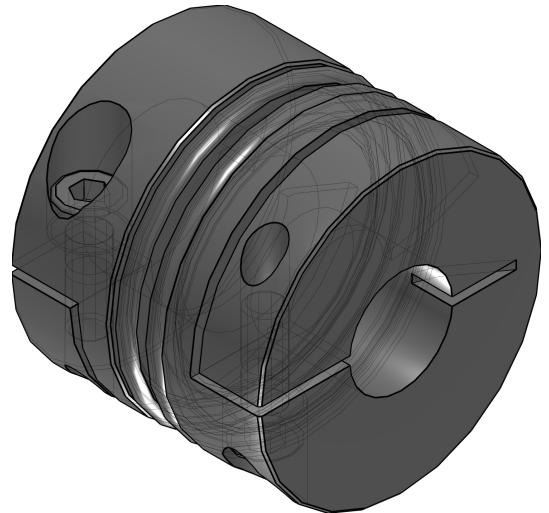
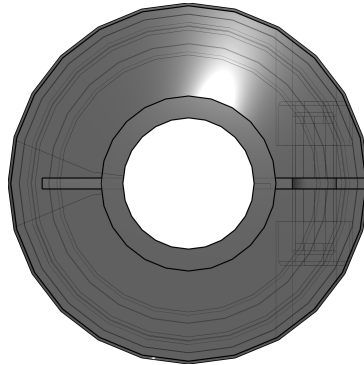
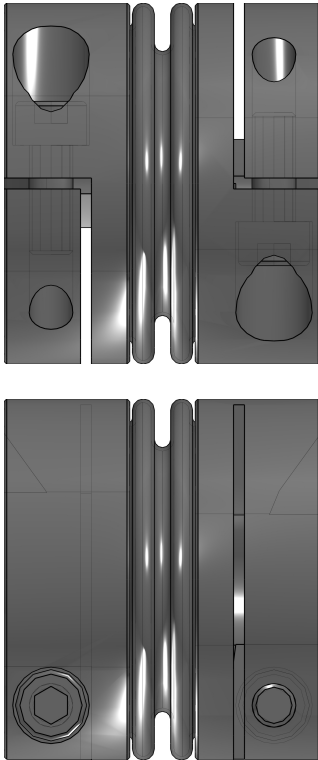


KB4K-200-60-32-24

Metallbalgkupplung mit Klemmnabe

2D-Ableitung

ISO Ansicht





eCATALOG solutions



BIM catalogs.net



PART solutions



Erstellen Sie Ihr Individuelles 3D PDF Datenblatt



Mehr über Produktkataloge für den Bereich Maschinenbau



Mehr über Produktkataloge für den Bereich Architektur/BIM

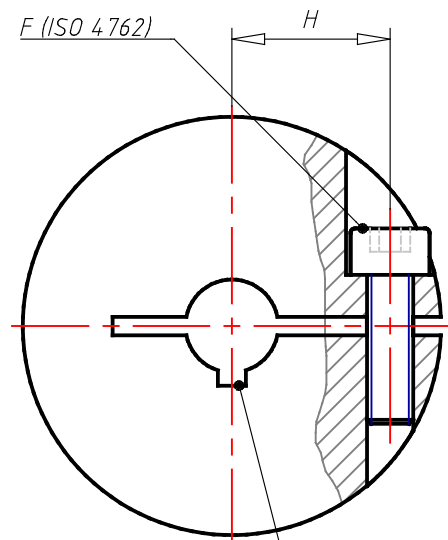
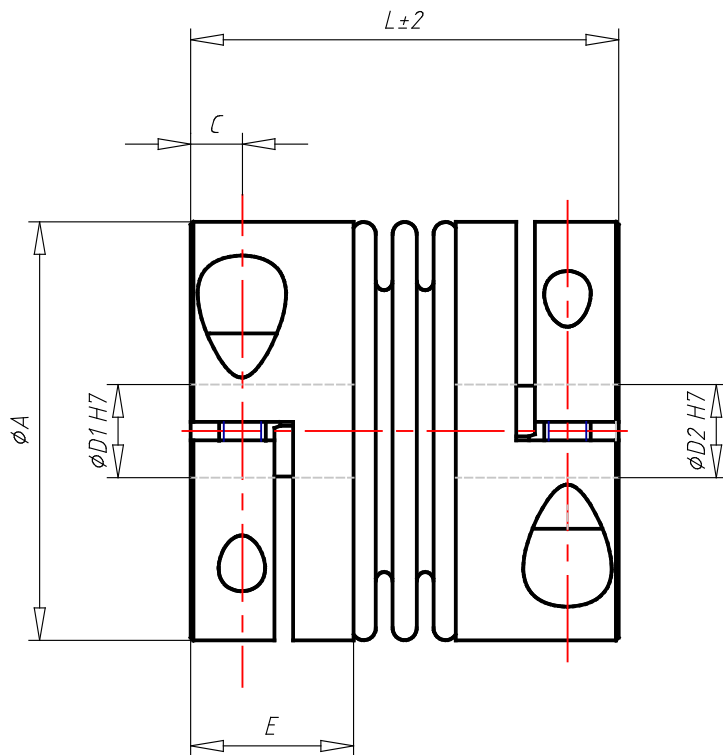


Kosten für Engineering und Einkauf reduzieren



KB4K-200-60-32-24
Metallbalgkupplung mit Klemmnabe

Technische Zeichnungen



*Passfedernut wahlweise
Keyway on request*



KB4K-200-60-32-24

Metallbalgkupplung mit Klemmnabe

Technische Daten

SIZE (Größe)	200
T (Drehmoment / Nm)	200
L (Länge (±2) / mm)	60
A (Aussendurchmesser / mm)	66
N (Passfedernut (DIN 6885))	ohne Passfedernut
D1 (Bohrung (H7) / mm)	32
D2 (Bohrung (H7) / mm)	24
H (Gewindeabstand / mm)	23
C (Gewindeabstand stirnseitig / mm)	8.6
E (Nabellänge / mm)	23
F (Schraube (ISO 4762))	M8
TA (Anzugsmoment / Nm)	40
CNSMASSEXACT (Gewicht / kg)	0.38
J (Massenträgheitsmoment / g*cm ²)	0.28
CT (Federsteifigkeit Torsion CT / Nm/rad)	40
CR (Federsteifigkeit radial / N/mm)	12442
CA (Federsteifigkeit axial / N/mm)	287
KR (Versatz radial max. / mm/m)	1
KA (Versatz axial max. / mm)	1
KW (Versatz Winkel max. / °)	0.5
RPM (Drehzahl max. / 1/min)	8700
INFO1 (Technisches Datenblatt)	Produktinformation
INFO2 (Betriebs- / Montageanleitung)	Produktinformation

3D PDF DATASHEET



 eCATALOG solutions



 BIM catalogs.net



 PART solutions



Erstellen Sie Ihr Individuelles 3D
PDF Datenblatt 

Mehr über Produktkataloge für
den Bereich Maschinenbau 

Mehr über Produktkataloge für
den Bereich Architektur/BIM 

Kosten für Engineering und
Einkauf reduzieren 



KB4K-200-60-32-24

Metallbalgkupplung mit Klemmnabe

Stückliste

N°	Bezeichnung	Menge
1.1	KB4K-200-60-32-24	1

Ihre Konfiguration

maverick
by SCHLEIFRING


SCHLEIFRING

Ihr Konfigurationscode lautet

7KC000008

Die Übermittlung des Konfigurationscodes ist sowohl in der Angebots- als auch in der Auftragsphase eine wichtige Information zur Identifikation Ihrer gewünschten Variante.

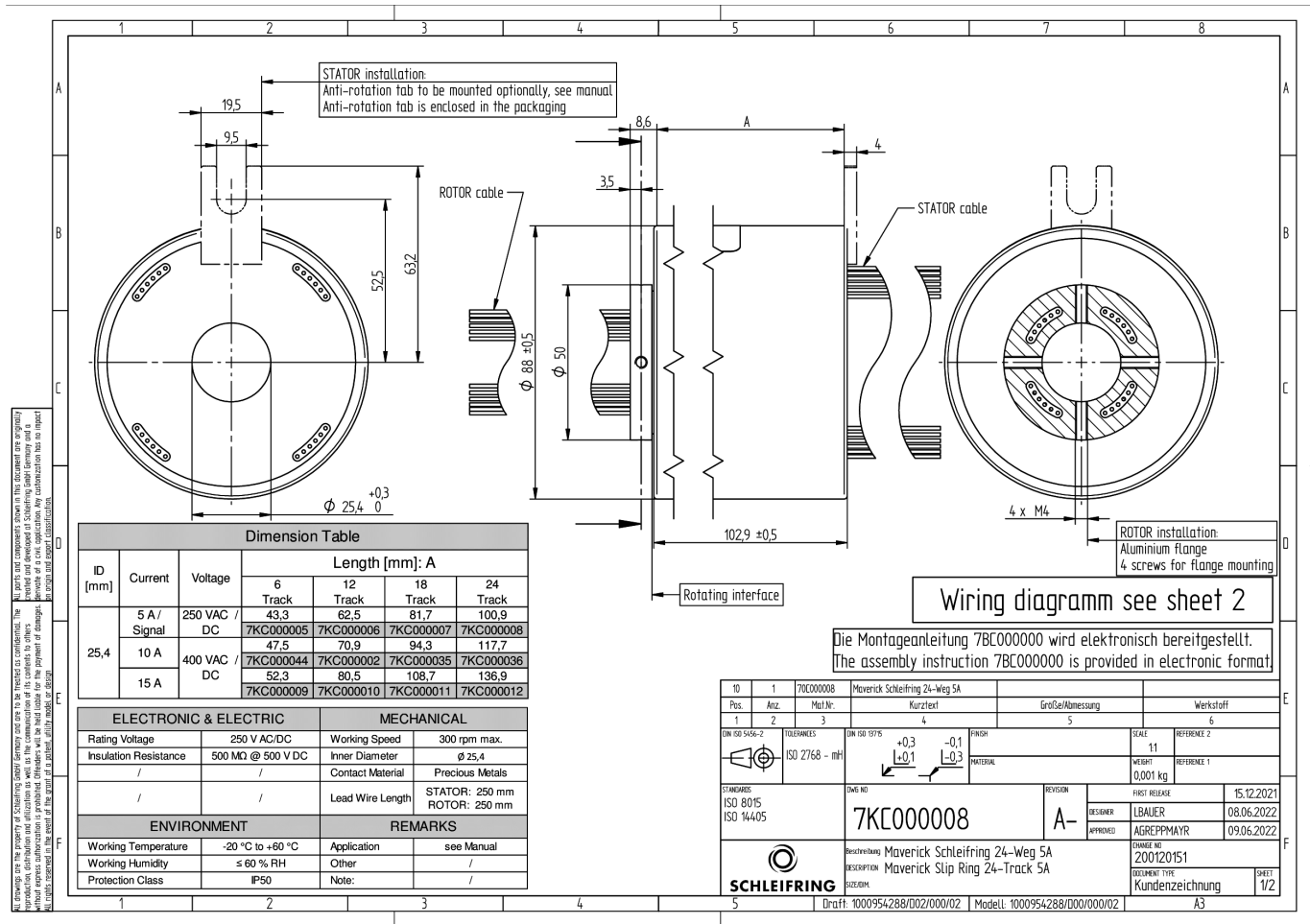


Technische Daten

Bezeichnung

Stromstärke	5A
Spannung	250VAC/DC
Wege	24
Länge	100.9
Freier Innendurchmesser	25.4
Durchmesser außen	86

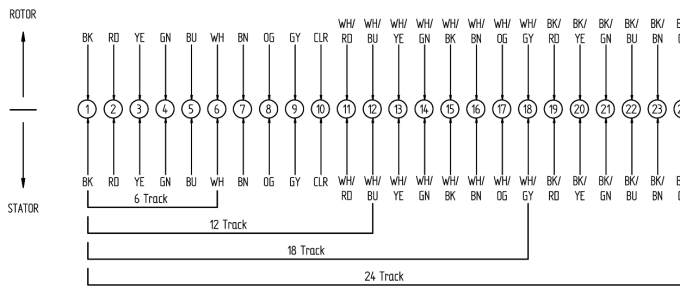
Zeichnung



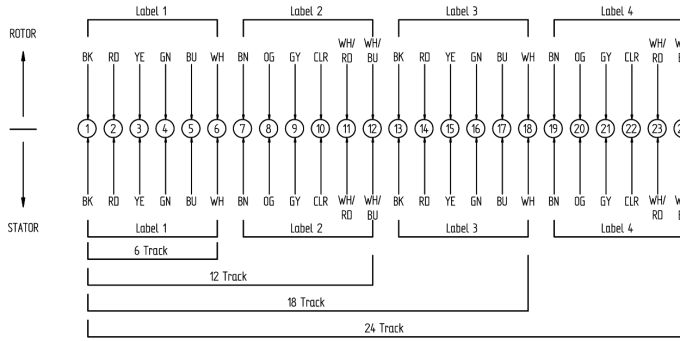
All drawings are the property of Schleifring GmbH. They are to be treated as confidential. The parts and components shown in this document are original products and developed at Schleifring GmbH. They are not to be reproduced, distributed or otherwise used without the written consent of Schleifring GmbH. All rights reserved in the event of a patent, utility model, or design.

Cable Table	
Current	Cable
5 A / Signal	AWG17
10 A	
15 A	AWG14

5 A / 10 A

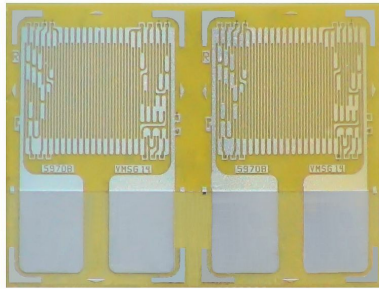


15 A



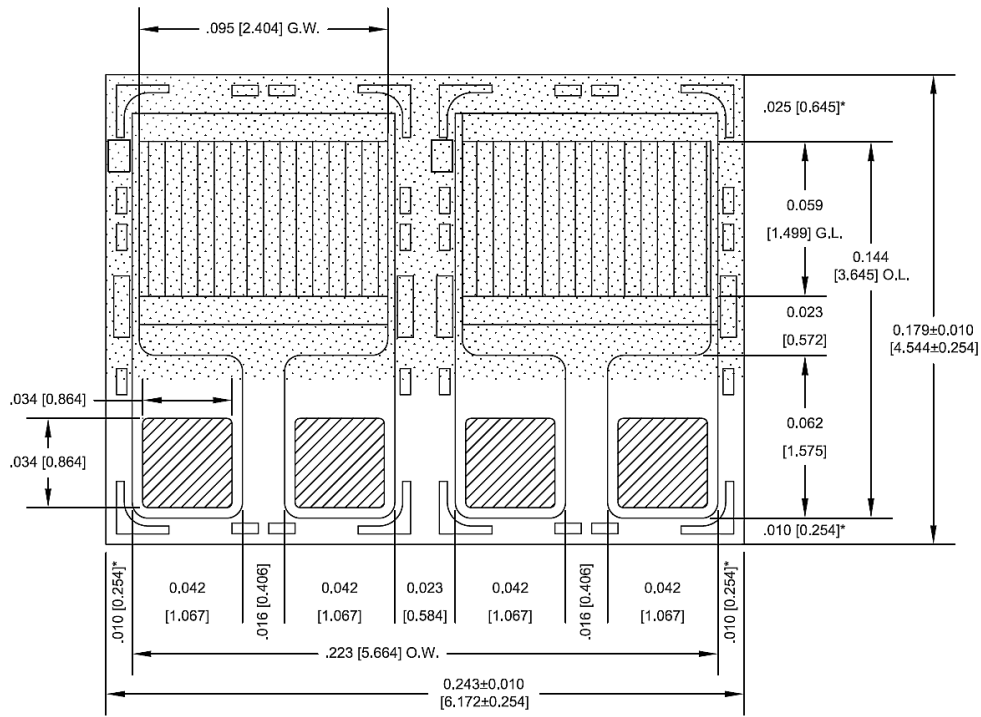
DIN ISO 5456-2	TOLERANCES	DIN ISO 1375	FINISH	SCALE	REFERENCE 2
	ISO 2768 - mH	+0,3 +0,1	-0,1 -0,3	1:1	REFERENCE 2
STANDARDS	DWG NO	REVISION	FIRST RELEASE	WEIGHT	REFERENCE 1
ISO 8015 ISO 14405	7KC000008	A-	15.12.2021	0,001 kg	REFERENCE 1
	DESCRIPTION	APPROVED	DESIGNER	APPROVED	DATE
SCHLEIFRING	Maverick Schleifring 24-Weg 5A Maverick Slip Ring 24-Track 5A		LBAUER	AGREPPMAYR	08.06.2022
	SIZE/DM	CHANGE NO	DOCUMENT TYPE	SHEET	
		200120151	Kundenzeichnung	2/2	
Draft: 1000954288/002/000/02 Modell: 1000954288/000/000/02					A3

N2A-06-S5092R-350/E4 Pack10 06



Beschreibung

Abmessungen

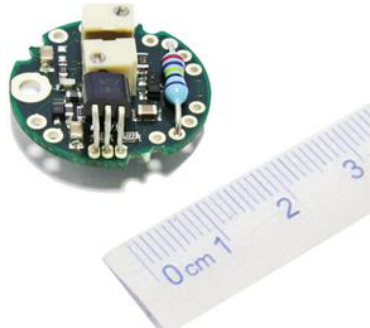


Technische Daten

Dehnungsmessstreifen

Zweck der Messung	Aufnehmerbau
Typ	Doppelgitter
Gitteranzahl	2
Gitterbreite	2.5 mm
maximale Breite	6.2 mm
Gitterlänge	1.5 mm
maximale Länge	4.5 mm
Widerstand	350 Ohm
Toleranz Widerstand	0,2 %
Anschluss	Lötpad
Sorte	Metallfolie
Trägermaterial	Polyimid
Temperaturkompensation	Stahl-06

Strain Gauge or Load Cell Embedded Analogue Amplifier



A range of high performance robust signal conditioners in a miniature OEM format and designed specifically for fitting inside load cells

Introduction

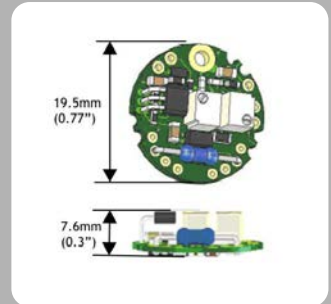
Mantracourt's ICA family offers high stability and fast response strain gauge or load cell amplifier, converting a strain gauge input into a volt or mA output. It's sub-miniature design enables it to be fitted into the majority of transducers for a wide range of signal conditioning for strain gauges, load cells, pressure and torque transducers. Available in 6 versions with two performance categories S & H (industrial & very high stability).

The ICAH range offer very low drift over wide operating temperatures.

Optional (ILE) in line enclosure to convert a standard load cell to a conditioned load cell output.

Specification at a Glance

- Standardised mounting hole for faster & easier installation
- New generation improved performance of up to 400% (High stability version) over operating temperature
- ROHS compliant
- Standardised excitation 5 V DC
- Multi layer printed circuit board & additional filtering to improve EMC performance
- New ICA6 model to provide ± 10 V output from uni-polar 14-24 V supply
- Plated through holes for wire connections
- Full CE approval



User Benefits

- Available in 6 different versions
- Small & compact, reduced height of just 7.6 mm
- Low drift
- Robust design, reverse polarity & short circuit protected
- Fast calibration procedure

Ideal Applications

- Automotive
- Lifting & Handling
- Silo & Weighing
- Hazardous Areas
- Agriculture



Related Product



ILE

Field enclosure for ICA analogue and DCell data converters



ICA5ATEX

ATEX Intrinsically Safe, OEM strain gauge converter, 4-20mA 2 wire

Case Study

The ETS Formula SAE Team from the University of Quebec is renowned for its lightweight and ergonomic car design, its excellent suspension design and its scientific approach to vehicle validation and development.

The 2011 car features new suspension and steering packages designed from scratch. The new steering system was designed to reduce driver effort while allowing clear feedback from the tyres back to the driver. In order to validate set up and troubleshoot various systems on the car, loads in all suspension and steering links needed to be quantified. To do so, the team needed strain gauges on all suspension and steering links.

The Application:

A race car generates a lot of electro-magnetic noise from the ignition and telemetry systems. This means that there must be minimal wiring length between the strain gauges and the amplifiers. Secondly, to provide representative data, the weight of the whole system must not alter the dynamics of the car.

The Solution:

The strain gauges and embedded ICA amplifiers were integrated to the data acquisition system already in place. The resulting data was used in several phases of the project. Here are a few examples:

The recorded suspension loads allowed further refinements of the chassis load case which yields a lighter, yet rules a compliant chassis design.

The recorded steering loads allowed the team to characterise driver effort and also allowed a new target to be set for a steering system design balancing steering response, feedback and effort.



During the validation and development phase, the strain gauges allowed the team to monitor the wheel load fluctuation for better spring-damper selection and

adjustment. Also, load transfer characteristics were monitored for validation and diagnosis purposes.

CE & Environmental

Storage temperature - 40 to +85°C
Operating temperature - 40 to +85°C

CE Environmental Approvals

European EMC Directive 2004/108/EC

For more information contact us today...



In the interests of continued product development, Mantracourt Electronics Limited reserves the right to alter product specifications without prior notice

ICA S & H - Miniature Strain Gauge Signal Conditioner Converts Load Cell to 4-20mA, 0-10V or $\pm 10V$

ICA1,2,3,6 Voltage Output Amplifiers

ICA1 0.1-10.1V

Parameter	Min	Typical	Max	Units/Notes
Electrical & Environmental				
Supply Voltage Range	13	24	30	Volts
Operating Current		23		mA Note 1
Operating Temp Range	-40		85	$^{\circ}C$
Storage Temp Range	-40		85	$^{\circ}C$
Reverse Polarity Protection			-30	Volts
Measurements				
Bridge Excitation	4.9	5	5.1	Volts
Bridge Impedance	330	350	5000	Ohms
Bridge Sensitivity	0.5	2.5	150	mV/V Note 2
Output Voltage Range	0.1		+10.1	Volts
Output Load	5000			Ohms
Band Width	DC		1000	Hz
Zero Adjustment		± 2		%FR
Span Adjustment		± 8		%FR
Linearity		0.02		%FR
Zero Temp Stability S		0.0009	0.0025	$\pm \%FR/^{\circ}C$
Zero Temp Stability H		0.0004	0.0015	$\pm \%FR/^{\circ}C$
Span Temp Stability S		0.0025	0.0064	$\pm \%FR/^{\circ}C$
Span Temp Stability H		0.002	0.0051	$\pm \%FR/^{\circ}C$

ICA2 0.1-5.1V

Electrical & Environmental				
Supply Voltage Range	8.5	12	28	Volts
Operating Current		23		mA Note 1
Operating Temp Range	-40		85	$^{\circ}C$
Storage Temp Range	-40		85	$^{\circ}C$
Reverse Polarity Protection			-30	Volts
Measurements				
Bridge Excitation	4.9	5	5.1	Volts
Bridge Impedance	330	350	5000	Ohms
Bridge Sensitivity	0.5	2.5	150	mV/V Note 2
Output Voltage Range	0.1		± 5.1	Volts
Output Load	5000			Ohms
Band Width	DC		1000	Hz
Zero Adjustment		± 2		%FR

Span Adjustment		±8		%FR
Linearity		0.02		%FR
Zero Temp Stability S		0.0009	0.0025	±%FR/°C
Zero Temp Stability H		0.0004	0.0015	±%FR/°C
Span Temp Stability S		0.0025	0.0064	±%FR/°C
Span Temp Stability H		0.002	0.0051	±%FR/°C

ICA3 ±10V

Electrical & Environmental

Supply Voltage Range	±13	±15	±15	Volts
Operating Current		23		mA Note 1
Operating Temp Range	-40		85	°C
Storage Temp Range	-40		85	°C
Reverse Polarity Protection			-30	Volts

Measurements

Bridge Excitation	4.9	5	5.1	Volts
Bridge Impedance	330	350	5000	Ohms
Bridge Sensitivity	0.5	2.5	150	mV/V Note 2
Output Voltage Range	-10		+10	Volts
Output Load	5000			Ohms
Band Width	DC		1000	Hz
Zero Adjustment		±2		%FR
Span Adjustment		±8		%FR
Linearity		0.02		%FR
Zero Temp Stability S		0.0009	0.0025	±%FR/°C
Zero Temp Stability H		0.0004	0.0015	±%FR/°C
Span Temp Stability S		0.0025	0.0064	±%FR/°C
Span Temp Stability H		0.002	0.0051	±%FR/°C

ICA6 ±10V

Electrical & Environmental

Supply Voltage Range	14	15	18	Volts Note 3
Operating Current		30		mA Note 1
Operating Temp Range	-40		85	°C
Storage Temp Range			-30	°C
Reverse Polarity Protection				Volts

Measurements

Bridge Excitation	4.9	5	5.1	Volts
Bridge Impedance	330	350	5000	Ohms
Bridge Sensitivity	0.5	2.5	150	mV/V Note 2
Output Voltage Range	-10		+10	Volts
Output Load	5000			Ohms
Band Width	DC		1000	Hz
Zero Adjustment		±2		%FR
Span Adjustment		±8		%FR

Linearity		0.02		%FR
Zero Temp Stability S		0.0009	0.0025	±%FR/°C
Zero Temp Stability H		0.0004	0.0015	±%FR/°C
Span Temp Stability S		0.0025	0.0064	±%FR/°C
Span Temp Stability H		0.002	0.0051	±%FR/°C

ICA4,5 Current Output Amplifiers

ICA4 4-20mA

Electrical & Environmental

Supply Voltage Range	10	24	30	Volts Note 4
Operating Current	27		43	mA Note 1
Operating Temp Range	-40		85	°C
Storage Temp Range	-40		85	°C
Reverse Polarity Protection			-30	Volts

Measurements

Bridge Excitation	4.9	5	5.1	Volts
Bridge Impedance	330	350	5000	Ohms
Bridge Sensitivity	0.5	2.5	150	mV/V Note 2
Output Current Range	4		20	mA
Output Load			500	Ohms
Band Width	DC		1000	Hz
Zero Adjustment		±2		%FR
Span Adjustment		±8		%FR
Linearity		0.02		%FR
Zero Temp Stability S		0.0009	0.0025	±%FR/°C
Zero Temp Stability H		0.0004	0.0015	±%FR/°C
Span Temp Stability S		0.0025	0.0064	±%FR/°C
Span Temp Stability H		0.002	0.0051	±%FR/°C

ICA5S 4-20mA

Electrical & Environmental

Supply voltage Range	7.5	24	30	Volts
Operating Current	4		20	mA (2 wire)
Operating Temp Range	-40		85	°C
Storage Temp Range	-40		125	°C
Reverse Polarity Protection			-30	Volts

Measurements

Bridge Excitation	1.05	1.11	1.16	Volts Note 5
Bridge Impedance	350	1000	5000	Ohms Note 6
Bridge Sensitivity	0.5	2.5	55	mV/V Note 2
Output Current Range	4		20	mA
Output Load			800	Ohms
Band Width	DC		1000	Hz
Zero Adjustment		±2		%FR Note 5

Span Adjustment		±8		%FR
Linearity		0.002		%FR
Zero Temp Stability S		0.001	0.005	±%FR/°C
Span Temp Stability S		0.007	0.014	±%FR/°C
ICA5A 4-20mA				
Electrical & Environmental				
Supply Voltage Range	9	24	30	Volts
Operating Current	4		20	mA (2 wire)
Operating Temp Range	-40		85	°C
Storage Temp Range	-40		125	°C
Reverse Polarity Protection			-30	Volts
Measurements				
Bridge Excitation	1.05	1.11	1.16	Volts Note 5
Bridge Impedance	350	1000	5000	Ohms Note 6
Bridge Sensitivity	0.5	2.5	55	mV/V Note 2
Output Current Range	4		20	mA
Output Load			800	Ohms
Band Width	DC		1000	Hz
Zero Adjustment		±2		%FR Note 5
Span Adjustment		±8		%FR
Linearity		0.02		%FR
Zero Temp Stability S		0.001	0.005	±%FR/°C
Span Temp Stability S		0.007	0.014	±%FR/°C
Notes	<p>Note 1 - With 350 Ohm load cell connected. Note 2 - Factory setting is the typical value shown. For other values fit an alternative calibration resistor. Note 3 - ICA6 maximum voltage can be increased to 24V with a 1000 Ohm load cell. Note 4 - The ICA4 can tolerate a lower supply voltage if the output load is reduced e.g. operation is possible at 8V provided that the load does not exceed 150 Ohm. Note 5 - ICA5 with 1000 Ohms load cell connected. Note 6 - ICA5 recommended bridge impedance is 1000 Ohms or greater.</p>			
General Notes	<p>The voltage between either of the power supply connections and the load cell shield should not exceed 50V. Any leakage will be greater than 10M Ohms. FR = Full Range</p>			
Environmental				
Storage Temperature	-40 to +85°C			
Operating Temperature	-40 to +85°C			
Relative Humidity	95% maximum non condensing			
CE Environmental Approvals	European EMC Directive 2004/108/EC, Low Voltage Directive 2006/95/EC			

DE M158 | Wassermelder 9 - 12 V/DC
 Wenn die 2 Fühleranschlüsse des Moduls mit Wasser in Verbindung kommen, schaltet das eingebaute Relais ein. Damit können Sirenen, andere Abschaltrelais usw. angesteuert werden.

EN M158 | Waterswitch 9 - 12 V/DC
 If the 2 sensor connections of the module come into contact with water, the built-in relay switches on. Sirens, other cutoff relays, etc. may be triggered with that.

ES M158 | Avisador de agua 9 - 12 V/DC
 Cuando las 2 conexiones de sensor del módulo entran en contacto con agua, el relé incorporado se conecta. Con eso se pueden controlar sirenas, otros relés de desconexión, etc.

FR M158 | Avertisseur d'eau 9 - 12 V/DC
 Le relais incorporé connecte quand les 2 raccords de palpeur du module entrent en contact avec l'eau. Avec cela on peut commander des sirènes, d'autres relais de déconnexion, etc.

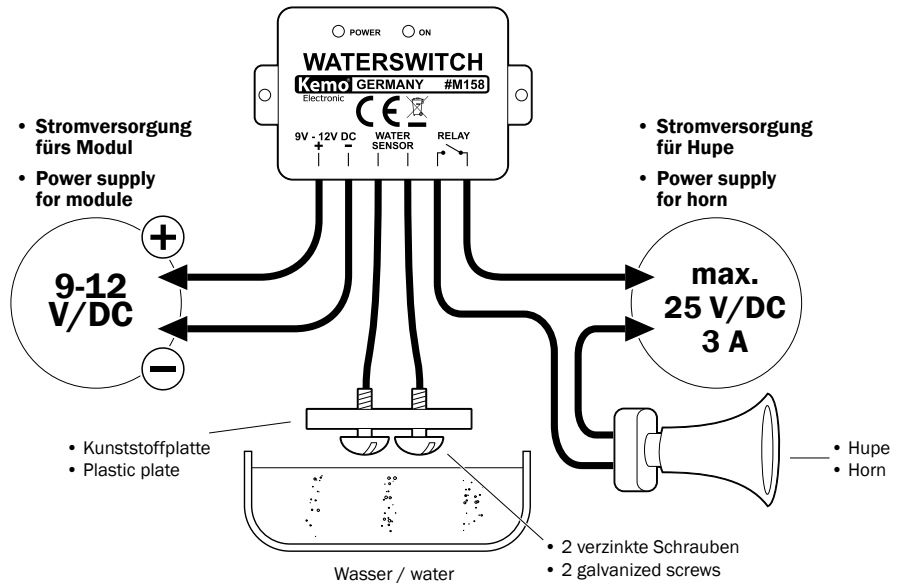
NL M158 | Watermelder 9 - 12 V/DC
 Als de 2 voelers van het moduul in contact komen met water, dan schakelt deze het moduul in. Daarmee kan bijvoorbeeld een sirene of een ander relais ingeschakeld worden.

PL M158 | Czujnik wody 9 - 12 V/DC
 Jeśli 2 końcówki czujnika zetkną się z wodą, wówczas wbudowany przekaźnik włącza się. Można w ten sposóbysterować syrenę, inne przekaźniki odłączające itp.

PT M158 | Avisador de água 9 - 12 V/DC
 Quando os dois sensores de conexão do módulo tiverem contacto com a água liga o montado relé. Com isso podem ser dirigidas sirenas, outros relés de interrupção etc.

RU M158 | Датчик уровня воды 9 - 12 V/DC
 Если 2 контактных вывода модуля опустить в воду, то в модуле включается встроенное реле. Таким образом можно включить сирену, другое реле, или нечто подобное.

ANSCHLUSSBEISPIEL | CONNECTION EXAMPLE



DE

Aufbauanweisung:

Das Modul wird außerhalb der auf Wasser zu überwachenden Fläche befestigt (im Keller z.B. oben an der Wand). Die Zuleitungen zur Stromversorgung werden mit einer Stromquelle, z.B. mit einem Steckernetzteil 9 V/DC verbunden. Das Netzteil sollte stabilisiert sein und eine Mindestleistung von 100 mA haben. Die beiden Kabel am Modul, die zu den Wasserfühlern führen, werden mit 2 blanken, nicht rostenden Metallteilen verbunden. Das können z.B. 2 verzinkte Schrauben (M4 - M8) sein. Die Schraubenköpfe werden dort montiert, wo die Feuchtigkeit überwacht werden soll. Die beiden Schrauben müssen voneinander isoliert sein und mit den blanken Schraubenköpfen an der wassergefährdeten Stelle montiert sein. Wenn jetzt beide Metallteile (Schraubenköpfe) in das Wasser tauchen, schaltet der Wasserschalter. Das eingebaute Relais schaltet „EIN“ und die Leuchtdiode „ON“ leuchtet auf. Wenn also 2 isoliert montierte Metallteile (Abstand ca. 1 - 2 cm) in der Größe von Schraubenköpfen (ca. 6 - 10 mm) gleichzeitig in Wasser tauchen, schaltet der Wasserschalter ein. Er schaltet erst dann wieder ab, wenn die beiden Metallköpfe nicht mehr in Wasser eingetaucht sind.

Mit dem eingebauten Relais können dann bei Wasserkontakt entweder akustische Alarmmelder aktiviert werden (z.B. Hupe) oder über Hilfsrelais können Pumpen eingeschaltet oder andere Geräte abgeschaltet werden.

Wichtig:

Die beiden Wasserelektroden können, je nach Häufigkeit der Wasserberührung und der Aggressivität des Wassers evtl. oxidieren. Im Normalbetrieb genügen verzinkte Metallteile, die ab und zu einmal abgewischt (gereinigt) werden, wenn erforderlich. Wenn die Elektroden wegen zu aggressiven Wassers (z.B. Jauche) zu schnell oxidieren, dann verwenden Sie bitte Elektroden mit einem nicht oxidierenden Edelmetallüberzug: z.B. vergoldet oder mit Platin überzogen (bei stark zähender Flüssigkeit eignen sich auch Elektroden aus Titan).

Bestimmungsgemäße Verwendung:

Sensor, der bei Wasserberührung der Fühlerdrähte über einen Relaiskontakt „Alarm“ gibt.

Inbetriebnahme:

Nach der Montage wird die Betriebsspannung von 9 V/DC eingeschaltet. Die LED am Modul leuchtet auf und zeigt, dass das Modul betriebsbereit ist. Sie können die Betriebsbereitschaft prüfen, indem Sie mit 2 nassen Fingern die beiden Wasserelektroden berühren. Der Wasserschalter reagiert dann.

Technische Daten:

Betriebsspannung: 9 V/DC ideal, (max. 12 V/DC), (bitte nur ein stabilisiertes Netzteil verwenden) | **Stromaufnahme:** „Bereit“ <10 mA. Bei Wasserberührung, wenn das Relais anzieht <90 mA jeweils bei 9 V/DC | **LED-Anzeigen:** 1 LED für die Bereitschaftsanzeige „POWER“, 1 LED für die Anzeige „ON“, wenn das Relais einschaltet | **Anschlüsse:** über herausgeführte Kabel | **Zugelassene Kabellänge zu den Wasserfühlern:** max. 5 m mit normalem Kabel, max. 100 m mit abgeschirmtem Kabel, wenn das Abschirmgeflecht mit dem Minuspol der Versorgungsspannung verbunden wird | **Maße:** vergossenes Modulgehäuse ca. 60 x 45 x 20 mm (ohne Befestigungslaschen)

EN

Assembly instructions:

The module is fastened outside the area which shall be monitored (in the cellar e.g. at the top of the wall). The leads towards the electrical power supply are connected with a power source, e.g. with a 9 V/DC plug power supply. The power supply should be stabilised and have a minimum power of 100 mA.

Both cables at the module leading to the water sensors are connected with 2 bare rustproof metal parts. These can be e.g. 2 galvanized screws (M4 - M8). The screw heads have to be mounted there where the humidity shall be monitored. Both screws must be insulated from each other and mounted with the bare screw heads at the spot endangered through water. If now both metal parts (screw heads) dip into water, the water switch connects: the built-in relay switches „ON“ and the light-emitting diode „ON“ lights up. So if 2 metal parts mounted in isolation (distance approx. 1 - 2 cm) being the size of screw heads (approx. 6 - 10 mm) dip into water at the same time, the water switch connects. It only switches off again, if both metal heads are no longer dipped into water.

Then either acoustic alarms (e.g. horns) can be activated or pumps may be switched on by means of a secondary relay or other devices may be

switched off with the built-in relay in case of contact with water.

Important:

Both water electrodes may possibly oxidise depending on the frequency of contact with water and the aggressiveness of water. Galvanized metal parts which are wiped (cleaned) from time to time, if required, are sufficient during normal operation. If the electrodes oxidise too quickly due to very aggressive water (e.g. liquid manure), please use electrodes with a non-oxidising precious metal coat: e.g. gold-plated or coated with platinum (in case of very corrosive liquids, electrodes of titanium are suitable, too).

Use as directed:

Sensor which gives „Alarm“ via a relay contact, if the sensor wires come into contact with water.

Setting into operation:

The 9 V/DC operating voltage is switched on after assembly. The LED at the module lights up and indicates that the module is ready for operation. You may check the readiness for service by touching both water electrodes with 2 wet fingers. The water electrodes then react.

Technical Data:

Operating voltage: 9 V/DC voltage are ideal (max. 12 V/DC), (please do only employ a stabilized power supply) | **Current consumption:** „Ready“ <10 mA. In case of contact with water when the relay picks up <90 mA each with 9 V/DC | **LED displays:** 1 LED for the indication of readiness „POWER“, 1 LED for the indication „ON“, if the relay switches on | **Connections:** via free cables | **Approved cable length towards the water sensors:** max. 5 m with normal cable, max. 100 m with shielded cable, if the shielding braid is connected with the negative pole of the distribution voltage | **Dimensions:** sealing case approx. 60 x 45 x 20 mm (without fastening straps)

ES

Instrucciones para el montaje:

Fijar el módulo fuera de la superficie que se debe controlar por agua (en el sótano p.ej. arriba en la pared). Las líneas de alimentación hacia el suministro de corriente se conectan con una fuente de corriente, p.ej. con un bloque de alimentación de clavija 9 V/DC. El bloque de alimentación debería ser estabilizado y tener un rendimiento mínimo de 100 mA. Conectar los dos cables al módulo que llevan a los sensores de agua con 2 piezas metálicas desnudas y inoxidables. Eso pueden ser p.ej. 2 tornillos galvanizados (M4 - M8). Montar las cabezas de tornillo allá donde se debe controlar la humedad. Los dos tornillos deben ser aislados uno de otro y montados con las cabezas de tornillo desnudas al sitio puesto en peligro por el agua. Si ahora ambas piezas metálicas (cabezas de tornillo) surgen en el agua, el interruptor de agua conmuta: el relé incorporado conecta y el diodo „ON“ electroluminiscente se ilumina. Pues si 2 piezas metálicas montadas aislado (distancia aprox. 1 - 2 cm) del orden de las cabezas de tornillo (aprox. 6 - 10 mm) surgen en el agua al mismo tiempo, el interruptor de agua conecta y desconecta solamente de nuevo cuando las cabezas metálicas no surgen más en el agua. Entonces en caso de contacto con agua se pueden activar por el relé incorporado avisadores de alarma acústicos (p.ej. bocinas) o se pueden conectar bombas por un relé auxiliar o desconectar otros aparatos.

Importante:

Según la frecuencia de contacto con agua y la agresividad del agua, ambos electrodos de agua pueden eventualmente oxidar. Piezas metálicas galvanizadas que se limpian de vez en cuando, si necesario, son suficientes durante el servicio normal. Si los electrodos oxidan demasiado pronto por causa de agua demasiado agresiva (p.ej. abono líquido), se deben emplear electrodos con un recubrimiento de metal precioso inoxidante: p.ej. dorado o recubrimiento de platino (en caso de un líquido corrosivo, electrodos de titanio son también adecuados).

Use previsto:

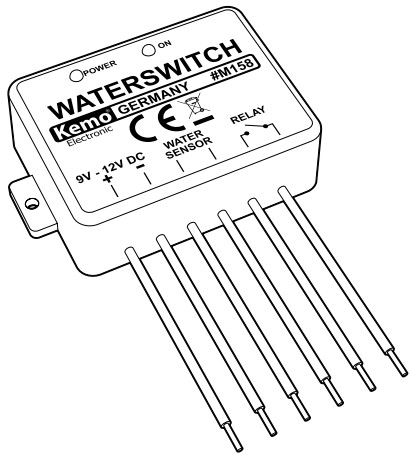
Sensor que da la „alarma“ por un contacto de relé cuando los hilos de sensor entran en contacto con agua.

Puesta en servicio:

Conectar la tensión de servicio de 9 V/DC después del montaje. El LED al módulo se ilumina y indica que el módulo está listo para el servicio. Vd. puede comprobar la disposición de servicio por tocar ambos electrodos de agua con 2 dedos mojados. Entonces el interruptor de agua reacciona.

Datos técnicos:

Tensión de servicio: una tensión continua de 9 V/DC es ideal (máx. 12 V/DC), (emplear solamente una fuente de alimentación estabilizada) | **Absorción de corriente:** „Dispuesto“: <10 mA. En caso de contacto con



DE | Entsorgung: Wenn das Gerät entsorgt werden soll, darf es nicht in den Hausmüll geworfen werden. Es muss an Sammelstellen für Fernsehgeräte, Computer usw. entsorgt werden (bitte erkundigen Sie sich in Ihrem Gemeindebüro oder in der Stadtverwaltung nach Elektronik-Müll-Sammelstellen).

EN | Disposal: This device may not be disposed with the household waste. It has to be disposed at collecting points for television sets, computers, etc. (please ask your local authority or municipal authorities for these collecting points for electronic waste).



agua cuando el relé opera: <90 mA respectivamente con 9 V/DC | **Indicaciones LED:** 1 LED para la indicación de disposición "POWER", 1 LED para la indicación "ON" cuando el relé conecta. | **Conexiones:** por cables libres al descubierto | **Longitud del cable admisible hacia los sensores de agua:** máx. 5 m con cable normal, máx. 100 m con cable apantallado si el trenzado de apantallamiento se conecta con el polo negativo de la tensión de alimentación | **Dimensiones:** sealing case aprox. 60 x 45 x 20 mm (sin eclisas de fijación)

FR

Instructions d'assemblage:

Le module est fixé en dehors de la surface qui doit être surveillée par l'eau (dans la cave p.ex. en haut du mur). Il faut raccorder les lignes électriques vers l'alimentation en courant avec une source de courant, p.ex. avec un bloc d'alimentation de fiche 9 V/DC. Le bloc d'alimentation devrait être stabilisé et avoir une puissance minimale de 100 mA.

Il faut raccorder les deux câbles au module qui mènent aux palpeurs d'eau avec 2 pièces métalliques dénudées et antirouilles. Celles-ci peuvent être p.ex. 2 vis galvanisées (M4 - M8). Montez les têtes de vis là où l'humidité doit être surveillée. Il faut que les vis soient isolées l'une de l'autre et montées avec les têtes de vis dénudées à l'endroit qui est en danger pour l'eau. Quand maintenant les deux pièces métalliques (têtes de vis) trempent dans l'eau, l'interrupteur d'eau commutera: le relais incorporé connecte et la diode électroluminescente « ON » s'allume. Donc si 2 pièces métalliques montées isolément (distance env. 1 - 2 cm) de l'ordre des têtes de vis (env. 6 - 10 mm) trempent dans l'eau en même temps, l'interrupteur d'eau connecte. Il déconnecte seulement de nouveau quand les deux têtes de vis ne trempent plus dans l'eau.

Alors en cas de contact avec l'eau on peut activer avec le relais incorporé des avertisseurs d'alarme acoustiques (p.ex. klaxons) ou connecter des pompes par un relais auxiliaire ou déconnecter d'autres appareils.

Important:

Selon la fréquence du contact avec l'eau et l'agressivité de l'eau, les deux électrodes d'eau peuvent éventuellement oxyder. Des pièces métalliques galvanisées qui sont essuyées (nettoyées) de temps en temps, si nécessaire, sont suffisantes pendant le service normal. Si les électrodes oxydent trop vite par suite de l'eau trop agressive (p.ex. purin), veuillez employer des électrodes avec une couche de métal précieux non-oxydante: p.ex. doré ou recouvert de platine (en cas d'un liquide très caustique, les électrodes de titane sont aussi convenables).

Emploi conformément aux dispositions:

Palpeur qui donne « l'alarme » par un contact du relais quand les fils de palpeur entrent en contact avec l'eau.

Mise en service:

La tension de service 9 V/DC est connectée après l'assemblage. La DEL au module s'allume et indique que le module est prêt à fonctionner. Vous pouvez contrôler l'ordre de marche par toucher les deux électrodes d'eau avec 2 doigts mouillés. Ensuite l'interrupteur d'eau réagit.

Données techniques:

Tension de service: une tension continue de 9 V/DC est idéale (max. 12 V/DC), (employer seulement un bloc d'alimentation stabilisé) | **Consommation de courant:** « Prêt »: <10 mA. En cas de contact avec l'eau quand le relais excite: <90 mA chaque fois à 9 V/DC | **Affichages DEL:** 1 DEL pour l'indication de la disponibilité « POWER », 1 DEL pour l'indication « ON » quand le relais connecte | **Raccords:** par des câbles sortis | **Longueur de câble admisible vers les palpeurs d'eau:** max. 5 m avec du câble normal, max. 100 m avec du câble blindé si le treillis de blindage est raccordé avec le pôle négatif de la tension d'alimentation | **Dimensions:** sealing case env. 60 x 45 x 20 mm (sans éclisses de fixation)

NL

Montage voorschriften:

Het moduul wordt buiten het wateroppervlak gemonteerd, bijvoorbeeld in de kelder, bovenin aan de muur. Als voeding moet u een gestabiliseerde 9 V/DC voeding gebruiken van minstens 100 mA.

De beide draden van het moduul, die als water voelers werken, worden met 2 blanke (geen roestige) draden aangesloten. Tip: 2 roestvaste schroeven (M4 - M8) kunt u hiervoor al gebruiken. De schroeven worden zo geplaatst dat het functioneert, dus niet scheef, of te hoog/laag. Als het water stijgt en de schroeven vochtig worden, er contact gemaakt wordt. Hierna schakelt het relais in, en de led "ON" gaat op lichten. Als de 2 geïsoleerde en gemonteerde (afstand ca. 1 - 2 cm) metaal delen, met een afmeting van schroefkoppen (ca. 6 - 10 mm) gelijktijdig het water aanraken, schakelt de watermelder in, deze melder gaat pas weer uit als beide voelers geen water of vochtigheid meer voelen.

Met het ingebouwde relais, kan bij watercontact, de akoestische alarmmelder activeren (bijvoorbeeld claxonneren) of met behulp van een zwaardere relais kan een waterpomp of iets anders ingeschakeld worden.

Belangrijk:

De beide water elektroden (stangen met de schroef er aan), kan afhankelijk van de vochtigheid of gebruik gaan oxideren (roesten). Als er roestvast materiaal is gebruikt, moet u dit toch af en toe gaan reinigen, en droog maken. Mocht water zeer agressief zijn (bijvoorbeeld gier), gebruik dan elektroden die verguld zijn of met platina geïmpregneerd is of titaan.

Speciale toepassing:

Sensor, die bij het aanraken van vochtigheid/water een relais in schakelen en alarm geeft.

Ingebruikname:

Na de montage wordt de 9 V/DC voedingsspanning aangesloten. De led van het moduul licht op en geeft aan dat het gereed is. U kunt alles controleren door middel van 2 natte vingers beide voelers aan te raken, als het. Goed is schakelt het moduul in.

Technische gegevens:

Voedingsspanning: 9 V/DC gelijkspanning max 12 V/DC, alleen een gestabiliseerde netvoeding gebruiken | **Stroomopname:** "gereed" <10 mA. Bij aanraking van water, en het relais schakelt in: <90 mA bij 9 V/DC | **Led indicatie:** 1 led voor "gereed", en 1 led voor "ON" als het relais in schakelt | **Aansluiting:** aan de draden die buiten het moduul bevinden | **Toegestane kabel lengtes naar de voelers toe:** max. 5 meter met een normale draad, en max.

100 meter met een afgeschermde kabel, en dat de afscherming aan de van de voeding aangesloten is | **Afmeting:** sealing case ca. 60 x 45 x 20 mm (zonder bevestigings ogen)

PL

Instrukcja montażu:

Moduł jest mocowany poza płaszczyznę, która ma być monitorowana pod kątem wody (w piwnicy np. na górze na ścianie). Przewody doprowadzające do zasilania prądowego zostają połączone ze źródłem prądu, np. z zasilaczem sieciowym 9 V/DC. Zasilacz powinien być stabilizowany i mieć moc przynajmniej 100 mA.

Oba kable na module, prowadzące do czujników wody, zostają połączone z 2 niez izolowanymi, nierdzewnymi metalowymi częściami. Mogą to być np. 2 ocynkowane śruby (M4 - M8). Łebki śrub zostają zamontowane tam, gdzie ma być monitorowana wilgoć. Obie śruby muszą być od siebie odizolowane i zamontowane odkrytymi łebkami śrub w miejscu zagrożonym wodą. Jeśli teraz obie metalowe części (łebki śrub) zetkną się z wodą, to wyłącznik wodny zadziała. Wbudowany przekaźnik przełączy na „WŁĄCZONE” i rozbłyska dioda świecąca „ON”. Jeśli 2 zaizolowane zamontowane metalowe części (odstęp ok. 1 - 2 cm) o wielkości łebków od śruby (ok. 6 - 10 mm) zetkną się jednocześnie z wodą, to zadziała wyłącznik wodny. Odłączy się on ponownie dopiero wtedy, gdy obie metalowe łebki nie będą już zanurzone w wodzie. Dzięki wbudowanemu przekaźnikowi można z chwilą zetknięcia z wodą albo aktywność akustyczne czujniki alarmowe (np. klakson, syrena) albo przy pomocy pomocniczych przekaźników włączyć pompę lub odłączyć inne urządzenia.

Ważne:

Obie elektrody wodne mogą ewentualnie się utleniać, w zależności od tego, jak często stykają się z wodą oraz od tego, jak żrąca jest ta woda. Zazwyczaj wystarczające są ocynkowane metalowe części, które od czasu do czasu zostają przetarte na mokro (oczyszczone), jeśli jest to konieczne. Jeśli elektrody utleniają się zbyt szybko, np. wskutek oddziaływania żrącej wody (np. gnojówka), wówczas należy użyć elektrod o nieoksydowanej powłoce ze szlachetnego metalu: np. polzacane albo polwoczonej platyną (w przypadku silnie żrącej cieczy odpowiednio są również elektrody z tytanu).

Użytkowanie zgodne z przeznaczeniem:

Czujnik, który przy zetknięciu końcówek z wodą wyzwala alarm poprzez przekaźnik.

Uruchomienie:

Po zamontowaniu włączone zostaje napięcie robocze 9 V/DC. Dioda LED na module rozbłyska i pokazuje, że moduł jest gotowy do pracy. Mogą Państwo sprawdzić tę gotowość, dotykając 2 mokrymi palcami do obu elektrod wodnych. Czujnik wody powinien wówczas zareagować.

Dane techniczne:

Napięcie robocze: 9 V/DC idealnie, (maks. 12 V/DC), (prosimy używać tylko stabilizowanego zasilacza) | **Pobór prądu:** „Gotowy” <10 mA. Przy zetknięciu z wodą, gdy przekaźnik przyciągnie <90 mA, każdorazowo przy 9 V/DC | **Wskazania na diodach LED:** 1 dioda LED do wskazywania gotowości do pracy „POWER”, 1 dioda LED do wskazywania „ON”, gdy przekaźnik włącza | **Podłączenia:** wyprowadzonymi kablami | **Dopuszczalna długość kabla do czujników wody:** maks. 5 m normalnym kablem, maks. 100 m kablem ekranowanym, jeśli plecionka ekranująca jest połączona z biegunem ujemnym napięcia zasilającego | **Wymiary:** szelczona obudowa modułu ok. 60 x 45 x 20 mm (bez końcówek do zamocowania)

PT

Instruções de montagem:

O modulo é fixado fora da área que é para vigiar a água (na cave por exp. em cima na parede). A linha adutora para o abastecimento de corrente é ligada com uma fonte de tensão, por exp. com uma ficha de equipamento de alimentação a partir da rede de 9 V/DC. O equipamento de alimentação a partir da rede deve ser estabilizado e ter uma potência mínima de 100 mA.

Os dois cabos no modulo, que levam aos sensores de água, são ligados com dois cabos nus, peças metálicas que não enferrugem. Podem ser por exp. 2 galvanizados parafusos (M4 - M8). As cabeças dos parafusos são montados onde a humidade deve ser vigiada. Os dois parafusos devem ser isolados um do outro e com as suas cabeças dos parafusos ser montados no lugar arriscado a água. Quando agora as duas peças metálicas (cabeças dos parafusos) mergulharem na água, liga o interruptor de água: o montado relé liga e o diodo luminoso "ON" brilha. Quando então 2 isoladas montadas (distância ca. 1 - 2 cm) peças metálicas do tamanho da cabeça de parafusos (ca. 6 - 10 mm) mergulharem na água ao mesmo tempo, liga o interruptor de água. Este desliga só então quando as duas cabeças dos parafusos não se encontram mergulhadas na água.

Com o montado relé podem então em contacto com água ser activados acústicos avisadores de alarme (por exp. buzinar) ou sobre relé auxiliar podem ser ligados bombas ou serem desligados outros aparelhos.

Importante:

Os dois eléctrodos da água podem possivelmente oxidar, conforme a frequência do tocar na água e a agressão da água. Em aviso normal é suficiente peças metálicas galvanizadas, que de vez em quando devem ser enxugadas (limpas) quando necessário. Quando os eléctrodos por causa de água muito agressiva (por exp. líquido que corre do estrome) oxidarem muito depressa, então deve usar eléctrodos com uma não oxidável cobertura de metal nobre: por exp. cobertura dourada ou com platina (em forte corrosivos líquidos são também adequados eléctrodos de titânio).

Use conforme as disposições legais:

Sensor que em contacto com água, os cabos dos sensores sobre um relé de contacto dá "Alarme".

Colocação em funcionamento:

Depois da montagem é a tensão de serviço de 9 V/DC ligada. O LED no modulo brilha e indica que o modulo está pronto para entrar em funcionamento. Pode examinar o estado de prontidão para entrar em serviço, quando com os dedos molhados tocar nos dois eléctrodos de água. Então reage o interruptor de água.

Dados técnicos:

Tensão de serviço: ideal tensão contínua 9 V/DC (máx. 12 V/DC), (por favor só utilizar estabilizados equipamentos de alimentação a partir da rede) | **Consumo de corrente:** "Pronto": <10 mA. Em contacto com água, quando o relé puxa: <90 mA respectivamente em 9 V/DC | **LED indicação:** 1 LED para a indicação de

prontidão "POWER", 1 LED para a indicação "ON", quando liga o relé | **Ligação:** sobre dois cabos saídos por fora | **Admitido comprimento dos cabos para os sensores de água:** máx. 5 m com cabo normal, máx 100 m com cabo blindado, quando o trançado de fios com o pólo negativo da tensão de alimentação é ligada | **Medida:** sealing case ca. 60 x 45 x 20 mm (sem braçadeira de fixação)

RU

Инструкция по монтажу:

Модуль необходимо прикрепить в сухом месте, неподалеку от места контроля уровня воды (напр. в подвале сверху на стене). После этого подключите к модулю постоянное напряжение питания 9 Вольт. Напр. стабилизированный сетевой источник питания мощностью не менее 100 мА.

Оба кабеля модуля для подключения датчиков уровня воды, необходимо соединить с двумя неизолированными, нержавеющими металлическими электродами. В качестве электродов могут послужить напр. два оцинкованных шурупа (M4 - M8). Головки шурупов необходимо закрепить в таком месте, где происходит контроль уровня воды. Шурупы должны быть между собой электрически изолированы и прикреплены в месте контроля. Если уровень воды поднимется и оба шурупа окажутся под водой, включается датчик уровня воды: встроенное реле включается и загорается светодиод «On» (Рэле включено). И так, если оба электрически изолированных между собой электрода (толщиной 6 - 10 мм) прикрепленные на расстоянии приблизительно 1 - 2 см между собой одновременно окажутся под водой, включается датчик уровня воды. И выключается он только тогда, если электроды больше не находятся в воде.

Посредством встроенного реле можно при достижении определенного уровня воды активировать акустический сигнал (напр. гудок) или с помощью вспомогательного реле включить насос или другие приборы.

Внимание:

При очень частом соприкосновении с водой оба электрода могут окислиться. При нормальных условиях достаточно применить оцинкованные металлические электроды и время от времени их очищать. Если электроды из-за агрессивной воды (напр. фекальная жидкость) очень быстро окисляются, используйте тогда пожалуйста электроды с покрытием из нержавеющей стали, напр. покрытые золотом или платиной (для щелочных жидкостей можно использовать титановые электроды).

Инструкция по применению:

Модуль представляет собой сенсорный датчик, который после соприкосновения его сенсорных контактов с водой подает сигнал при помощи встроенного реле.

Пуск в рабочий режим:

После монтажа нужно подключить к модулю постоянное рабочее напряжение 9 Вольт. Светодиод на модуле загорается и дает индикацию, что модуль готов к работе. Готовность к работе вы можете проверить следующим образом: мокрыми пальцами прикоснитесь к обоим электродам. Датчик уровня воды сразу реагирует.

Технические данные:

Рабочее напряжение: 9 Вольт (макс. 12 Вольт), (пожалуйста применяйте только стабилизированный сетевой источник питания) | **Потребление тока:** При выключенном реле: <10 мА. При включенном реле после соприкосновения с водой: <90 мА в обоих случаях при напряжении 9 Вольт | **Индикация посредством светодиодов:** «Power» - светодиод для индикации готовности, «On» - светодиод показывает, что реле включено | **Подсоединение:** посредством выведенных кабелей | **Допустимая длина кабеля для сенсора воды:** Макс. 5 м нормального кабеля, или макс. 100 м экранированного кабеля, и если экранировка соединена с минусовым полюсом источника напряжения питания | **Габариты:** sealing case приблизительно 60 x 45 x 20 мм (без крепящих планок)

DE | Wichtig: Bitte beachten Sie die extra beiliegenden "Allgemeingültigen Hinweise" in der Drucksache Nr. M1002. Diese enthält wichtige Hinweise der Inbetriebnahme und den wichtigen Sicherheitshinweisen! Diese Drucksache ist Bestandteil der Beschreibung und muss vor dem Aufbau sorgfältig gelesen werden.

EN | Important: Please pay attention to the "General Information" in the printed matter no. M1002 attached in addition. This contains important information starting and the important safety instructions! This printed matter is part of the product description and must be read carefully before assembling!

ES | Importante: Observar las "Indicaciones generales" en el impreso no. M1002 que se incluyen además, ¡Elas contienen informaciones importantes la puesta en servicio y las instrucciones de seguridad importantes! ¡Este impreso es una parte integrante de la descripción y se debe leer con esmero antes del montaje!

FR | Important: Veuillez observer les « Renseignements généraux » dans l'imprimé no. M1002 ci-inclus. Ceci contient des informations importantes la mise en marche et les indications de sécurité importantes! Cet imprimé est un élément défini de la description et il faut le lire attentivement avant l'ensemble!

NL | Belangrijk: Belangrijk is de extra bijlage van "Algemene toepassingen" onder nr. M1002. Deze geeft belangrijke tips voor het monteren het ingebruik nemen en de veiligheids voorschriften. Deze pagina is een onderdeel van de beschrijving en moet voor het bouwen zorgvuldig gelezen worden.

PL | Ważne: Proszę przestrzec uw uwagę zawartych w dołączonym druku „Ogólne obowiązujące zalecenia” Nr M1002. Broszura ta zawiera ważne informacje dotyczące uruchomienia i bezpieczeństwa! Jest ona częścią instrukcji i musi być przed montażem dokładnie przeczytana.

PT | Importante: Por favor tomar atenção com o extra "Indicações gerais válidas" o junto impreso M1002. Este contém importantes indicações a colocação em funcionamento e importantes indicações de segurança! Este impreso é um elemento da descrição que deve cuidadosamente ler antes da montagem!

RU | Важное примечание: Пожалуйста обратите внимание на отдельно приложенные «Общедействующие инструкции» в описании No. M1002. Это описание содержит важные инструкции введения в эксплуатацию, и важные замечания по безопасности. Этот документ является основной частью описания по монтажу и должен быть тщательно прочитан до начала работы!